Understanding Hydrological Cycling at High Elevations and in Forest Canopies using Stable Water Isotopes

by

Richard Pascal Fiorella

A dissertation submitted in partial fulfillment
of the requirements for the degree of
Doctor of Philosophy
(Geology)
in the University of Michigan
2016

Doctoral Committee:

Professor Christopher J. Poulsen, Chair
Professor Maria C. Cruz Da Silva Castro
Associate Professor Mark G. Flanner
Associate Professor Nathan A. Niemi
Associate Professor Nathan D. Sheldon

Acknowledgments

I am extremely thankful for the support I have received from many, many individuals during my graduate school journey; without this support, this dissertation would not have been possible. First and foremost, I owe my success to my advisor Chris Poulsen and his constant support, guidance, patience and motivation to improve the quality of my work and build my career as a scientist. The projects in this dissertation would not have been possible without such a supportive and open-minded advisor. I hope to continue both our scientific collaboration and friendship in the future. I would also like to thank the rest of my dissertation committee for their helpful, friendly suggestions and support to improve the quality of this dissertation: Clara Castro, Mark Flanner, Nathan Niemi, and Nathan Sheldon. I owe a great debt to the office staff of the University of Michigan Department of Earth and Environmental Sciences, especially Anne Hudon and Nancy Kingsbury, for their patience and assistance in helping me navigate any and all administrative tasks that arose. Finally, I am thankful to the funding sources that supported my research as a graduate student: the NSF Graduate Research Fellowship Program, the UM Department of Earth and Environmental Sciences Turner Fund, the UM Rackham International Research and Graduate Research Awards, and the GSA Graduate Student Research Award.

I have also been lucky enough to be surrounded by a tremendously supportive network of friends and family that have helped me grow as a researcher, teacher, and person. My lab group has been incredibly supportive and I have learned a great deal from them; a big thanks to Clay, Ran, Dan H., Louise, Nadja, Brian, Jing, Chris S., Sierra, Phoebe, Dan L., Chana, and Dora. Outside of the lab group, it is hard to imagine a more supportive and friendly environment than that created by my fellow graduate students in the Department of Earth and Environmental Sciences; thanks especially to Ethan, Carli, Jen, Tim, Allie, Tara, Tom, Meghan, Laura, Lydia, Rohit, Petr, and Alex. Thanks to my family, especially my parents, for their constant encouragement and support to be the best that I can be. Finally, thanks to Caitlin for joining me on this adventure, and for her patience, support, love, and understanding during my graduate career. I am prepared and excited to face what comes next because of all of you.

For specific chapters:

A staggering amount of individuals contributed to chapter 2. Chris Poulsen, Ramiro Pillco Zolá, Jason Barnes, Clay Tabor, and Todd Ehlers contributed to and provided feedback on the manuscript, which substantially improved the quality of this study. I would also like to thank two anonymous reviewers and editor Chidong Zhang. Jaime Tito, Sohrab Tawackoli, Gregorio Gonzalez, Louise Jeffery, and Michelle Tracy provided field support and logistics. I'd like to thank the observers at the isotope measuring stations for their diligence in collecting precipitation samples: Juan José Montalvo, Justina Vacaflor, Freddy Chinchi, Felix Tito Coca, Gabriel Puquimia, Donicio Choque, Miguel Delgado Choque, Porfirio Huarta Llave, Luisa Aizama de Chavarría, Ivan Farfan Huallpa, Freddy Vargas, and Fidel Guerrero. Finally, I would like to thank the funding sources that contributed to this work. At the University of Michigan, the Rackham Graduate School supported this work through a Graduate Student Grant and an International Research Award. The Department of Earth and Environmental Sciences supported this work through two Scott Turner Research awards. The UM Associate Professor Fund also provided funding to CJP for this project. Finally, NSF supported this work under EAR grants 0738822 and 0907817 to CJP and TAE.

For chapter 3, I would like to thank my coauthors on this manuscript for their input and suggestions that improved this work greatly: Chris Poulsen, Ramiro Pillco Zolá, Louise Jeffery, and Todd Ehlers. Clay Tabor and Michelle Tracy provided assistance in the field collecting samples. I would also like to thank Jaime Tito and Gregorio Gonzalez for ensuring that we could get anywhere we wanted to go in Bolivia safely. I would also like to thank an anonymous reviewer, Joel Saylor, and editor An Yin for comments during the manuscript review process that improved the quality of this chapter.

For chapter 4, I would like to thank my coauthors for their input and support: Chris Poulsen, Ashley Matheny, and Gil Bohrer. Clay Tabor and Caitlin Weber also provided assistance in the field that helped make this work possible. I would also like to thank my hiking partners that indulged my need to grab stream samples throughout the Gros Ventres and Bridger-Teton Wildernesses: Tara Smiley and Sam Walker. I would also like to thank Chris Malvica for helping to accommodate this research at Camp Davis, and his work assisting us with installing necessary research infrastructure. Finally, I would like to thank Andrew Collins for helping me

assemble the isotope shed at Camp Davis, which provided the home to the Picarro analyzer for three summers.

Finally, for chapter 5: The exceptionally collaborative environment at the University of Michigan Biological Station (UMBS) was revelatory to me. I would like to thank Knute Nadelhoffer for originally inviting Chris Poulsen to UMBS to show us the breadth of ongoing projects at UMBS. Several other researchers at UMBS provided data and ideas in putting together this study: Ashley Matheny, Gil Bohrer, Christoph Vogel, Alex Fotis, Chris Gough, and Luke Nave.

Table of Contents

List of Figures

List of Tables

Abstract

Stable water isotopes represent a powerful tracer of the thermodynamic history of water in an air parcel, and are also thought to be preserved in a wide array of geologic proxy materials. As a result, the isotopic compositions of proxy materials in continental environments are commonly used to estimate past climates, elevations, or environments. However, the modern controls on the spatiotemporal distribution of stable water isotopes are poorly understood in many environments.

This dissertation addresses uncertainties in modern water cycling in high elevation regions and in forest canopies, with an eye toward understanding how these processes may impact our interpretation of proxy material isotopic compositions. Chapters 2 and 3 present multiyear records of the isotopic composition of precipitation and surface waters in the central Andes, respectively. Chapter 2 elucidates a strong connection between the isotopic composition of precipitation and continental-scale climate dynamics. These measurements affirm elevation as a primary control on isotopic composition, but this relationship varies substantially in space and time. Chapter 3 demonstrates that surface water isotopes reflect precipitation isotopes along the eastern Andean flank, but are evaporatively modified on the high elevation plateau, where the majority of paleoelevation proxies have been recovered. Coupled with paleoclimate simulations that indicate the Andes were likely more evaporative when they were lower, these results suggest that prior estimates of Neogene elevation change from stable isotope proxies are likely too high. Chapter 4 presents seasonal and interannual records of the isotopic composition of near-surface water vapor in a deep mountain valley, and demonstrates the influences that local and remote processes have on near-surface vapor. Chapter 5 investigates how an intermediate canopy disturbance influences water cycling in a northern Michigan forest by analyzing the vertical structure of the isotopic composition of near-surface vapor. These observations highlight the utility of stable water isotopes to constrain a wide array of process-level information unavailable from measurements of water mass fluxes alone. Further, they illustrate the potential for long-term isotope monitoring to detect local-to-regional changes in atmospheric moisture transport

and ecohydrology and validate predictions of land-atmosphere water exchange fluxes in land surface and Earth system models.

Chapter 1. Introduction and Context

Water is a critical component of the Earth's energy and carbon cycles. The terrestrial hydrological cycle represents a balance between precipitation, surface runoff, and evapotranspiration (ET). Perhaps as much as 50% of the total solar energy absorbed at the land surface is consumed by the ET flux as latent heat from evaporating water [*Trenberth et al.*, 2009]. Once in the atmosphere, water vapor exerts the strongest radiative effect of any atmospheric greenhouse gas [*Held and Soden*, 2000] and is essential to Earth's habitability. Atmospheric water vapor is also acutely responsive to changes in global temperature. Changes in the radiative influence of water vapor with temperature represents the single largest amplifying feedback in the modern climate [*Held and Soden*, 2000; *Bony et al.*, 2006; *Soden and Held*, 2006]. In terrestrial environments, transpiration flux (T in ET) couples the water cycle to the carbon cycle, as plants release water in order to assimilate carbon. Therefore, addressing uncertainties in the modern hydrologic cycle also informs our understanding of how energy and carbon move through the environment.

In addition to its influence on modern climate, past changes in the hydrological cycle have direct impacts on how we understand and reconstruct past environments [*Barron et al.*, 1989; *Pierrehumbert*, 2002]. Many paleoenvironmental proxies in continental settings either directly preserve paleowaters (e.g., ice cores and fossil groundwater), or form in contact with water (e.g., pedogenic carbonates, hydrated clays, and volcanic glass). Many of these materials preserve a proxy record of the stable isotope composition of past waters. The modern distribution of water isotopes is broadly dependent on climatology and elevation [e.g., *Dansgaard*, 1964; *Siegenthaler and Oeschger*, 1980; *Bowen and Wilkinson*, 2002], and therefore, past water isotopic compositions are thought to provide a record of past climates and/or past elevations.

This thesis seeks to address uncertainties in modern water cycling processes using stable water isotopes, with an eye toward using improved understanding of modern processes to inform the interpretation of proxy material isotopic compositions. The first half of this thesis explores isotopic compositions of precipitation and surface waters in the high central Andes, and relates them to proxy records of paleoclimate and paleoelevation. The second half of this thesis focuses

on the isotopic composition of atmospheric water vapor in two different environments: a deep, high elevation mountain valley and two forest canopies thought to represent different forest successional states.

1.1 Stable isotope introduction

Stable water isotopes are a useful recorder of environmental processes that transport water and water vapor. Their utility arises from an unequal partitioning of heavy and light stable isotopes during phase changes. In any phase change, the more condensed phase (e.g., liquid or ice) retains or gains more of the heavy stable isotope than the less condensed phase (e.g., vapor or liquid) [*Gat*, 1996]. The partitioning is small, and therefore, isotopic compositions (δ) are typically expressed as part-per-thousand deviations from an international standard:

$$\delta = 1000\left(\frac{R_{sample}}{R_{std}} - 1\right)$$

where R is the heavy-to-light isotope ratio of the element of interest. Water compositions are typically expressed relative to Vienna Standard Mean Ocean Water, VSMOW [*Coplen*, 1996]. Partitioning between phases can occur due to both equilibrium and kinetic fractionations. Equilibrium fractionation between two phases of water depends solely on temperature [*Majoube*, 1971; *Horita and Wesolowski*, 1994]. Kinetic fractionation occurs when phases are unable to reach equilibrium, and is most commonly associated with evaporation. During evaporation, isotopes of hydrogen and oxygen are partitioned unequally due to differences in molecular diffusivity [*Merlivat and Jouzel*, 1979; *Cappa et al.*, 2003; *Barkan and Luz*, 2007]. Due to the changes in isotopic composition induced by these fractionations, the isotopic composition of water in an air parcel represents an integrated history of evaporation, condensation, advection, and atmospheric mixing [e.g., *Gat*, 2000; *Galewsky and Hurley*, 2010; *Noone*, 2012].

Stable water isotopes have been applied to many disparate areas of the modern and paleo hydrological cycle. Precipitation isotopes, for example, have been used as tracers of moisture transport pathways [*Dansgaard*, 1964; *Rozanski et al.*, 1993]. Water isotopes in plant xylem record the water pools used within different ecosystems, and have shown that not all environmental water pools near the surface are accessible to plants [*Brooks et al.*, 2009; *Good et al.*, 2015]. Water vapor isotope compositions have also been used to understand microphysical processes within clouds [*Galewsky et al.*, 2011; *Bailey et al.*, 2015]. Stable water isotopes have

also been an invaluable tool to reconstruct the paleohydrologic cycle, as many proxies of past environments rely on stable water isotopes. Proxy materials such as ice cores [*Jouzel et al.*, 1982; *Grootes et al.*, 1989; *Petit et al.*, 1999; *Schoenemann et al.*, 2014] and fossil groundwaters [e.g., *Rozanski*, 1985; *Dutton et al.*, 2005] directly preserve the isotopic composition of paleowaters. An even wider array of geological and biological proxy materials are thought to form in equilibrium with environmental waters and thus indirectly preserve paleowater compositions. The stable isotopic compositions of pedogenic carbonates [e.g., *Cerling and Quade*, 1993], meteoric calcite cements [e.g., *Fan et al.*, 2014], speleothems [e.g., *Novello et al.*, 2012], hydrated volcanic glass [e.g., *Cassel et al.*, 2014; *Saylor and Horton*, 2014], authigenic clays [e.g., *Mulch and Chamberlain*, 2007], mollusk shells [e.g., *Dettman and Lohmann*, 2000], and fossil enamel [e.g., *Clementz and Sewall*, 2011], among other materials, have all been used as paleoenvironmental proxy materials. Their use as proxy materials requires an understanding of the mechanism of how proxy materials acquire their isotopic composition from the water they are in contact with, as well as the environmental controls on environmental water compositions today as well as in the past. This thesis focuses primarily on the latter of these issues.

1.2 Overview of this dissertation

In addition to this introduction (Chapter 1) and concluding remarks (Chapter 6), this dissertation contains four studies that use stable water isotopes to better understand modern and past hydrologic cycling. Chapters 2 and 3 explore stable isotopes in natural waters of the high central Andes and their implications for paleoproxy interpretations. Chapter 2 investigates the relationship between precipitation isotopes and continental-scale atmospheric circulation [*Fiorella et al.*, 2015b]. These results were the first observational dataset of the isotopic composition of precipitation on the high central Andean plateau (the Altiplano), and validate predictions of South American climate controls on high Andean precipitation isotopes [*Insel et al.*, 2013]. Chapter 3 builds on the study of central Andean precipitation isotopes by incorporating surface water isotopes from the Altiplano and from along its eastern flank [*Fiorella et al.*, 2015a]. Surface waters on the Altiplano, where the bulk of paleoproxy materials have been sampled, exhibit evidence of evaporation not observed along the eastern flank transects. Using a regional climate model, we show that uplift of the Andes through the Cenozoic has decreased regional aridity. Together, these observational and modeling results suggest that

proxy values taken to represent baseline elevations in central Andes paleoaltimetry studies have likely been evaporatively altered, and interpretations from these values would be prone to underestimate baseline elevations. A revised paleoaltimetric history using only the most negative carbonate compositions recorded, based on the assumption that they are the least influenced by evaporation, suggest an uplift history more concordant with inferred crustal deformation [e.g., *Oncken et al.*, 2006] than previous interpretations that used mean isotopic compositions [e.g., *Garzione et al.*, 2006; 2014]. Chapters 4 and 5 investigate water cycling through modern terrestrial environments using the isotopic composition of near surface water vapor. Chapter 4 examines hydrologic cycling in a deep, continental mountain valley in northwestern Wyoming across seasonal and diurnal timescales. This work demonstrates that both large-scale and local processes leave distinctive, seasonally-dependent fingerprints on near surface humidity. Chapter 5 explores how forest canopy disturbance can influence transpiration and atmospheric mixing. Forest canopy structure and species composition can influence the magnitude and variability of environmental fluxes of carbon and water. The University of Michigan Biological Station has two forest plots located ~2 km apart, where an accelerated ecological succession experiment was initiated in 2008. In this treatment, mortality was induced in all individuals of the early successional species. Vertical profiles of isotopic composition show stark differences in diurnal cycles between the two sites, indicating that forest canopy structure and species composition strongly influences water vapor cycling within the canopy. Together, chapters 4 and 5 demonstrate the potential role for atmospheric water vapor isotopes to examine changes in regional hydrological budgets, such as changes in the amount of atmospheric advection relative to evapotranspiration, and provide additional constraints to improved parameterizations of land surface processes in Earth system models.

1.3 Publications and Conference Abstracts Resulting from this dissertation

1.3.1 Publications (peer-reviewed)

Fiorella, R.P., Poulsen, C.J., Pillco Zolá, R.S., Barnes, J.B., Tabor, C.R., and Ehlers, T.A. (2015). Spatiotemporal variability of modern precipitation $\delta^{18}O$ in the central Andes and implications for paleoclimate and paleoaltimetry estimates. Journal of Geophysical Research - Atmospheres, vol. 120(10), p. 4630-4656. doi: 10.1002/2014JD022893. (Chapter 2)

Fiorella, R.P., Poulsen, C.J., Pillco Zolá, R.S., Jeffery, M.L., and Ehlers, T.A. (2015). Modern and long-term evaporation of central Andes surface waters suggests paleo archives underestimate Neogene elevations. Earth and Planetary Science Letters, vol. 432, pp. 59-72. doi:10.1016/j.epsl.2015.09.045 (Chapter 3)

Fiorella, R.P., Poulsen, C.J., Matheny, A.M., and Bohrer, G. (In preparation). Seasonal and diurnal patterns of water vapor cycling in a deep, continental mountain valley inferred from water vapor stable isotopes and sap flux measurements. (Chapter 4)

Fiorella, R.P., Matheny, A.M., Poulsen, C.J., Bohrer, G., Rey Sanchez, A.C., Fotis, A.F., and Vogel, C.S. (in preparation). The impacts of moderate forest disturbance on the stable isotopic composition on forest canopy vapor and forest-atmosphere water exchange (Chapter 5)

1.3.2 Conference Abstracts

Fiorella, R.P., Matheny, A.M., Poulsen, C.J., and Bohrer, G. (2015). Constraints on water cycling in a deep mountain valley from stable water isotope and sap flux measurements. Abstract PP11B-2220 presented at 2015 Fall Meeting, AGU, San Francisco, California, 14-18 December.

Poulsen, C.J., Feng, R., and Fiorella, R.P. (2014). The role of topography on continental water cycling and water stable isotope compositions over geological time scales. Abstract PP33F-01 presented at 2014 Fall Meeting, AGU, San Francisco, California, 15-19 December.

Fiorella, R.P., Poulsen, C.J., Pillco Zolá, R.S., Jeffery, M.L., and Ehlers, T.A. (2014). Incorporating evaporation histories into paleoaltimetry reconstructions: An Andean case-study: Geological Society of America Abstracts with Programs, vol. 46, no. 6, p. 806. Vancouver, British Columbia, Canada, 19-22 October.

Fiorella, R.P., Poulsen, C.J., Pillco Zolá, R.S., Jeffery, M.L., and Ehlers, T.A. (2012). Exceptional isotopic variability in stream waters of the central Andes: Large-scale or local controls? Abstract B32A-07 presented at 2012 Fall Meeting, AGU, San Francisco, California, 3-7 December.

1.4 References

Bailey, A., J. Nusbaumer, and D. Noone (2015), Precipitation efficiency derived from isotope ratios in water vapor distinguishes dynamical and microphysical influences on subtropical atmospheric constituents, *J Geophys Res-Atmos*, 1–19, doi:10.1002/(ISSN)2169-8996.

Barkan, E., and B. Luz (2007), Diffusivity fractionations of $H_2{}^{16}O/H_2{}^{17}O$ and $H_2{}^{16}O/H_2{}^{18}O$ in air and their implications for isotope hydrology, *Rapid Commun. Mass Spectrom.*, *21*(18), 2999–3005, doi:10.1002/rcm.3180.

Barron, E. J., W. W. Hay, and S. Thompson (1989), The hydrologic cycle: A major variable during earth history, *Palaeogeography, Palaeoclimatology, Palaeoecology*, *75*(3), 157–174, doi:10.1016/0031-0182(89)90175-2.

Bony, S. et al. (2006), How Well Do We Understand and Evaluate Climate Change Feedback Processes? *J. Climate*, *19*(15), 3445–3482, doi:10.1175/jcli3819.1.

Bowen, G. J., and B. Wilkinson (2002), Spatial distribution of $\delta^{18}O$ in meteoric precipitation, *Geology*, *30*(4), 315, doi:10.1130/0091-7613(2002)030<0315:sdooim>2.0.co;2.

Brooks, J. R., H. R. Barnard, R. Coulombe, and J. J. McDonnell (2009), Ecohydrologic separation of water between trees and streams in a Mediterranean climate, *Nature Publishing Group*, *3*(2), 100–104, doi:10.1038/ngeo722.

Cappa, C. D., M. B. Hendricks, D. J. DePaolo, and R. C. Cohen (2003), Isotopic fractionation of water during evaporation, *Journal of Geophysical Research*, *108*(D16), doi:10.1029/2003jd003597.

Cassel, E. J., D. O. Breecker, C. D. Henry, T. E. Larson, and D. F. Stockli (2014), Profile of a paleo-orogen: High topography across the present-day Basin and Range from 40 to 23 Ma, *Geology*, *42*(11), 1007–1010, doi:10.1130/G35924.1.

Cerling, T. E., and J. Quade (1993), Stable carbon and oxygen isotopes in soil carbonates, in *Climate Change and Continental Isotopic Records,* vol. 78, edited by P.K. Swart, K.C. Lohmann, J. Mckenzie, and S.M. Savin, pp. 217-231, American Geophysical Union.

Clementz, M. T., and J. O. Sewall (2011), Latitudinal Gradients in Greenhouse Seawater ^{18}O: Evidence from Eocene Sirenian Tooth Enamel, *Science*, *332*(6028), 455–458, doi:10.1126/science.1201182.

Coplen, T. B. (1996), New guidelines for reporting stable hydrogen, carbon, and oxygen isotope-ratio data, *Geochimica et Cosmochimica Acta*, *60*(17), 3359–3360, doi:10.1016/0016-7037(96)00263-3.

Dansgaard, W. (1964), Stable isotopes in precipitation, *Tellus A*, 436–468, doi:10.3402/tellusa.v16i4.8993.

Dettman, D. L., and K. C. Lohmann (2000), Oxygen isotope evidence for high-altitude snow in the Laramide Rocky Mountains of North America during the Late Cretaceous and Paleogene, *Geology*, *28*(3), 243–5, doi:10.1130/0091-7613(2000)28<243:OIEFHS>2.0.CO;2.

Dutton, A., B. H. Wilkinson, J. M. Welker, G. J. Bowen, and K. C. Lohmann (2005), Spatial distribution and seasonal variation in $^{18}O/^{16}O$ of modern precipitation and river water across the conterminous USA, *Hydrol. Process.*, *19*(20), 4121–4146, doi:10.1002/hyp.5876.

Fan, M., P. Heller, S. D. Allen, and B. G. Hough (2014), Middle Cenozoic uplift and concomitant drying in the central Rocky Mountains and adjacent Great Plains, *Geology*, *42*(6), 547–550, doi:10.1130/G35444.1.

Fiorella, R. P., C. J. Poulsen, R. S. P. Zolá, M. L. Jeffery, and T. A. Ehlers (2015a), Modern and

long-term evaporation of central Andes surface waters suggests paleo archives underestimate Neogene elevations, *Earth and Planetary Science Letters*, *432*(C), 59–72, doi:10.1016/j.epsl.2015.09.045.

Fiorella, R. P., C. J. Poulsen, R. S. Pillco Zolá, J. B. Barnes, C. R. Tabor, and T. A. Ehlers (2015b), Spatiotemporal variability of modern precipitation $\delta^{18}O$ in the central Andes and implications for paleoclimate and paleoaltimetry estimates, *Journal of Geophysical Research: Atmospheres*, *120*(10), 4630–4656, doi:10.1002/2014JD022893.

Galewsky, J., and J. V. Hurley (2010), An advection-condensation model for subtropical water vapor isotopic ratios, *Journal of Geophysical Research*, *115*(D16), D16116–10, doi:10.1029/2009JD013651.

Galewsky, J., C. Rella, Z. Sharp, K. Samuels, and D. Ward (2011), Surface measurements of upper tropospheric water vapor isotopic composition on the Chajnantor Plateau, Chile, *Geophys. Res. Lett.*, *38*(17), doi:10.1029/2011GL048557.

Garzione, C. N., D. J. Auerbach, J. J.-S. Smith, J. J. Rosario, B. H. Passey, T. E. Jordan, and J. M. Eiler (2014), Clumped isotope evidence for diachronous surface cooling of the Altiplano and pulsed surface uplift of the Central Andes, *Earth and Planetary Science Letters*, *393*(C), 173–181, doi:10.1016/j.epsl.2014.02.029.

Garzione, C. N., P. Molnar, J. C. Libarkin, and B. J. MacFadden (2006), Rapid late Miocene rise of the Bolivian Altiplano: Evidence for removal of mantle lithosphere, *Earth and Planetary Science Letters*, *241*(3-4), 543–556, doi:10.1016/j.epsl.2005.11.026.

Gat, J. R. (1996), Oxygen and Hydrogen Isotopes in the Hydrologic Cycle, *Annu. Rev. Earth Planet. Sci.*, *24*(1), 225–262, doi:10.1146/annurev.earth.24.1.225.

Gat, J. R. (2000), Atmospheric water balance—the isotopic perspective, *Hydrol. Process.*, *14*(8), 1357–1369, doi:10.1002/1099-1085(20000615)14:8<1357::AID-HYP986>3.0.CO;2-7.

Good, S. P., D. Noone, and G. Bowen (2015), Hydrologic connectivity constrains partitioning of global terrestrial water fluxes, *Science*, *349*(6244), 175–177, doi:10.1126/science.aaa5931.

Grootes, P. M., M. Stuiver, L. G. Thompson, and E. Mosley Thompson (1989), Oxygen isotope changes in tropical ice, Quelccaya, Peru, *Journal of Geophysical Research*, *94*(D1), 1187–1194, doi:10.1029/JD094iD01p01187.

Held, I. M., and B. J. Soden (2000), Water vapor feedback and global warming, *Annual Review of Energy and the Environment*, *25*(1), 441–475, doi:10.1146/annurev.energy.25.1.441.

Horita, J., and D. J. Wesolowski (1994), Liquid-vapor fractionation of oxygen and hydrogen isotopes of water from the freezing to the critical temperature, *Geochimica et Cosmochimica Acta*, *58*(16), 3425–3437, doi:10.1016/0016-7037(94)90096-5.

Insel, N., C. J. Poulsen, C. Sturm, and T. A. Ehlers (2013), Climate controls on Andean precipitation $\delta^{18}O$ interannual variability, *Journal of Geophysical Research: Atmospheres*, *118*(17), 9721–9742, doi:10.1002/jgrd.50619.

Jouzel, J., L. Merlivat, and C. Lorius (1982), Deuterium excess in an East Antarctic ice core suggests higher relative humidity at the oceanic surface during the last glacial maximum, *Nature*, *299*(5885), 688–691, doi:10.1038/299688a0.

Majoube, M. (1971), Fractionnement en oxygène-18 et en deuterium entre la l'eau et sa vapeur d, *Journal de Chemie Physique et de Physico-Chimie Biologique,* 68(10), 1423.

Merlivat, L., and J. Jouzel (1979), Global climatic interpretation of the deuterium-oxygen 18 relationship for precipitation, *Journal of Geophysical Research*, 84(C8), 5029-5033.

Mulch, A., and C. P. Chamberlain (2007), Stable Isotope Paleoaltimetry in Orogenic Belts The Silicate Record in Surface and Crustal Geological Archives, *Reviews in Mineralogy and*

Geochemistry, *66*(1), 89–118, doi:10.2138/rmg.2007.66.4.
Noone, D. (2012), Pairing Measurements of the Water Vapor Isotope Ratio with Humidity to Deduce Atmospheric Moistening and Dehydration in the Tropical Midtroposphere, *J. Climate*, *25*(13), 4476–4494, doi:10.1175/JCLI-D-11-00582.1.
Novello, V. F. et al. (2012), Multidecadal climate variability in Brazil's Nordeste during the last 3000 years based on speleothem isotope records, *Geophys. Res. Lett.*, *39*(23), doi:10.1029/2012GL053936.
Oncken, O., D. Hindle, J. Kley, K. Elger, P. Victor, and K. Schemmann (2006), Deformation of the Central Andean Upper Plate System — Facts, Fiction, and Constraints for Plateau Models, in *The Andes*, edited by O. Oncken, G. Chong, G. Franz, P. Giese, H.-J. Götze, V. A. Ramos, M. R. Strecker, and P. Wigger, pp. 3–27, Springer Berlin Heidelberg.
Petit, J. R. et al. (1999), Climate and atmospheric history of the past 420,000 years from the Vostok ice core, Antarctica, *Nature*, *399*(6735), 429–436, doi:10.1038/20859.
Pierrehumbert, R. T. (2002), The hydrologic cycle in deep-time climate problems, *Nature*, *419*(6903), 191–198, doi:10.1038/nature01088.
Rozanski, K. (1985), Deuterium and oxygen-18 in European groundwaters—links to atmospheric circulation in the past, *Chemical Geology: Isotope Geoscience section*, *52*(3-4), 349–363, doi:10.1016/0168-9622(85)90045-4.
Rozanski, K., L. Araguás-Araguás, and R. Gonfiantini (1993), Isotopic Patterns in Modern Global Precipitation, in *Climate Change and Continental Isotopic Records,* vol. 78, edited by P.K. Swart, K.C. Lohmann, J. Mckenzie, and S.M. Savin, pp. 217-231, American Geophysical Union.
Saylor, J. E., and B. K. Horton (2014), Nonuniform surface uplift of the Andean plateau revealed by deuterium isotopes in Miocene volcanic glass from southern Peru, *Earth and Planetary Science Letters*, *387*(C), 120–131, doi:10.1016/j.epsl.2013.11.015.
Schoenemann, S. W., E. J. Steig, Q. Ding, B. R. Markle, and A. J. Schauer (2014), Triple water-isotopologue record from WAIS Divide, Antarctica: Controls on glacial-interglacial changes in 17Oexcess of precipitation,, 1–23, doi:10.1002/(ISSN)2169-8996.
Siegenthaler, U., and H. Oeschger (1980), Correlation of ^{18}O in precipitation with temperature and altitude, *Nature*, *285*(5763), 314–317, doi:10.1038/285314a0.
Soden, B. J., and I. M. Held (2006), An Assessment of Climate Feedbacks in Coupled Ocean–Atmosphere Models, *J. Climate*, *19*(14), 3354–3360, doi:10.1175/jcli3799.1.
Trenberth, K. E., J. T. Fasullo, and J. Kiehl (2009), Earth's Global Energy Budget, *Bull. Amer. Meteor. Soc.*, *90*(3), 311–323, doi:10.1175/2008BAMS2634.1.

Chapter 2. Spatiotemporal Variability of Modern Precipitation $\delta^{18}O$ in the Central Andes and Implications for Paleoclimate and Paleoaltimetry Estimates[1]

2.1 Abstract

Understanding the patterns of rainfall isotopic composition in the central Andes is hindered by sparse observations. Despite limited observational data, stable isotope tracers have been commonly used to constrain modern-to-ancient Andean atmospheric processes, as well as to reconstruct paleoclimate and paleoaltimetry histories. Here, we present isotopic compositions of precipitation ($\delta^{18}O_p$ and δD_p) from 11 micrometeorological stations located throughout the Bolivian Altiplano and along its eastern flank at ~21.5°S. We collected and isotopically analyzed 293 monthly bulk precipitation samples (August 2008 - April 2013). $\delta^{18}O_p$ values ranged from -28.0‰ to 9.6‰, with prominent seasonal cycles expressed at all stations. We observed a strong relationship between the $\delta^{18}O_p$ and elevation, though it varies widely in time and space. Constraints on air sourcing estimated from atmospheric back-trajectory calculations indicate that continental-scale climate dynamics control the interannual variability in $\delta^{18}O_p$ with upwind precipitation anomalies having the largest effect. The impact of precipitation anomalies in distant air source regions to the central Andes is in turn modulated the Bolivian High. The importance of the Bolivian High is most clearly observed on the southern Bolivian Altiplano. However, monthly variability among Altiplano stations can exceed 10‰ in $\delta^{18}O_p$ on the plateau and cannot be explained by elevation or source variability, indicating a nontrivial role for local scale effects on short timescales. The strong influence of atmospheric circulation on central Andean $\delta^{18}O_p$ requires that paleoclimate and paleoaltimetry studies consider the role of South American atmospheric paleocirculation in their interpretation of stable isotopic values as proxies.

1 Official citation: Fiorella, R.P.; C.J. Poulsen; R.S. Pillco-Zolá; J.B. Barnes; C.R. Tabor; and T.A. Ehlers (2015). Spatiotemporal Variability of Modern Precipitation $\delta^{18}O$ in the central Andes and Implications for Paleoclimate and Paleoaltimetry Estimates. *Journal of Geophysical Research – Atmospheres.* doi: 10.1002/2014JD022893

2.2 Introduction

Stable isotopes in precipitation serve as tracers of modern and past environmental processes. Phase changes through processes including evaporation and condensation unequally partition the stable isotopes of water with the heavier isotopes (^{18}O, ^{2}H or D) favoring the more condensed phase [*Dansgaard*, 1964; *Gat*, 1996]. Progressive condensation from an air parcel leaves the residual vapor and subsequent precipitation along a trajectory more depleted in heavy isotopes. The isotopic composition of precipitation (δ_p) is expressed as the per mil (‰) deviation of the heavy-to-light isotope ratio (R) from the Vienna Standard Mean Ocean Water standard (VSMOW) ($\delta_p = 1000(R_p/R_{VSMOW}-1)$) [*Coplen*, 1996; *Gat*, 1996]. A predictable spatial distribution of δ_p emerges when the factors controlling condensation are well known [*Bowen and Wilkinson*, 2002; *Bowen and Revenaugh*, 2003]. Because δ_p preserves information about hydrologic cycling, it is widely applied to understand modern hydrologic processes [*Rozanski et al.*, 1993; *Vuille and Werner*, 2005; *Liu et al.*, 2010]. Paleoenvironmental reconstructions also use δ_p because several geologic proxy materials preserve δ_p directly [e.g., ice cores, *Grootes et al.*, 1989; *Thompson et al.*, 1998] or form in equilibrium with δ_p [e.g., pedogenic carbonates, *Cerling and Quade*, 1993; *Quade et al.*, 2007]. Unfortunately, interpretations of δ_p patterns remain hindered in many regions because local measurements of the spatiotemporal variability of modern δ_p are scarce [e.g., *Lechler and Niemi*, 2012]. One robust trend that is observed on a global scale, however, is a general decrease in δ_p with increased elevation [e.g., *Dansgaard*, 1964; *Siegenthaler and Oeschger*, 1980; *Rozanski et al.*, 1993]. This pattern results from the topographically initiated adiabatic lifting of and rainout from air parcels [*Rowley and Garzione*, 2007]. The rate of isotopic change with elevation is commonly referred to the isotopic lapse rate. Observed isotopic lapse rates at local-to-regional scales are highly variable in space and time [*Blisniuk and Stern*, 2005].

Despite limited data, stable isotope compositions of natural waters have been widely used to infer (paleo)environmental conditions in the central Andes. Existing observations of precipitation [*Aravena et al.*, 1999; *Gonfiantini et al.*, 2001; *Vimeux et al.*, 2005; 2011] and surface waters [*Hoke et al.*, 2009; *Bershaw et al.*, 2010; *Giovanni et al.*, 2010; *Rohrmann et al.*, 2014] along the flanks of the central Andean plateau (the Altiplano) form the basis of our knowledge of regional water isotopologue distributions (Figure 2.1a). These observations reveal that the central Andean isotopic distribution and lapse rate varies considerably in space and time.

For example, the $\delta^{18}O_p$ lapse rate was -1.9 ‰/km on the eastern Andean flank from July 1984-June 1985 [*Gonfiantini et al.*, 2001] compared to ~ -3.3 ‰/km on the western Andean flank in 1986 [*Aravena et al.*, 1999]. Estimates of the isotopic lapse rate derived from stream waters also vary substantially and range from -1.9 ‰/km [2004-05, ~16°S, *Bershaw et al.*, 2010] to -0.2 ‰/km [2010-13, ~26°S, *Rohrmann et al.*, 2014]. The high observed variability in the δ_p is thought to be related to continental-scale climate variability; precipitation anomalies in upwind vapor source regions have been shown to influence eastern Andean flank δ_p values [*Vimeux et al.*, 2005; 2009; 2011; *Vuille et al.*, 2012].

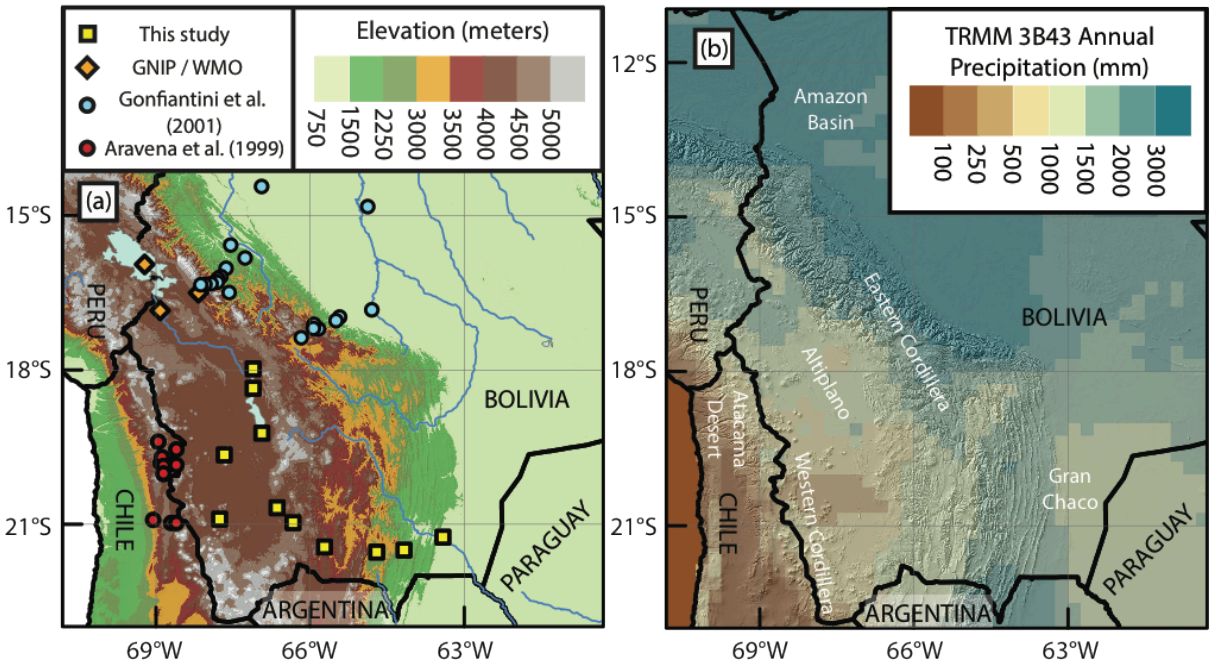

Figure 2.1. Topography and climatology of the central Andes region: (a) Elevation [m; HydroSHEDS; Lehner et al., 2008] and relevant climate stations, (b) 1998-2013 mean annual precipitation (MAP; mm/yr) from TRMM 3B43 [Liu et al., 2012]. Prominent topographic features are the broad, flat Altiplano centered between higher peaks to the east and west. Elevation and rainfall gradients are strong in the northeastern flanks of the Altiplano transitioning to lower gradients east of the southern Altiplano. Precipitation is more seasonal on the Altiplano than in the lowlands.

Key uncertainties about controls on central Andean δ_p remain for several reasons. First, observations are neither broadly distributed, particularly within the Altiplano, nor contemporaneous. Second, existing modern δ_p records are short in duration (< 2 years), despite known high interannual variability in central Andean climate [*Garreaud et al.*, 2003; 2009]. Finally, the δ_p data lack a consistent sampling method. Some studies measured δ_p of monthly

precipitation [*Gonfiantini et al.*, 2001; *Vimeux et al.*, 2005], while others measured δ_p from individual precipitation events [*Aravena et al.*, 1999; *Vimeux et al.*, 2011]. Thus, it has proven difficult to determine if these limited records represent modern climatological mean conditions, much less how applicable they may be over geologic time [e.g., *Barnes and Ehlers*, 2009].

Climate simulations using isotope-tracking general circulation models have sought to fill the gap of limited δ_p observations and explore how δ_p changes in response to surface uplift, climate change, and different moisture sources [*Vuille et al.*, 2003a; 2003b; *Sturm et al.*, 2007; *Ehlers and Poulsen*, 2009; *Lee et al.*, 2009a; *Insel et al.*, 2010; *Lewis et al.*, 2010; *Poulsen and Jeffery*, 2011; *Insel et al.*, 2012; *Jeffery et al.*, 2012; *Insel et al.*, 2013]. Simulations of modern δ_p confirm a distinct decrease with elevation on the Altiplano margin, yet also predict high interannual variability of δ_p across the entire central Andean region that equals or even exceeds the observed flank δ_p variability [*Sturm et al.*, 2007; *Insel et al.*, 2013]. The simulations demonstrate that salient features of South American atmospheric circulation, such as the upper-level (200 hPa) Bolivian High and the South American Low-Level Jet (SALLJ, 850 hPa), govern the patterns of δ_p, including the steering of air parcels towards the central Andes [*Insel et al.*, 2013]. Upstream precipitation amounts along the parcel trajectories also contributes to δ_p variability [*Vuille et al.*, 2003a; 2003b; *Vuille and Werner*, 2005; *Sturm et al.*, 2007; *Insel et al.*, 2013]. However, observations to validate these simulated large spatiotemporal variations in δ_p remain inadequate.

We present a long (~5 yrs) observational record of δ_p in Andes precipitation to augment our knowledge of central Andes δ_p. We next integrate the isotopic data with climate reanalysis and air parcel back-trajectory modeling to evaluate whether previously identified controls on δ_p along the eastern Andean flank extend to the high plateau region. Specifically, we test the hypotheses that: (a) elevation is a dominant control on Altiplano δ_p and (b) Altiplano δ_p inherits variability from precipitation anomalies in distant air source regions, as it does along the flanks. In addition, we measure δ_p along a previously unsampled eastern flank transect at ~21.5°S and compare it to existing studies to investigate the spatial variability in the δ_p-elevation relationship. Finally, we suggest that prior observational records of modern precipitation may be too short in duration to fully sample the natural variability. We then use these insights to discuss how improved knowledge of the spatiotemporal patterns of central Andean δ_p may progress interpretation of regional proxies for paleoclimate and paleoelevation.

2.3 Background

2.3.1 Central Andes Climate and Topography

Strong elevation and annual precipitation gradients in the central Andes likely influence δ_p. In the central Andes, the range splits into two distinct cordilleras each with ~5 km of relief that bound the interior, low-relief Altiplano (at ~3800 m elevation) (Figure 2.1). To the west, the Atacama Desert in northern Chile receives less than 20 mm/yr precipitation on average, while in the Amazon Basin to the northeast, mean annual precipitation (MAP) amounts can exceed 5000 mm/yr [*Garreaud et al.*, 2009]. On the Bolivian Altiplano, precipitation amounts range from ~1000 mm/yr in the north (16-18°S) to < 200 mm/yr in the south (20-22°S; Figure 2.1b). Across the Atacama Desert located on the western flank, hyperarid conditions arise from strong atmospheric subsidence collocated with the cold, coastal Humboldt current [*Rodwell and Hoskins*, 2001; *Takahashi and Battisti*, 2007; *Garreaud et al.*, 2010].

Central Andean climate exhibits a strong seasonal cycle as well. The majority of precipitation occurs during austral summer (compare Figure 2.2a,c to 2.2b,d) [*Garreaud and Aceituno*, 2001; *Garreaud et al.*, 2003]. On the Bolivian Altiplano, the proportion of MAP falling during December-January-February (DJF) often exceeds 60% [*Garreaud et al.*, 2003]. DJF rainfall is typically convective and results from increased moisture convergence that occurs with the development of the Bolivian High [*Lenters and Cook*, 1999] and an increase in SALLJ moisture transport [*Campetella and Vera*, 2002; *Insel et al.*, 2013]. In contrast, arid conditions prevail in the absence of the Bolivian High during June-July-August (JJA) (Figure 2.2b,d).

Precipitation amounts over the Altiplano vary substantially from year to year [*Garreaud and Aceituno*, 2001], perhaps with changes in the position and intensity of the Bolivian High. Strengthening or southward displacement of the Bolivian High both favor increased Altiplano precipitation, while a weaker or more northerly Bolivian High favors decreased Altiplano precipitation [*Lenters and Cook*, 1999; *Garreaud and Aceituno*, 2001]. In addition, the amount of precipitation on the plateau appears related to the state of El Niño/Southern Oscillation (ENSO) [*Thompson et al.*, 1984; *Aceituno*, 1988; *Lenters and Cook*, 1999; *Vuille*, 1999]. Changes in precipitation amount and vapor sourcing through such modes of interannual-to-decadal climate variability likely portend high variability in δ_p.

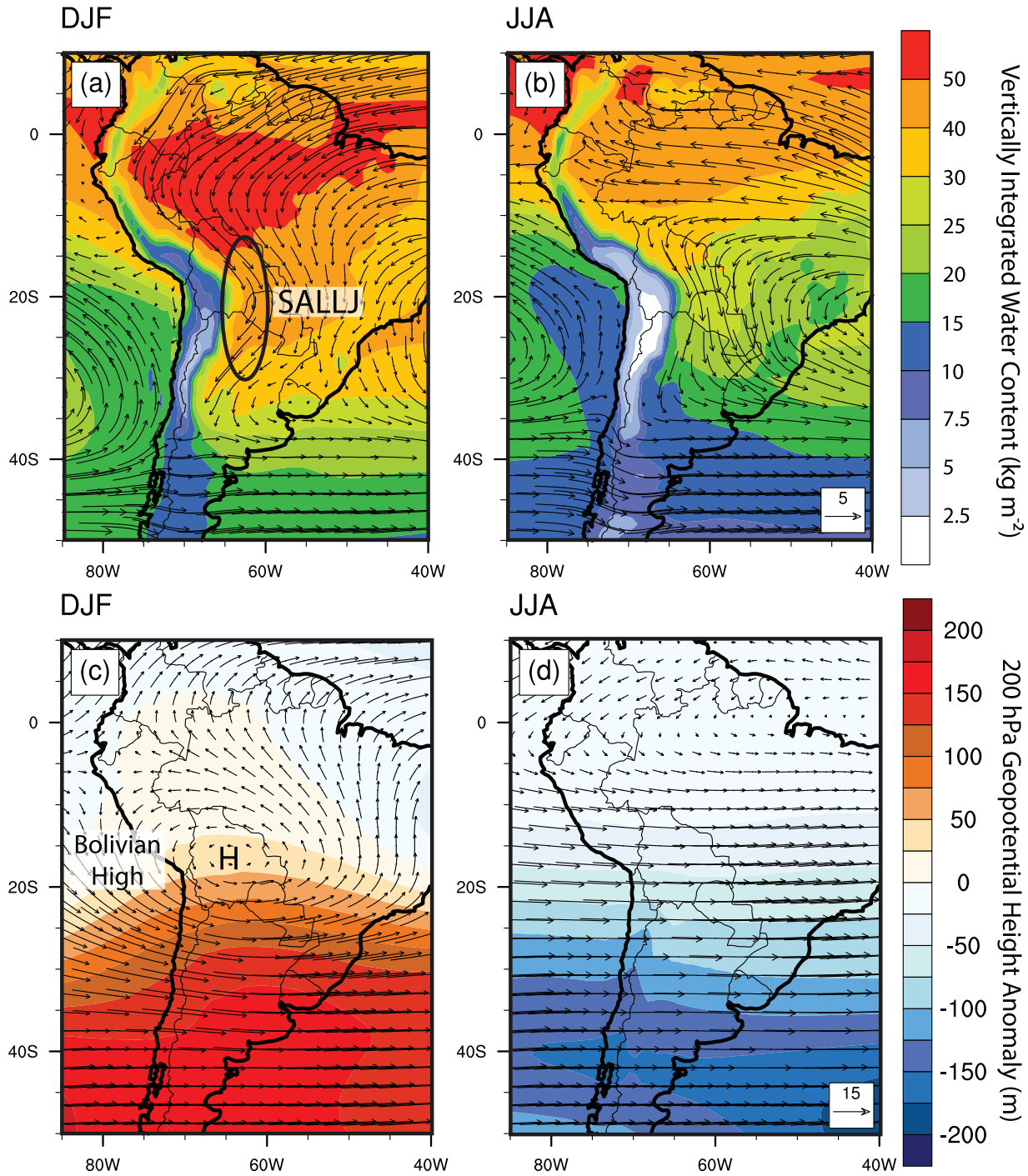

Figure 2.2. Seasonal climatology for the central Andes from ERA-Interim reanalysis data [Dee et al., 2011]. Climatological (1979-2013) mean 850 hPa winds (vectors, m/s) overlying vertically-integrated column water (kg/m^2) for (a) austral summer (DJF) and (b) winter (JJA). Climatological (1979-2013) upper-level (200 hPa) winds overlying anomalous 200 hPa geopotential height relative to the zonal average for (c) DJF and (d) JJA. Major features of DJF large-scale circulation drive increased moisture convergence to the central Andes like the South American Low-Level Jet (SALLJ, a) and the Bolivian High (c).

2.3.2 Stable Isotope Systematics

The degree of partitioning of water isotopologues (e.g. $H_2{}^{16}O$ vs. $H_2{}^{18}O$) during phase changes depends on the local environmental conditions. The saturation vapor pressure of heavier isotopologues of water is slightly lower than for lighter water isotopologues, which promotes a thermodynamic preference for the heavier water isotopologues entering or remaining in the more condensed phase. The degree of partitioning at equilibrium, also called the equilibrium fractionation factor, decreases with increasing temperature [*Majoube*, 1971; *Horita and Wesolowski*, 1994]. Kinetic isotopic fractionation can also occur when two phases cannot attain isotopic equilibrium. A prominent example of kinetic fractionation is evaporation from the ocean surface, where transport of water vapor from the water surface occurs mainly through diffusion and turbulent transport [*Craig and Gordon*, 1965]. The deuterium excess parameter (*d*-excess = $\delta D_p - 8\delta^{18}O_p$) is seen as a tracer of the kinetic isotope fractionation history of an air parcel and precipitation [e.g., *Dansgaard*, 1964; *Uemura et al.*, 2008].

Following initial evaporation from the ocean, the isotopic composition of precipitation has commonly been explained by Rayleigh distillation [e.g., *Dansgaard*, 1964; *Gat*, 1996]. In a pure Rayleigh system, adiabatic cooling of an air parcel results in condensation occurring in isotopic equilibrium with the remaining vapor. Rayleigh distillation assumes that all condensate is immediately removed and no mixing of vapor occurs between the air parcel and the environment. Continued cooling results in more vapor being removed from the air parcel. Under these conditions, the isotopic composition of an air mass is a function of parcel temperature during condensation and the fraction of vapor remaining in the air parcel relative to its initial value [*Dansgaard*, 1964; *Gat*, 1996; *Noone*, 2012]:

$$\ln\left(\frac{R}{R_0}\right) = \left(\alpha_{l-v}(T) - 1\right)\ln\left(\frac{w}{w_0}\right) \approx (\delta - \delta_0)$$

where R is the heavy-to-light isotope ratio, $\alpha_{l\text{-}v}(T)$ is the temperature dependent fractionation factor between liquid water and vapor [*Majoube*, 1971; *Horita and Wesolowski*, 1994], *w* is the water vapor mixing ratio, and a subscript zero indicates initial conditions of the parcel. The isotopic composition of water removed from the parcel at any point during condensation can be calculated using the equilibrium fractionation factor, $\alpha_{l\text{-}v}(T)$:

$$\delta_l = \left(\delta_v + 1000\right)\alpha_{l-v}(T) - 1000$$

where δ_l and δ_v are the isotopic compositions of liquid and vapor, respectively.

The traditional view is that extratropical δ_p obeys Rayleigh distillation to first order [*Dansgaard*, 1964; *Rozanski et al.*, 1993]. Surface and cloud-base temperature both correlate well with δ_p on monthly and annual timescales outside of the tropics, with the strongest correlations observed at high latitudes [*Dansgaard*, 1964; *Rindsberger et al.*, 1983; *Rozanski et al.*, 1993]. In the tropics, however, annual variability in δ_p persists despite more uniform annual temperatures. Instead, δ_p values tend to be lighter during periods of increased precipitation [*Dansgaard*, 1964; *Rozanski et al.*, 1993], and are often negatively correlated with the water vapor content of an air parcel, counter to the Rayleigh distillation relationship [e.g., *Aggarwal et al.*, 2012]. This relationship is referred to as the "amount effect" [*Dansgaard*, 1964; *Rozanski et al.*, 1993].

The amount effect results from multiple convective processes. First, subcloud rainfall evaporation decreases at higher precipitation rates, as droplets tend to be larger and fall faster [*Lee and Fung*, 2007; *Bony et al.*, 2008; *Risi et al.*, 2008]. Subcloud evaporation of rainfall eventually saturates the air column, further suppressing evaporation. Decreased subcloud evaporation of raindrops results in lighter isotopic compositions reaching the surface. Second, convective downdrafts contribute by recycling vapor derived from partial evaporation of raindrops [*Risi et al.*, 2008] and by mixing vapor from the mid-to-upper troposphere down toward the surface that has a lighter isotopic composition than near surface vapor [*Dessler and Sherwood*, 2003; *Kuang et al.*, 2003]. Third, subsidence in large scale atmospheric circulation can also result in downward mixing of isotopically light vapor [*Blossey et al.*, 2010]. These processes decrease the concentration of heavy isotopologues in surface vapor, resulting in lighter δ_p values when this surface vapor is entrained in subsequent convective updrafts. Finally, more vigorous convection entrains more vapor from the mid-to-upper troposphere, which is isotopically lighter than surface vapor, further contributing to lighter δ_p values in strong convective systems [*Moore et al.*, 2014]. The relative importance of each of these factors likely changes with precipitation rates, with subcloud evaporation dominating at low precipitation rates [*Lee and Fung*, 2007; *Risi et al.*, 2008] and increased importance of vapor recycling and entrainment occurring at higher precipitation rates [*Risi et al.*, 2008; *Moore et al.*, 2014]. Convective precipitation dominates the Amazon basin [*Garreaud et al.*, 2009], and therefore, these processes influence the source vapor for central Andes precipitation.

2.4 Methods

2.4.1 Data Collection and Isotopic Analysis Methods

We built a network of eleven micrometeorological stations that collected temperature, relative humidity, and precipitation amounts (Figure 2.1). Six stations spanned the Altiplano (18-21°S; 66.5-68°W) and five transected its eastern margin in southern Bolivia at ~21.5°S (E-W; elevations from 395 to 4340 m). The Bolivian meteorological service (SENAMHI) managed four of the Altiplano stations (Oruro, El Choro, Quillacas, and Salinas) and we installed the remaining seven in July 2008. The equipment we installed in the stations was manufactured by Onset Computer Corporation. All stations began collecting samples in August 2008. The six Altiplano stations (Oruro, El Choro, Quillacas, Salinas, San Juan, Noel Mariaca) and the highest elevation station along the plateau flank (Gran Chocaya) operated until April 2013. We retired the four remaining stations along the elevation transect (Tupiza, Tarija, Entre Ríos, and Villamontes) at the end of September 2011. At each location, we employed resident observers to maintain the station and collect monthly precipitation samples for subsequent isotopic analysis. Precipitation samples were captured with rain buckets, the inner bottoms of which were covered with a layer of mineral oil to prevent evaporation [after *Friedman et al.*, 1992; *Scholl et al.*, 1996]. On the first of each month, observers collected precipitation samples from the bottom of the bucket using a syringe and transferred it to a 20 mL glass vial with poly-cone cap (made by Wheaton). The bucket was then emptied, cleaned, dried, the bottom refilled with mineral oil, and replaced. During semiannual trips to collect the precipitation samples, we interviewed the observers to learn about recent rainfall conditions and confirm that the precipitation was collected correctly.

Upon our visits to the stations, we discovered that equipment had occasionally malfunctioned due to the harsh and remote conditions at the stations. As a result, some meteorological data was lost, and we used several methods to fill in the resulting data gaps. Gaps in relative humidity (46.4% missing) and temperature (32.1% missing) data were filled using the ERA-Interim reanalysis product at native resolution (T255, ~80 km) [*Dee et al.*, 2011] with data from the grid cell overlying the station. Missing temperatures for stations with few missing values were estimated using a least-squares linear regression between reanalysis and available temperatures for that station to calibrate the reanalysis data to each individual station. We used a regional regression technique for the three Altiplano stations where >35% of temperature values were missing: Salinas (100%), El Choro (100%), and Quillacas (45.6%). In these cases, we

regressed between available station and reanalysis data from the other three Altiplano stations (Oruro, Noel Mariaca, and San Juan), and used this relationship to predict the missing values for Salinas, El Choro, and Quillacas. Missing relative humidity values were estimated using relative humidity values at the lowest available pressure level above the surface pressure. We applied no correction to the ERA-Interim relative humidity values. Missing monthly precipitation values were estimated using the TRMM 3B43 (0.25° resolution) dataset for the grid cell overlying the station [*Huffman et al.*, 2007; *Liu et al.*, 2012]. Rain gauges at Noel Mariaca (November 2009-April 2011) and Villamontes (August 2010-September 2011) malfunctioned for ~1 year; we filled these gaps with TRMM data as well. Because we could not be certain when the rain gauges first malfunctioned, we assumed they stopped operating when the data diverged from nearby stations or TRMM data. We estimate that average TRMM-derived precipitation values are within ~25% of measured values (Figure 2.3, Table 2.1). Precipitation amounts are underestimated by ~25% by TRMM relative to station measurements for the transect stations, while Altiplano stations are overestimated by ~15% on average (Table 2.1). However, TRMM overestimates precipitation at the Noel Mariaca and Gran Chocaya stations by ~38% and 23% respectively, relative to available station measurements (Table 2.1). We provide the monthly micrometeorological data in Appendix 2A, and indicate the points derived from ERA-Interim or TRMM for transparency.

We analyzed the precipitation isotopic compositions using a Picarro L2120-i cavity ringdown spectrometer with an integrated A211 High-Precision Vaporizer and autosampler. The Picarro ChemCorrect software package monitored samples for organic contamination [e.g., *West et al.*, 2011]. Standard errors are < 0.1 ‰ for $\delta^{18}O$ and <0.4 ‰ for δD. The raw monthly data for the 11 stations are presented in Appendix 2A, and annual and DJF average values in Tables 2.4 and 2.5. As the rainy season occurs across two calendar years, we calculated annual averages using a 12-month period from July-June instead of January-December. This method improves representation of the central Andes hydrologic year, and therefore better isolates sources of interannual variability by keeping whole rainy season periods intact.

Table 2.1. Slope, intercept, and correlations between monthly measured and TRMM 3B43 precipitation amounts (mm) for each station.

Station	Slope	Intercept	r^2
Oruro (ORU)	1.01 ± 0.04	-2.70 ± 2.37	0.910 (n = 57)
El Choro (ECH)	N/A	N/A	N/A (n = 0)
Quillacas (QUI)	0.86 ± 0.07	-7.25 ± 4.02	0.843 (n = 32)
Salinas (SAL)	-0.02 ± 0.02	1.40 ± 1.23	0.059 (n = 8)
San Juan (SJU)	0.51 ± 0.14	1.09 ± 4.45	0.254 (n = 44)
Noel Mariaca (NMA)	1.38 ± 0.13	-5.80 ± 3.10	0.748 (n = 39)
Gran Chocaya (GCH)	1.23 ± 0.09	-1.62 ± 2.37	0.832 (n = 39)
Tupiza (TUP)	0.67 ± 0.06	-0.12 ± 3.59	0.794 (n = 38)
Tarija (TAR)	0.82 ± 0.04	4.30 ± 3.64	0.922 (n = 38)
Entre Ríos (ERI)	0.83 ± 0.07	7.72 ± 7.47	0.859 (n = 26)
Villamontes (VMO)	0.60 ± 0.05	3.77 ± 5.81	0.856 (n = 24)
ALTIPLANO STATIONS	**0.86 ± 0.04**	**-2.79 ± 1.93**	**0.702 (n = 180)**
FLANK STATIONS	**0.75 ± 0.03**	**3.40 ± 2.07**	**0.845 (n = 165)**
ALL STATIONS	**0.78 ± 0.02**	**0.74 ± 1.37**	**0.802 (n = 345)**

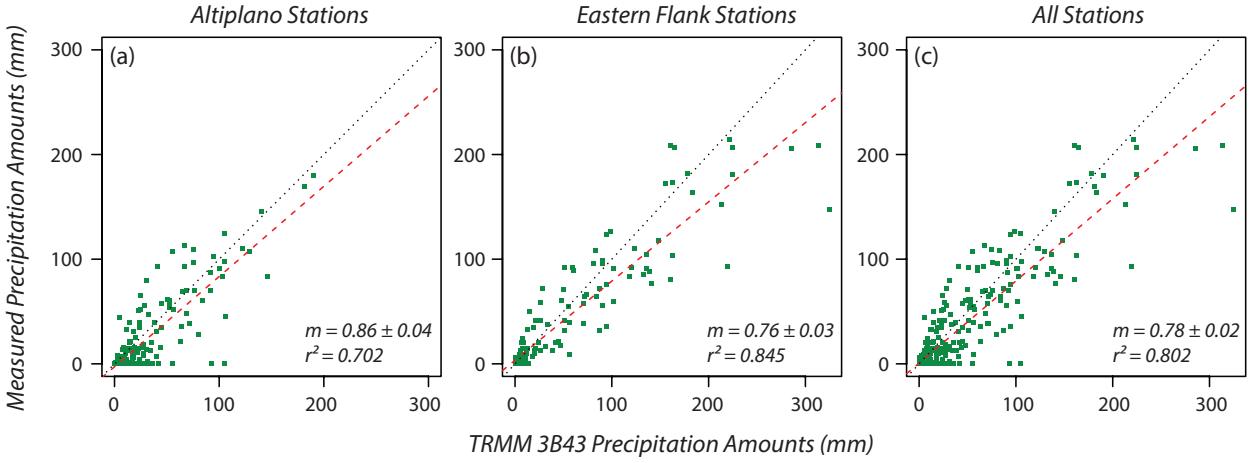

Figure 2.3. Comparison of TRMM 3B43 precipitation values with measured precipitation amounts. The three scatter plots divide the eleven stations into (a) plateau stations, (b) flank stations, and (c) all stations. In each plot, the short dashed black line is the 1:1 relationship and the long dashed red line is the best least-squares linear regression to the data.

A strong correlation between $\delta^{18}O_p$ and δD_p forms the basis for the global meteoric water line (GMWL, $\delta D_p = 8\delta^{18}O_p + 10$, [*Craig*, 1961]). The GMWL describes the coevolution of water isotopologues as rainout from an air parcel occurs. On local and regional scales, deviations from the GMWL can occur due to local climate conditions [e.g., *Rozanski et al.*, 1993]. We calculated annual, DJF, and JJA local meteoric water lines for each station (Table 2.2). We found the relationship between $\delta^{18}O_p$ and δD_p is similar for all stations on an annual and DJF basis (Figure 2.4), but can vary substantially in JJA. For brevity, however, we focus the bulk of the analysis on the $\delta^{18}O_p$ values as analyzing δD_p on an annual or rainy season basis yields near similar results. JJA variability in the local meteoric water lines is briefly discussed in the results.

We removed 11 monthly values at the Salinas station from analysis because they failed our data quality criteria, which we attribute to observer error. Four were eliminated for exhibiting substantial evaporation (i.e., negative *d*-excess values) not observed in other samples, and seven samples from the dry season for having identical δ values. We infer that these samples are likely from groundwater or tap water provided by the observer rather than precipitation (indicated in Appendix 2A).

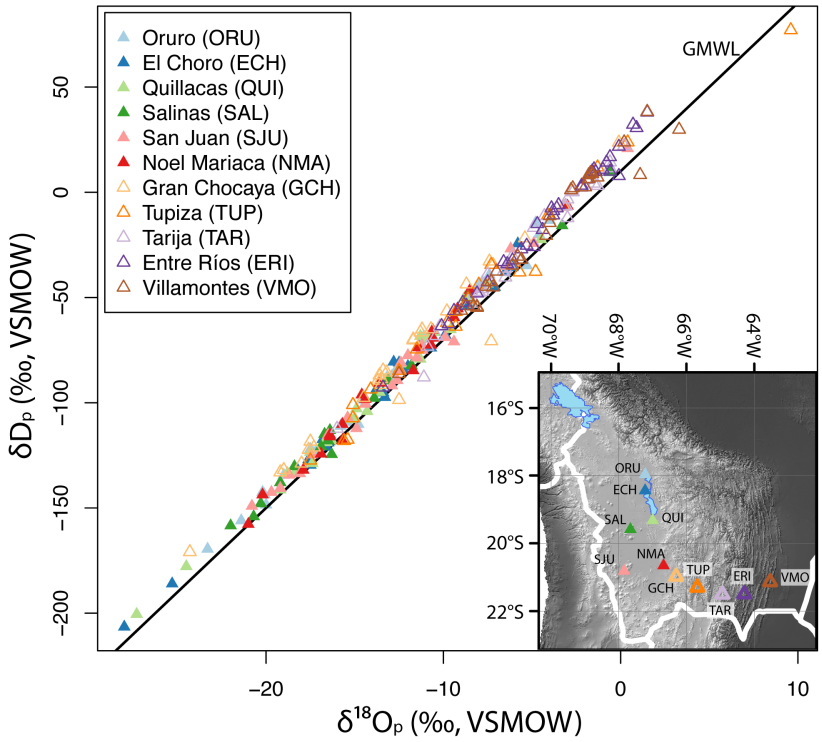

Figure 2.4. Monthly isotopic composition of precipitation in $\delta^{18}O_p$-δD_p space. Values for all 11 stations in this study are shown as separate colors. GMWL = heavy black line. Inset map shows station locations with symbols (filled = Altiplano stations, open = elevation transect) and colors used throughout the paper.

Table 2.2. Annual, DJF, and JJA local meteoric water lines for each site.

Station	Full Year		DJF Only		JJA Only	
	LMWL	r^2	LMWL	r^2	LMWL	r^2
Oruro (ORU)	$\delta D = (8.17\pm0.11)\delta^{18}O + (18.28\pm1.50)$	0.994 (n=36)	$\delta D = (8.26\pm0.16)\delta^{18}O + (20.51\pm2.55)$	0.995 (n=14)	$\delta D = 9.57\delta^{18}O + 31.44$	N/A (n=2)
El Choro (ECH)	$\delta D = (7.98\pm0.13)\delta^{18}O + (14.37\pm1.88)$	0.994 (n=23)	$\delta D = (7.88\pm0.16)\delta^{18}O + (13.69\pm2.68)$	0.996 (n=10)	$\delta D = 12.79\delta^{18}O + 72.70$	N/A (n=2)
Quillacas (QUI)	$\delta D = (8.01\pm0.12)\delta^{18}O + (15.37\pm1.82)$	0.994 (n=27)	$\delta D = (7.93\pm0.15)\delta^{18}O + (14.76\pm2.43)$	0.996 (n=13)	$\delta D = 9.96\delta^{18}O + 44.25$	N/A (n=2)
Salinas (SAL)	$\delta D = (7.86\pm0.15)\delta^{18}O + (12.03\pm2.36)$	0.996 (n=14)	$\delta D = (8.22\pm0.31)\delta^{18}O + (18.84\pm5.40)$	0.990 (n=8)	N/A	N/A (n=0)
San Juan (SJU)	$\delta D = (8.11\pm0.16)\delta^{18}O + (15.83\pm2.19)$	0.992 (n=23)	$\delta D = (8.15\pm0.15)\delta^{18}O + (16.92\pm2.03)$	0.995 (n=14)	N/A	N/A (n=1)
Noel Mariaca (NMA)	$\delta D = (8.35\pm0.19)\delta^{18}O + (20.11\pm2.68)$	0.991 (n=19)	$\delta D = (8.33\pm0.18)\delta^{18}O + (20.28\pm2.47)$	0.994 (n=14)	N/A	N/A (n=0)
Gran Chocaya (GCH)	$\delta D = (7.98\pm0.28)\delta^{18}O + (19.12\pm3.79)$	0.967 (n=28)	$\delta D = (8.25\pm0.12)\delta^{18}O + (25.76\pm1.83)$	0.997 (n=14)	N/A	N/A (n=1)
Tupiza (TUP)	$\delta D = (7.87\pm0.25)\delta^{18}O + (13.39\pm2.73)$	0.982 (n=19)	$\delta D = (8.55\pm0.32)\delta^{18}O + (23.00\pm3.69)$	0.990 (n=8)	N/A	N/A (n=0)
Tarija (TAR)	$\delta D = (8.47\pm0.20)\delta^{18}O + (19.38\pm1.39)$	0.985 (n=28)	$\delta D = (8.57\pm0.28)\delta^{18}O + (21.78\pm2.53)$	0.993 (n=8)	$\delta D = 9.00\delta^{18}O + 14.80$	N/A (n=2)
Entre Ríos (ERI)	$\delta D = (8.50\pm0.15)\delta^{18}O + (21.38\pm0.83)$	0.989 (n=35)	$\delta D = (8.65\pm0.24)\delta^{18}O + (22.43\pm1.99)$	0.994 (n=8)	$\delta D = (6.61\pm0.97)\delta^{18}O + (17.41\pm2.27)$	0.869 (n=8)
Villamontes (VMO)	$\delta D = (8.21\pm0.31)\delta^{18}O + (17.26\pm1.78)$	0.963 (n=28)	$\delta D = (8.76\pm0.33)\delta^{18}O + (20.20\pm2.44)$	0.991 (n=8)	$\delta D = (7.61\pm0.37)\delta^{18}O + (21.96\pm0.68)$	0.995 (n=4)

2.4.2 Data Analysis and Statistical Methods

We performed a suite of multivariate least-squares linear regressions to assess the influence of climatic and geographic factors on $\delta^{18}O_p$ (Table 2.6). We first determined the best-fit model for our stations, then repeated the regression calculations including monthly bulk $\delta^{18}O_p$ data from prior precipitation studies in the central Andes [hereafter, referred to as all available data, *Aravena et al.*, 1999; *Gonfiantini et al.*, 2001; *WMO/IAEA*, 2013]. We calculated precipitation amount-weighted annual average $\delta^{18}O_p$ values where monthly precipitation amounts were available. Predictor variables that may modify $\delta^{18}O_p$ include station elevation, latitude,

longitude, MAP, and mean annual temperature (MAT) [*Bowen and Wilkinson*, 2002; *Bowen and Revenaugh*, 2003; *Lechler and Niemi*, 2012]. We note that latitude and longitude are not processes that fractionate water isotopologues directly, but they do represent the combined effects of multiple factors that influence their distribution, such as temperature or distance from monsoon circulations. As observational records of $\delta^{18}O_p$ are not contemporaneous, we standardized estimates of MAP and MAT to a common observational data source and reference time period. We extracted MAP and MAT for each station using the University of Delaware 0.5° gridded monthly climate dataset (1960-1990 average) [*Legates and Willmott*, 1990a; 1990b]. However, after compilation we observed that several predictor (i.e., independent) variables strongly covaried. Thus, in our multivariate regressions, we excluded MAT and longitude as predictor variables, as they are highly correlated with elevation in our dataset (our stations: r = -0.920 and -0.918; all available data: r = -0.740 and -0.611). However, we retain the potential influence of zonal average temperature changes with latitude by including latitude as a predictor variable. MAP is also strongly correlated with elevation (our stations: r = -0.861; all available data: r = -0.717), but we retain MAP as a possible predictor variable here due to the strong influence precipitation amount can have on $\delta^{18}O_p$ through the amount effect in the tropics [*Dansgaard*, 1964; *Rozanski et al.*, 1993]. We then used the small-sample Akaike Information Criterion (AICc) to select the best multivariate model because it optimizes the trade-off between model complexity and quality of the fit [*Burnham and Anderson*, 2002]. Low AICc scores signal a multivariate model more parsimonious with the data.

We calculated correlation coefficients (Pearson's r) and p-values for all possible station pairs to access the spatial coherence in observed variability across our stations. High r-values (> ~0.5) between two stations indicate a high likelihood that similar factors affect $\delta^{18}O_p$ at both. We used monthly average outgoing longwave radiation (OLR) from the ERA-Interim reanalysis dataset as a proxy for deep convection and high cloud tops [*Kousky*, 1988; *Xie and Arkin*, 1998]. Low values of OLR indicate high cloud tops and deep convective activity.

2.4.3 Atmospheric Back-Trajectory Modeling

To constrain moisture source directions, we calculated 7-day air parcel back-trajectories for the rainy season (DJF only) using the HYSPLIT4 model (HYbrid Single-Parcel Lagrangian Integrated Trajectory 4; hereafter HYSPLIT). HYSPLIT model algorithms are well documented

[*Draxler and Hess*, 1998], and they have been applied to demonstrate links between $\delta^{18}O_p$ and air transport pathways [e.g., *Strong et al.*, 2007; *Bershaw et al.*, 2012; *Lechler and Galewsky*, 2013]. We modeled air parcel three-dimensional motion using the ERA-Interim reanalysis winds. The ERA-Interim dataset has a horizontal resolution of approximately ~80 km [*Dee et al.*, 2011], resulting in a more realistic representation of Andean topography with smaller topographic truncation errors than prior reanalysis products. We initiated back-trajectories at a height of 1500 m above ground level at five different station coordinates: Oruro, Quillacas, and Noel Mariaca to represent the northern, central, and southern Bolivian Altiplano respectively, and Tarija and Villamontes to represent the eastern flank (Figure 2.4 inset). We started at 1500 m above ground level because it reflects a balance between being low enough to be important for moisture transport yet high enough to reduce atmospheric flow attenuation by surface friction [e.g., *Bershaw et al.*, 2012]. Sensitivity tests using initial heights of 500, 1000, and 2000 m (not shown) resulted in qualitatively similar results to those presented here at 1500 m. We calculated trajectories every six hours during the rainy season (DJF), resulting 360 total trajectories (364 for leap years) per station per year.

We calculated areal mean frequencies for three prominent 2° x 4° source pathways to more quantitatively evaluate the partitioning of DJF air sources emerging from back-trajectory modeling. Three regions capture most of the transport to the central Andes: (a) the Yungas-Amazon Basin (YAB) (13-15°S, 65-69°W), (b) the South Pacific (SP) (20-24°S, 69-71°W), and (c) the Gran Chaco (GC) (24-26°S, 62-66°W). We binned hourly parcel position counts from the HYSPLIT back-trajectories on a 0.75° grid, then used them to calculate the percentage of trajectories that pass through each 0.75° grid cell. We focused on DJF because this period captures the majority of annual precipitation for all stations (Tables 2.4 and 2.5), and thus, largely determines annual weighted $\delta^{18}O_p$. We normalized the partitioning of air transport from these three regions to 100% to compare between the three main source regions more directly. Non-normalized trajectory partitioning values are provided in the supporting information (Appendix 2B).

To assess the sensitivity of our results to the HYSPLIT data source used, we also calculated back trajectories using the NCEP/NCAR reanalysis dataset. We found that air transport patterns with the NCEP/NCAR reanalysis are qualitatively similar to those calculated from ERA-Interim data, though with less advection from the South Pacific region (Appendix

2C). We attribute these changes to resolution differences between the two reanalysis datasets: NCEP/NCAR is ~2.5° while ERA-Interim is ~0.75°. We therefore consider results from the ERA-Interim dataset to more accurately represent the influence of regional topography on air source pathways.

2.4.4 Data Caveats

We acknowledge our analyses are subject to two major limitations. First, the isotopic data represent point measurements, yet the reanalysis products we used are gridded values averaged over much larger areas. Fortunately, the recent release of high-resolution reanalysis products reduces the severity of this problem [*Dee et al.*, 2011]. Regardless, resolutions remain at ~50-75 km and many key precipitation processes occur on smaller spatial scales (~1-10 km). Thus, simulated precipitation amounts depend highly on the choice of model parameterizations [*Grell*, 1993; *Zhang and McFarlane*, 1995]. Second, TRMM precipitation amounts inferred from continental deep convective systems are uncertain [*Iguchi et al.*, 2009; *Rasmussen et al.*, 2013]. Precipitation variability within the TRMM radar footprint also tends to underestimate rainfall amounts in deep convective systems [*Iguchi et al.*, 2009]. However, these studies used the TRMM 2A25 product, which relies on TRMM precipitation radar measurements. The TRMM 3B43 product we used reduces the potential satellite bias by incorporating surface observations [*Huffman*, 1997; *Huffman et al.*, 2007]. Due to the variable distribution of meteorological stations, however, the bias reduction is also spatially variable. Therefore, though our monthly precipitation estimates for missing values are reasonable when compared to nearby stations, they are likely still biased. We have estimated the bias at each station by regressing station measurements against TRMM values; recall we find it to be < 25% (see section 2.3.1, Figure 2.3, Table 2.1). This bias could contribute to the anomalously low observed correlations between precipitation and $\delta^{18}O_p$ at the stations most reliant on the TRMM data (El Choro, Quillacas, and Salinas) relative to the other stations. Additionally, we avoided making quantitative comparisons between upwind precipitation anomalies and central Andean $\delta^{18}O_p$ due to the uncertain size of this TRMM bias. As this bias affects all measurements, we maintain that the sign of the precipitation anomalies observed is more likely to be robust than their magnitudes.

2.5 Results

All our stations show annual- and DJF-scale relationships between $\delta^{18}O_p$ and δD_p that are close to the GMWL (Figure 2.4, Table 2.2). This indicates that the annual and DJF relationships between $\delta^{18}O_p$ and δD_p do not vary systematically in space or time in our dataset. Seasonal variations during JJA result in markedly different local meteoric water lines (Table 2.2) that are associated with high d-excess values (Table 2.3). High d-excess observed in these samples likely results from two different effects during the dry season. First, changes in vapor sourcing to the region, such as increased advection from the mid- to high-latitudes over the ocean, would transport higher *d*-excess vapor to the central Andes resulting from increased kinetic fractionation at the oceanic source [*Uemura et al.*, 2008]. Second, large scale subsidence during the dry season can mix high d-excess vapor from higher in the troposphere down toward the surface [e.g., *Blossey et al.*, 2010; *Samuels-Crow et al., 2014b*]. However, as central Andes JJA precipitation represents a small fraction (< 10%) of the annual total, we focus the following analysis on $\delta^{18}O_p$ for brevity because analyzing δD_p yields near identical results.

Table 2.3. Deuterium excess in precipitation samples as a function of season. Errors presented in the unweighted d-excess mean values are 1-sigma.

Station	Mean d-excess (unweighted)			Precipitation Weighted Mean d-excess		
	Full Year	DJF Only	JJA Only	Full Year	DJF Only	JJA Only
Oruro (ORU)	16.0 ± 3.4	16.4 ± 2.4	15.9 ± 11.5	16.5 ± 2.4	16.6 ± 2.1	22.6 ± 11.5
El Choro (ECH)	14.6 ± 3.3	15.4 ± 3.0	13.4 ± 5.9	15.3 ± 3.0	15.5 ± 2.8	13.9 ± 5.9
Quillacas (QUI)	15.2 ± 2.8	15.7 ± 2.7	17.2 ± 6.6	15.9 ± 2.6	16.2 ± 2.6	21.8 ± 4.1
Salinas (SAL)	14.3 ± 3.3	15.1 ± 2.4	N/A	15.2 ± 2.6	15.1 ± 2.3	N/A
San Juan (SJU)	14.4 ± 3.9	15.1 ± 3.2	11.2 (n=1)	14.5 ± 4.0	15.1 ± 3.0	11.2 (n=1)
Noel Mariaca (NMA)	15.3 ± 3.8	15.9 ± 3.5	N/A	15.4 ± 3.9	15.6 ± 3.9	N/A
Gran Chocaya (GCH)	19.4 ± 7.7	22.1 ± 2.3	-12.4 (n=1)	20.8 ± 5.3	21.8 ± 2.2	-12.4 (n=1)
Tupiza (TUP)	14.5 ± 7.1	17.2 ± 4.4	N/A	16.8 ± 4.9	17.3 ± 4.7	N/A
Tarija (TAR)	16.6 ± 4.3	16.9 ± 3.2	12.6 ± 1.8	17.1 ± 3.4	16.9 ± 3.4	13.0 ± 1.8
Entre Ríos (ERI)	19.3 ± 3.7	17.4 ± 2.8	19.9 ± 4.5	17.7 ± 2.6	17.1 ± 2.7	18.0 ± 5.9
Villamontes (VMO)	16.3 ± 6.0	14.9 ± 3.6	22.4 ± 1.0	15.1 ± 3.8	14.4 ± 3.4	22.5 ± 1.0

Central Andes monthly $\delta^{18}O_p$ varies considerably across annual to seasonal timescales. Values ranged from -28.0‰ (El Choro, February 2009, Figure 2.5a) to 9.6‰ (Tupiza, September 2011, Figure 2.6a). Plateau $\delta^{18}O_p$ values were generally more negative than along the eastern flank (compare Figures 2.5a and 2.6a). All 11 of our stations exhibited seasonal variability in $\delta^{18}O_p$. The most negative $\delta^{18}O_p$ values occurred during the rainy season (DJF), as more than two

thirds of rainy season average $\delta^{18}O_p$ values were more negative than the annual average (Tables 2.4 and 2.5). In contrast, the least negative $\delta^{18}O_p$ values occurred during the dry season (JJA). Gaps in our $\delta^{18}O_p$ records correspond to periods where no precipitation was recorded (Figures 2.5a and 2.6a). The plateau stations tended to experience longer dry periods, and therefore, possessed more discontinuous $\delta^{18}O_p$ records (Figure 2.5a). In addition, plateau stations exhibited larger amplitude seasonal differences between DJF minimum and JJA maximum $\delta^{18}O_p$ values than the flank stations (10-15‰ vs 5-10‰, compare Figures 2.5a and 2.6a).

Annual minimums in $\delta^{18}O_p$ occurred in conjunction with annual precipitation maximums, annual OLR minimums, and annual minimums in 200 hPa zonal winds (Figures 2.5 and 2.6). Plateau annual precipitation amounts ranged from 64 mm to 623 mm (Tables 2.4 and 2.5), with a maximum measured monthly value of 180 mm (Quillacas, Feb. 2011) or, if remote-sensed TRMM data are included, 273 mm (El Choro, Feb. 2011) (Figure 2.5b, Appendix 2A). Flank annual precipitation amounts ranged from 186 mm (Gran Chocaya, Jul. 2012-June 2013) to 860 mm (Entre Ríos, 11 months, Aug. 2008-June 2009) (Tables 2.4 and 2.5). Measured monthly values on the flank ranged from 0 mm (various) to 214 mm (Entre Ríos, Dec. 2008), or 324 mm (Villamontes, Feb. 2010) including TRMM estimates (Figure 2.6b, Appendix 2A). The percentage of annual rain received at each station during DJF ranged from 67 to 78% (El Choro and Noel Mariaca, respectively) on the plateau and 59 to 80% on the flanks (Entre Ríos and Tupiza).

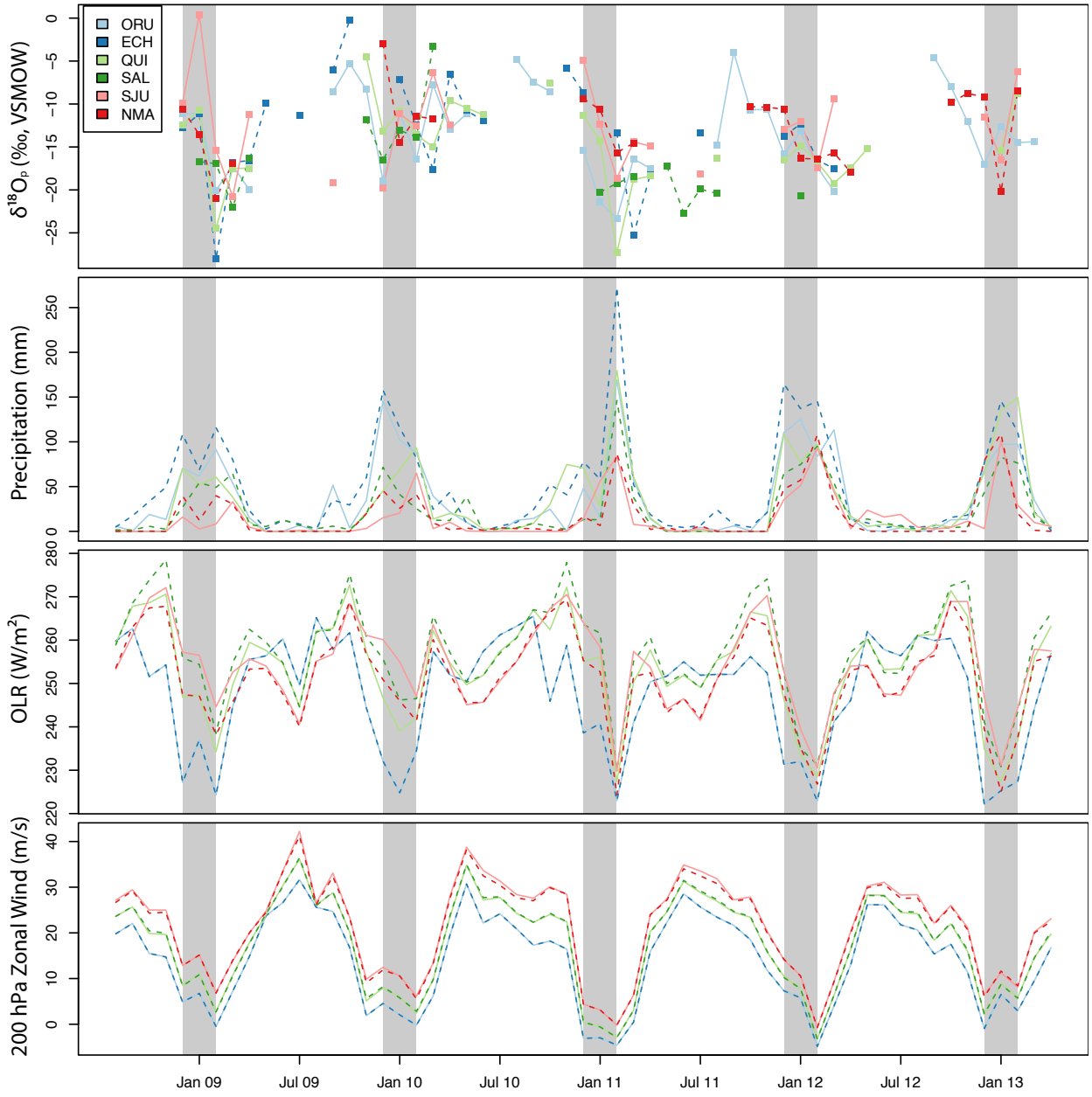

Figure 2.5. Time series for Altiplano stations of monthly (a) $\delta^{18}O_p$ (‰), (b) precipitation amount (mm), (c) outgoing longwave radiation (OLR, W/m^2), and (d) 200 hPa zonal wind (U, m/s). Missing values in (a) are months where no precipitation was recorded or no sample was retrieved from the observer. Values in (c) and (d) were calculated from the ERA Interim reanalysis dataset. Missing values in (b) are from the TRMM 3B43 dataset (Table 2.11). The rainy season (DJF) is highlighted in gray columns. Note the strong seasonal cycling across all variables. High precipitation and low $\delta^{18}O$ are associated with OLR and zonal wind minimums.

Table 2.4. Annual amount-weighted isotopic composition and precipitation amounts for Altiplano stations

	Isotopic Samples Retrieved	Annual			DJF Only		
		Precip (mm)	$\delta^{18}O$ (‰)	δD (‰)	Precip (mm)	$\delta^{18}O$ (‰)	δD (‰)
1. Oruro (ORU, 17.98°S, 67.11°W, 3718 masl)							
Aug 2008 – June 2009	5	331	-15.5	-106.4	223	-14.8	-99.4
July 2009 – June 2010	9	503	-13.7	-92.9	336	-15.9	-110.6
July 2010 – June 2011	8	357	-18.5	-131.5	233	-21.5	-156.1
July 2011 – June 2012	8	482	-16.0	-111.6	319	-15.2	-105.5
June 2012 – April 2013	7	333	-14.1	-96.6	264	-14.5	-99.7
Total/Average	**37**	**2006**	**-15.5**	**-107.1**			
2. El Choro (ECH, 18.36°S, 67.11°W, 3706 masl)							
Aug 2008 – June 2009	6	516	-17.9	-125.9	293	-18.4	-129.1
July 2009 – June 2010	8	568	-10.6	-70.7	355	-11.3	-75.6
July 2010 – June 2011	5	623	-19.5	-140.0	408	-23.2	-170.0
July 2011 – June 2012	5	619	-14.7	-103.7	447	-14.2	-99.1
June 2012 – April 2013	0	407	N/A	N/A	333	N/A	N/A
Total/Average	**24**	**2733**	**-15.6**	**-109.2**			
3. Quillacas (QUI, 19.23°S, 66.94°W, 3780 masl)							
Aug 2008 – June 2009	5	233	-16.3	-112.9	183	-15.9	-110.0
July 2009 – June 2010	8	296	-11.6	-78.2	208	-12.6	-85.1
July 2010 – June 2011	6	494	-19.4	-139.1	285	-21.7	-158.1
July 2011 – June 2012	7	359	-16.6	-118.5	283	-16.2	-114.3
June 2012 – April 2013	2	416	-11.9	-77.5	350	-11.9	-77.4
Total/Average	**28**	**1798**	**-15.5**	**-108.1**			
4. Salinas (SAL, 19.65°S, 67.64°W, 3719 masl)							
Aug 2008 – June 2009	6	232	-20.6	-145.3	130	-16.8	-117.7
July 2009 – June 2010	5†	237	-8.7	-61.0	138	-15.0	-105.8
July 2010 – June 2011	5†	241	-18.2	-101.6	172	-19.3	-138.7
July 2011 – June 2012[a]	3	322	-20.7	-154.1	234	-20.7	-154.1
June 2012 – April 2013	0	244	N/A	N/A	202	N/A	N/A
Total/Average	**19**	**1276**	**-17.5**	**-122.6**			
5. San Juan (SJU, 20.90°S, 67.76°W, 3663 masl)							
Aug 2008 – June 2009	5	64	-15.8	-111.5	27	-10.5	-71.9
July 2009 – June 2010	6	119	-13.1	-91.9	101	-13.4	-94.5
July 2010 – June 2011	5	169	-15.1	-106.0	154	-15.1	-106.1
July 2011 – June 2012	5	270	-13.9	-98.5	180	-15.0	-104.8
June 2012 – April 2013	3	190	-14.1	-95.2	133	-14.1	-95.2
Total/Average	**24**	**812**	**-14.3**	**-99.8**			
6. Noel Mariaca (NMA, 20.68°S, 66.64°W, 3780 masl)							
Aug 2008 – June 2009	4	124	-15.9	-114.0	92	-15.5	-110.5
July 2009 – June 2010	4	148	-8.9	-54.6	112	-8.7	-52.1
July 2010 – June 2011	4	159	-14.4	-104.3	110	-14.4	-106.4
July 2011 – June 2012	5	256	-15.2	-106.0	212	-15.1	-104.5
June 2012 – April 2013	3	160	-14.9	-100.2	141	-14.9	-100.2
Total/Average	**20**	**847**	**-14.1**	**-97.8**			

†: Where this symbol appears, some samples were judged to be suspect and excluded from subsequent analysis. Details are provided in Appendix 2A.

OLR values also exhibited a prominent seasonal cycle characterized by minimum values during DJF, indicating summer convection and increased cloud cover (Figures 2.5c and 2.6c). Monthly plateau and flank values had similar ranges; plateau values ranged from 222 W/m^2 (Oruro and El Choro, Dec. 2012) to 279 W/m^2 (Salinas, Nov. 2008) (Figure 2.5c), and flank values ranged from 221 W/m^2 (Tupiza, Feb. 2011) to 280 W/m^2 (Villamontes, Aug. 2009) (Figure 2.6c). However, there is a prominent difference in amplitude of the seasonal cycle between the plateau and flank regions. Plateau annual OLR variability can exceed 40 W/m^2 whereas along the flank it is closer to 20-30 W/m^2 (Figures 2.5d and 2.6d). The lone exception is Gran Chocaya, which exhibits an annual cycle more similar to plateau stations, though it is located in the high Cordillera adjacent to the plateau.

The annual cycle of upper-level zonal winds mirrors the annual cycle in OLR. During JJA, westerly winds prevail across both the plateau and its flank (Figures 2.5d and 2.6d). DJF wind speeds are slower and can be either easterly or westerly. Monthly average upper-level zonal wind speeds fluctuate by ~40 m/s across all stations throughout the year. Wind speeds vary spatially on the plateau by ~10 m/s throughout the annual cycle, with consistently greater westerly wind speeds observed in the southern plateau (Figure 2.5d). In contrast, little variability in upper-level wind speeds occurs across flank stations (Figure 2.6d).

The central Andes annual $\delta^{18}O_p$ variations correspond to cycles of monthly precipitation, OLR, and upper-level wind speed, indicating that $\delta^{18}O_p$ responds to seasonal changes in synoptic circulation. Despite these relationships, however, significant spatial, interannual, and month-to-month variability exists in $\delta^{18}O_p$ that cannot be explained solely by these environmental variables. In the following sections, we examine the dominant spatial controls on $\delta^{18}O_p$ and use reanalysis data and back-trajectory modeling to identify sources of spatiotemporal variability.

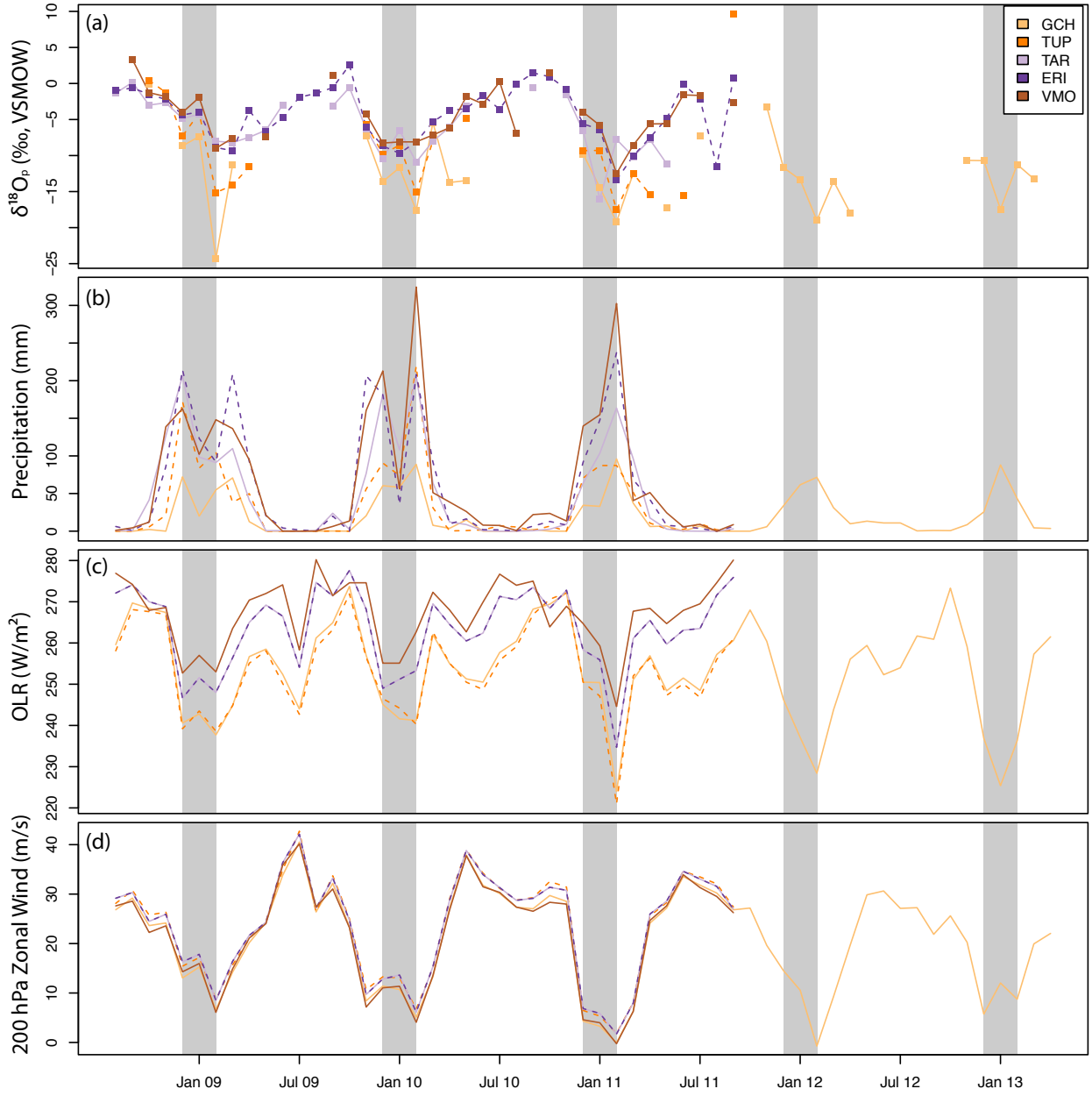

Figure 2.6. Time series for eastern flank stations of monthly (a) $\delta^{18}O_p$ (‰), (b) precipitation amount (mm), (c) outgoing longwave radiation (OLR, W/m^2), and (d) 200 hPa zonal wind (U, m/s). Missing values in (a) are months where no precipitation was recorded or no sample was retrieved from the observer. Values in (c) and (d) were calculated from the ERA Interim reanalysis dataset. Missing values in (b) are from the TRMM 3B43 dataset (Table 2.11). The rainy season (DJF) is highlighted in gray columns. Note the strong seasonal cycling across all variables. High precipitation and low $\delta^{18}O$ are associated with OLR and zonal wind minimums.

Table 2.5. Annual amount-weighted isotopic composition and precipitation amounts for eastern flank stations.

	Isotopic Samples Retrieved	Annual			DJF Only		
		Precipitation (mm)	$\delta^{18}O$ (‰)	δD (‰)	Precipitation (mm)	$\delta^{18}O$ (‰)	δD (‰)
7. Gran Chocaya (GCH, 20.97°S, 66.33°W, 4340 masl)							
Aug 2008 – June 2009	5	233	-13.2	-81.1	147	-14.3	-89.7
July 2009 – June 2010	7	255	-13.8	-89.4	208	-14.8	-97.3
July 2010 – June 2011	4	216	-13.6	-96.4	163	-13.3	-96.4
July 2011 – June 2012	7	246	-14.7	-97.8	167	-15.4	-102.0
June 2012 – April 2013	5	186	-14.4	-93.2	157	-14.6	-95.0
Total/Average	**28**	**1136**	**-14.0**	**-92.0**			
8. Tupiza (TUP, 21.44°S, 65.72°W, 2974 masl)							
Aug 2008 – June 2009	7	476	-9.1	-51.2	361	-8.8	-48.3
July 2009 – June 2010	6	243	-11.2	-74.0	215	-11.7	-78.1
July 2010 – June 2011	6	203	-13.0	-90.0	162	-13.0	-89.6
Total/Average	**19**	**922**	**-10.5**	**-65.8**			
9. Tarija (TAR, 21.54°S, 64.70°W, 1884 masl)							
Aug 2008 – June 2009	11	718	-5.3	-22.8	396	-5.4	-22.4
July 2009 – June 2010	9	686	-8.8	-55.1	496	-9.8	-63.4
July 2010 – June 2011	8	460	-9.8	-62.8	331	-10.1	-65.7
Total/Average	**29**	**1864**	**-7.7**	**-44.5**			
10. Entre Ríos (ERI, 21.50°S, 64.17°W, 1261 masl)							
Aug 2008 – June 2009	11	860	-5.7	-26.0	429	-5.2	-22.2
July 2009 – June 2010	11	774	-7.1	-40.0	425	-8.5	-51.8
July 2010 – June 2011	12	631	-9.0	-55.6	477	-9.7	-61.9
Total/Average	**36**	**2265**	**-7.0**	**-38.9**			
11. Villamontes (VMO, 21.25°S, 63.41°W, 395 masl)							
Aug 2008 – June 2009	8	630	-5.4	-25.4	351	-5.3	-25.6
July 2009 – June 2010	9	489	-7.2	-45.6	339	-8.2	-54.3
July 2010 – June 2011	10	793	-7.9	-46.7	597	-8.8	-54.2
Total/Average	**29**	**1912**	**-6.8**	**-39.0**			

2.5.1 Relationships between $\delta^{18}O_p$, Topography, and Climate

Linear regression indicates elevation is the strongest single predictor of $\delta^{18}O_p$ for our stations (r = -0.907), as well as for all available data (r = -0.773) (Figure 2.7a). Weaker relationships exist between $\delta^{18}O_p$ and our stations and across all available data for latitude (r = -0.736 and 0.147, Figure 2.7b) and MAP (r = 0.783 and 0.496, Figure 2.7c). Multiple studies have indicated, however, that $\delta^{18}O_p$ can depend on multiple spatial or climatic variables [e.g., *Dansgaard*, 1964; *Bowen and Wilkinson*, 2002; *Lechler and Niemi*, 2012]. Therefore, we tested possible combinations of latitude, elevation, and MAP predictor variables to determine the best multivariate model.

The lowest AICc score shows that the best model for our stations retains elevation and latitude predictors (Table 2.6). Removing either of these predictor variables increases the AICc score and reduces the goodness of model fit. In contrast, the best AICc model for the entire available dataset retains only the elevation predictor (Table 2.6). However, the AICc score neglects any potential correlation between predictor variables. High correlations between these three predictor variables can be problematic for our multivariate regression models. Elevation and MAP correlate highly for both datasets (r = -0.861 stations from this study, r = -0.717 for the entire dataset). Depending on which dataset is used, correlations between latitude and elevation (r = 0.531 stations from this study, r = -0.319 for the entire dataset) and latitude and MAP (r =-0.277 stations from this study, r = 0.717 for the entire dataset) can also be high. As a result, the best-fit model should retain only one of these predictor variables. We propose that the best model for our stations includes only elevation because it has the highest univariate correlation with $\delta^{18}O_p$ (Table 2.6). Furthermore, in both cases, modeled relationships between $\delta^{18}O$ and latitude or MAP are weak and highly sensitive to data subsetting, indicating that neither predictor is a strong regional control on $\delta^{18}O_p$ (Figure 2.7b,c). Despite this apparent control of elevation on $\delta^{18}O_p$ across multi-year timescales, however, elevation is a poor predictor of $\delta^{18}O_p$ on the Altiplano itself (Figure 2.7a), and the $\delta^{18}O_p$-elevation relationship is highly variable in space and time.

Table 2.6. Multivariate linear model fits to amount-weighted mean $\delta^{18}O_p$ to the geographic parameters of elevation, mean annual precipitation, and latitude. Rows containing N/A indicate that that variable was not included in that particular regression model.

Stations from this study only						
Regression model	Elevation Coefficient (‰/m)	Latitude Coefficient (‰/°)	MAP Coefficient (‰/mm/yr)	Intercept (‰)	r^2	AICc
lat + elev + MAP	-1.25×10^{-3}	-1.29	4.38×10^{-3}	-36.78	0.933	43.63
elev + MAP	-2.74×10^{-3}	N/A	2.38×10^{-4}	-4.22	0.824	50.29
elev + lat	-2.21×10^{-3}	-1.04	N/A	-27.11	0.911	42.75
elev	-2.78×10^{-3}	N/A	N/A	-4.22	0.824	47.23
lat	N/A	-2.19	N/A	-57.10	0.541	57.77
MAP	N/A	N/A	0.011	-17.34	0.613	55.90
All Available Data						
Regression model	Elevation Coefficient (‰/m)	Latitude Coefficient (‰/°)	MAP Coefficient (‰/mm/yr)	Intercept (‰)	r^2	AICc
lat + elev + MAP	-2.05×10^{-3}	-0.169	-9.69×10^{-5}	-8.68	0.608	206.20
elev + MAP	-2.15×10^{-3}	N/A	-6.47×10^{-4}	-4.89	0.604	204.34
elev + lat	-2.03×10^{-3}	-0.186	N/A	-9.11	0.608	203.90
elev	-1.94×10^{-3}	N/A	N/A	-5.97	0.597	202.90
lat	N/A	0.249	N/A	-6.87	0.022	241.94
MAP	N/A	N/A	2.72×10^{-3}	-13.44	0.246	230.47

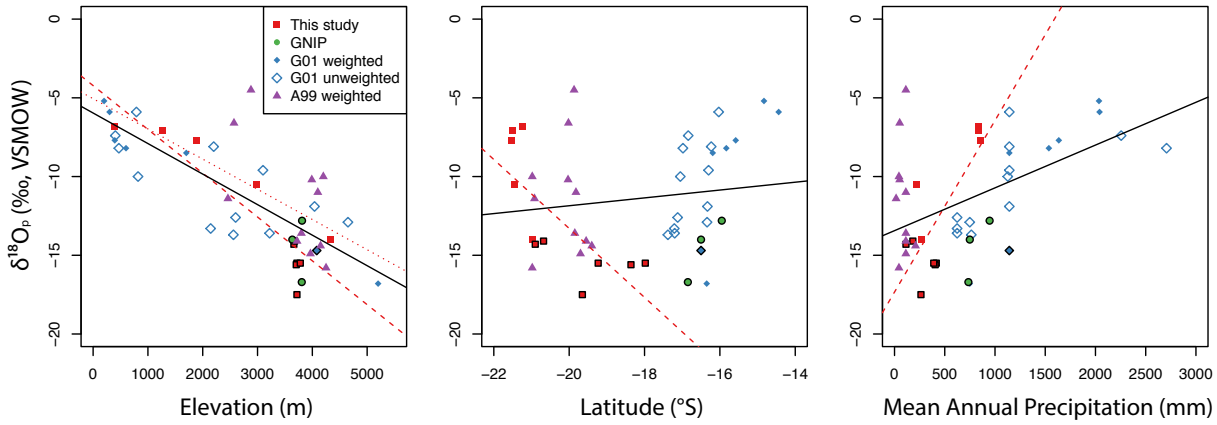

Figure 2.7. Scatterplots relating weighted annual mean $\delta^{18}O_p$ with elevation (a), latitude (b), and mean annual precipitation (MAP, c) for the central Andes. Red squares are data from our 11 study area stations, purple triangles are data from Aravena et al. [1999], filled (open) blue diamonds are weighted (unweighted) data from Gonfiantini et al. [2001], and green circles are data from the GNIP stations. Values outlined in black are stations on the plateau. Dashed red line is the best-fit linear relationship between $\delta^{18}O_p$ and the predictor variable for stations from this study only, while the solid black line is the best-fit linear relationship using all data sources. An additional dotted regression line in (a) excludes the six plateau stations.

2.5.2 Spatial Variability of $\delta^{18}O$ and Air Sources

We observe a strong $\delta^{18}O_p$-elevation relationship across our elevation transect (Figure 2.7). Amount-weighted $\delta^{18}O_p$ decreases with increasing elevation; the lowest elevation site has an amount-weighted annual average $\delta^{18}O_p$ composition of -6.7‰ (Villamontes, 395 masl) and the highest elevation site -14.0‰ (Gran Chocaya, 4340 masl). For the entire study period, the isotopic lapse rate (defined as the slope of the elevation-$\delta^{18}O_p$ relationship) along this transect was -1.9 ± 0.3 ‰/km, but ranged from -2.1 ± 0.5 ‰/km in 2008-09 to -1.6 ± 0.2 ‰/km in 2010-11. These compositions and isotopic lapse rates are comparable to those further north along the eastern Altiplano flank [*Gonfiantini et al.*, 2001]. The northernmost transect (Yungas-Altiplano, centered at ~15°S) in *Gonfiantini et al.* [2001] possessed isotopic lapse rates of -2.1 ± 0.5 ‰/km and -1.9 ± 0.2 ‰/km for July 1983-June 1984 and July 1984-June 1985, respectively. The Chaparé-Cochabamba transect (centered at ~17°S) in *Gonfiantini et al.* [2001] exhibited an isotopic lapse rate of -1.6 ± 0.2 ‰/km in 1985 (calendar year, location in Figure 2.1a). Calendar year and hydrologic (i.e., July-June) year isotopic lapse rates are similar (Table 2.7). Our isotopic lapse rates are comparable with *Gonfiantini et al.* [2001], though unlike their study, we find no

robust relationship between the isotopic lapse rate and precipitation amount. Finally, when combining our data with *Gonfiantini et al.* [2001], we cannot determine if the isotopic lapse rate varies along the length of the eastern flank as estimates from different portions of the flank overlap within error. However, we document that isotopic lapse rates vary by up to ~1.0 ‰/km from year to year along our plateau flank transect.

Table 2.7. Calendar and hydrologic year isotopic lapse rates for this study and Gonfiantini et al. [2001].

Calendar Year	***Transect***	***Isotopic Lapse Rate***	***Reference***
1983	Yungas-Altiplano	-1.5 ± 0.2 ‰ / km	Gonfiantini et al. 2001
1984	Yungas-Altiplano	-2.4 ± 0.2 ‰ / km	Gonfiantini et al. 2001
1985	Chaparé-Cochabamba	-1.6 ± 0.2 ‰ / km	Gonfiantini et al. 2001
2008[a]	Villamontes-Gran Chocaya	-1.2 ± 0.8 ‰ / km	this study
2009	Villamontes-Gran Chocaya	-2.0 ± 0.3 ‰ / km	this study
2010	Villamontes-Gran Chocaya	-2.2 ± 0.2 ‰ / km	this study
2011[b]	Villamontes-Gran Chocaya	-1.3 ± 0.4 ‰ / km	this study
Hydrologic Years	***Transect***	***Isotopic Lapse Rate***	***Reference***
7/1983-6/1984	Yungas-Altiplano	-2.1 ± 0.5 ‰ / km	Gonfiantini et al. 2001
7/1984-6/1985	Yungas-Altiplano	-1.9 ± 0.2 ‰ / km	Gonfiantini et al. 2001
7/1984-6/1985	Chaparé-Cochabamba	not available	Gonfiantini et al. 2001
8/2008-6/2009	Villamontes-Gran Chocaya	-2.1 ± 0.5 ‰ / km	this study
7/2009-6/2010	Villamontes-Gran Chocaya	-1.8 ± 0.2 ‰ / km	this study
7/2010-6/2011	Villamontes-Gran Chocaya	-1.6 ± 0.2 ‰ / km	this study

a: September – December only
b: January – September only

Several modes of spatial variability arise in Altiplano $\delta^{18}O_p$ that are not accounted for by the common empirically-derived isotopic lapse rates. First, values for all our Altiplano stations (Figure 2.1a) are more negative than (a) predicted for their elevation (Figure 2.7a) and (b) the values observed at the upwind, but higher-elevation Gran Chocaya station along the eastern Altiplano margin (0.1-3.6‰ more negative, despite elevations 500 m lower, Figure 2.8). This trend toward more negative $\delta^{18}O_p$ values indicates that heavy water isotopologues in air parcels on the Altiplano continue to be removed following their ascent over the Cordillera. The most likely processes to explain this pattern are continued rainout of air parcels through Rayleigh-like processes as well as vapor recycling [e.g., Risi et al., 2008] and entrainment of mid- and upper tropospheric vapor associated with deep convection on the Altiplano [e.g., Moore et al., 2014]. Second, annual average $\delta^{18}O_p$ values for the same year can vary by ~5‰ (Figure 2.8a). Similarly, for single months, $\delta^{18}O_p$ values can vary by >10‰ (Figures 2.5a and 2.6a). For example, in February 2009, $\delta^{18}O_p$ values were -28.0‰ at El Choro and -15.4‰ at San Juan, and in January 2011, $\delta^{18}O_p$ values were -21.4‰ at Oruro, but -10.7‰ at Noel Mariaca. Elevation cannot account for this variability. To better understand this variability, we calculated a correlation matrix comparing $\delta^{18}O_p$ values for each station with every other station (Table 2.8). Our southernmost stations on the Altiplano—Noel Mariaca and San Juan—exhibit low correlations with our other stations, while our northern Altiplano and eastern flank stations express high correlations with their neighbor stations. This pattern indicates a high likelihood that controls on southern Altiplano air sourcing and $\delta^{18}O_p$ differ from those on the northern Altiplano and the eastern flank.

Spatial patterns in $\delta^{18}O_p$ appear related to trends in air source (Figure 2.9). Back-trajectory modeling indicates that air sources vary substantially for individual stations. Northern and central Altiplano stations (Oruro and Quillacas) show strong air sourcing from the Yungas-Amazon Basin (YAB) to the north and along a narrow pathway from the South Pacific (SP) (Figure 2.9). Air source regions from eastern flank stations are more diffuse, but show clear maxima in the YAB and Gran Chaco (GC) regions and significantly reduced advection from the SP. In contrast, the southern Altiplano station of Noel Mariaca shows strong air sourcing from the SP and GC regions, with a relatively reduced contribution from the YAB (Table 2.9, 15.3% vs 40.0% for Oruro).

Table 2.8. Correlation coefficient matrix comparing the $\delta^{18}O_p$ for all stations. Relationships that are significant at the p = 0.05 level are bolded and at the p = 0.10 level are italicized.

	El Choro	Quillacas	Salinas	San Juan	Noel Mariaca	Gran Chocaya	Tupiza	Tarija	Entre Ríos	Villamontes
Oruro	**0.734**	**0.745**	**0.631**	*0.357*	0.044	**0.676**	**0.805**	**0.746**	**0.754**	**0.641**
El Choro		**0.855**	0.413	0.214	**0.702**	**0.753**	**0.778**	0.386	**0.665**	**0.659**
Quillacas			0.354	**0.537**	**0.564**	**0.645**	**0.826**	0.383	**0.669**	**0.743**
Salinas				0.460	0.238	**0.641**	**0.642**	*0.463*	**0.555**	0.444
San Juan					0.240	**0.504**	**0.741**	0.224	0.283	0.237
Noel Mariaca						**0.536**	0.441	-0.223	0.346	0.294
Gran Chocaya							**0.828**	*0.480*	**0.604**	**0.666**
Tupiza								**0.658**	**0.809**	**0.755**
Tarija									**0.711**	**0.742**
Entre Ríos										**0.786**

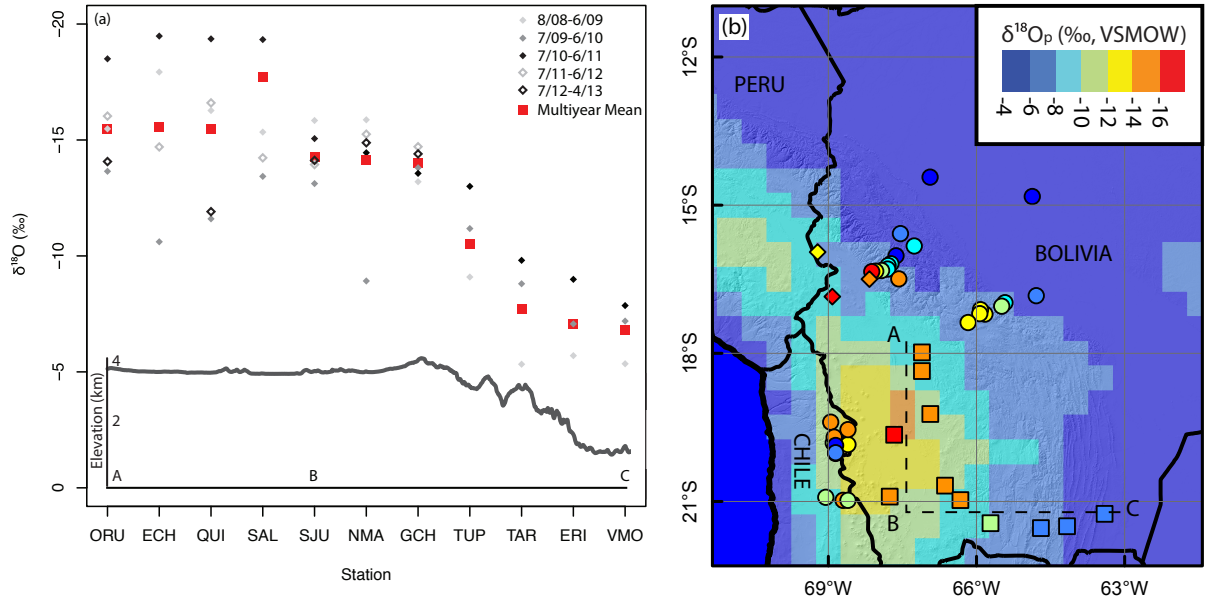

Figure 2.8. Spatiotemporal variability in central Andes annual mean weighted $\delta^{18}O_p$. (a) All study area stations (unit is ‰, VSMOW). Individual year values are in black / gray symbols and station mean values are in solid red squares. Along the elevation transect (B-C), interannual variability is twice the magnitude at the low elevation stations than at the highest elevation station. Interannual variability in stations on the Altiplano is much larger than interannual variability along the elevation transect. A swath topographic profile representing local topography is shown below the isotopic values. (b) All available central Andes data. Averages from this study are squares, GNIP stations are diamonds, and data from Aravena et al. [1999] and Gonfiantini et al. [2001] are circles in Chile and Bolivia, respectively. Symbol fill color indicates the average $\delta^{18}O_p$, with red (blue) values showing more (less) depleted $\delta^{18}O_p$ values. Background contours indicate 10-year amount-weighted annual mean $\delta^{18}O_p$ simulated by the REMOiso regional climate model [Insel et al., 2013, model years 1989-1998].

Table 2.9. Composite normalized areal mean DJF back-trajectory partitioning (percentage).

Station	Yungas-Amazon (13-15°S, 65-69°W)		South Pacific (20-24°S, 69-71°W)		Gran Chaco (24-26°S, 62-66°W)	
	All	Rain Only	All	Rain Only	All	Rain Only
ORU	40.7	44.5	53.2	49.9	6.1	5.6
QUI	26.4	40.0	65.1	49.6	8.5	10.3
NMA	15.3	38.3	73.5	33.2	11.2	28.5
TAR	30.0	36.0	37.6	25.0	32.4	39.0
VMO	55.3	60.1	18.9	11.0	25.7	28.9

Table 2.10. Correlations between DJF air source regions and Bolivian High latitude, monthly precipitation amount and $\delta^{18}O_p$. Correlation coefficients are calculated using all available trajectories, or only trajectories resulting in precipitation at the station as forecasted by the ERA-Interim reanalysis dataset. Coefficients that are significant at the p = 0.05 level are bolded.

		Oruro	Quillacas	Noel Mariaca	Tarija	Villamontes
Bolivian High Latitude						
All available trajectories	Yungas-Amazon (YAB)	0.004	-0.220	**-0.614**	**-0.808**	-0.027
	South Pacific (SP)	0.323	0.303	**0.545**	**-0.890**	-0.562
	Gran Chaco (GC)	-0.099	-0.174	0.103	0.036	0.289
Rain event trajectories only	YAB	-0.001	-0.202	**-0.574**	**-0.731**	-0.277
	SP	-0.016	0.329	0.072	**0.729**	0.383
	GC	0.030	-0.138	0.509	0.199	-0.079
Monthly Precipitation Amount						
All available trajectories	YAB	-0.009	0.306	0.028	-0.203	-0.414
	SP	-0.057	-0.394	-0.417	0.149	-0.053
	GC	0.127	0.194	**0.538**	0.084	0.430
Rain event trajectories only	YAB	-0.030	0.176	-0.265	-0.208	-0.030
	SP	-0.120	0.107	0.319	0.515	-0.404
	GC	0.244	-0.295	0.020	-0.191	0.349
Bolivian High Latitude		0.160	-0.094	-0.139	0.221	-0.577
Monthly $\delta^{18}O_p$						
All available trajectories	YAB	0.093	-0.051	-0.140	-0.578	-0.282
	SP	0.236	0.205	**0.547**	0.252	0.161
	GC	0.164	-0.298	**-0.563**	0.404	0.203
Rain event trajectories only	YAB	-0.056	0.135	0.052	-0.582	-0.347
	SP	-0.048	-0.129	0.213	0.186	0.366
	GC	0.149	-0.004	-0.211	0.478	-0.005
Bolivian High Latitude		**0.663**	0.409	0.079	0.463	0.560

Three major trends become clear from the mean partitioning between the three main air sources (Table 2.9). First, the northern Altiplano receives air parcels from the YAB more frequently than the southern Altiplano, consistent with prior regional climate model simulations [*Insel et al.*, 2013]. Correspondingly, the frequency of air parcels arriving from the SP and GC regions on the plateau increases from north to south. Second, the frequency of YAB-derived air parcels is higher along the eastern flank than on the southern Altiplano. This result supports the strong correlations between northern Altiplano stations and percentage of YAB parcels (Table 2.10). Finally, the eastern flank stations show diminished air sourcing from the SP and augmented air sourcing from the GC region compared to the plateau stations.

The proportion of trajectories from the YAB converges to ~40% for all plateau stations when we calculate air source partitioning using only trajectories that co-occur with precipitation (Table 2.9). The tendency of YAB trajectories to have equal importance at all Altiplano stations during precipitation events suggests that plateau $\delta^{18}O_p$ variability is related to changes in the $\delta^{18}O$ of YAB vapor and the partitioning of air between SP and GC sources. This pattern also indicates that moisture advection from the YAB is important for initiating precipitation on the southern Altiplano, but occurs less frequently overall.

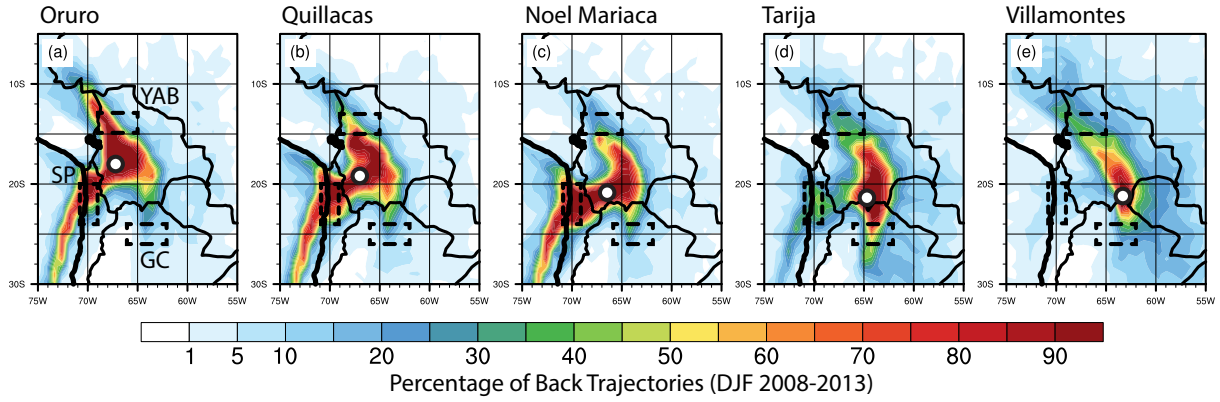

Figure 2.9. Composite main vapor trajectory maps for five central Andes stations. We binned available trajectories to a 0.75° grid and then calculated the frequency of a trajectory passing through each grid cell. White circles denote the station location. All stations exhibit high concentrations of source trajectories along three main pathways (a): from the Yungas-Amazon Basin (YAB), the South Pacific (SP) ocean along the Chilean margin, and the Gran Chaco (GC) region, east and southeast of the Altiplano. YAB trajectory frequencies decrease from the northern to southern Altiplano (a-c). In contrast, air sourcing along the eastern flank is more diffuse, but still tends to be from the YAB and GC regions (d-e).

2.5.3 Temporal Variability of $\delta^{18}O_p$ and Air Sourcing

Our measurements of central Andes $\delta^{18}O_p$ also show significant temporal variability. Amount weighted mean $\delta^{18}O_p$ varies from year to year for all stations, with higher interannual variability observed in the northern Altiplano and the eastern flank compared to the southern Altiplano (Figure 2.8). For example, annual $\delta^{18}O_p$ varied from -11.6‰ (July 2009-June 2010) to -19.4‰ (July 2010-June 2011) at Quillacas and -5.3‰ (August 2008-June 09) to -9.8‰ (July 2010-June 2011) at Tarija, but only varied from -13.1‰ (July 2009-June 2010) to -15.8‰ (August 2008-June 2009) at San Juan. Furthermore, the total range in annual average $\delta^{18}O_p$ observed on the plateau itself (~9‰) is approximately the same range as is observed across the entire elevation transect (Figure 2.8).

High interannual variability in mean annual $\delta^{18}O_p$ could have several different causes. First, interannual variability in the large-scale circulation could result in changes in moisture source partitioning between the Atlantic and Pacific Oceans as well as the YAB or GC regions. Air masses from each of these regions are likely isotopically distinct [*Vuille et al.*, 2003a; *Sturm et al.*, 2007; *Insel et al.*, 2013], and variations in the relative balance of moisture advection in each region could alter isotopic compositions observed in the Central Andes. Alternatively, interannual variability could be related to remote precipitation processes. For example, anomalously high (low) precipitation upstream along a trajectory from the Central Andes could increase (decrease) rainout from an air parcel, and result in more (less) negative $\delta^{18}O_p$ values in the Central Andes. We investigate these two mechanisms below.

2.5.3.1 Changes in Large-Scale Circulation and Air Sourcing

Partitioning of air trajectories between YAB, SP, and GC pathways varies from year to year (Figure 2.10, Appendix 2D). For example, the northern Altiplano consistently receives YAB vapor more often than the eastern flank or the central and southern plateau (Figure 2.10). Variability in central Andes moisture sourcing can be related to the Bolivian High, as it guides moisture transport to the central Andes through its influence on upper level winds [*Vuille et al.*, 1998; *Lenters and Cook*, 1999; *Vuille*, 1999; *Garreaud and Aceituno*, 2001; *Insel et al.*, 2013]. 200 hPa winds from ERA-Interim show that the Bolivian High position varies from season to season. During our study period, the Bolivian High reached its most northerly position during the 2011-2012 rainy season (centered at 15°S), and its most southerly position during the 2010-2011

rainy season (centered at 20°S). Positions in the other three years are all closer to the northern extreme, with maximum monthly northward (southward) excursions to 13°S (21°S) (Appendix 2D).

Despite considerable variability in both the position of the Bolivian High and air sources, we observe few significant correlations between air sourcing and the Bolivian High. For example, we observed statistically significant ($p = 0.05$) negative correlations between the Bolivian High latitude and YAB and SP trajectory densities at Noel Mariaca ($r = -0.614$ and 0.545, respectively) and Tarija ($r = -0.808$ and 0.890) stations (Table 2.10). In contrast, we found no statistically significant relationships between the Bolivian High and GC region parcel amounts (Table 2.10). If we limit back-trajectories to those that co-occur with station precipitation, the same patterns emerge (Table 2.10). In this case, however, the relationship between SP air sourcing and Bolivian High latitude at Noel Mariaca is no longer significant ($r = 0.072$).

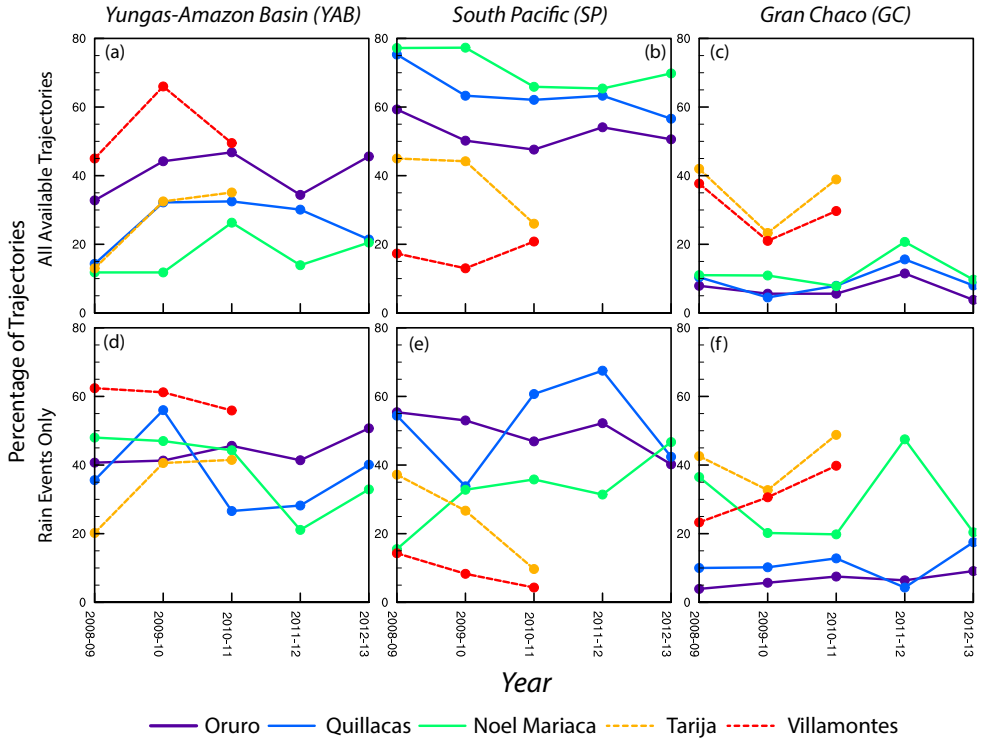

Figure 2.10. Rainy season trajectory frequencies for five stations in this study from the three main source regions. (a-c) Frequency of DJF trajectories sourced from the YAB (a), SP (b), and GC (c) regions using all trajectories. (d-f) DJF trajectory densities for only those resulting in precipitation at the station. Partitioning of air sources between stations changes on an interannual basis. Precipitation occurs most along the YAB and GC trajectories for all stations and less along the SP trajectories compared to all trajectories. We did not calculate values for Tarija and Villamontes for the 2011-12 and 2012-13 rainy seasons as the stations had been retired at this point.

Linear regressions between monthly precipitation amount and monthly $\delta^{18}O_p$ values show few strong and significant ($p = 0.05$) relationships with trajectory pathway partitioning or Bolivian High latitude (Table 2.10). No stations have a statistically significant relationship between precipitation amount and the Bolivian High latitude; only Oruro exhibits a significant relationship between monthly $\delta^{18}O_p$ values and the Bolivian High latitude ($r = 0.663$). Similarly, no salient relationships are found between monthly $\delta^{18}O_p$ and trajectory densities. The only significant relationships between monthly $\delta^{18}O_p$ and trajectory densities (SP and GC) we found are at Noel Mariaca ($r = 0.547$ and -0.563 respectively) (Table 2.10). In summary, although the position of the Bolivian High influences air source pathways for parts of the central Andes, particularly for the southern plateau and portions of the eastern flank, it is not significantly correlated with either local precipitation amount or $\delta^{18}O_p$.

2.5.3.2 Remote Precipitation Processes

Interannual variability in precipitation amount along prominent air trajectories may result in differences in central Andean $\delta^{18}O_p$ through changes in the degree of upstream parcel rainout and vapor recycling and mixing resulting from upstream convection. Vapor sourced from regions with below average precipitation are likely to have above average (i.e., less negative) isotopic compositions, whereas vapor sourced from regions with above average precipitation are likely to have below average (i.e., more negative) isotopic compositions. To assess this possibility, we calculated areal average DJF precipitation anomalies for the Greater Amazon Basin (GAB, 7.5°N-10°S, 50-75°W) and Chaco-Pampean plain (CPP, 20-35°S, 55-65°W) (Figure 2.11a). These upstream regions feed vapor to the YAB and GC, respectively, and connect them to their oceanic vapor source (Figures 2.2a and 2.11a). We calculated DJF anomalies from the 1998-2013 mean for each rainy season for the GAB and CPP using the TRMM 3B43 dataset [*Huffman et al.*, 2007]. SP parcels originate under a region of strong atmospheric subsidence and rarely lead to precipitation upstream of the Altiplano [*Garreaud et al.*, 2010; *Insel et al.*, 2010]; thus, we did not calculate precipitation anomalies here.

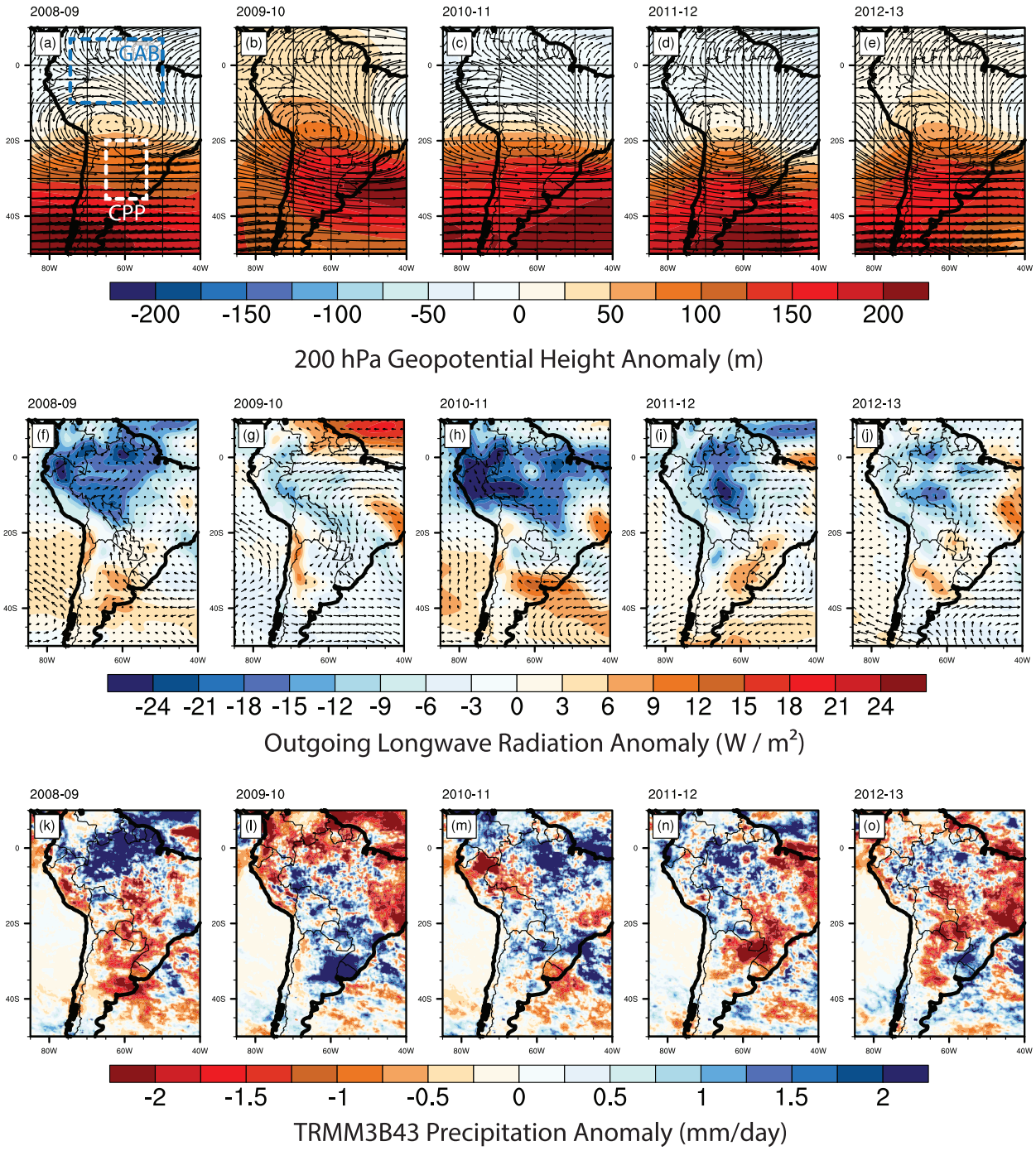

Figure 2.11. DJF climatic conditions relevant to central Andes $\delta^{18}O_p$ during the study period. Mean DJF 200 hPa winds (vectors, m/s) and anomalous 200 hPa geopotential height (contours, m) (a-e), anomalous DJF 850 hPa winds (vectors, m/s) and anomalous OLR (contours, W/m^2) (f-j), and anomalous DJF precipitation (k-o) for each rainy season from 2008 to 2013. Anomalies in the top two rows (a-j) were calculated as departure from the DJF 1979-2013 average using ERA Interim reanalysis data and as departure from the 1998-2013 DJF average using the TRMM3B43 dataset in the bottom row (k-o). The Greater Amazon Basin (GAB) and Chaco-Pampean Plain (CPP) are outlined in (a).

GAB and CPP precipitation amounts vary strongly from year to year. GAB precipitation was 23.0, 9.3, 9.4, and 2.3% above average during the 2008-09, 2010-11, 2011-12 and 2012-13 rainy seasons, respectively (Figure 2.11k,m,n,o), and 7.8% below average during DJF 2009-10 (Figure 2.11l). Positive (negative) GAB precipitation anomalies occur with more (less) negative annual average $\delta^{18}O_p$ for both the northern and southern Altiplano (Figure 2.12a). Stations along the eastern flank, however, show no clear relationship between annual average $\delta^{18}O_p$ and GAB precipitation anomalies. CPP precipitation was 42.8 and 8.5% above average during the 2009-10 and 2010-11 rainy seasons (Figure 2.11l,m) and 22.0, 16.7, and 9.5% below average precipitation during the 2008-09, 2011-12, and 2012-13 (Figure 2.11k,n,o) rainy seasons. Positive (negative) precipitation anomalies in the CPP region occur with more (less) negative annual average $\delta^{18}O_p$ for low elevation eastern flank sites (< 2500 m, Tarija, Entre Rios, and Villamontes). We observe no relationships between precipitation anomalies and annual average $\delta^{18}O_p$ at the high elevation eastern flank sites or on the plateau (Figure 2.12b). Both the GAB and CPP regions received above average precipitation during the year with the most negative $\delta^{18}O_p$ values across the northern Altiplano and eastern flank (2010-2011). No other year during our study exhibited above average precipitation for both regions. Further, the strong southerly excursion of the Bolivian High occurs with increased advection from GC and CPP regions relative to other years studied (Figure 2.11c, h; Appendix 2D). In contrast, the year with the least negative $\delta^{18}O_p$ values across the northern Altiplano and eastern flank (2009-10) is the only year with below average precipitation in the GAB (Figure 2.11l). We observe that the interannual variability is largely consistent with precipitation anomalies in major air source regions, supporting the idea that remote and upstream precipitation amount anomalies are preserved in and provide a primary control on central Andes $\delta^{18}O_p$ values and patterns. Studies investigating precipitation along the eastern Andes flank [*Vimeux et al.*, 2005; 2011], the isotopic composition of ice cores [*Grootes et al.*, 1989; *Thompson et al.*, 2013], and calcite in lake sediment cores [*Bird et al.*, 2011], have also concluded that the isotopic composition of high central Andes precipitation depends on processes in the Amazon basin.

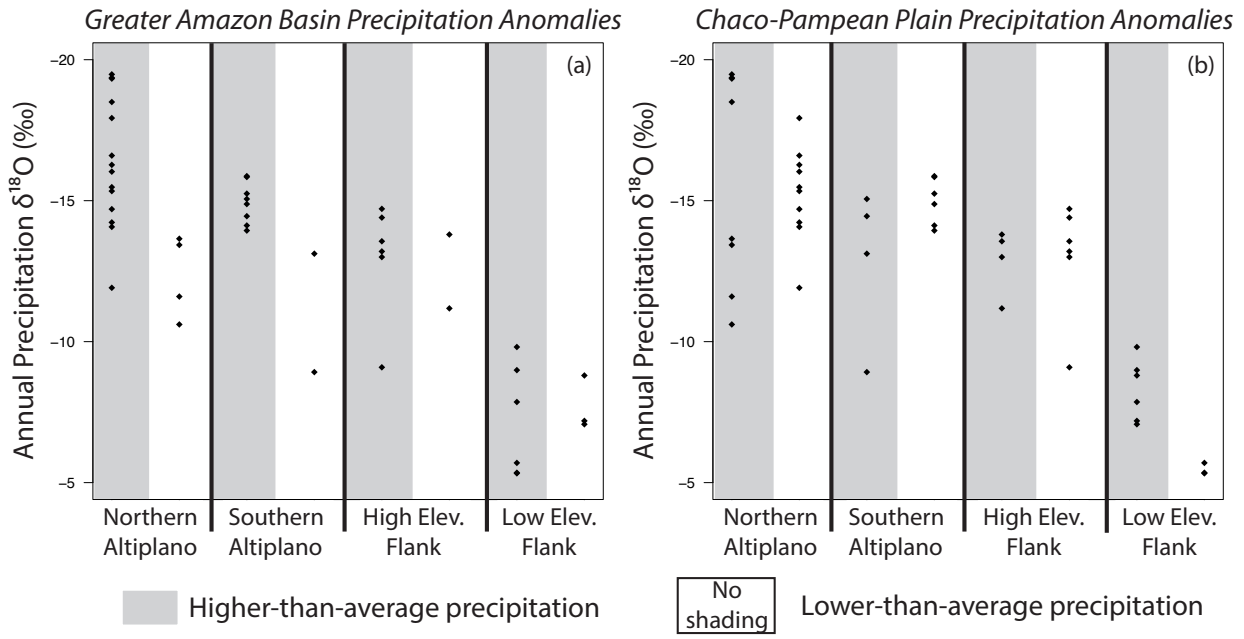

Figure 2.12. Variability in $\delta^{18}O_p$ for the northern Altiplano (ORU, ECH, QUI, SAL), southern Altiplano (SJU, NMA), high elevation eastern flank (GCH, TUP) and low elevation eastern flank (TAR, ERI, VMO) associated with anomalies in the Greater Amazon Basin (GAB) (a) and Chaco-Pampean Plain (CPP) (b) precipitation. Periods with above average precipitation are shaded green. Positive GAB precipitation anomalies correspond with more negative Altiplano $\delta^{18}O_p$ values. Positive CPP precipitation anomalies correspond with more negative $\delta^{18}O$ values at the low elevation stations along the plateau flank.

2.6 Discussion

2.6.1 Controls on central Andes $\delta^{18}O_p$

Elevation is the strongest regional control on $\delta^{18}O_p$ at multiyear timescales (Figures 2.7 and 2.8). Adiabatic ascent of air masses up the eastern Andean flank promotes condensation from air parcels and subsequent and progressive removal of heavy isotopes via Rayleigh distillation, resulting in an inverse relationship between surface elevation and $\delta^{18}O_p$ [*Dansgaard*, 1964; *Siegenthaler and Oeschger*, 1980; *Rowley and Garzione*, 2007]. In addition, convective precipitation both within and upstream of the central Andes can drive measured $\delta^{18}O_p$ to lighter compositions than anticipated by Rayleigh distillation, and further introduce interannual variability into $\delta^{18}O_p$ with a given increase in elevation [*Lee and Fung*, 2007; *Brown et al.*, 2008; *Risi et al.*, 2008; *Moore et al.*, 2014].

Central Andes $\delta^{18}O_p$ is highly variable in space and time (Figures 2.5a, 2.6a, and 2.8a). Our $\delta^{18}O_p$ time series indicate that month-to-month changes from station-to-station track each other in the northern Altiplano and along the eastern Andean flank (Table 2.8). Southern

Altiplano $\delta^{18}O_p$ correlates poorly with eastern flank and northern Altiplano $\delta^{18}O_p$, indicating a difference in $\delta^{18}O_p$ controls. We interpret the high interannual variability observed to be principally related to precipitation anomalies upwind of the central Andes based on their close association with $\delta^{18}O_p$ anomalies (Figure 2.12). Increased precipitation upstream of the central Andes likely led to vapor that was more depleted in heavy isotopes through two distinct effects. First, processes related to atmospheric convection in source regions, including partial evaporation of raindrops, vapor recycling, and increased entrainment and subsequent downward mixing of isotopically lighter mid and upper troposphere vapor [*Lee and Fung*, 2007; *Risi et al.*, 2008; *Moore et al.*, 2014], all contribute to depleting low-level vapor in heavy stable isotopes. Second, increased upwind precipitation also enhances the fraction of water vapor removed from a parcel through its transport from the Atlantic to the central Andes, which would result in lighter isotopic compositions through Rayleigh distillation. We use back-trajectory analysis to demonstrate that large-scale circulation in South America, namely the position of the Bolivian High, can alter the relative importance of vapor source regions (Figures 2.9 and 2.10; Tables 2.9 and 2.10, Appendix 2C). As a result, the Bolivian High modulates the influence of upstream precipitation anomalies from different regions of the continent. For example, when the Bolivian High occurs toward the northern end of its range, vapor advection decreases from the GC and CPP regions. In this way, the large-scale circulation can shield central Andean $\delta^{18}O_p$ from the influence of the strong precipitation anomalies observed in the CPP region (Figure 2.11g). Our $\delta^{18}O_p$ data analysis affirms prior work that notes strong associations between remote source region precipitation anomalies and eastern flank $\delta^{18}O_p$ [e.g., *Vimeux et al.*, 2005; 2011; *Samuels-Crow et al.*, 2014a], and extends them into the plateau itself. These results are also consistent with interpretations of lake sediment and ice cores relating $\delta^{18}O$ compositions to remote precipitation intensity in the Amazon Basin [e.g., *Grootes et al.*, 1989; *Hoffmann*, 2003; *Vimeux et al.*, 2009; *Bird et al.*, 2010; 2011; *Vuille et al.*, 2012].

We cannot rule out a potentially important role for local scale controls, particularly at high temporal frequencies and small spatial scales. For example, $\delta^{18}O_p$ at two different stations at similar elevations on the Altiplano for the same month were observed to vary by up to 13‰ (Figure 2.5a). The magnitude of this variability is unlikely to be explained by regional scale circulation controls and their influence on moisture sourcing. Therefore, we suggest that local variability in convective precipitation or valley-ridge scale forcing of moisture convergence and

convection may also play a role in the observed variability in central Andean $\delta^{18}O_p$ values [*Giovannettone and Barros*, 2009].

Our results support the influence of the Bolivian High position in partitioning air sources for portions of the central Andes inferred from climate modeling studies [*Vuille et al.*, 1998; *Vuille and Werner*, 2005; *Insel et al.*, 2013]. For example, we observed a uniform dependence across the plateau for YAB sourced air during precipitation events (Figure 2.9, Table 2.9). More broadly, however, we find no relationship between the Bolivian High latitude, local precipitation amount, and $\delta^{18}O_p$ (Table 2.10). This result calls into question links drawn from climate model results between the Bolivian High, moisture sources, precipitation amount, and central Andes $\delta^{18}O_p$ [e.g., *Vuille et al.*, 2003a; *Insel et al.*, 2013]. Our $\delta^{18}O_p$ results indicate that upstream precipitation anomalies influence $\delta^{18}O_p$ values more than the position of the Bolivian High. Additionally, multiyear amount weighted annual mean $\delta^{18}O_p$ values derived from the REMOiso regional isotope-tracking general circulation model are heavier than observations by a few per mil at high elevations (Figure 2.8b) [*Insel et al., 2013*]. We attribute these differences to the regional climate model grid, which may still be too coarse (~55 km) to resolve important topographic features and truncates the highest peaks. Despite this, the model captures the spatial patterns well. Regardless, our dataset, climate model simulations, and lake sediment calcite and glacial ice $\delta^{18}O$ values highlight the importance of remote processes to central Andes $\delta^{18}O_p$. We suspect that some climate model parameterizations may be responsible for the mechanistic differences inferred. In particular, limitations in precipitation parameterization schemes used in regional climate model studies might overstate (understate) the role of local (remote) precipitation processes. Many models simulate coupling between the land surface and atmosphere that is too strong, as shown by Amazon precipitation and evapotranspiration fluxes that exceed observations by ~20% [*Insel et al.*, 2013]. Additionally, simulated precipitation amounts at the Andean flank are too large and are a result of overestimated moisture convergence in regions with steep topography [*Codron and Sadourny*, 2002; *Bala et al.*, 2008; *Insel et al.*, 2013]. Finally, assumptions made in model parameterizations of convection also influence the simulated $\delta^{18}O_p$ patterns [e.g., *Lee et al.*, 2009b]. Bias between observed and simulated $\delta^{18}O_p$ patterns and values is uncertain and likely model dependent because different models often employ different convection schemes. Despite these uncertainties, climate model simulations remain valuable tools to understand the dynamic processes influencing $\delta^{18}O_p$.

2.6.2 ENSO and central Andes $\delta^{18}O_p$

ENSO introduces significant interannual variability into South American climate patterns [*Garreaud et al.*, 2009]. This variability likely influences central Andes $\delta^{18}O_p$ values. ENSO variability significantly impacts precipitation amount and large-scale circulation on the Altiplano as well as in the main source regions such as the Amazon Basin and southeastern South America [*Garreaud and Battisti*, 1999; *Vuille et al.*, 2000; *Garreaud et al.*, 2009]. In general, ENSO is associated with strong precipitation anomalies in different regions and results in more (less) negative $\delta^{18}O_p$ values when source regions experience enhanced (suppressed) rainout [*Garreaud et al.*, 2009; *Insel et al.*, 2013]. ENSO variability has also been observed in central Andes ice cores [*Henderson et al.*, 1999; *Bradley et al.*, 2003; *Vimeux et al.*, 2009].

Several ENSO events occurred during the study period: a relatively strong El Niño occurred during winter 2009-2010, while a relatively strong La Niña occurred during 2010-2011 and weak La Niña conditions were observed during 2008-2009 and 2011-2012 [after *Smith et al.*, 2008; *National Center of Environmental Prediction*, 2014]. On the Altiplano, El Niño (La Niña) conditions are frequently associated with decreased (increased) moisture advection from the east by strengthened (weakened) westerly mid- and upper-level winds [*Vuille*, 1999; *Vuille et al.*, 2000; *Garreaud and Aceituno*, 2001]. This trend is consistent with observed shifts in the position of the Bolivian High during the study period during the strongest ENSO events. During the 2010/2011 La Niña, the Bolivian High was at its southernmost position during the study (Figure 2.11c), promoting abnormally strong easterly winds over the Altiplano and facilitating moisture convergence from both the GAB and CPP regions and driving $\delta^{18}O_p$ to more negative values. In contrast, during the 2009/10 El Niño, the Bolivian High was positioned further northward and abnormally strong (Figure 2.11b), enhancing upper level westerly winds and inhibiting moisture convergence, suppressing parcel rainout, and causing less negative $\delta^{18}O_p$ values.

ENSO influences the GAB in the same manner as it influences the Altiplano. El Niño (La Niña) events are associated with decreased (increased) DJF precipitation in the GAB. This pattern occurs with increased (decreased) continental subsidence coincident with increased (decreased) convection off the western coast of South America [*Marengo*, 1992; *Liebmann and Marengo*, 2001]. Together, this pattern facilitates decreased (increased) parcel rainout and less (more) negative $\delta^{18}O_p$ values. This pattern is observed during this study, with positive precipitation anomalies observed in all La Niña years and strong negative precipitation

anomalies observed during the lone El Niño year. ENSO also similarly affects precipitation amounts along the eastern margin, potentially through changes in the SALLJ [*Ronchail et al.*, 2005; *Ronchail and Gallaire*, 2006]. In contrast, ENSO manifests in the opposite pattern in the CPP compared to the Altiplano or GAB, as a result of changes in the mid-latitude jet [*Barros and Silvestri*, 2002; *Silvestri*, 2004]. This pattern is generally observed in our study except during the 2010-2011 rainy season, when precipitation in the CPP is above average despite a strong La Niña, further facilitating more negative central Andean $\delta^{18}O_p$. Our results indicate that the relationship between central Andes $\delta^{18}O_p$ and ENSO is complex, as previously suggested in interpretations of regional ice cores [e.g., *Henderson et al.*, 1999; *Vimeux et al.*, 2009].

2.6.3 Implications for Paleoclimate and Paleoaltimetry

The isotopic composition of precipitation is preserved in proxy materials that trap or form from precipitation (e.g., ice cores and hydrated volcanic glass), or form in equilibrium with precipitation (e.g., pedogenic carbonates and authigenic clays). In the central Andes and South America as a whole, these proxies have been used to constrain and understand changes in paleohydrology [e.g., *Baker et al.*, 2001; *Wang et al.*, 2004; *Ekdahl et al.*, 2008], paleoclimate [e.g., *Thompson et al.*, 1998; *Vimeux et al.*, 2009; *Mulch et al.*, 2010], and paleoelevation [e.g., *Garzione et al.*, 2008; *Leier et al.*, 2013; *Saylor and Horton*, 2014]. A challenge for interpreting these proxy records is that the modern distribution and spatial variability of modern water isotopologues have historically been poorly known, particularly across the Altiplano. Moreover, the data demonstrate a high degree of interannual and spatial variability in the region, an understanding of which is required for informed interpretations of the paleoclimate and paleoaltimetric proxy record [e.g., *Vuille et al.*, 2003a; *Lee et al.*, 2009a; *Lewis et al.*, 2010; *Insel et al.*, 2012]. High variability is also observed in modern Nevado Sajama snow $\delta^{18}O$ [*Hardy et al.*, 2003], indicating that this variability can also be reflected in materials such as ice that preserve a $\delta^{18}O$ sequence. This high interannual variability collectively indicates that modern observational records with short time spans may be biased toward climatic extremes. For example, data from the Yungas-Altiplano transect in *Gonfiantini et al.* [2001] spans the 1983 El Niño and the 1984 La Niña. Thus, none of the modern precipitation data prior to this study actually constrain $\delta^{18}O_p$ patterns during a neutral ENSO phase. Therefore, modern isotopologue distributions can be biased and hence be poor representations of the past. This reality may impact

how robust interpretations of proxy compositions are when they are compared to possibly poorly representative modern values.

The impact of this modern observational bias will vary depending on the length of time represented by the proxy. The frequency of climate variability resolved by proxies varies by proxy type and age, and ranges from subannual to several millennia. Ice and lake sediment cores record subannual to decadal variability [*Thompson et al.*, 1984; *Bird et al.*, 2010; 2011; *Thompson et al.*, 2013], while pedogenic carbonates and hydrated volcanic glass acquire their isotopic composition over thousands of years [*Cerling and Quade*, 1993; *Friedman et al.*, 1993; *Mulch and Chamberlain*, 2007; *Quade et al.*, 2007]. As a result of the wide range of timescales encapsulated by proxy materials, we suggest that our results have greater implications for proxies with longer integration periods for two primary reasons. First, as ice cores and lake cores resolve subannual to decadal variability, the large range of (near) modern isotopic compositions is well known [*Hardy et al.*, 2003], as is its relationship to tropical climate variability [e.g., *Bradley et al.*, 2003; *Bird et al.*, 2010]. Second, for proxies that form over longer periods (century to millennia), it remains less clear whether the compositions preserved in pedogenic carbonates or hydrated volcanic glass represent long-term mean annual conditions, seasonal conditions, or even extreme conditions [e.g., *Cerling and Quade*, 1993; *Breecker et al.*, 2009; *Peters et al.*, 2013]. Our extended (~5 years) isotopic record presented here can be used to better evaluate the fidelity with which various proxies represent the environments under which they form.

Finally, controls on central Andean $\delta^{18}O_p$ vary spatially, and therefore, proxies from different regions may not record equivalent processes nor be directly comparable due to the strong north-south gradients we observed. It is also likely these gradients were not constant throughout the Cenozoic due to the strong alteration of South American climate induced by the rise of the Andes [e.g., *Ehlers and Poulsen*, 2009; *Insel et al.*, 2010; *Mulch et al.*, 2010; *Poulsen et al.*, 2010; *Barnes et al.*, 2012]. Furthermore, Andean uplift may have contributed to the evolution of modern ENSO dynamics [*Feng and Poulsen*, 2014]. Thus, the strong influence of atmospheric circulation on central Andes $\delta^{18}O_p$ compels future paleometeoric water isotopologue studies to carefully consider that coevolving changes in atmospheric circulation, climate, and topography combine to influence these proxy records in ways that remain difficult to simplify and disentangle. Despite uncertainties and limitations, further (paleo)climate model simulations

and field-based observations offer a multi-pronged approach for disentangling these coupled processes and addressing proxy interpretation ambiguities.

2.7 Conclusions

We address key gaps and uncertainties in our observations and understanding of $\delta^{18}O_p$ patterns in modern central Andes rainfall. Elevation provides the dominant control across multiyear timescales. However, the $\delta^{18}O_p$-elevation relationship varies in space and time and does not adequately predict $\delta^{18}O_p$ across the Bolivian Altiplano. We also show that observed interannual variability in $\delta^{18}O_p$ is directly related to South American synoptic circulation. First, we confirm anomalous precipitation amounts in upwind air source regions control both Altiplano and eastern flank $\delta^{18}O_p$. The most likely explanation is changes in the fraction of water vapor removed from an air parcel upwind, which influences Altiplano $\delta^{18}O_p$ via convective processes and Rayleigh fractionation associated with parcel rainout [*Vimeux et al.*, 2005; *Vuille and Werner*, 2005; *Samuels-Crow et al.*, 2014a]. Second, we show that the Bolivian High modulates the influence of the Amazon and Gran Chaco air source regions, and thus, their potential effect on central Andes $\delta^{18}O_p$. These controls are consistent with prior studies along other parts of the Eastern Cordillera in the Andes [*Vimeux et al.*, 2005; 2011], but we extend them to the central plateau. Further, our results support insights from isotope-tracking climate models that central Andes $\delta^{18}O_p$ patterns respond to continental-scale climate variability [e.g., *Vuille et al.*, 2003a; *Vuille and Werner*, 2005; *Insel et al.*, 2013]. However, our results suggest that models overestimate the direct role of large-scale circulation and underestimate the role of anomalous upwind precipitation, which we attribute to shortcomings in the model parameterization of precipitation. On short timescales (1 month to < 1 year), we find variability on small spatial scales (~50 km) that cannot be explained by elevation nor aligns with regional-scale circulation patterns. We speculate that local variability in precipitation amount and convection intensity further depletes heavy isotopes in precipitation leading to more negative $\delta^{18}O_p$ values than would be otherwise expected. Finally, we find high interannual variability (approaching 50% of the mean) in the average isotopic lapse rate often used in paleoelevation reconstructions [e.g., *Rowley and Garzione*, 2007], which is consistent with isotope-tracking climate model results [*Insel et al.*, 2013]. Prior and limited observations of modern central Andes $\delta^{18}O_p$ coincided with ENSO extremes, and thus, have likely been biased by such climatic extremes and hence may not

be representative over geologic timescales. Our longer dataset better constrains the role of climate variability on central Andes $\delta^{18}O_p$ and elucidates a close link with South American circulation. Therefore, we recommend that future paleoclimate and paleoaltimetric studies based on $\delta^{18}O_p$ require both an (a) understanding of paleocirculation dynamics, and (b) improved acknowledgement, perhaps by incorporating more conservative uncertainty estimates, for the natural variability in $\delta^{18}O_p$-elevation relationships across space and time.

2.8 References

Aceituno, P. (1988), On the functioning of the Southern Oscillation in the South American sector. Part I: Surface climate, *Monthly Weather Review*, *116*(3), 505–524.

Aggarwal, P. K., O. A. Alduchov, K. O. Froehlich, L. J. Araguas-Araguas, N. C. Sturchio, and N. Kurita (2012), Stable isotopes in global precipitation: A unified interpretation based on atmospheric moisture residence time, *Geophys Res Lett*, *39*(11), doi:10.1029/2012GL051937.

Aravena, R., O. Suzuki, H. Pena, A. Pollastri, H. Fuenzalida, and A. Grilli (1999), Isotopic composition and origin of the precipitation in Northern Chile, *Applied Geochemistry*, *14*, 411–422, doi:10.1016/S0883-2927(98)00067-5.

Baker, P., C. Rigsby, G. Seltzer, S. Fritz, T. Lowenstein, N. Bacher, and C. Veliz (2001), Tropical climate changes at millennial and orbital timescales on the Bolivian Altiplano, *Nature*, *409*(6821), 698–701.

Bala, G., R. B. Rood, D. Bader, A. Mirin, D. Ivanova, and C. Drui (2008), Simulated climate near steep topography: Sensitivity to methods for atmospheric transport, *Geophys Res Lett*, *35*, L14807, doi:10.1029/2008GL033204.

Barnes, J. B., and T. A. Ehlers (2009), End member models for Andean Plateau uplift, *Earth-Science Reviews*, *97*(1-4), 105–132, doi:10.1016/j.earscirev.2009.08.003.

Barnes, J. B., T. A. Ehlers, N. Insel, N. McQuarrie, and C. J. Poulsen (2012), Linking orography, climate, and exhumation across the central Andes, *Geol*, *40*(12), 1135–1138, doi:10.1130/G33229.1.

Barros, V. R., and G. E. Silvestri (2002), The relation between sea surface temperature at the subtropical south-central Pacific and precipitation in southeastern South America, *Journal of Climate*, *15*(3), 251–267.

Bershaw, J., C. N. Garzione, P. Higgins, B. J. MacFadden, F. Anaya, and H. Alvarenga (2010), Spatial–temporal changes in Andean plateau climate and elevation from stable isotopes of mammal teeth, *Earth Planet Sc Lett*, *289*(3-4), 530–538, doi:10.1016/j.epsl.2009.11.047.

Bershaw, J., S. M. Penny, and C. N. Garzione (2012), Stable isotopes of modern water across the Himalaya and eastern Tibetan Plateau: Implications for estimates of paleoelevation and paleoclimate, *J Geophys Res*, *117*(D2), D02110, doi:10.1029/2011JD016132.

Bird, B. W. et al. (2011), A 2,300-year-long annually resolved record of the South American summer monsoon from the Peruvian Andes, *Proceedings of the National Academy of Sciences*, *108*(21), 8583–8588, doi:10.1073/pnas.1003719108.

Bird, B. W., M. B. Abbott, D. T. Rodbell, and M. Vuille (2010), Holocene tropical South American hydroclimate revealed from a decadally resolved lake sediment $\delta^{18}O$ record, *Earth Planet Sc Lett*, *310*(3-4), 192–202, doi:10.1016/j.epsl.2011.08.040.f

Blisniuk, P. M., and L. Stern (2005), Stable isotope paleoaltimetry: A critical review, *Am J Sci*, *305*(10), 1033–1074, doi:10.2475/ajs.305.10.1033.

Blossey, P. N., Z. Kuang, and D. M. Romps (2010), Isotopic composition of water in the tropical tropopause layer in cloud-resolving simulations of an idealized tropical circulation, *J Geophys Res*, *115*(D24), D24309, doi:10.1029/2010JD014554.

Bony, S., C. Risi, and F. Vimeux (2008), Influence of convective processes on the isotopic composition ($\delta^{18}O$ and δD) of precipitation and water vapor in the tropics: 1. Radiative-convective equilibrium and Tropical Ocean–Global Atmosphere–Coupled Ocean-Atmosphere Response Experiment (TOGA-COARE) simulations, *J Geophys Res*, *113*,

doi:10.1029/2008JD009942.
Bowen, G. J., and B. H. Wilkinson (2002), Spatial distribution of $\delta^{18}O$ in meteoric precipitation, *Geol*, *30*(4), 315–318.
Bowen, G. J., and J. Revenaugh (2003), Interpolating the isotopic composition of modern meteoric precipitation, *Water Resour Res*, *39*(10), 1299, doi:10.1029/2003WR002086.
Bradley, R. S., M. Vuille, and D. R. Hardy (2003), Low latitude ice cores record Pacific sea surface temperatures, *Geophys Res Lett*, *30*(4), 1174–4, doi:10.1029/2002GL016546.
Breecker, D. O., Z. D. Sharp, and L. D. McFadden (2009), Seasonal bias in the formation and stable isotopic composition of pedogenic carbonate in modern soils from central New Mexico, USA, *Geological Society of America Bulletin*, *121*(3-4), 630–640, doi:10.1130/B26413.1.
Brown, D. P., J. Worden, and D. C. Noone (2008), Comparison of atmospheric hydrology over convective continental regions using water vapor isotope measurements from space, *J Geophys Res*, *113*(D15), doi:10.1029/2007JD009676.
Burnham, K. P., and D. R. Anderson (2002), *Model Selection and Multimodel Inference: A Practical Information-Theoretic Approach*, 2nd ed., Springer.
Campetella, C. M., and C. S. Vera (2002), The influence of the Andes mountains on the South American low-level flow, *Geophys Res Lett*, *29*(17), 1826, doi:10.1029/2002GL015451.
Cerling, T. E., and J. Quade (1993), Stable carbon and oxygen isotopes in soil carbonates, in *Climate Change in Continental Isotopic Records*, vol. 78, edited by P. K. Swart, K. C. Lohmann, J. Mckenzie, and S. M. Savin, pp. 217–231, American Geophysical Union.
Codron, F., and R. Sadourny (2002), Saturation limiters for water vapour advection schemes: impact on orographic precipitation, *Tellus A*, *54*(4), 338–349.
Craig, H. (1961), Isotopic variations in meteoric waters, *Science*, *133*(3465), 1702.
Craig, H., and L. I. Gordon (1965), Deuterium and oxygen-18 variations in the ocean and the marine atmosphere, edited by E. Tongiorgi, pp. 9–130, Stable Isotopes in Oceanographic Studies and Paleotemperatures.
Dansgaard, W. (1964), Stable isotopes in precipitation, *Tellus*, *16*(4), 436–468.
Dee, D. P. et al. (2011), The ERA-Interim reanalysis: configuration and performance of the data assimilation system, *Quarterly Journal of the Royal Meteorological Society*, *137*(656), 553–597, doi:10.1002/qj.828.
Dessler, A. E., and S. C. Sherwood (2003), A model of HDO in the tropical tropopause layer, *Atmos. Chem. Phys.*, *3*(6), 2173–2181.
Draxler, R. R., and G. D. Hess (1998), An overview of the HYSPLIT_4 modelling system for trajectories, dispersion and deposition, *Australian Meteorological Magazine*, *47*(4), 295–308.
Ehlers, T. A., and C. J. Poulsen (2009), Influence of Andean uplift on climate and paleoaltimetry estimates, *Earth Planet Sc Lett*, *281*(3-4), 238–248, doi:10.1016/j.epsl.2009.02.026.
Ekdahl, E., S. Fritz, P. Baker, C. Rigsby, and K. Coley (2008), Holocene multidecadal-to millennial-scale hydrologic variability on the South American Altiplano, *The Holocene*, *18*(6), 867.
Feng, R., and C. J. Poulsen (2014), Andean elevation control on tropical Pacific climate and ENSO, *Paleoceanography*, *29*(8), 795–809, doi:10.1002/2014PA002640.
Friedman, I., G. I. Smith, J. D. Gleason, A. Warden, and J. M. Harris (1992), Stable isotope composition of waters in southeastern California 1. Modern precipitation, *J Geophys Res*, *97*(D5), 5795–5812.

Friedman, I., J. Gleason, and A. Warden (1993), Ancient climate from deuterium content of water in volcanic glass, in *Climate Change in Continental Isotopic Records*, vol. 78, edited by P. K. Swart, P. K. Swart, K. C. Lohmann, J. Mckenzie, and S. M. Savin, pp. 309–319.
Garreaud, R. D., A. Molina, and M. Farias (2010), Andean uplift, ocean cooling and Atacama hyperaridity: A climate modeling perspective, *Earth Planet Sc Lett*, *292*(1-2), 39–50, doi:10.1016/j.epsl.2010.01.017.
Garreaud, R. D., and D. S. Battisti (1999), Interannual (ENSO) and Interdecadal (ENSO-like) Variability in the Southern Hemisphere Tropospheric Circulation*, *Journal of Climate*, *12*(7), 2113–2123.
Garreaud, R. D., and P. Aceituno (2001), Interannual rainfall variability over the South American Altiplano, *Journal of Climate*, *14*(12), 2779–2789.
Garreaud, R. D., M. Vuille, and A. Clement (2003), The climate of the Altiplano: observed current conditions and mechanisms of past changes, *Palaeogeography, Palaeoclimatology, Palaeoecology*, *194*(1-3), 5–22.
Garreaud, R. D., M. Vuille, R. Compagnucci, and J. A. Marengo (2009), Present-day South American climate, *Palaeogeography, Palaeoclimatology, Palaeoecology*, *281*(3-4), 180–195, doi:10.1016/j.palaeo.2007.10.032.
Garzione, C. N., G. D. Hoke, J. C. Libarkin, S. Withers, B. J. MacFadden, J. M. Eiler, P. Ghosh, and A. Mulch (2008), Rise of the Andes, *Science*, *320*(5881), 1304–1307, doi:10.1126/science.1148615.
Gat, J. R. (1996), Oxygen and hydrogen isotopes in the hydrologic cycle, *Annu. Rev. Earth Planet. Sci.*, *24*(1), 225–262, doi:10.1146/annurev.earth.24.1.225.
Giovannettone, J. P., and A. P. Barros (2009), Probing Regional Orographic Controls of Precipitation and Cloudiness in the Central Andes Using Satellite Data, *J. Hydrometeor*, *10*(1), 167–182, doi:10.1175/2008JHM973.1.
Giovanni, M. K., B. K. Horton, C. N. Garzione, B. McNulty, and M. Grove (2010), Extensional basin evolution in the Cordillera Blanca, Peru: Stratigraphic and isotopic records of detachment faulting and orogenic collapse in the Andean hinterland, *Tectonics*, *29*(6), doi:10.1029/2010TC002666.
Gonfiantini, R., M. A. Roche, J. C. Olivry, J. C. Fontes, and G. M. Zuppi (2001), The altitude effect on the isotopic composition of tropical rains, *Chemical Geology*, *181*(1), 147–167.
Grell, G. A. (1993), Prognostic Evaluation of Assumptions Used by Cumulus Parameterizations, *Monthly Weather Review*, *121*(3), 764–787.
Grootes, P. M., M. Stuiver, L. G. Thompson, and E. Mosley-Thompson (1989), Oxygen isotope changes in tropical ice, Quelccaya, Peru, *J Geophys Res*, *94*(D1), 1187–1194.
Hardy, D. R., M. Vuille, and R. S. Bradley (2003), Variability of snow accumulation and isotopic composition on Nevado Sajama, Bolivia, *J Geophys Res*, *108*(D22), 4693–4702, doi:10.1029/2003JD003623.
Henderson, K. A., L. G. Thompson, and P.-N. Lin (1999), Recording of El Niño in ice core $\delta^{18}O$ records from Nevado Huascarán, Peru, *J Geophys Res*, *104*(D24), 31053–31065, doi:10.1029/1999JD900966.
Hoffmann, G. (2003), Coherent isotope history of Andean ice cores over the last century, *Geophys Res Lett*, *30*(4), 1–4, doi:10.1029/2002GL014870.
Hoke, G. D., C. N. Garzione, D. Araneo, C. Latorre, M. R. Strecker, and K. Williams (2009), The stable isotope altimeter: Do Quaternary pedogenic carbonates predict modern elevations? *Geol*, *37*(11), 1015–1018.

Horita, J., and D. J. Wesolowski (1994), Liquid-vapor fractionation of oxygen and hydrogen isotopes of water from the freezing to the critical temperature, *Geochimica et Cosmochimica Acta*, *58*(16), 3425–3437.

Huffman, G. J. (1997), Estimates of root-mean-square random error for finite samples of estimated precipitation, *Journal of Applied Meteorology*, *36*(9), 1191–1201.

Huffman, G. J., D. T. Bolvin, E. J. Nelkin, D. B. Wolff, R. F. Adler, G. Gu, Y. Hong, K. P. Bowman, and E. F. Stocker (2007), The TRMM Multisatellite Precipitation Analysis (TMPA): Quasi-Global, Multiyear, Combined-Sensor Precipitation Estimates at Fine Scales, *J. Hydrometeor*, *8*(1), 38–55, doi:10.1175/JHM560.1.

Iguchi, T., T. Kozu, J. Kwiatkowski, R. Meneghini, J. Awaka, and K. Okamoto (2009), Uncertainties in the Rain Profiling Algorithm for the TRMM Precipitation Radar, *Journal of the Meteorological Society of Japan*, *87A*, 1–30, doi:10.2151/jmsj.87A.1.

Insel, N., C. J. Poulsen, and T. A. Ehlers (2010), Influence of the Andes Mountains on South American moisture transport, convection, and precipitation, *Climate Dynamics*, *35*(7-8), 1477–1492, doi:10.1007/s00382-009-0637-1.

Insel, N., C. J. Poulsen, C. Sturm, and T. A. Ehlers (2013), Climate controls on Andean precipitation $\delta^{18}O$ interannual variability, *J Geophys Res-Atmos*, *118*(17), 9721–9742, doi:10.1002/jgrd.50619.

Insel, N., C. J. Poulsen, T. A. Ehlers, and C. Sturm (2012), Response of meteoric $\delta^{18}O$ to surface uplift - Implications for Cenozoic Andean Plateau Growth, *Earth Planet Sc Lett*, *317-318*, 262–272, doi:10.1016/j.epsl.2011.11.039.

Jeffery, M. L., C. J. Poulsen, and T. A. Ehlers (2012), Impacts of Cenozoic global cooling, surface uplift, and an inland seaway on South American paleoclimate and precipitation $\delta^{18}O$, *Geological Society of America Bulletin*, *124*(3-4), 335–351, doi:10.1130/B30480.1.

Kousky, V. E. (1988), Pentad outgoing longwave radiation climatology for the South American sector, *Revista Brasileira de Meteorologia*, *3*(1), 217–231.

Kuang, Z., G. Toon, P. O. Wennberg, and Y. L. Yung (2003), Measured HDO/H_2O ratios across the tropical tropopause, *Geophys Res Lett*, *30*(7), 1372, doi:10.1029/2003GL017023.

Lechler, A. R., and J. Galewsky (2013), Refining paleoaltimetry reconstructions of the Sierra Nevada, California, using air parcel trajectories, *Geol*, *41*(2), 259–262, doi:10.1130/G33553.1.

Lechler, A. R., and N. A. Niemi (2012), Controls on the Spatial Variability of Modern Meteoric ^{18}O: Empirical Constraints from the Western U.S. and East Asia and Implications for Stable Isotope Studies, *Am J Sci*, *311*(8), 664–700, doi:10.2475/08.2011.02.

Lee, J.-E., and I. Fung (2007), "Amount effect" of water isotopes and quantitative analysis of post-condensation processes, *Hydrol. Process.*, *22*(1), 1–8, doi:10.1002/hyp.6637.

Lee, J.-E., K. Johnson, and I. Fung (2009a), Precipitation over South America during the Last Glacial Maximum: An analysis of the "amount effect" with a water isotope-enabled general circulation model, *Geophys Res Lett*, *36*(19), L19701, doi:10.1029/2009GL039265.

Lee, J.-E., R. T. Pierrehumbert, A. Swann, and B. R. Lintner (2009b), Sensitivity of stable water isotopic values to convective parameterization schemes, *Geophys Res Lett*, *36*(23), L23801, doi:10.1029/2009GL040880.

Legates, D. R., and C. J. Willmott (1990a), Mean seasonal and spatial variability in gauge-corrected, global precipitation, *International Journal of Climatology*, *10*(2), 111–127.

Legates, D. R., and C. J. Willmott (1990b), Mean seasonal and spatial variability in global surface air-temperature, *Theor. Appl. Climatol.*, *41*(1-2), 11–21.

Lehner, B., K. Verdin, and A. Jarvis (2008), New Global Hydrography Derived From Spaceborne Elevation Data, *Eos Trans. AGU*, *89*(10), 93, doi:10.1029/2008EO100001.
Leier, A., N. McQuarrie, C. Garzione, and J. Eiler (2013), Stable isotope evidence for multiple pulses of rapid surface uplift in the Central Andes, Bolivia, *Earth Planet Sc Lett*, *371-372*(C), 49–58, doi:10.1016/j.epsl.2013.04.025.
Lenters, J., and K. Cook (1999), Summertime precipitation variability over South America: Role of the large-scale circulation, *Monthly Weather Review*, *127*(3), 409–431.
Lewis, S. C., A. N. LeGrande, M. Kelley, and G. A. Schmidt (2010), Water vapour source impacts on oxygen isotope variability in tropical precipitation during Heinrich events, *Climate of the Past*, *6*(3), 325–343, doi:10.5194/cp-6-325-2010.
Liebmann, B., and J. Marengo (2001), Interannual variability of the rainy season and rainfall in the Brazilian Amazon Basin, *Journal of Climate*, *14*(22), 4308–4318.
Liu, Z., D. Ostrenga, W. Teng, and S. Kempler (2012), Tropical Rainfall Measuring Mission (TRMM) Precipitation Data and Services for Research and Applications, *Bulletin of the American Meteorological Society*, *93*(9), 1317–1325, doi:10.1175/BAMS-D-11-00152.1.
Liu, Z., G. J. Bowen, and J. M. Welker (2010), Atmospheric circulation is reflected in precipitation isotope gradients over the conterminous United States, *J Geophys Res*, *115*(D22), D22120, doi:10.1029/2010JD014175.
Majoube, M. (1971), Fractionnement en oxygene-18 et en deuterium entre l'eau et sa vapeur, *Journal de Chemie Physique et de Physico-Chimie Biologique*, *68*(10), 1423.
Marengo, J. A. (1992), Interannual variability of surface climate in the Amazon basin, *International Journal of Climatology*, *12*(8), 853–863.
Moore, M., Z. Kuang, and P. N. Blossey (2014), A moisture budget perspective of the amount effect, *Geophys Res Lett*, *41*(4), 1329–1335, doi:10.1002/2013GL058302.
Mulch, A., and C. P. Chamberlain (2007), Stable Isotope Paleoaltimetry in Orogenic Belts The Silicate Record in Surface and Crustal Geological Archives, in *Paleoaltimetry: geochemical and thermodynamic approaches*, vol. 66, edited by M. J. Kohn, pp. 89–118, Minerology Society of America.
Mulch, A., C. E. Uba, M. R. Strecker, R. Schoenberg, and C. P. Chamberlain (2010), Late Miocene climate variability and surface elevation in the central Andes, *Earth Planet Sc Lett*, *290*(1-2), 173–182, doi:10.1016/j.epsl.2009.12.019.
National Center of Environmental Prediction (2014), *NCEP Oceanic Niño Index*. Available from: http://www.cpc.ncep.noaa.gov/products/analysis_monitoring/ensostuff/ensoyears.shtml (Accessed 12 November 2014)
Noone, D. C. (2012), Pairing Measurements of the Water Vapor Isotope Ratio with Humidity to Deduce Atmospheric Moistening and Dehydration in the Tropical Midtroposphere, *Journal of Climate*, *25*(13), 4476–4494, doi:10.1175/JCLI-D-11-00582.1.
Peters, N. A., K. W. Huntington, and G. D. Hoke (2013), Hot or not? Impact of seasonally variable soil carbonate formation on paleotemperature and O-isotope records from clumped isotope thermometry, *Earth Planet Sc Lett*, *361*, 208–218, doi:10.1016/j.epsl.2012.10.024.
Poulsen, C. J., and M. L. Jeffery (2011), Climate change imprinting on stable isotopic compositions of high-elevation meteoric water cloaks past surface elevations of major orogens, *Geol*, doi:10.1130/G32052.1.
Poulsen, C. J., T. A. Ehlers, and N. Insel (2010), Onset of Convective Rainfall During Gradual Late Miocene Rise of the Central Andes, *Science*, *328*(5977), 490–493,

doi:10.1126/science.1185078.
Quade, J., C. N. Garzione, and J. M. Eiler (2007), Paleoelevation Reconstruction using Pedogenic Carbonates, *Reviews in Mineralogy and Geochemistry*, *66*(1), 53–87, doi:10.2138/rmg.2007.66.3.
Rasmussen, K. L., S. L. Choi, M. D. Zuluaga, and R. A. Houze Jr. (2013), TRMM precipitation bias in extreme storms in South America, *Geophys Res Lett*, *40*(13), 3457–3461, doi:10.1002/grl.50651.
Rindsberger, M., M. Magaritz, I. Carmi, and D. Gilad (1983), The Relation Between Air-Mass Trajectories and the Water Isotope Composition of Rain in the Mediterranean-Sea Area, *Geophys Res Lett*, *10*(1), 43–46, doi:10.1029/GL010i001p00043.
Risi, C., S. Bony, and F. Vimeux (2008), Influence of convective processes on the isotopic composition ($\delta^{18}O$ and δD) of precipitation and water vapor in the tropics: 2. Physical interpretation of the amount effect, *J Geophys Res*, *113*, doi:10.1029/2008JD009943.
Rodwell, M. J., and B. J. Hoskins (2001), Subtropical anticyclones and summer monsoons, *Journal of Climate*, *14*(15), 3192–3211.
Rohrmann, A., M. R. Strecker, B. Bookhagen, A. Mulch, D. Sachse, H. Pingel, R. N. Alonso, T. F. Schildgen, and C. Montero (2014), Can stable isotopes ride out the storms? The role of convection for water isotopes in models, records, and paleoaltimetry studies in the central Andes, *Earth Planet Sc Lett*, *407*, 187–195, doi:10.1016/j.epsl.2014.09.021.
Ronchail, J., and R. Gallaire (2006), ENSO and rainfall along the Zongo valley (Bolivia) from the Altiplano to the Amazon basin, *International Journal of Climatology*, *26*(9), 1223–1236, doi:10.1002/joc.1296.
Ronchail, J., L. Bourrel, G. Cochonneau, P. Vauchel, L. Phillips, A. Castro, J.-L. Guyot, and E. de Oliveira (2005), Inundations in the Mamoré basin (south-western Amazon—Bolivia) and sea-surface temperature in the Pacific and Atlantic Oceans, *Journal of Hydrology*, *302*(1-4), 223–238, doi:10.1016/j.jhydrol.2004.07.005.
Rowley, D. B., and C. N. Garzione (2007), Stable Isotope-Based Paleoaltimetry, *Annu. Rev. Earth Planet. Sci.*, *35*(1), 463–508, doi:10.1146/annurev.earth.35.031306.140155.
Rozanski, K., L. Araguas-Araguas, and R. Gonfiantini (1993), Isotopic patterns in modern global precipitation, in *Climate Change in Continental Isotopic Records*, edited by P. K. Swart, K. C. Lohmann, J. Mckenzie, and S. M. Savin, pp. 1–36, American Geophysical Union.
Samuels-Crow, K. E., J. Galewsky, D. R. Hardy, Z. D. Sharp, J. Worden, and C. Braun (2014a), Upwind convective influences on the isotopic composition of atmospheric water vapor over the tropical Andes, *J Geophys Res-Atmos*, doi:10.1002/2014JD021487.
Samuels-Crow, K. E., J. Galewsky, Z. D. Sharp, and K. J. Dennis (2014b), Deuterium excess in subtropical free troposphere water vapor: Continuous measurements from the Chajnantor Plateau, northern Chile, *Geophys Res Lett,* doi:10.1002/2014GL062302.
Saylor, J. E., and B. K. Horton (2014), Nonuniform surface uplift of the Andean plateau revealed by deuterium isotopes in Miocene volcanic glass from southern Peru, *Earth Planet Sc Lett*, *387*(C), 120–131, doi:10.1016/j.epsl.2013.11.015.
Scholl, M. A., S. E. Ingebritsen, C. J. Janik, and J. P. Kauahikaua (1996), Use of precipitation and groundwater isotopes to interpret regional hydrology on a tropical volcanic island: Kilauea volcano area, Hawaii, *Water Resour Res*, *32*(12), 3525–3537.
Siegenthaler, U., and H. Oeschger (1980), Correlation of ^{18}O in precipitation with temperature and altitude, *Nature*, *285*, 314–317.
Silvestri, G. E. (2004), El Niño signal variability in the precipitation over southeastern South

America during austral summer, *Geophys Res Lett*, *31*(18), L18206, doi:10.1029/2004GL020590.
Smith, T. M., R. W. Reynolds, T. C. Peterson, and J. Lawrimore (2008), Improvements to NOAA's Historical Merged Land–Ocean Surface Temperature Analysis (1880–2006), *Journal of Climate*, *21*(10), 2283–2296, doi:10.1175/2007JCLI2100.1.
Strong, M., Z. D. Sharp, and D. S. Gutzler (2007), Diagnosing moisture transport using D/H ratios of water vapor, *Geophys Res Lett*, *34*(3), doi:10.1029/2006GL028307.
Sturm, C., G. Hoffmann, and B. Langmann (2007), Simulation of the stable water isotopes in precipitation over South America: Comparing regional to global circulation models, *Journal of Climate*, *20*(15), 3730–3750.
Takahashi, K., and D. S. Battisti (2007), Processes Controlling the Mean Tropical Pacific Precipitation Pattern. Part I: The Andes and the Eastern Pacific ITCZ, *Journal of Climate*, *20*(14), 3434–3451, doi:10.1175/JCLI4198.1.
Thompson, L. G., E. Mosley-Thompson, and B. M. Arnao (1984), El Niño-Southern Oscillation events recorded in the stratigraphy of the tropical Quelccaya ice cap, Peru, *Science*, *226*(4670), 50–53.
Thompson, L. G., E. Mosley-Thompson, M. E. Davis, V. S. Zagorodnov, I. M. Howat, V. N. Mikhalenko, and P.-N. Lin (2013), Annually Resolved Ice Core Records of Tropical Climate Variability over the Past ~1800 Years, *Science*, *340*(6135), 945–950, doi:10.1126/science.1234210.
Thompson, L. G., M. E. Davis, E. Mosley-Thompson, T. A. Sowers, K. A. Henderson, V. S. Zagorodnov, P.-N. Lin, V. N. Mikhalenko, R. K. Campen, and J. F. Bolzan (1998), A 25,000-year tropical climate history from Bolivian ice cores, *Science*, *282*(5395), 1858–1864, doi:10.1126/science.282.5395.1858.
Uemura, R., Y. Matsui, K. Yoshimura, H. Motoyama, and N. Yoshida (2008), Evidence of deuterium excess in water vapor as an indicator of ocean surface conditions, *J Geophys Res*, *113*(D19), D19114–10, doi:10.1029/2008JD010209.
Vimeux, F., G. Tremoy, C. Risi, and R. Gallaire (2011), A strong control of the South American SeeSaw on the intra-seasonal variability of the isotopic composition of precipitation in the Bolivian Andes, *Earth Planet Sc Lett*, *307*(1-2), 47–58, doi:10.1016/j.epsl.2011.04.031.
Vimeux, F., P. Ginot, M. Schwikowski, M. Vuille, G. Hoffmann, L. Thompson, and U. Schotterer (2009), Climate variability during the last 1000 years inferred from Andean ice cores: A review of methodology and recent results, *Palaeogeography, Palaeoclimatology, Palaeoecology*, *281*(3-4), 229–241, doi:10.1016/j.palaeo.2008.03.054.
Vimeux, F., R. Gallaire, S. Bony, G. Hoffmann, and J. C. H. Chiang (2005), What are the climate controls on δD in precipitation in the Zongo Valley (Bolivia)? Implications for the Illimani ice core interpretation, *Earth Planet Sc Lett*, *240*(2), 205–220, doi:10.1016/j.epsl.2005.09.031.
Vuille, M. (1999), Atmospheric circulation over the Bolivian Altiplano during dry and wet periods and extreme phases of the Southern Oscillation, *International Journal of Climatology*, *19*, 1579–1600.
Vuille, M., and M. Werner (2005), Stable isotopes in precipitation recording South American summer monsoon and ENSO variability: observations and model results, *Climate Dynamics*, *25*(4), 401–413, doi:10.1007/s00382-005-0049-9.
Vuille, M., D. R. Hardy, C. Braun, F. Keimig, and R. S. Bradley (1998), Atmospheric circulation anomalies associated with 1996/1997 summer precipitation events on Sajama Ice Cap,

Bolivia, *J Geophys Res*, *103*(D10), 11191–11204.
Vuille, M., R. S. Bradley, and F. Keimig (2000), Interannual climate variability in the Central Andes and its relation to tropical Pacific and Atlantic forcing, *J Geophys Res*, *105*(D10), 12447–12460.
Vuille, M., R. S. Bradley, M. Werner, R. Healy, and F. Keimig (2003a), Modeling $\delta^{18}O$ in precipitation over the tropical Americas: 1. Interannual variability and climatic controls, *J Geophys Res*, *108*(D6), 4174, doi:10.1029/2001JD002038.
Vuille, M., R. S. Bradley, R. Healy, M. Werner, D. R. Hardy, L. G. Thompson, and F. Keimig (2003b), Modeling $\delta^{18}O$ in precipitation over the tropical Americas: 2. Simulation of the stable isotope signal in Andean ice cores, *J Geophys Res*, *108*(D6), 4175–4192, doi:10.1029/2001JD002039.
Vuille, M., S. J. Burns, B. L. Taylor, F. W. Cruz, B. W. Bird, L. C. Kanner, H. Cheng, and V. F. Novello (2012), A review of the South American monsoon history as recorded in stable isotopic proxies over the past two millennia, *Climate of the Past*, *8*(4), 1309–1321, doi:10.5194/cp-8-1309-2012.
Wang, X., A. Auler, R. Edwards, H. Cheng, P. Cristalli, P. Smart, D. Richards, and C. Shen (2004), Wet periods in northeastern Brazil over the past 210 kyr linked to distant climate anomalies, *Nature*, *432*(7018), 740–743, doi:10.1038/nature03067.
West, A. G., G. R. Goldsmith, I. Matimati, and T. E. Dawson (2011), Spectral analysis software improves confidence in plant and soil water stable isotope analyses performed by isotope ratio infrared spectroscopy (IRIS), *Rapid Commun. Mass Spectrom.*, *25*(16), 2268–2274, doi:10.1002/rcm.5126.
WMO/IAEA. (2013), Global Network of Isotopes in Precipitation, *The GNIP Database. Accessible at: http://www.iaea.org/water*. Available from: http://www-naweb.iaea.org/napc/ih/IHS_resources_gnip.html (Accessed 6 September 2013)
Xie, P. P., and P. A. Arkin (1998), Global monthly precipitation estimates from satellite-observed outgoing longwave radiation, *Journal of Climate*, *11*(2), 137–164.
Zhang, G. J., and N. A. McFarlane (1995), Sensitivity of climate simulations to the parameterization of cumulus convection in the Canadian climate centre general circulation model, *Atmosphere-Ocean*, *33*(3), 407–446, doi:10.1080/07055900.1995.9649539.

Appendix 2A. Monthly meteorological and isotopic records for central Andes micrometeorological stations

Table 2.11. Monthly meteorological and isotopic composition of precipitation for eleven central Andes micrometeorological stations

1. Oruro, Oruro Department (18.0°S, 67.1°W, 3718 m asl)							
Year	**Month**	**Temperature (°C)**	**Relative Humidity (%)**	**Precipitation (mm)**	**TRMM Precipitation Error (mm)**	**$\delta^{18}O$ (‰, VSMOW)**	**δD (‰, VSMOW)**
2008	8	6	26	5.9			
2008	9	8.1	27	0.3			
2008	10	10.8	31	18.9			
2008	11	12.8	32	13.3			
2008	12	12.4	39	70.1		-11.1	-68.5
2009	1	12.7	40	61.9		-11.1	-69.2
2009	2	12.5	45	91.3		-20.1	-143.6
2009	3	11.6	42	53.9		-17.2	-123.7
2009	4	10.4	36	15.1		-20.0	-148.5
2009	5	7.2	*49*	0			
2009	6	3.4	*31*	0			
2009	7	4.4	*40*	6.9			
2009	8	5.1	*27*	0			
2009	9	8.6	*33*	51.5		-8.6	-53.4
2009	10	11.1	*30*	3.7		-5.3	-34.8
2009	11	13.2	*43*	34.4		-8.3	-53.4
2009	12	13.3	*70*	145.8		-19.0	-134.4
2010	1	13.5	*82*	102.2		-11.0	-69.8
2010	2	14.2	*77*	87.6		-16.4	-118.5
2010	3	13.2	*69*	39.3		-7.8	-42.5
2010	4	11.1	*68*	21.8		-12.9	-87.3
2010	5	7.7	*54*	10		-11.2	-72.7
2010	6	6.6	*46*	0			
2010	7	4.6	*31*	0			
2010	8	6.9	*38*	12.3		-4.8	-14.5
2010	9	10.2	*36*	14.4		-7.4	-39.2
2010	10	10.4	*48*	24.7		-8.6	-50.2
2010	11	11.9	*33*	0			
2010	12	14.1	*59*	48.3		-15.4	-109.2
2011	1	13.9	*72*	15.5		-21.4	-156.0
2011	2	12.1	*84*	169.1		-23.3	-169.4
2011	3	11.7	*84*	57.4		-16.4	-117.1
2011	4	10.7	*67*	13.9		-17.5	-122.1
2011	5	7.5	*60*	1			
2011	6	6.3	*48*	0			
2011	7	5.5	*48*	4.5			
2011	8	7.6	*42*	1.2		-14.8	-110.2
2011	9	9.6	*50*	6.2		-4.0	-13.3
2011	10	10.8	*44*	0.7		-10.7	-69.1

2011	11	13.2	62	21.7		-10.6	-68.7
2011	12	15	76	110.5		-15.8	-111.1
2012	1	12.5	80	125		-13.2	-88.3
2012	2	11.9	85	83.6		-17.3	-123.9
2012	3	11.4	80	113.4		-20.2	-142.5
2012	4	10.9	73	14.3			
2012	5	7.5	45	1			
2012	6	4.7	39	0			
2012	7	5.3	43	4.1			
2012	8	7	44	0			
2012	9	10.3	42	1.5		-4.6	-20.1
2012	10	12.4	40	12.9		-8.0	-44.5
2012	11	13.3	41	13.5		-12.1	-84.5
2012	12	13.2	71	69.6		-17.0	-124.0
2013	1	12.8	82	97.1		-12.6	-83.5
2013	2	12.4	83	97.5		-14.5	-98.6
2013	3	12.7	76	34.6		-14.4	-100.2
2013	4	9.5	56	2.2			

2. El Choro, Oruro Department (18.4°S, 67.1°W, 3607 m asl)							
Year	**Month**	**Temperature (°C)**	**Relative Humidity (%)**	**Precipitation (mm)**	**TRMM Precipitation Error (mm)**	**$\delta^{18}O$ (‰, VSMOW)**	**δD (‰, VSMOW)**
2008	8	**7.6**	40	4.9	11.2		
2008	9	**10**	46	17.3	10.0		
2008	10	**11.3**	52	33.3	10.1		
2008	11	**12.6**	54	49.3	13.9		
2008	12	**11**	79	108.3	26.5	-12.8	-80.6
2009	1	**11**	80	68.6	33.4	-11.2	-74.9
2009	2	**11.2**	82	115.9	40.5	-28.0	-206.5
2009	3	**10.6**	78	80.1	33.8	-16.8	-117.4
2009	4	**9.6**	71	23.1	13.8	-16.6	-121.0
2009	5	**8.4**	49	2.5	12.4	-9.9	-67.8
2009	6	**5.8**	31	12.5	17.2		
2009	7	**7.2**	40	8.1	12.5	-11.4	-73.1
2009	8	**8**	27	2.8	14.3		
2009	9	**11.5**	33	35	13.8	-6.1	-35.6
2009	10	**13.5**	30	29.4	11.0		
2009	11	**14.8**	43	59.9	25.5		
2009	12	**12.8**	70	157.8	33.6	-7.1	-45.1
2010	1	**12.2**	82	115.7	25.2	-12.5	-81.0
2010	2	**12.8**	77	81.8	40.9	-17.6	-126.9
2010	3	**12.5**	69	24.6	15.9	-6.5	-38.0
2010	4	**11.2**	68	43.6	14.0	-10.7	-73.9
2010	5	**9.3**	54	9.1	16.9	-12.0	-82.7
2010	6	**8.4**	46	0.4	10.7		
2010	7	**7.4**	31	5.8	11.9		
2010	8	**9.8**	38	10	11.4		
2010	9	**11.3**	36	23.9	11.6		
2010	10	**11.6**	48	52.1	11.0	-5.8	-24.4
2010	11	**13.3**	33	40.9	10.4	-8.6	-53.8

2010	12	**13.5**	*59*	*77.6*	*21.2*		
2011	1	**12.3**	*72*	*58.1*	*17.7*	-13.4	-95.2
2011	2	**10.7**	*84*	*272.8*	*53.7*	-25.3	-186.0
2011	3	**10.6**	*84*	*52.2*	*29.0*	-18.2	-132.2
2011	4	**10.4**	*67*	*18.8*	*12.1*		
2011	5	**8.4**	*60*	*6.6*	*14.2*		
2011	6	**7.5**	*48*	*4.3*	*12.8*		
2011	7	**6.4**	*48*	*6.4*	*19.8*	-13.3	-97.4
2011	8	**8.8**	*42*	*24*	*11.8*		
2011	9	**9.9**	*50*	*7.7*	*11.9*		
2011	10	**11.6**	*44*	*4.6*	*9.6*		
2011	11	**12.2**	*62*	*20.9*	*13.8*		
2011	12	**11.4**	*76*	*164.7*	*27.7*	-13.8	-94.0
2012	1	**10.9**	*80*	*137.1*	*40.1*	-12.3	-84.0
2012	2	**10.6**	*85*	*145.3*	*44.3*	-16.5	-119.0
2012	3	**10.2**	*80*	*81*	*25.4*	-17.5	-129.6
2012	4	**10**	*73*	*14.2*	*16.4*		
2012	5	**8.2**	*45*	*9.4*	*17.4*		
2012	6	**7.3**	*39*	*3.9*	*16.9*		
2012	7	**7.4**	*43*	*6.5*	*16.6*		
2012	8	**8.6**	*44*	*4.5*	*9.2*		
2012	9	**11.1**	*42*	*6.4*	*10.0*		
2012	10	**13**	*40*	*15.6*	*9.4*		
2012	11	**14**	*41*	*18.1*	*15.8*		
2012	12	**12.5**	*71*	*76.2*	*24.7*		
2013	1	**11.1**	*82*	*145.9*	*53.5*		
2013	2	**11.1**	*83*	*110.9*	*35.0*		
2013	3	**11.4**	*76*	*21.7*	*11.7*		
2013	4	**10.1**	*56*	*1.1*	*12.3*		

3. Quillacas, Oruro Department (19.2°S, 66.9°W, 3780 m asl)							
Year	**Month**	**Temperature (°C)**	**Relative Humidity (%)**	**Precipitation (mm)**	**TRMM Precipitation Error (mm)**	**$\delta^{18}O$ (‰, VSMOW)**	**δD (‰, VSMOW)**
2008	8	6.9	*14*	1.4			
2008	9	9.1	*10*	0			
2008	10	12.7	*13*	0			
2008	11	14.5	*18*	0			
2008	12	14.9	*47*	70.2		-12.4	-81.5
2009	1	14.5	*61*	51.9		-10.8	-69.5
2009	2	14.8	*72*	60.7		-24.5	-177.8
2009	3	13	*69*	38.2		-17.5	-123.5
2009	4	11.7	*56*	10.8		-17.5	-123.5
2009	5	7.9	*27*	0			
2009	6	4.4	*14*	0			
2009	7	6.5	*19*	0			
2009	8	7.7	*12*	0			
2009	9	11.1	*13*	0			
2009	10	14.2	*11*	0			
2009	11	16.9	*36*	21		-4.5	-22.4
2009	12	17	*49*	45.2		-13.2	-89.8

2010	1	16.9	68	69.2		-10.8	-68.9
2010	2	17	65	93.3		-13.6	-95.0
2010	3	15.6	60	13.8		-15.0	-107.4
2010	4	9	48	20	24.4	-9.6	-65.2
2010	5	6.2	31	15.5	20.2	-10.5	-66.6
2010	6	5.4	21	2.7	14.9	-11.3	-68.3
2010	7	3.9	14	3	22.8		
2010	8	7.1	16	3	11.1		
2010	9	8.7	15	8.9	23.8		
2010	10	10.6	13	30.1	24.8	-7.5	-43.5
2010	11	12.2	13	74.7	20.1		
2010	12	13.4	31	70.7	17.2	-11.3	-79.2
2011	1	15.1	45	27.9		-14.3	-104.1
2011	2	13.5	80	179.7		-27.3	-200.5
2011	3	12.9	75	61		-18.8	-133.5
2011	4	10.3	47	15.2		-18.4	-133.6
2011	5	6.9	36	0			
2011	6	6	25	0			
2011	7	3.7	22	0			
2011	8	7.2	18	0		-16.3	-118.1
2011	9	7.2	27	0			
2011	10	7.4	14	0			
2011	11	12.8	29	0			
2011	12	11.5	45	107.7		-16.6	-118.9
2012	1	9.9	73	77.4	30.3	-14.9	-102.8
2012	2	9.8	80	97.4	38.6	-16.7	-118.5
2012	3	9.2	71	46.2	18.5	-19.2	-141.4
2012	4	8.8	49	16.9	15.8	-17.4	-128.8
2012	5	5.7	27	5.4	22.9	-15.2	-107.9
2012	6	3.8	20	7.9	21.1		
2012	7	4.3	20	4.2	22.1		
2012	8	6.3	20	0.5	16.1		
2012	9	9.3	23	7.3	14.7		
2012	10	11.5	12	4.8	14.9		
2012	11	13.6	17	22.9	18.9		
2012	12	11.8	63	65.6	16.7		
2013	1	10.3	72	134.7	58.1	-15.4	-107.9
2013	2	9.8	76	149.7	35.9	-8.8	-50.0
2013	3	9.8	55	20.4	16.2		
2013	4	7.7	33	5.3	15.7		

4. Salinas de Garci Mendoza, Oruro Department (19.7°S, 67.6°W, 3719 m asl)							
Year	**Month**	**Temperature (°C)**	**Relative Humidity (%)**	**Precipitation (mm)**	**TRMM Precipitation Error (mm)**	**$\delta^{18}O$ (‰, VSMOW)**	**δD (‰, VSMOW)**
2008	8	4.9	12	8.3	13.1		
2008	9	8	9	20.4	9.3		
2008	10	11.3	12	24.7	10.7	-0.6	9.5
2008	11	12.7	16	19.9	12.0		
2008	12	13	31	29.9	19.4	-16.4	-113.1
2009	1	12.5	46	37.6	30.6	-16.7	-114.9

2009	2	12.1	59	32.3	33.5	-16.9	-120.8
2009	3	9.5	63	33.9	30.3	-22.0	-158.4
2009	4	9.2	45	1	11.4	-16.3	-124.5
2009	5	5.9	24	8.7	11.9		
2009	6	3.6	12	35.3	16.7		
2009	7	4	18	9.6	12.1		
2009	8	5.3	10	9.4	15.9		
2009	9	9	13	24	13.4		
2009	10	12	11	4.2	8.9		
2009	11	14.5	27	4.2	23.2	-11.8	-82.3
2009	12	14.2	32	77.6	32.3	-16.5	-118.0
2010	1	13.1	53	17.9	24.3	-13.1	-89.4
2010	2	13.4	53	57.4	32.6	-13.9	-97.8
2010	3	12.7	47	24.4	15.4	-3.3	-15.8
2010	4	10.3	36	0.7	10.8	-9.3	-68.8
2010	5	6.5	27	15.9	11.7	-9.2	-68.9
2010	6	6.1	18	0.7	10.3	-9.3	-56.9
2010	7	4.5	11	7.9	12.1	-9.0	-56.4
2010	8	7.2	14	2.9	11.8		
2010	9	9.2	12	9.3	11.9		
2010	10	10.4	13	22.5	10.0	-9.7	-70.2
2010	11	11.8	14	25.7	10.9	-9.7	-70.3
2010	12	13.8	27	5.5	19.5	-9.1	-60.0
2011	1	14.1	36	40.8	14.0	-20.3	-147.9
2011	2	10.8	76	194.6	53.2	-19.2	-137.9
2011	3	10.1	65	18.9	27.6	-18.4	-130.3
2011	4	9.2	37	7.7	11.2		
2011	5	6.7	28	0	15.4		
2011	6	5.4	22	0	16.4		
2011	7	4.3	21	0	19.9		
2011	8	6.3	15	0	13.1		
2011	9	8.8	22	0	14.1		
2011	10	10.4	13	0	9.6		
2011	11	13.9	20	0	12.6		
2011	12	13.1	35	104.9	26.4	-17.1	-139.2
2012	1	10.5	71	92.9	36.3	-20.7	-154.1
2012	2	10.5	77	110	38.4	-7.4	-80.7
2012	3	10	66	42.2	19.7	-10.7	-91.4
2012	4	9.1	45	1	14.6	-7.2	-80.1
2012	5	6.2	25	2.5	24.2		
2012	6	4.2	19	6.9	18.2		
2012	7	4.6	18	25.2	14.9		
2012	8	6.7	17	6.6	9.9		
2012	9	9.9	19	3.5	9.3		
2012	10	11.6	12	2.6	8.6		
2012	11	13.6	15	5	14.6		
2012	12	13	49	21.2	26.5		
2013	1	11.8	56	33.5	48.4		
2013	2	10.9	69	25.6	31.3		
2013	3	10.8	45	16.7	9.9		
2013	4	8.7	24	1.7	9.2		

5. San Juan del Rosario, Potosí Department (20.9°S, 27.8°W, 3663 m asl)							
Year	**Month**	**Temperature (°C)**	**Relative Humidity (%)**	**Precipitation (mm)**	**TRMM Precipitation Error (mm)**	**$\delta^{18}O$ (‰, VSMOW)**	**δD (‰, VSMOW)**
2008	8	5.1	12	0			
2008	9	7	11	0			
2008	10	10.3	14	0			
2008	11	11.9	14	0			
2008	12	12.4	32	16		-9.9	-68.9
2009	1	*9.3*	*50*	2.6		0.4	20.8
2009	2	*9.2*	*62*	8.2		-15.4	-107.1
2009	3	*7.2*	*67*	33		-20.8	-149.1
2009	4	*6.8*	*50*	4.6		-11.2	-72.6
2009	5	6.5	19	0			
2009	6	2.8	16	0			
2009	7	4.1	18	1			
2009	8	4.4	12	0			
2009	9	8.5	17	0.4		-19.2	-140.6
2009	10	11.1	12	0			
2009	11	14.7	24	3.2			
2009	12	13.9	34	15.2		-19.7	-142.5
2010	1	13.9	41	20.4		-11.2	-75.0
2010	2	14.1	45	65.2		-12.6	-89.4
2010	3	*9.5*	*46*	3		-6.4	-35.1
2010	4	*8*	*32*	10.2		-12.4	-81.0
2010	5	6.3	25	0.4			
2010	6	6	20	0			
2010	7	3.8	12	0.2			
2010	8	7	13	0			
2010	9	7.9	14	0			
2010	10	9.1	12	0			
2010	11	10.8	12	0			
2010	12	13.8	27	14.2		-4.9	-24.2
2011	1	13.3	37	56.2		-12.4	-84.9
2011	2	11	58	83.6		-18.6	-134.3
2011	3	12.1	36	7.8		-14.4	-100.6
2011	4	9.7	27	5.6		-14.9	-112.2
2011	5	5.9	27	1.4			
2011	6	4.8	26	0			
2011	7	3	29	2.4		-18.1	-133.6
2011	8	4.9	18	0			
2011	9	7.6	19	0			
2011	10	9	15	0			
2011	11	12.8	20	0			
2011	12	12.4	36	35.4		-12.9	-91.8
2012	1	11.5	47	51.4		-12.0	-77.4

2012	2	11.1	55	93.4		-17.4	-124.7
2012	3	11.3	48	44.4		-9.4	-71.0
2012	4	*7.1*	*39*	*2.9*	*16.6*		
2012	5	*5.3*	*24*	*23.7*	*18.2*		
2012	6	*3.8*	*18*	*16*	*16.4*		
2012	7	*4.1*	*16*	*18.9*	*14.1*		
2012	8	*5.4*	*16*	*4.8*	*11.7*		
2012	9	*7.6*	*17*	*2.7*	*12.7*		
2012	10	*8.6*	*12*	*4.3*	*12.3*		
2012	11	*9.9*	*16*	*11.4*	*13.5*		
2012	12	*10.1*	*47*	*3*	*31.9*	-11.5	-78.6
2013	1	*9.2*	*55*	*101*	*49.0*	-16.5	-115.3
2013	2	*8.8*	*70*	*29.1*	*46.5*	-6.2	-26.8
2013	3	*8.4*	*41*	*9.9*	*17.7*		
2013	4	*6.6*	*28*	*5.4*	*12.9*		

6. Noel Mariaca, Potosí Department (20.7°S, 66.6°W, 3674 m asl)							
Year	**Month**	**Temperature (°C)**	**Relative Humidity (%)**	**Precipitation (mm)**	**TRMM Precipitation Error (mm)**	**$\delta^{18}O$ (‰, VSMOW)**	**δD (‰, VSMOW)**
2008	8	0.7	15	0			
2008	9	3.5	13	0			
2008	10	8.7	19	0.2			
2008	11	10.5	22	0			
2008	12	12.3	45	39.4		-10.6	-69.2
2009	1	*7.8*	*59*	12.4		-13.6	-90.6
2009	2	*7.7*	*68*	39.8		-21.0	-157.6
2009	3	*5.4*	*72*	30.6		-16.9	-124.3
2009	4	*4.9*	*54*	1.6			
2009	5	2.7	23	0.2			
2009	6	-0.8	18	0			
2009	7	0.7	22	0			
2009	8	1.4	16	0			
2009	9	6.1	20	0.2			
2009	10	8.7	16	0			
2009	11	13.8	34	*19.6*	*40.6*		
2009	12	13.4	45	*45.6*	*75.9*	-3.0	-6.5
2010	1	13.6	54	*25.7*	*62.5*	-14.4	-98.3
2010	2	13.8	54	*41*	*52.9*	-11.4	-73.8
2010	3	*9.5*	*50*	*9.4*	*25.3*	-11.7	-84.6
2010	4	*8*	*34*	*1.9*	*32.3*		
2010	5	3.7	31	*3.7*	*16.2*		
2010	6	2.4	24	*1.3*	*9.6*		
2010	7	-0.2	16	*4*	*13.8*		
2010	8	3.3	17	*3.2*	*16.9*		
2010	9	5.6	18	*3.1*	*24.8*		
2010	10	7.1	16	*1.3*	*36.2*		
2010	11	9.3	18	*1.8*	*30.7*		
2010	12	13.7	38	*16.6*	*48.4*	-9.4	-59.5
2011	1	13.8	46	*6.5*	*38.8*	-10.7	-72.4
2011	2	11.5	67	*87*	*113.7*	-15.7	-117.9

2011	3	11.7	55	*29.4*	*38.7*	-14.6	-96.2
2011	4	8	35	*2.2*	*22.7*		
2011	5	3.8	35	4.2			
2011	6	1.9	31	0			
2011	7	0.7	42	6			
2011	8	2.1	24	0			
2011	9	5.4	25	0			
2011	10	6.9	21	0			
2011	11	12	32	0			
2011	12	12	47	47.2		-10.6	-65.5
2012	1	11.8	57	57.2		-16.4	-115.3
2012	2	11.2	69	107.6		-16.4	-116.1
2012	3	11.2	60	31.2		-15.7	-110.2
2012	4	8.6	44	6.6		-17.9	-132.0
2012	5	3	30	0			
2012	6	-0.8	28	0			
2012	7	0.6	25	0			
2012	8	2.8	24	0			
2012	9	6.7	24	0			
2012	10	8.3	21	0.2			
2012	11	12	27	0			
2012	12	13.3	56	79.2		-9.2	-55.3
2013	1	12.1	58	108.8		-20.2	-143.7
2013	2	12.6	61	20		-8.5	-46.5
2013	3	11	41	1.2			
2013	4	6.3	25	0			

7. Gran Chocaya, Potosí Department (21.0°S, 66.3°W, 4340 m asl)							
Year	**Month**	**Temperature (°C)**	**Relative Humidity (%)**	**Precipitation (mm)**	**TRMM Precipitation Error (mm)**	**$\delta^{18}O$ (‰, VSMOW)**	**δD (‰, VSMOW)**
2008	8	2.1	13	0			
2008	9	4.2	12	0			
2008	10	7	25	2.2		-0.1	23.7
2008	11	8.1	32	0			
2008	12	7.2	62	72.2		-8.7	-43.7
2009	1	*5.9*	*80*	20		-7.4	-32.8
2009	2	*6.2*	*76*	54.8		-24.3	-170.9
2009	3	*5.2*	*77*	70.8		-11.3	-66.5
2009	4	*4.6*	*65*	12.6			
2009	5	3.7	21	0			
2009	6	1.1	16	0			
2009	7	0.6	21	0			
2009	8	2.5	14	0			
2009	9	4.3	21	0.2			
2009	10	7.7	17	0			
2009	11	10	40	20.4		-7.2	-34.4
2009	12	8.8	56	60.4		-13.6	-86.9
2010	1	8.5	64	58.4		-11.7	-69.9
2010	2	9	64	88.8		-17.6	-122.3
2010	3	*6.7*	*62*	7.8		-5.4	-21.8

2010	4	*5.7*	*46*	3.8		-13.7	-89.5
2010	5	2.9	31	15		-13.5	-91.4
2010	6	2.7	22	0			
2010	7	0.9	13	0			
2010	8	4.5	16	0			
2010	9	4.7	18	2.2			
2010	10	5.9	18	0			
2010	11	7.4	23	0			
2010	12	9.2	48	34.4		-9.8	-56.5
2011	1	8.7	58	33		-14.4	-97.6
2011	2	6.3	78	96		-19.2	-133.0
2011	3	7.4	63	37.2		-12.5	-98.6
2011	4	6.4	37	6.2			
2011	5	3.9	31	6.8		-17.2	-121.2
2011	6	1.7	29	0			
2011	7	-0.6	37	6.8		-7.3	-70.7
2011	8	2.4	20	0			
2011	9	4.8	25	0			
2011	10	5.5	25	0			
2011	11	8.6	42	*0.9*	*11.2*	-3.2	-6.8
2011	12	7.6	57	*5.9*	*48.0*	-11.7	-70.3
2012	1	6.3	69	*33.7*	*62.1*	-13.4	-84.6
2012	2	6.1	77	*61.6*	*46.4*	-19.0	-131.9
2012	3	6.4	68	*71.6*	*31.1*	-13.5	-88.7
2012	4	5.8	44	*31.1*	*21.0*	-18.0	-128.8
2012	5	3.5	26	*9.8*	*13.2*		
2012	6	1.3	23	*13.3*	*16.1*		
2012	7	2	22	*10.9*	*10.0*		
2012	8	3.9	20	*10.9*	*9.1*		
2012	9	6.4	23	*0.4*	*10.6*		
2012	10	7.5	22	*0.9*	*15.8*		
2012	11	9.4	36	*0.7*	*29.6*	-10.6	-65.0
2012	12	8.5	64	*8.6*	*30.7*	-10.7	-65.0
2013	1	7	67	*25.5*	*75.1*	-17.4	-118.4
2013	2	7.1	73	*88*	*69.2*	-11.2	-65.1
2013	3	7.6	44	*43.3*	*22.4*	-13.2	-85.6
2013	4	5.6	23	*4.4*	*7.8*		

8. Tupiza, Potosí Department (21.4°S, 65.7°W, 2974 m asl)							
Year	**Month**	**Temperature (°C)**	**Relative Humidity (%)**	**Precipitation (mm)**	**TRMM Precipitation Error (mm)**	**$\delta^{18}O$ (‰, VSMOW)**	**δD (‰, VSMOW)**
2008	8	11.9	14	0			
2008	9	14.7	18	0			
2008	10	17.8	31	5.6		0.4	23.8
2008	11	18.2	39	21.2		-1.3	11.9
2008	12	16.7	56	172.2		-7.3	-34.4
2009	1	*15.3*	*77*	83.8		-4.1	-11.0
2009	2	*15.5*	*78*	104.8		-15.1	-101.0
2009	3	*14.4*	*77*	38.4		-14.1	-93.6
2009	4	*13.6*	*66*	49.8		-11.5	-74.6

2009	5	12.1	29	0			
2009	6	9	21	0			
2009	7	10.1	18	0.2			
2009	8	12.1	17	0			
2009	9	16.5	17	0.2			
2009	10	18.8	26	0			
2009	11	20.4	38	9.2		-5.7	-38.0
2009	12	18.6	53	56.2		-9.8	-62.0
2010	1	18.1	57	66.2		-8.6	-50.8
2010	2	18.8	58	93		-15.1	-107.3
2010	3	*16.1*	*44*	16.6		-8.0	-43.8
2010	4	*14.8*	*28*	0.4			
2010	5	12.4	29	1.2		-4.8	-37.7
2010	6	11.7	23	0			
2010	7	10.5	15	0			
2010	8	13.8	18	0			
2010	9	15.8	19	0			
2010	10	17.2	29	0			
2010	11	17.8	35	0			
2010	12	19	47	57.8		-9.3	-56.8
2011	1	18.6	51	32.2		-9.3	-63.8
2011	2	16.7	60	72.2		-17.5	-127.4
2011	3	17.2	54	32		-12.5	-84.8
2011	4	16.1	42	3.4		-15.4	-117.5
2011	5	12.7	33	5.2		-15.6	-118.1
2011	6	11.6	25	0			
2011	7	10.8	24	0			
2011	8	12.9	18	0			
2011	9	15.5	27	0		9.6	77.1

9. Tarija, Tarija Department (21.5°S, 64.7°W, 1884 m asl)							
Year	**Month**	**Temperature (°C)**	**Relative Humidity (%)**	**Precipitation (mm)**	**TRMM Precipitation Error (mm)**	**$\delta^{18}O$ (‰, VSMOW)**	**δD (‰, VSMOW)**
2008	8	14.8	48	1		-1.3	3.1
2008	9	15.4	48	0.6		0.2	22.1
2008	10	19.1	59	41.4		-3.0	-3.3
2008	11	19.8	66	126.6		-2.7	0.4
2008	12	19.1	73	206.4		-4.9	-16.8
2009	1	19.6	72	98.4		-4.3	-11.2
2009	2	20.1	70	91.2		-8.0	-47.2
2009	3	19.2	74	109.8		-8.2	-52.9
2009	4	18.5	71	41		-7.5	-39.0
2009	5	16	66	0.6		-6.5	-40.4
2009	6	11.5	55	0.6		-3.0	-12.2
2009	7	11.9	54	0			
2009	8	14.9	47	0.8			
2009	9	15.6	51	23.8		-3.1	-6.7
2009	10	19.1	55	2.4		-0.6	14.3
2009	11	23.1	65	76.4		-6.3	-34.4
2009	12	20.1	77	182.2		-10.4	-68.2

2010	1	20	76	108		-6.5	-36.2
2010	2	20.9	79	206.2		-10.9	-73.3
2010	3	20.3	76	64.2		-8.0	-47.8
2010	4	16.6	72	12.2		-6.0	-30.2
2010	5	13	70	8.8		-3.1	-6.4
2010	6	11.4	68	0.6			
2010	7	9.5	59	0			
2010	8	12.8	58	0			
2010	9	17.4	54	0.6			
2010	10	17.6	60	2.6		-0.6	11.5
2010	11	19	54	9.2		-1.5	4.2
2010	12	21.1	63	64		-6.6	-37.6
2011	1	20.2	73	103.6		-16.0	-112.3
2011	2	18.5	80	163.6		-7.8	-47.2
2011	3	17.9	80	96.2		-10.2	-63.8
2011	4	17	78	17.6		-7.8	-45.9
2011	5	12.9	74	2.8		-11.1	-87.9
2011	6	12	65	0.2			
2011	7	11.3	63	0			
2011	8	12.9	55	0			
2011	9	16.4	53	3		-2.6	0.1

10. Entre Ríos, Tarija Department (21.5°S, 64.2°W, 1261 m asl)							
Year	**Month**	**Temperature (°C)**	**Relative Humidity (%)**	**Precipitation (mm)**	**TRMM Precipitation Error (mm)**	**$\delta^{18}O$ (‰, VSMOW)**	**δD (‰, VSMOW)**
2008	8	14.4	65	6.2		-1.0	10.8
2008	9	15.8	53	1		-0.6	16.8
2008	10	19.5	66	12.4		-1.5	11.0
2008	11	21.2	70	85.6		-2.2	2.4
2008	12	20.7	78	214.2		-4.4	-17.8
2009	1	20.5	79	123.2		-3.9	-7.5
2009	2	21.1	81	91.8		-8.9	-52.4
2009	3	20.1	84	208.4		-9.4	-56.3
2009	4	18.6	85	92.4		-3.8	-8.8
2009	5	16.1	86	20.4		-6.6	-33.1
2009	6	11.2	81	4.2		-4.7	-15.0
2009	7	11.2	74	1.6		-1.9	6.2
2009	8	15	58	0.2		-1.4	9.7
2009	9	15.6	59	20		-0.6	9.9
2009	10	21.2	55	0			
2009	11	24.1	73	206.6		-6.1	-32.3
2009	12	21.6	82	181.2		-8.7	-53.9
2010	1	22.4	76	35.8		-9.7	-62.6
2010	2	22.5	82	208.2		-8.1	-48.0
2010	3	21.7	85	92		-5.3	-25.2
2010	4	17.1	85	9.6		-3.8	-10.9
2010	5	13	83	*16.3*	*16.3*	-3.5	-6.0
2010	6	13	81	*2*	*10.3*	-1.6	10.0
2010	7	9.7	70	*1.7*	*10.1*	-3.6	-7.5
2010	8	13.6	60	*0.3*	*6.8*	-0.1	21.7

2010	9	17.8	60	*6.7*	*17.5*	1.5	38.0
2010	10	19.2	63	*12.9*	*19.8*	0.9	30.6
2010	11	21.3	51	*8.1*	*13.4*	-0.8	14.2
2010	12	22.7	68	*91.8*	*50.3*	-5.6	-27.0
2011	1	22	78	*147.7*	*52.7*	-6.4	-34.1
2011	2	20.2	84	*237.2*	*85.6*	-13.4	-92.7
2011	3	18.9	86	*68.4*	*21.2*	-10.0	-63.5
2011	4	18.1	88	*42*	*27.1*	-7.5	-42.7
2011	5	14.7	85	7.8		-4.9	-25.9
2011	6	12.9	83	6		-0.1	7.8
2011	7	11.8	77	3.6		-2.2	3.2
2011	8	13.8	63	0			
2011	9	18.2	52	6.4		0.7	32.2

11. Villamontes, Tarija Department (21.3°S, 63.4°W, 395 m asl)							
Year	**Month**	**Temperature (°C)**	**Relative Humidity (%)**	**Precipitation (mm)**	**TRMM Precipitation Error (mm)**	**$\delta^{18}O$ (‰, VSMOW)**	**δD (‰, VSMOW)**
2008	8	21.2	45	0.4			
2008	9	22	38	0		3.3	29.8
2008	10	25.9	52	9.6		-1.3	7.1
2008	11	28.3	53	87.8		-1.8	6.4
2008	12	27	67	173.6		-4.0	-14.5
2009	1	26.2	68	59.8		-2.0	2.5
2009	2	26.9	72	117.4		-9.0	-56.2
2009	3	26.1	74	91.2		-7.6	-44.8
2009	4	23.8	78	76		-7.3	-42.5
2009	5	21.3	75	14.6			
2009	6	15.6	67	0			
2009	7	16.7	57	0			
2009	8	20.6	46	0			
2009	9	22.6	42	0		1.1	8.2
2009	10	27.8	44	0.2			
2009	11	30.2	60	80.2		-4.2	-20.6
2009	12	27.1	73	152		-8.3	-54.1
2010	1	27.6	68	39.8		-8.1	-54.8
2010	2	27.9	73	147		-8.1	-54.4
2010	3	27.3	73	41		-7.2	-45.0
2010	4	22.5	71	13.2		-6.1	-34.7
2010	5	17.2	73	12.8		-1.8	8.2
2010	6	17.4	69	2.4		-2.8	1.1
2010	7	16.4	59	14.6		0.2	23.8
2010	8	18.9	48	*0.8*	*12.1*		
2010	9	23.8	48	*22*	*16.3*	-7.0	-37.6
2010	10	25.9	49	*23.6*	*26.4*	1.5	38.3
2010	11	27.5	42	*13.5*	*43.2*		
2010	12	28.7	58	*139.7*	*41.8*	-4.0	-11.2
2011	1	27.1	74	*154.7*	*43.3*	-5.8	-30.5
2011	2	25	81	*302.5*	*88.9*	-12.5	-86.2
2011	3	23.6	81	*40.6*	*37.7*	-8.6	-49.8
2011	4	22.6	81	*51.3*	*16.7*	-5.6	-32.0

2011	5	19.7	76	*24.5*	*15.4*	-5.6	-31.9
2011	6	17.6	73	*5.7*	*12.4*	-1.6	8.8
2011	7	16.8	65	*9.1*	*14.8*	-1.7	9.2
2011	8	20	47	*0*	*16.0*		
2011	9	24.6	41	*8.7*	*18.5*	-2.7	2.0

Formatting notes (see Chapter 2.3.1 for more information)

Bold, blue text – temperatures estimated from ERA-Interim data using a regional regression

Regular weight blue text – temperatures estimated from ERA-Interim data using a local regression

Red italic text – Relative humidity estimated using the lowest ERA-Interim model level above the surface

Green italic text – Precipitation values estimated from the TRMM 3B43 product. TRMM reported error estimates are also provided in these cases.

Highlighted samples – These 11 monthly isotope values are considered suspect. The April-December 2010 samples are considered suspect as the isotope values are nearly identical from month to month and many occur during the dry season when trace amounts of precipitation were recorded. In contrast, the December 2011-April 2014 samples exhibit evidence of evaporation not observed in other samples on the Altiplano (i.e., a negative d-excess value).

Appendix 2B. Unnormalized ERA-Interim Back Trajectory Analyses and Air Sourcing

Table 2.12. Summary table of the composite areal mean DJF back trajectory density for the three main source regions to the Altiplano across the 2008-2013 study period. In contrast to the main paper, these are not normalized to 100% considering only these three source regions. The three source regions studied include the YAB (13-15°S, 65-69°W), the SP (20-24°S, 69-71°W), and the GC regions (24-26°S, 62-66°W). Values listed below represent the areal mean percentage of trajectories passing through each of the 2x4° regions. Values are provided for all DJF trajectories or only trajectories resulting in precipitation as forecasted by the ERA-Interim reanalysis dataset.

Station	Yungas-Amazon Basin		South Pacific		Gran Chaco	
	All	Rain Only	All	Rain Only	All	Rain Only
Oruro	46.94	47.99	61.48	53.89	7.04	6.09
Quillacas	32.09	47.59	78.95	59.02	10.31	12.27
Noel Mariaca	18.51	41.44	88.89	35.93	13.52	30.89
Tarija	27.57	34.41	34.60	23.86	29.84	37.33
Villamontes	28.74	33.93	9.83	6.20	13.36	16.33

Table 2.13. Summary table of DJF monthly and seasonal average Bolivian High latitude and longitude, and areal mean back trajectory density for each subregion (unnormalized). For each month, the areal means are split into two columns, with the left column showing the calculation using all available back trajectories and the right column showing the calculation using only trajectories resulting in rain at the station as calculated by the ERA-Interim reanalysis dataset.

		December 2008		January 2009		February 2009		2008-09 Seasonal Average	
Bolivian High Latitude (°S)		15.0		15.0		18.8		16.2	
Bolivian High Latitude (°W)		63.0		61.5		60.0		61.6	
Yungas-Amazon Basin (YAB) South Pacific (SP) Gran Chaco (GC)		All Trajectories	Precipitating Trajectories Only	All Trajectories	Precipitating Trajectories Only	All Trajectories	Precipitating Trajectories Only	All Trajectories	Precipitating Trajectories Only
Oruro	YAB	16.76	12.96	18.59	29.22	51.35	31.60	32.03	40.43
	SP	57.12	52.08	48.86	37.04	40.02	48.96	57.85	55.02
	GC	10.70	5.83	8.28	3.46	3.54	2.71	7.71	3.86
Quillacas	YAB	3.67	11.11	5.56	0.00	31.25	30.39	13.62	28.83
	SP	69.42	28.13	70.80	63.89	42.71	14.22	71.63	44.14
	GC	4.78	0.00	17.45	11.67	7.20	5.49	9.88	8.11
Noel Mariaca	YAB	0.00	0.00	3.32	0.00	32.43	32.10	11.23	41.01
	SP	73.05	9.38	68.68	0.00	46.70	13.43	73.35	13.24
	GC	8.98	37.50	15.27	47.50	4.98	15.19	10.45	31.18
Tarija	YAP	1.43	4.13	1.84	2.26	31.00	35.08	11.00	16.01
	SP	35.89	27.52	33.80	14.58	26.41	25.71	38.19	29.47
	GC	33.44	31.01	43.87	42.08	23.93	16.76	35.70	33.76
Villamontes	YAB	11.02	9.26	20.42	25.00	26.84	33.33	19.50	31.22
	SP	1.81	0.00	10.37	10.61	7.89	4.71	7.50	7.14
	GC	14.84	6.30	22.11	15.45	10.77	8.41	16.36	11.64

		December 2009		January 2010		February 2010		2009-10 Seasonal Average	
Bolivian High Latitude (°S)		15.8		16.5		18.8		16.9	
Bolivian High Latitude (°W)		62.3		63.0		63.8		63.0	
		All Trajectories	Precipitating Trajectories Only	All Trajectories	Precipitating Trajectories Only	All Trajectories	Precipitating Trajectories Only	All Trajectories	Precipitating Trajectories Only
Oruro	YAB	21.18	27.01	43.41	27.41	46.28	47.22	44.71	44.37
	SP	66.06	53.16	37.37	30.56	37.50	49.07	50.74	57.03
	GC	3.63	2.53	11.02	9.56	2.02	0.00	5.68	6.15
Quillacas	YAB	14.74	11.11	32.48	39.32	41.17	50.00	35.46	58.02
	SP	82.93	28.33	60.35	12.18	54.09	23.08	69.76	34.95
	GC	0.32	2.67	8.28	17.44	6.37	0.00	4.94	10.56
Noel Mariaca	YAB	9.80	0.00	6.85	0.00	21.43	31.31	12.66	34.66
	SP	75.88	25.00	67.81	6.48	76.12	18.18	83.01	24.21
	GC	0.00	0.00	13.66	22.22	20.48	7.27	11.68	14.92
Tarija	YAP	20.17	21.43	28.27	17.81	32.74	28.93	32.71	31.32
	SP	52.53	30.56	38.64	10.05	22.02	12.36	44.51	20.63
	GC	23.93	30.48	27.26	19.22	16.85	13.10	23.41	25.21
Villamontes	YAB	35.93	30.08	41.35	23.39	33.28	19.26	39.85	26.46
	SP	6.72	5.75	9.14	0.00	7.14	1.11	7.82	3.57
	GC	16.13	14.02	13.17	16.14	8.33	6.22	12.69	13.23

		December 2010		January 2011		February 2011		2010-11 Seasonal Average	
Bolivian High Latitude (°S)		19.5		19.5		21.0		20.0	
Bolivian High Latitude (°W)		58.5		69.8		63.8		64.0	
		All Trajectories	Precipitating Trajectories Only	All Trajectories	Precipitating Trajectories Only	All Trajectories	Precipitating Trajectories Only	All Trajectories	Precipitating Trajectories Only
Oruro	YAB	23.51	16.90	29.66	29.01	37.35	38.03	42.44	42.73
	SP	65.63	47.22	26.75	25.93	32.07	40.06	43.16	44.00
	GC	0.39	1.11	5.00	0.00	10.18	16.92	5.06	7.06
Quillacas	YAB	30.44	29.37	24.60	0.00	14.43	14.93	31.30	19.44
	SP	80.18	0.00	46.71	0.00	53.79	42.97	64.58	44.38
	GC	0.11	0.00	12.26	20.00	12.26	6.88	8.19	9.33
Noel Mariaca	YAB	27.45	49.07	16.58	26.39	22.72	34.23	26.42	44.09
	SP	78.88	0.00	42.21	0.00	58.33	44.59	66.29	35.64
	GC	0.40	0.00	6.07	0.00	17.74	23.42	7.88	19.72
Tarija	YAP	38.80	38.74	22.72	30.88	21.38	23.64	30.36	36.53
	SP	34.99	3.38	17.61	10.85	5.43	7.27	22.48	8.53
	GC	27.82	44.86	21.94	30.08	41.79	45.82	33.61	42.99
Villamontes	YAB	25.09	36.47	29.26	29.93	14.88	17.30	26.18	29.03
	SP	15.78	0.00	9.54	4.84	7.44	0.00	11.01	2.25
	GC	15.46	23.48	11.77	17.63	19.05	14.29	15.72	20.67

		December 2011		January 2012		February 2012		2011-12 Seasonal Average	
Bolivian High Latitude (°S)		12.8		14.3		21.0		15.9	
Bolivian High Latitude (°W)		63.8		65.3		66.0		64.3	
		All Trajectories	Precipitating Trajectories Only	All Trajectories	Precipitating Trajectories Only	All Trajectories	Precipitating Trajectories Only	All Trajectories	Precipitating Trajectories Only
Oruro	YAB	31.57	23.06	18.59	17.54	40.18	28.35	37.80	32.44
	SP	50.95	41.67	55.11	30.70	46.55	31.32	59.44	40.95
	GC	1.03	0.81	8.87	0.00	21.49	13.10	12.67	5.02
Quillacas	YAB	21.36	14.81	9.45	12.61	25.86	27.59	25.73	27.62
	SP	50.47	24.44	70.09	34.29	66.95	60.63	76.01	66.19
	GC	4.12	3.56	12.15	1.28	29.77	4.60	18.75	4.19
Noel Mariaca	YAB	9.18	0.00	1.84	0.00	25.34	9.19	16.87	16.13
	SP	51.14	0.00	73.72	14.58	66.74	23.72	79.37	24.04
	GC	16.02	32.00	16.13	8.75	33.22	34.10	25.15	36.41

		December 2012		January 2013		February 2013		2012-13 Seasonal Average	
Bolivian High Latitude (°S)		18.8		14.3		16.5		16.5	
Bolivian High Latitude (°W)		62.3		60.0		67.5		64.1	
		All Trajectories	Precipitating Trajectories Only	All Trajectories	Precipitating Trajectories Only	All Trajectories	Precipitating Trajectories Only	All Trajectories	Precipitating Trajectories Only
Oruro	YAB	42.43	28.70	43.64	29.51	44.15	53.17	47.58	47.81
	SP	60.42	53.61	21.91	0.00	42.93	26.90	52.80	37.96
	GC	0.00	0.00	7.85	18.33	3.75	0.57	4.00	8.56
Quillacas	YAB	37.77	35.38	37.05	28.49	40.38	50.72	40.17	44.60
	SP	69.09	47.37	37.23	22.04	56.85	32.25	64.38	47.15
	GC	6.24	8.42	15.75	24.73	4.76	0.00	9.09	19.45
Noel Mariaca	YAB	25.22	27.16	16.89	27.92	24.57	43.40	22.52	33.07
	SP	75.87	13.89	56.59	22.65	49.32	34.90	76.67	47.01
	GC	8.87	23.70	18.44	21.20	2.52	0.00	10.62	20.52

Appendix 2C. Back-trajectory analysis of central Andes air sourcing from the NCEP/NCAR Reanalysis Project

Table 2.14. Summary table of the composite areal mean NCEP/NCAR DJF back trajectory density for the three main source regions to the Altiplano across the 2008-2013 study period. Trajectories are normalized to 100% and initiated at 1500 m above ground level. The three source regions studied include the YAB (13-15°S, 65-69°W), the SP (20-24°S, 69-71°W), and the GC regions (24-26°S, 62-66°W). Values listed below represent the areal mean percentage of trajectories passing through each of the 2x4° regions.

Station	Yungas-Amazon Basin		South Pacific		Gran Chaco	
	All	Rain Only	All	Rain Only	All	Rain Only
Oruro	69.0	78.1	17.3	10.0	13.7	11.9
Quillacas	58.6	68.0	25.6	11.9	15.8	20.1
Noel Mariaca	32.1	43.0	47.0	24.9	20.9	32.1
Tarija	30.3	43.1	36.1	16.1	33.6	40.8
Villamontes	54.7	68.9	16.3	12.1	29.0	19.0

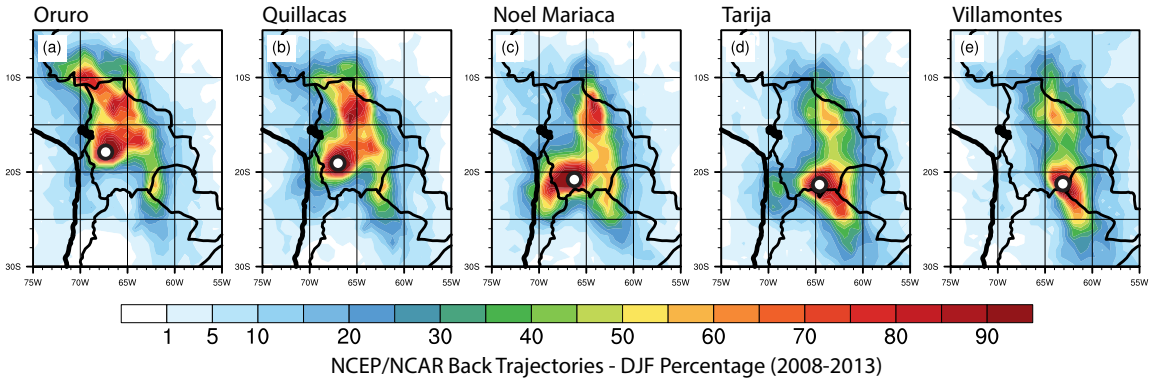

Figure 2.13. Composite DJF air source maps for five stations in this study using the NCEP/NCAR reanalysis [Kalnay et al., 1996]. Seven day back trajectories were launched at each station starting at 1500 m above ground level. Trajectories were binned to a 0.75° grid, and contours show the proportion of trajectories that pass through each grid cell. Air source pathways calculated using the NCEP/NCAR reanalysis are qualitatively similar to those calculated using ERA-Interim data [Dee et al., 2011].

References

Dee, D. P. et al. (2011), The ERA-Interim reanalysis: configuration and performance of the data assimilation system, *Quarterly Journal of the Royal Meteorological Society*, *137*(656), 553–597, doi:10.1002/qj.828.

Kalnay, E., M. Kanamitsu, and R. Kistler (1996), The NCEP/NCAR 40-year reanalysis project, *Bulletin of the American Meteorological Society, 77*(3), doi:10.1175/1520-0477(1996)0772.0.CO.

Appendix 2D. Normalized Monthly Back Trajectory Analysis and Bolivian High Position from ERA-Interim Winds

Table 2.15. Summary table of DJF monthly and seasonal average Bolivian High latitude and longitude, and areal mean back trajectory density for each subregion (unnormalized). For each month, the areal means are split into two columns, with the left column showing the calculation using all available back trajectories and the right column showing the calculation using only trajectories resulting in rain at the station as calculated by the ERA-Interim reanalysis dataset.

		December 2008		January 2009		February 2009		2008-09 Seasonal Average	
Bolivian High Latitude (°S)		15.0		15.0		18.8		16.2	
Bolivian High Latitude (°W)		63.0		61.5		60.0		61.6	
		All Trajectories	Precipitating Trajectories Only	All Trajectories	Precipitating Trajectories Only	All Trajectories	Precipitating Trajectories Only	All Trajectories	Precipitating Trajectories Only
Oruro	Yungas-Amazon Basin (YAB)	19.8	18.3	24.6	41.9	54.1	37.9	32.8	40.7
	South Pacific (SP)	67.5	73.5	64.5	53.1	42.2	58.8	59.3	55.4
	Gran Chaco (GC)	12.6	8.2	10.9	5.0	3.7	3.3	7.9	3.9
Quillacas	YAB	4.7	28.3	5.9	0.0	38.5	60.7	14.3	35.6
	SP	89.1	71.7	75.5	84.6	52.6	28.4	75.3	54.4
	GC	6.1	0.0	18.6	15.4	8.9	10.9	10.4	10.0
Noel Mariaca	YAB	0.0	0.0	3.8	0.0	38.6	52.9	11.8	48.0
	SP	89.1	20.0	78.7	0.0	55.5	22.1	77.2	15.5
	GC	10.9	80.0	17.5	100.0	5.9	25.0	11.0	36.5
Tarija	YAP	2.0	6.6	2.3	3.8	38.1	45.2	13.0	20.2
	SP	50.7	43.9	42.5	24.7	32.5	33.2	45.0	37.2
	GC	47.3	49.5	55.2	71.4	29.4	21.6	42.0	42.6
Villamontes	YAB	39.8	59.5	38.6	49.0	59.0	71.8	45.0	62.4
	SP	6.6	0.0	19.6	20.8	17.3	10.1	17.3	14.3
	GC	53.6	40.5	41.8	30.3	23.7	18.1	37.7	23.3

		December 2009		January 2010		February 2010		2009-10 Seasonal Average	
Bolivian High Latitude (°S)		15.8		16.5		18.8		16.9	
Bolivian High Latitude (°W)		62.3		63.0		63.8		63.0	
		All Trajectories	Precipitating Trajectories Only	All Trajectories	Precipitating Trajectories Only	All Trajectories	Precipitating Trajectories Only	All Trajectories	Precipitating Trajectories Only
Oruro	YAB	23.3	32.7	47.3	40.6	53.9	49.0	44.2	41.3
	SP	72.7	64.3	40.7	45.3	43.7	51.0	50.2	53.0
	GC	4.0	3.1	12.0	14.2	2.4	0.0	5.6	5.7
Quillacas	YAB	15.0	26.4	32.1	57.0	40.5	68.4	32.2	56.0
	SP	84.6	67.3	59.7	17.7	53.2	31.6	63.3	33.8
	GC	0.3	6.3	8.2	25.3	6.3	0.0	4.5	10.2
Noel Mariaca	YAB	11.4	0.0	7.8	0.0	18.2	55.2	11.8	47.0
	SP	88.6	100.0	76.8	22.6	64.5	32.0	77.3	32.8
	GC	0.0	0.0	15.5	77.4	17.3	12.8	10.9	20.2
Tarija	YAP	20.9	26.0	30.0	37.8	45.7	53.2	32.5	40.6
	SP	54.4	37.1	41.0	21.3	30.8	22.7	44.2	26.7
	GC	24.8	37.0	28.9	40.8	23.5	24.1	23.3	32.7
Villamontes	YAB	61.1	60.3	65.0	59.2	68.3	72.4	66.0	61.2
	SP	11.4	11.5	14.4	0.0	14.6	4.2	13.0	8.3
	GC	27.4	28.1	20.7	40.8	17.1	23.4	21.0	30.6

		December 2010		January 2011		February 2011		2010-11 Seasonal Average	
Bolivian High Latitude (°S)		19.5		19.5		21.0		20.0	
Bolivian High Latitude (°W)		58.5		69.8		63.8		64.0	
		All Trajectories	Precipitating Trajectories Only	All Trajectories	Precipitating Trajectories Only	All Trajectories	Precipitating Trajectories Only	All Trajectories	Precipitating Trajectories Only
Oruro	YAB	26.3	25.9	48.3	52.8	46.9	40.0	46.8	45.6
	SP	73.3	72.4	43.6	47.2	40.3	42.2	47.6	46.9
	GC	0.4	1.7	8.1	0.0	12.8	17.8	5.6	7.5
Quillacas	YAB	27.5	100.0	29.4	0.0	17.9	23.1	30.1	26.6
	SP	72.4	0.0	55.9	0.0	66.8	66.3	62.1	60.7
	GC	0.1	0.0	14.7	100.0	15.2	10.6	7.9	12.8
Noel Mariaca	YAB	25.7	100.0	25.6	100.0	23.0	33.5	26.3	44.3
	SP	73.9	0.0	65.1	0.0	59.0	43.6	65.9	35.8
	GC	0.4	0.0	9.4	0.0	18.0	22.9	7.8	19.8
Tarija	YAP	38.2	44.5	36.5	43.0	31.2	30.8	35.1	41.5
	SP	34.4	3.9	28.3	15.1	7.9	9.5	26.0	9.7
	GC	27.4	51.6	35.2	41.9	60.9	59.7	38.9	48.8
Villamontes	YAB	44.5	60.8	57.8	57.1	36.0	54.8	49.5	55.9
	SP	28.0	0.0	18.9	9.2	18.0	0.0	20.8	4.3
	GC	27.5	39.2	23.3	33.7	46.0	45.2	29.7	39.8

		December 2011		January 2012		February 2012		2011-12 Seasonal Average	
Bolivian High Latitude (°S)		12.8		14.3		21.0		15.9	
Bolivian High Latitude (°W)		63.8		65.3		66.0		64.3	
		All Trajectories	Precipitating Trajectories Only	All Trajectories	Precipitating Trajectories Only	All Trajectories	Precipitating Trajectories Only	All Trajectories	Precipitating Trajectories Only
Oruro	YAB	37.8	35.2	22.5	36.4	37.1	39.0	34.4	41.4
	SP	61.0	63.6	66.7	63.6	43.0	43.0	54.1	52.2
	GC	1.2	1.2	10.7	0.0	19.9	18.0	11.5	6.4
Quillacas	YAB	28.1	34.6	10.3	26.2	21.1	29.7	21.4	28.2
	SP	66.5	57.1	76.4	71.2	54.6	65.3	63.3	67.5
	GC	5.4	8.3	13.3	2.6	24.3	5.0	15.6	4.3
Noel Mariaca	YAB	12.0	0.0	2.0	0.0	20.2	13.7	13.9	21.1
	SP	67.0	0.0	80.4	62.5	53.3	35.4	65.4	31.4
	GC	21.0	100.0	17.6	37.5	26.5	50.9	20.7	47.5

		December 2012		January 2013		February 2013		2012-13 Seasonal Average	
Bolivian High Latitude (°S)		18.8		14.3		16.5		16.5	
Bolivian High Latitude (°W)		62.3		60.0		67.5		64.1	
		All Trajectories	Precipitating Trajectories Only	All Trajectories	Precipitating Trajectories Only	All Trajectories	Precipitating Trajectories Only	All Trajectories	Precipitating Trajectories Only
Oruro	YAB	41.3	34.9	59.5	61.7	48.6	65.9	45.6	50.7
	SP	58.7	65.1	29.8	0.0	47.3	33.4	50.6	40.2
	GC	0.0	0.0	10.7	38.3	4.1	0.7	3.8	9.1
Quillacas	YAB	33.4	38.8	41.2	37.9	39.6	61.1	35.3	40.1
	SP	61.1	52.0	41.4	29.3	55.7	38.9	56.6	42.4
	GC	5.5	9.2	17.5	32.9	4.7	0.0	8.0	17.5
Noel Mariaca	YAB	22.9	42.0	18.4	38.9	32.2	55.4	20.5	32.9
	SP	69.0	21.4	61.6	31.6	64.5	44.6	69.8	46.7
	GC	8.1	36.6	20.1	29.5	3.3	0.0	9.7	20.4

Chapter 3. Modern and long-term evaporation of central Andes surface waters suggests paleo archives underestimate Neogene elevations[2]

3.1 Abstract

Central Andean paleoelevations reconstructed from stable isotope and paleofloral data imply a large magnitude (>2 km) Miocene-to-modern surface uplift. However, the isotopic relationships between precipitation, surface waters, and soil waters upon which these reconstructions are based remain poorly constrained for both past, and in many cases, modern conditions. We quantify the relationships between central Andean precipitation and surface waters by measuring the isotopic composition of 249 stream water samples ($\delta^{18}O$ and δD) collected between April 2009 and October 2012. The isotopic compositions of stream waters match precipitation along the eastern flank. In contrast, Altiplano surface waters possess a lower δD-$\delta^{18}O$ slope (4.59 vs ~8 for meteoric waters) not observed in precipitation, which signals heavy isotope evaporative enrichment in surface waters. Paleoclimate models indicate that highly evaporative conditions have persisted on the plateau throughout Andean uplift, and that conditions may have been more evaporative when the Andes were lower. Thus, more ancient proxy materials may have a greater evaporative bias than previously recognized and paleoelevation reconstructions from stable isotope based central Andean plateau proxy materials likely overstate Miocene-to-present surface uplift. We propose Altiplano paleoelevations of 1-2 km at 24.5 Ma, 1.5-2.9 km by 11.45 Ma, and modern elevations by ~6 Ma based on the lightest isotopic compositions observed in Altiplano proxy materials, which are least likely to be influenced by evaporation. These constraints limit total late-Miocene-to-modern uplift to < 2.2 km, are more consistent with crustal shortening records, and suggest that plateau uplift may have been more spatially uniform than suggested by previous interpretations of stable isotope proxies.

2 Official citation: Fiorella, R.P.; C.J. Poulsen; R.S. Pillco-Zolá; M.L. Jeffery; and T.A. Ehlers (2015). Modern and long-term evaporation of central Andes surface waters suggests paleo archives underestimate Neogene elevations. Earth and Planetary Science Letters. doi: 10.1016/j.epsl.2015.09.045

3.2 Introduction

Mountain topography is an expression of subsurface tectonic processes and can present significant barriers to atmospheric circulation and biological dispersal. Elevation histories therefore have broad implications for understanding the geodynamic processes that promote orogenesis, reconstructing regional paleoclimates, and discerning spatiotemporal patterns of evolution. Stable isotope paleoaltimetry is one of the few quantitative methods available to reconstruct past elevations. Surface elevations and the stable isotopic composition of precipitation ($\delta^{18}O_p$ and $\delta^{2}H_p$ or δD_p) are related through atmospheric thermodynamics [e.g., *Rowley*, 2007]. Orographic lifting of an airmass results in adiabatic cooling and precipitation, which preferentially removes the heavy isotopes of water relative to the light isotopes [e.g., *Rozanski et al.*, 1993]. Progressive rainout along a trajectory leaves the precipitation from an airmass increasingly depleted in heavy isotopes at higher elevations. If surface water isotopic compositions mirror $\delta^{18}O_p$ or δD_p, proxy materials that form in contact with surface waters, such as pedogenic carbonate, authigenic clays, or hydrated volcanic glass, can be used to estimate paleoelevations [*Mulch and Chamberlain*, 2007; *Quade et al.*, 2007].

In the central Andes, changes in the stable isotope compositions of proxy materials through time have been interpreted to signify >2.0 km of uplift since the early-to-mid Miocene, with variable uplift timing along strike. From north to south, changes in stable isotope compositions of proxy materials have been taken to reflect uplift of the Altiplano by: (a) 2.2-3.7 km between 19-16 Ma at ~15°S [*Saylor and Horton*, 2014], (b) 2.5 ± 1.0 km between 10-6 Ma at ~18°S [*Garzione et al.*, 2006; 2008], and (c) 2.6 ± 0.7 km between 16-9 Ma at ~20°S [*Garzione et al.*, 2014]. Isotopic compositions from the Salla and Upper Salla Beds in the adjacent Eastern Cordillera at ~17°S have been interpreted to represent paleoelevations of 0.0-1.5 km at 29-24 Ma, ~2.5 km at 20-15 Ma, and ~4 km at 6 Ma [*Leier et al.*, 2013]. The spatial and temporal heterogeneity of surface uplift of the central Andean plateau inferred from stable isotope paleoaltimetry appears contrary to observations of broadly synchronous deformation between ~15-23°S that pre- and postdates the proposed uplift events [*Oncken et al.*, 2006; *Barnes and Ehlers*, 2009]. Deformation began at ~40 Ma and ceased at ~10 Ma in the Eastern Cordillera [*McQuarrie*, 2002; *McQuarrie et al.*, 2005], and propagated into the Bolivian Altiplano at ~30 Ma and ceased by ~7 Ma [*Lamb and Hoke*, 1997; *Elger et al.*, 2005]. Therefore, if these paleoelevation constraints are accurate, the uplift mechanism must allow for a substantial amount

of surface uplift from processes other than crustal thickening (e.g., via lithospheric mantle removal), and accommodate several million years of deformation without producing significant uplift.

Paleoclimate model simulations of Andean uplift challenge the assertion that isotopic changes in these proxy materials primarily record changes in surface elevation. Climate changes attendant to Andean uplift contribute to and may dominate the isotopic signal observed in proxy materials. These changes include an increase in precipitation rate, an intensification of convective precipitation, and a shift from in vapor source for the central Andes from primarily Pacific to Atlantic dominated [*Ehlers and Poulsen*, 2009; *Poulsen et al.*, 2010]. Abrupt, large (~5-6 ‰ in $\delta^{18}O_p$) isotopic changes occur when the Andes reach a threshold of 70-75% of their modern elevation, suggesting large isotopic change can occur in the absence of significant uplift [*Poulsen et al.*, 2010; *Insel et al.*, 2012]. Climate model simulations have generally used a simplified model of Andean uplift, where elevations are scaled as percentages of their modern elevation across the entire orogen. Despite their simplistic representation of uplift, these simulations demonstrate that uplift strongly alters continental climate and regional $\delta^{18}O_p$, and challenge the interpretation that proxy materials primarily record rapid surface uplift.

However, both the proxy and model based paleoaltimetry studies have assumed that changes in precipitation $\delta^{18}O$ or δD are fully reflected in proxy $\delta^{18}O$ or δD. This assumption may not be universally valid, as proxy materials ultimately acquire their isotopic composition from surface waters (e.g., in soils or streams) and not directly from precipitation. Stream waters reflect a spatially and temporally integrated signal of precipitation composition, and proxy materials forming in contact with these waters would therefore record the integrated composition of catchment precipitation. However, in arid regions, evaporation may enrich surface waters in heavy stable isotopes [e.g., *Kendall and Coplen*, 2001], and will undermine the relationship between elevation and $\delta^{18}O$ or δD.

The relationship between precipitation and surface water isotope compositions across the central Andes is poorly known due to temporally and spatially limited observations. One transect across the eastern Andes flank (~16°S) indicates a close match between stream water and precipitation $\delta^{18}O$ [*Bershaw et al.*, 2010], but this relationship may not hold across the strong climate and elevation gradients of the central Andes [e.g., *Garreaud et al.*, 2003]. Critically, until now, no stream water data were available for the central plateau to evaluate their relationship to

precipitation. To assess whether surface waters reflect precipitation across the central Andes (~17-22°S), we measured the isotopic compositions of 249 streams distributed across the Altiplano and its eastern flank. We then compared them to published values of regional precipitation $\delta^{18}O$ (Figure 3.1) [*Aravena et al.*, 1999; *Gonfiantini et al.*, 2001; *Fiorella et al.*, 2015]. We find that evaporation biases the isotopic composition of streams on the central Andean plateau to heavier isotope ratios than precipitation. In contrast, streams along the eastern flank generally do not exhibit this evaporative bias. If these heavier isotopic values across the plateau were preserved in proxy materials, the records would be interpreted to reflect elevations that are too low. Paleoclimate model simulations of Andean uplift indicate that regional conditions were more evaporative when elevations were lower, raising the concern that greater bias in older proxy materials has led to overestimations of Neogene uplift. Finally, we note that this interpretation of the stable isotope proxy record may resolve some of the controversy in uplift rates and magnitudes apparent across different approaches applied to the central Andes, and suggests that Andean plateau uplift may have been more synchronous than it may appear from stable isotope proxy records.

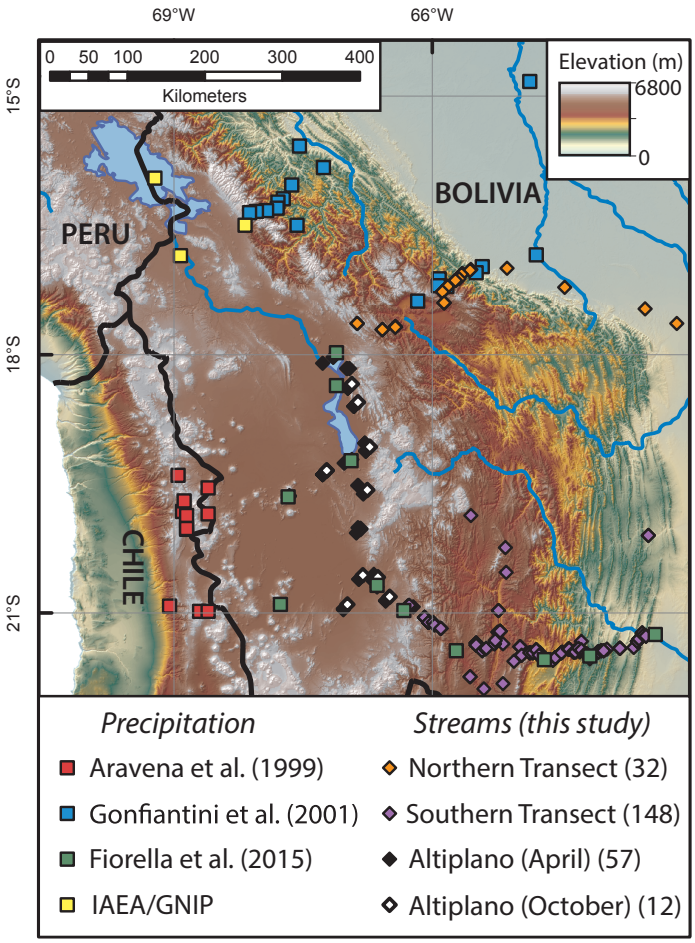

Figure 3.1. Geographic overview of compiled isotopic composition of precipitation (colored squares) and stream waters collected for this study (colored diamonds). Streams were collected in three separate physiographic regions: two elevation transects at ~17°S (orange diamonds) and ~21°S (purple diamonds), and streams entirely within the Altiplano (white diamonds were collected in April, black diamonds in October). Elevation data are from the ASTER DEM product (METI and NASA).

3.3 Methods

3.3.1 Stream water collection and analysis

We collected annual stream water samples across the Bolivian Altiplano and along two transects of its eastern flank (at ~17.5°S and ~21.5°S, Figure 3.1). Stream samples for the Altiplano and the southern transect were collected from April 2009 until May 2012; the northern transect was added in April 2010 and collected until May 2012. We also collected 12 stream samples in October 2012 to determine the seasonal variability of Altiplano surface waters. Samples were collected from streams by filling 20 mL glass vials completely to minimize headspace. The vials were then sealed with a poly-cone lid until analysis. Samples were collected at the end of the central Andes rainy season [April and May, *Garreaud et al.*, 2003] to capture

the integrated isotopic signal of rainy season precipitation [*Kendall and Coplen*, 2001]. Additionally, sampling at the end of the rainy season provides a record of surface water isotopic compositions coincident with soil drying and likely carbonate formation [e.g., *Breecker et al.*, 2009].

We measured isotopic compositions using a Picarro L2120-i Cavity Ringdown Spectrometer coupled to an A0211 high precision vaporizer and autosampler. Compositions are reported in delta notation as per mil deviations from VSMOW ($\delta = 1000(R_{sample}/R_{VSMOW} - 1)$, where R is the heavy to light isotope ratio) [*Coplen*, 1996]. Standard error is ~0.1 ‰ for δ18O and ~0.4 ‰ for δD. As spectroscopic isotope methods are sensitive to contamination by organic molecules, we monitored for sample contamination using the ChemCorrect software package (Picarro). Isotopic compositions presented are the mean values for at least eight analyses. For clarity in the following discussion, isotopic compositions of precipitation, surface waters, and pedogenic calcite are designated as δ_p, δ_w, or δ_{cc} respectively.

We calculated hypsometric mean catchment elevation and drainage areas using the Advanced Spaceborne Thermal Emission and Reflection Radiometer (ASTER, v.2) global digital elevation model (30 m resolution) (METI and NASA) and GIS software (ArcGIS 10). Stream sampling locations ranged from 230 m to 4430 m, corresponding to mean catchment elevations of 319 m to 4499 m. Catchment areas range from <1 km^2 to 61,840 km^2, with a median area of 12.1 km^2. In some low-relief cases, GIS drainage basin calculations were ambiguous. We verified GIS delineations of low-relief drainage basins using satellite imagery. In addition, we computed catchment mean annual precipitation and precipitation amount-weighted mean elevations with the Tropical Rainfall Monitoring Mission (TRMM) product 2B31 data [after *Bookhagen and Strecker*, 2008]. Precipitation weighted mean elevations were nearly identical to unweighted mean elevations. Stream water isotopic compositions, catchment elevations, and sampling dates are presented in Appendix 3A.

3.3.2 Prediction of catchment elevations from isotopic composition

We compare hypsometric mean elevations to predicted elevations from two different isotope-elevation models. First, we predicted elevations using a semi-empirical thermodynamic model that extracts low-latitude surface temperature and relative humidity over the oceans from reanalysis data to generate relationships between isotopic composition, condensation amount,

and surface elevation [*Rowley*, 2007]. The amount of condensate removed from an air parcel with increasing elevation is determined by the moist adiabat above the elevation where condensation begins. If all the condensate is removed as precipitation, δ_p follows Rayleigh fractionation [e.g., *Rozanski et al.*, 1993], and the difference in δ_p from its value at sea level is directly related to elevation. Where it reflects δ_p, δ_w follows the same relationship if catchment δ_p is also weighted hypsometrically. We use the quartic regression of Rowley [2007, equation 5] to estimate the hypsometric mean catchment elevations based on their isotopic compositions:

$$z_{\text{weighted mean}} = -0.0129\Delta\left(\delta^{18}\text{O}\right)^4 - 1.121\Delta\left(\delta^{18}\text{O}\right)^3 - 38.214\Delta\left(\delta^{18}\text{O}\right)^2 - 715.22\Delta\left(\delta^{18}\text{O}\right)$$

where $\Delta(\delta^{18}O)$ refers to the difference in $\delta^{18}O$ from its initial low-elevation value. We estimate initial δ_w values of -6.0‰ and -4.0‰ for streams sampled north and south of 20°S respectively, based on observations of low-elevation δ_p and δ_w [*Gonfiantini et al.*, 2001; *Fiorella et al.*, 2015]. This division both separates the two flank transects, and reflects differences in vapor transport to the northern and southern Altiplano [e.g., *Fiorella et al.*, 2015].

Second, we predicted catchment elevations using a linear regression between isotopic composition and elevation. Following the same logic employed for the semi-empirical thermodynamic model above, two separate linear regressions were produced for the northern and southern transect catchments to match observations of vapor transport to the Altiplano. We calculate a best-fit linear equation for the northern transect of (uncertainty on coefficients is 1σ):

$$elev\ (m) = -500.1 \pm 73.0\delta^{18}O - 2849.6 \pm 838.8$$
$$(r^2 = 0.61, 2\sigma\ prediction\ int. = 2000\ m)$$

and for the southern transect of:

$$elev\ (m) = -358.5 \pm 23.9\delta^{18}O - 477.1 \pm 214.1$$
$$(r^2 = 0.61, 2\sigma\ prediction\ int. = 1420\ m)$$

We predicted mean catchment elevations for all samples north (south) of 20°S with the northern (southern) transect equation. To assess whether our results were sensitive to the choice of linear model, we also calculated several alternate linear models based on different divisions of our stream dataset. We restricted our candidate models to those that account for the direction of vapor transport to the Altiplano. All alternate models exhibited a weaker fit based on r^2 and AIC values (Appendix 3B). The general conclusions from our analysis are not sensitive to the choice of the linear models when vapor source direction is accounted for (Appendix 3B).

For both the empirical and semi-empirical thermodynamic model predictions, we then calculated the residual between model predictions and GIS-derived elevations for each catchment. Where model predictions match measured elevations, the residual should approach zero.

3.3.3 Paleoclimate Model Simulations of Andean Uplift

Central Andean precipitation and evapotranspiration fluxes were evaluated throughout uplift using the climate modeling experiments of *Ehlers and Poulsen* [2009]. In these simulations, the elevation of the Andes is varied in 25% increments relative to modern in the Regional Climate Model (RegCM), version 3 [*Pal et al.*, 2007]. The horizontal resolution used in these simulations is ~60 km, which provides more realistic representation of Andean topography than typical resolutions for global models (>100 km). All other boundary conditions are specified at modern values to isolate the effect of topographic changes on continental climate.

We use model-derived monthly precipitation and evapotranspiration fluxes to constrain seasons of pedogenic carbonate formation. Pedogenic carbonates form when dissolved calcium ion concentrations are high and soil CO_2 concentrations are low, both of which occur when soils lose water [*Breecker et al.*, 2009]. Thus, we highlight months where evapotranspiration exceeds precipitation as periods of carbonate formation.

3.4 Results

3.4.1 Stream water isotopic compositions

Stream waters along both elevation transects are more depleted in heavy isotopes at high elevations than at low elevations (Figure 3.2). Isotopic compositions on the northern transect range from -6.56 ‰ (-41.62 ‰) to -14.86 ‰ (-110.87 ‰) for $\delta^{18}O_w$ (δD_w), and correspond to measured mean catchment elevations of 380 and 4499 m respectively. Isotopic compositions along the southern transect range from -1.77 ‰ (-24.25 ‰) to -15.82 ‰ (-112.89 ‰) for $\delta^{18}O_w$ (δD_w), and correspond to mean catchment elevations of 2300 and 4050 m, respectively. Stream water compositions exhibit a larger isotopic range on the Altiplano than on the eastern flanks (Figure 3.2). Altiplano $\delta^{18}O_w$ (δD_w) values vary from 5.44 ‰ (-18.73 ‰) to -16.38 ‰ (-123.60 ‰). Both extreme values for the Altiplano occur in catchments with mean elevations exceeding 3800 m.

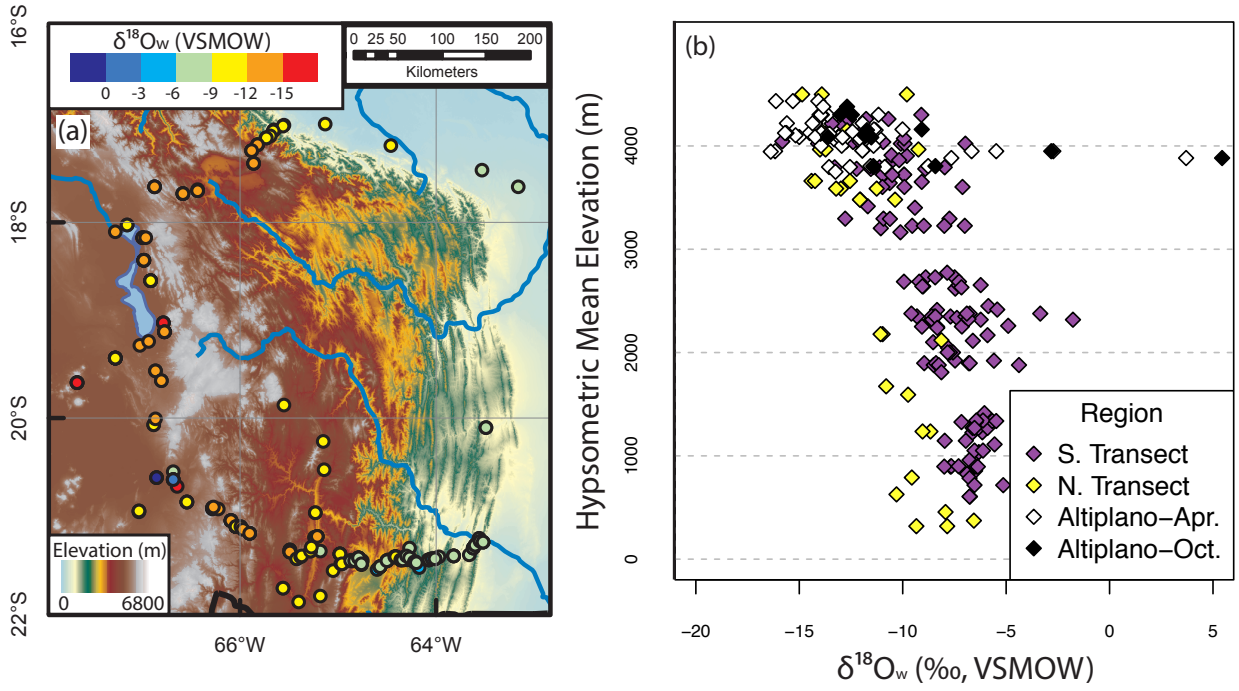

Figure 3.2. Spatial distribution of the $\delta^{18}O_w$ of central Andes stream waters. (a) Map view of collected stream waters. Colored circles denote each stream sample, with blue (red) indicating the compositions least (most) depleted in ^{18}O. (b) Scatter plot of $\delta^{18}O_w$ of central Andes stream waters versus hypsometric mean elevation (m). Higher elevation catchments tend to have more negative isotopic compositions for elevations below 3500 m. On the Altiplano above 3500 m, however, compositions are more variable. Standard errors for $\delta^{18}O_w$ are ~0.1 ‰.

Multivariate least-squares linear regression (see Appendix 3B for methods) between $\delta^{18}O_w$ and geographic variables indicates significant ($p < 0.05$) associations of $\delta^{18}O_w$ with elevation and sampling latitude across all sampled streams (Table 3.4). A similar best model emerges when only flank catchments are considered (Table 3.5). When only Altiplano stream $\delta^{18}O_w$ is considered, the best model retains elevation and annual precipitation, but not latitude, as predictor variables (Table 3.6). However, the preferred model for Altiplano $\delta^{18}O_w$ only describes a small portion of the observed variance ($r^2 = 0.322$).

3.4.2 Isotopic Lapse Rates and Elevation Catchment Predictions

Isotopic lapse rates along the two transects, determined by univariate linear regression, differ from year to year (Table 3.1). Northern transect $\delta^{18}O_w$ lapse rates vary from -0.79 ± 0.31 ‰/km in 2010 to -1.66 ± 0.16 ‰/km in 2011. Southern transect $\delta^{18}O_w$ lapse rates are generally larger in magnitude, and vary from -1.52 ± 0.32 ‰/km in 2010 to and -1.77 ± 0.14 ‰/km in 2012. Other portions of the eastern Andean flank exhibit similar isotopic lapse rates in both stream waters and precipitation, though all archives exhibit substantial interannual variability

(Table 3.1) [*Gonfiantini et al.*, 2001; *Bershaw et al.*, 2010; *Rohrmann et al.*, 2014; *Fiorella et al.*, 2015].

GIS-derived mean catchment elevations were compared to predictions from δ_w using two models of the isotope-elevation relationship. Both the semi-empirical thermodynamic model [*Rowley*, 2007] and locally calculated empirical linear regressions produce overestimates of the true elevation of low-elevation (< 2000 m) catchments, and both models also underestimate the true elevation of high-elevation catchments for both the northern and southern transects (Figure 3.3a-d), similar to observations further north in the Eastern Cordillera [*Saylor et al.*, 2009]. For the semi-empirical thermodynamic model, this pattern is more pronounced in the northern transect than in the southern transect. Half of the predictions from catchments below 1000 m in the northern transect overestimate their true elevation by more than 1000 m, and all ten of the predicted elevations for catchments below 2000 m are higher than their actual elevation (Figure 3.3c). The linear empirical model produces a similar trend in the residuals that is approximately equal for both transects (Figure 3.3d). At high elevations, model predictions tend to underestimate measured elevations, most notably on the plateau (Figure 3.3a-d).

Model predicted elevations appear to perform well along the flanks when considered as a distribution. For the *Rowley* [2007] model, the mean residuals between predicted and observed catchment elevations are 20 m and -140 m for the northern and southern transects respectively, and the most frequent values inferred from the distributions are both within ±200 m of zero (Figure 3.3e). The mean residual for the flank distributions in both linear regression models is ~0 m. Distribution mean residuals for both models are low on the flanks, with overestimations at low elevations are counterbalanced by underestimations at high elevations, resulting in distributions that appear normal and centered near zero. In contrast, residuals for Altiplano streams are skewed toward negative values, with several predictions underestimating measured catchment elevations by > 2.0 km (Figure 3.3ef). For both models, substantially more than half of the elevation predictions for Altiplano catchments have residuals below zero (79% Rowley, 65% linear empirical), indicating that Altiplano catchment elevations are poorly described by both models.

Table 3.1. Compilation of central Andes eastern flank isotopic lapse rates.

Stream Waters					
Latitude	**Year**	**Mean Catchment Elevation Range (m)**	**Sample Count**	**$\delta^{18}O$ Lapse Rate (‰/km)**	**Reference**
15°S	2004	829-4683[a]	36	-1.90 ± 0.08	Bershaw et al. 2010
15°S	2005	408-4823[a]	46	-1.53 ± 0.06	Bershaw et al. 2010
15°S	**all**	**408-4823[a]**	**82**	**-1.67 ± 0.05**	**Bershaw et al. 2010**
17.5°S	2010	456-4499	9[b]	-0.79 ± 0.31	this study
17.5°S	2011	319-4499	10[b]	-1.66 ± 0.16	this study
17.5°S	2012	319-4499	11[b]	-1.24 ± 0.11	this study
17.5°S	**all**	**319-4499**	**30[b]**	**-1.15 ± 0.18**	**this study**
21°S	2009	784-4301	45[b]	-1.76 ± 0.18	this study
21°S	2010	895-4261	29[b]	-1.52 ± 0.32	this study
21°S	2011	373-4116	33[b]	-1.69 ± 0.14	this study
21°S	2012	606-4261	43[b]	-1.77 ± 0.14	this study
21°S	**all**	**373-4301**	**150[b]**	**-1.67 ± 0.11**	**this study**
22-24°S	2010	701-4416	14[c]	-1.93 ± 0.34	Rohrmann et al. 2014
22-24°S	2011	3069-4197	11	-0.23 ± 0.63	Rohrmann et al. 2014
22-24°S	2012	3623-4013	7	-5.46 ± 1.21	Rohrmann et al. 2014
22-24°S	2013	625-4326	17	-1.35 ± 0.27	Rohrmann et al. 2014
22-24°S	**all**	**625-4416**	**49**	**-1.69 ± 0.17**	**Rohrmann et al. 2014**
24-26°S	2010	1236-4587	11	-0.23 ± 0.29	Rohrmann et al. 2014
24-26°S	2011	1856-4006	12	-0.63 ± 0.68	Rohrmann et al. 2014
24-26°S	2012	1112-4836	77	-1.09 ± 0.12	Rohrmann et al. 2014
24-26°S	**all**	**1112-4836**	**100**	**-0.88 ± 0.12**	**Rohrmann et al. 2014**
26-28°S	2011	340-4437	83	-0.21 ± 0.09	Rohrmann et al. 2014
26-28°S	2012	1647-3764	4	0.14 ± 0.69	Rohrmann et al. 2014
26-28°S	**all**	**340-4437**	**87**	**-0.21 ± 0.09**	**Rohrmann et al. 2014**
Precipitation Samples					
Latitude	**Year**	**Station Elevation Range (m)**	**Number of stations**	**$\delta^{18}O$ Lapse Rate (‰/km)**	**Reference**
15°S	1983	200-5200	12	-1.5 ± 0.2	Gonfiantini et al. 2001
15°S	1984	200-5200	12	-2.4 ± 0.2	Gonfiantini et al. 2001
17.5°S	1985	405-3220	7	-1.6 ± 0.2	Gonfiantini et al. 2001
21°S	2008[d]	395-4340	5	-1.2 ± 0.8	Fiorella et al. 2015 (chapter 2)
21°S	2009	395-4340	5	-2.0 ± 0.3	Fiorella et al. 2015 (chapter 2)
21°S	2010	395-4340	5	-2.2 ± 0.2	Fiorella et al. 2015 (chapter 2)
21°S	2011[e]	395-4340	5	-1.3 ± 0.4	Fiorella et al. 2015 (chapter 2)

a: Published elevations were given as sampling elevations, not mean catchment elevations.
b: Includes only flank catchments that are not within the internally-drained Altiplano
c: Sample W10-PUR02 removed from regression due to excessive evaporation, as in Rohrmann et al., 2014.
d: Precipitation samples collected from September-December only.
e: Precipitation samples collected from January-September only.

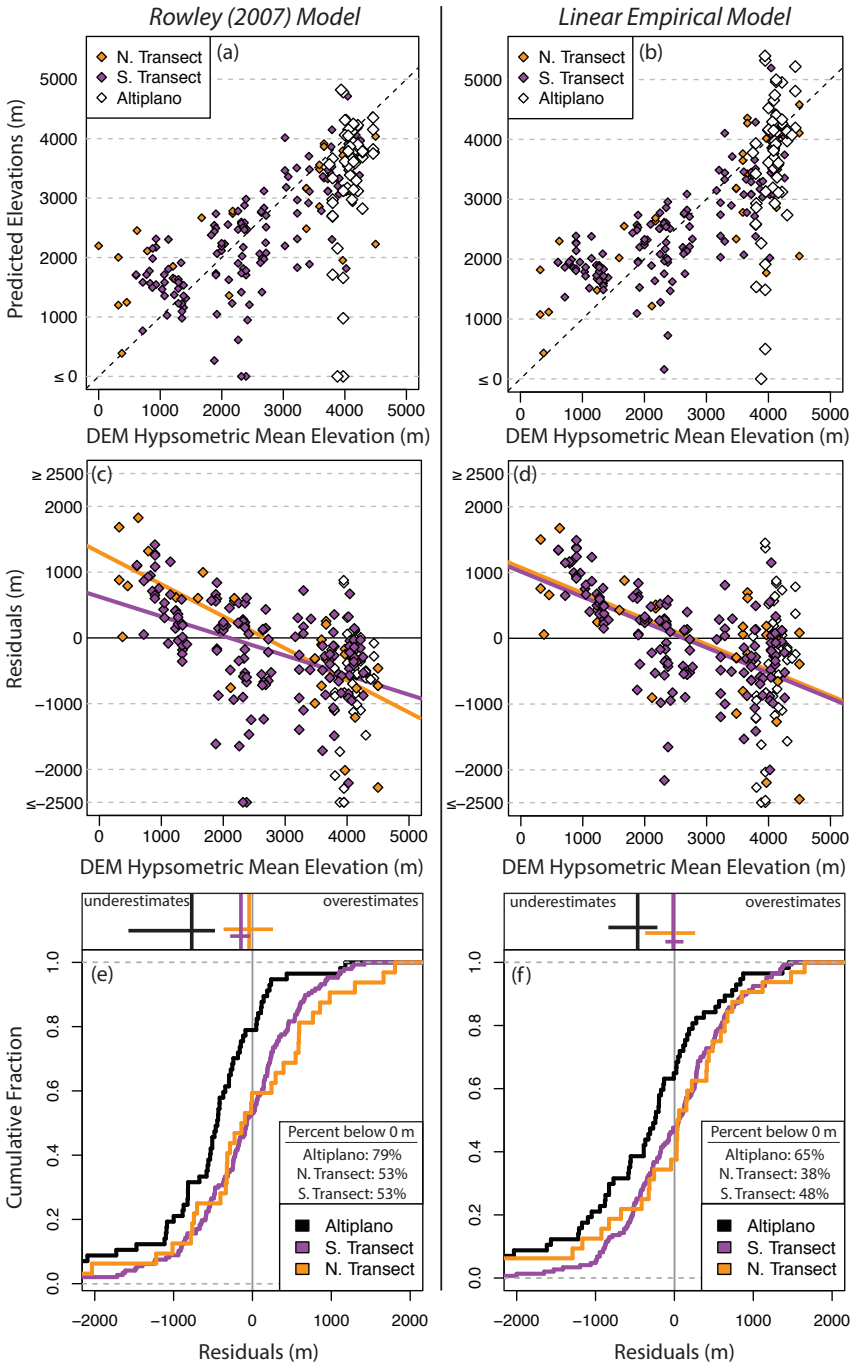

Figure 3.3. Comparison of measured and model predicted catchment elevations for the Rowley semi-empirical thermodynamic model (2007, left column) and a linear empirical model (right column). (a,b) Direct comparison between predicted and measured elevations by physiographic region. Elevation predictions deviate from model expectations by >3000 m at several of the highest elevation Altiplano catchments. (c,d) Residual between prediction and measurement. The best-fit line is plotted for the north (orange) and south (purple) transects. (e,f) Empirical cumulative distribution functions of residuals between predicted and measured elevations. Residuals for the two elevation transects are both normally distributed and centered around zero. Stream waters on the Altiplano, however, are consistently biased to predict lower-than-observed elevations, and skewed toward multi-kilometer underestimation and away from overestimation. Distribution mean values are shown as vertical lines above the distributions, and 95% confidence intervals based on 50,000 bootstrap replicates with replacement are shown as horizontal lines.

3.4.3 Central Andes Precipitation and Evapotranspiration Rates through Uplift

When the Andes are low (0-25% of modern elevations), RegCM simulations estimate a higher evapotranspiration to precipitation (E/P) ratio in the central Andes, and thus more arid conditions (Figure 3.4ab) [*Ehlers and Poulsen*, 2009]. In contrast, when the Andes exceed 50% of their modern elevations, regional aridity decreases, most markedly along the flanks (Figure 3.4cde). Predicted precipitation rates for the Altiplano region [defined as the 126 grid cells within the red polygon in Figure 3.4a-e, after *Isacks*, 1988; *McQuarrie et al.*, 2005] increase from 0.86 mm/day at 0% of modern elevations to 6.61 mm/day at 100% of modern elevations (Figure 3.4f). Evapotranspiration rates also increase during Andean uplift, but not at every stage. Mean evapotranspiration rates more than triple between 0% (0.78 mm/day) and 75% of modern elevations (2.85 mm/day) (Figure 3.4g). Increased water availability from additional precipitation and an increase in shortwave radiation associated with a higher elevation surface fuels the higher evapotranspiration rates. Continued uplift above 75% of modern elevations decreases evapotranspiration rates slightly (to 2.62 mm/day, Figure 3.4g), which is consistent with lower surface temperatures and higher relative humidity. Together, these trends indicate that the average E/P ratio decreases in the region throughout uplift, but also becomes more spatially variable as shown by the increasing range of values (Figure 3.4h).

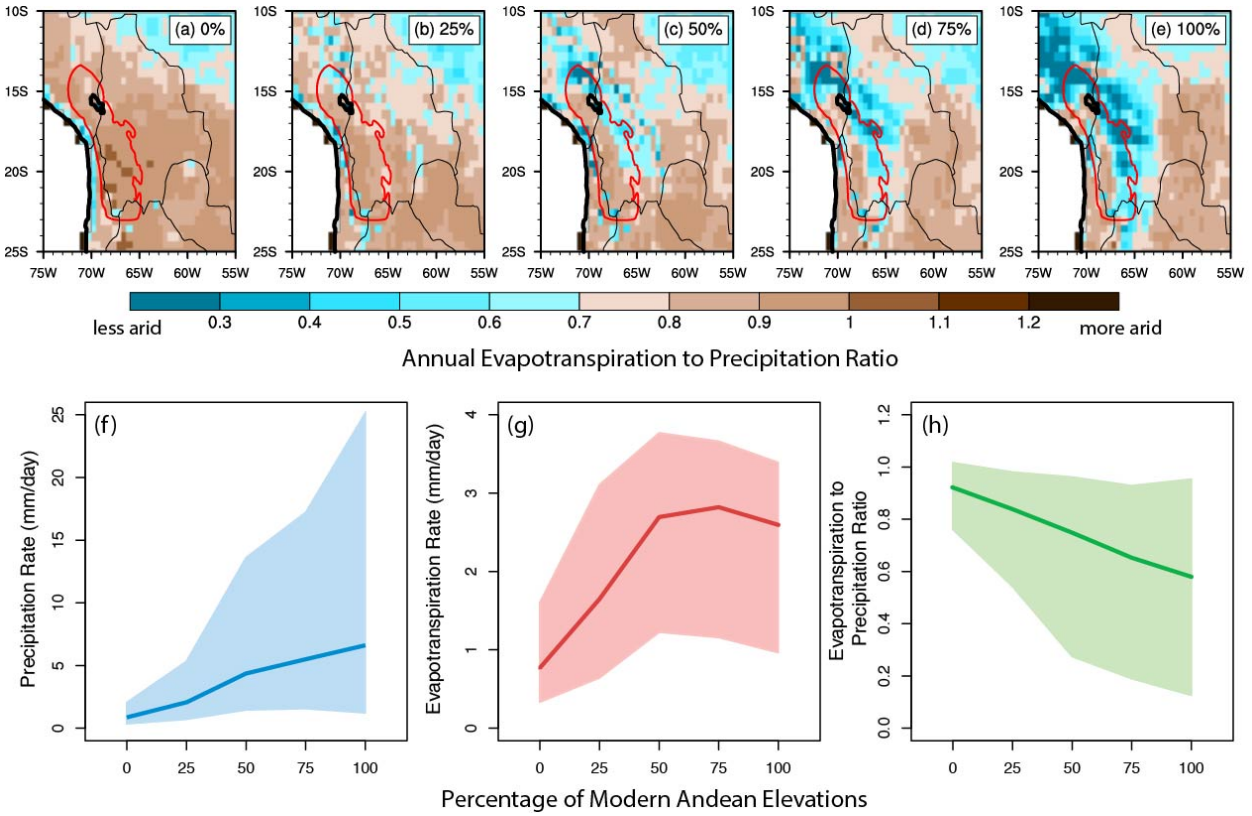

Figure 3.4. Climate model predicted regional mean precipitation and evapotranspiration rates through Andean uplift. (a)-(e). Evapotranspiration to precipitation ratio across the central Andes region, with elevations increasing from 0% to modern in 25% increments from (a) to (e). Higher values (shown as progressively more brown) indicate increasingly arid conditions. Throughout uplift, the central Andes region becomes progressively less arid throughout uplift, but with stronger spatial gradients effected by topography. Annual precipitation (mm/day) (f), evapotranspiration (mm/day) (g), and evapotranspiration to precipitation ratio (unitless) (h) are also shown, with the range shown for all the model grid cells in the Altiplano region (defined as red outlined area in (a)-(e)). Areal mean values are shown as a heavy line in (f)-(h), and 2σ variability indicated by the shaded polygon. Andean uplift results in increases in both precipitation and evapotranspiration, but a decrease in the evapotranspiration to precipitation ratio as precipitation rates increase by a greater amount.

3.5 Interpretation of the modern δ_w distribution

Elevation provides a dominant control on central Andes $\delta^{18}O_p$ [*Gonfiantini et al.*, 2001; *Fiorella et al.*, 2015]. Stream water $\delta^{18}O$ compositions generally preserve the relationship between $\delta^{18}O_p$ and elevation along the flanks (Figure 3.5ab), while on the Altiplano we observe substantial variability in $\delta^{18}O_w$ not observed in $\delta^{18}O_p$ (Figure 3.5c). The spread in Altiplano δ_w cannot be explained by catchment elevations, as both extreme values occur in catchments with mean measured elevations of > 3800 m. Instead, these trends imply that different processes govern the isotopic composition of surface waters on the Altiplano compared to its eastern flank.

To investigate this possibility, we compare the $\delta^{18}O_w$-δD_w relationship of flank and Altiplano streams to the $\delta^{18}O_p$-δD_p relationship for published precipitation values [*Aravena et al.*,

1999; *Gonfiantini et al.*, 2001; *Fiorella et al.*, 2015] (Figure 3.6). The $\delta^{18}O$-δD relationship reflects the integrated condensation and evaporation history of the water pool, and the Altiplano $\delta^{18}O_w$-δD_w relationship should differ from the flanks if different processes control the isotope distribution in the two regions. Regional precipitation shows a consistent $\delta^{18}O_p$-δD_p relationship (Figure 3.6a) that falls along the global meteoric water line (GMWL, black line in each panel of Figure 3.6) [*Rozanski et al.*, 1993]. Transect δ_w values also follow the GMWL (Figure 3.6b); however, Altiplano δ_w values follow a distinctly shallower slope (Figure 3.6c, slope = 4.59 ± 0.11), which is consistent with evaporation of Altiplano surface waters. Evaporation also decreases the deuterium excess of natural waters (d-excess = δD-$8\delta^{18}O$), as kinetic fractionation during evaporation results in a stronger fractionation between ^{18}O and ^{16}O relative to that between D and H [e.g., *Rozanski et al.*, 1993]. The global average d-excess in precipitation implied by the GMWL is ~10 [*Rozanski et al.*, 1993], though d-excess in central Andes precipitation has been observed to range between 14-20 [*Gonfiantini et al.*, 2001; *Fiorella et al.*, 2015]. If we characterize any stream water sample with a d-excess value below 5 as evaporated, 68% of Altiplano stream samples exhibit evaporation (April only, 74% including October samples), compared to only 13% of catchments along both elevation transects. Evaporation does not appear to occur during precipitation as a subcloud process [e.g., *Rohrmann et al.*, 2014], as Altiplano precipitation does not have low d-excess values comparable to the stream waters [*Fiorella et al.*, 2015]. Therefore, evaporation of surface waters must occur following rainout, promoting the different $\delta^{18}O$-δD relationship observed between Altiplano precipitation and stream waters.

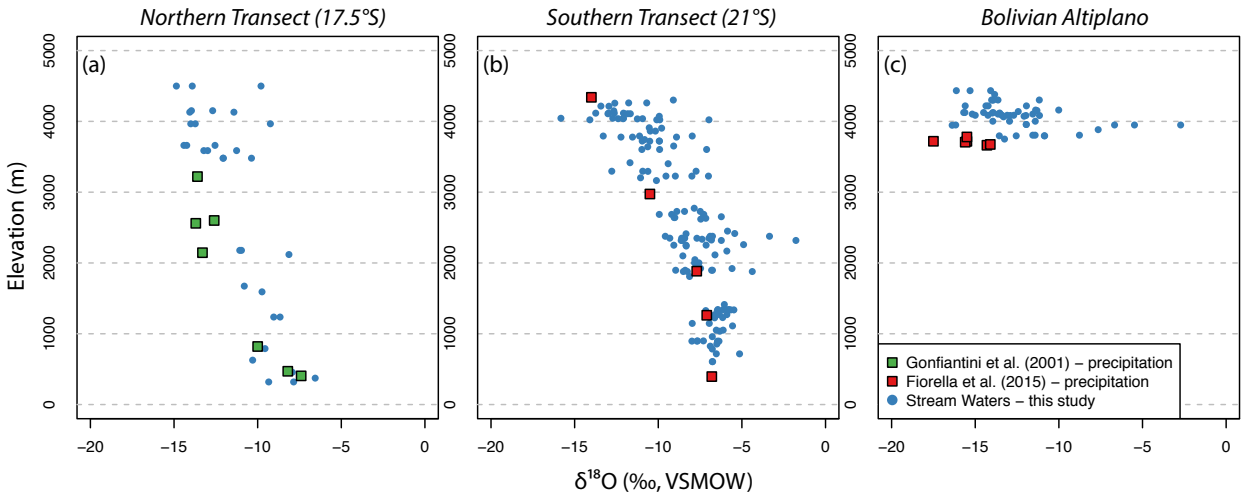

Figure 3.5. Scatter plots of the isotopic composition of precipitation and stream waters compared to elevation along the northern transect (a), southern transect (b), and Altiplano (c) regions. Precipitation compositions are plotted at the station elevation, while stream elevations are plotted as catchment mean elevations. Precipitation and stream water samples show similar relationships between $\delta^{18}O$ and elevation along the flanks (a and b), but show different relationships on the Altiplano (c) due to evaporative enrichment of the heavy isotopes in stream waters that is not observed in precipitation.

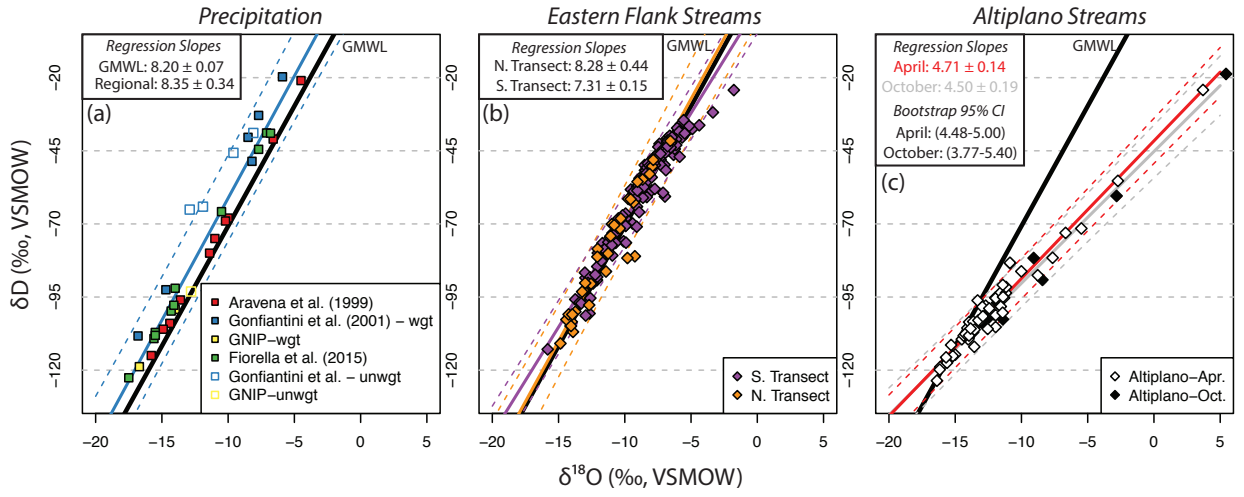

Figure 3.6. δD versus $\delta^{18}O$ for compiled precipitation data (a), streams along the eastern flank (b), and streams contained within the Altiplano (c). The Global Meteoric Water Line [GWML, Rozanski et al., 1993] is plotted in (a)-(c) for reference and represents a global composite of the δD-$\delta^{18}O$ relationship for precipitation. In (a), filled symbols represent precipitation amount-weighted averages. Open symbols represent stations where precipitation measurements were not available; thus, these represent unweighted averages of delta values. Regression slope and uncertainties (2σ) are shown in the inset, and the best-fit line and 2-sigma prediction interval is plotted for each region and water type. For (c), 95% confidence intervals of the slope are calculated separately for April and October using 50,000 bootstrap replicates with replacement. Precipitation (a) and flank stream (b) compositions plot closely to the GMWL, while streams on the Altiplano (c) follow a lower slope line (shown in red for April, gray for October). This lower slope line is characteristic of evaporation.

Evaporation of Altiplano surface waters biases model predictions to lower elevations, and is responsible for the biased distribution observed (Figure 3.3ef). The most evaporated Altiplano stream waters, which have the heaviest compositions, yield elevation predictions that are below sea level (Figure 3.3ab). These predictions clearly demonstrate the potential of evaporation to impair elevation estimates. Though the most frequently observed Altiplano residuals occur between -250 and -750 m, the influence of the most evaporated streams lowers the mean Altiplano residual to -840 m for the Rowley model (Figure 3.3e), and -460 m for the linear empirical model (Figure 3.3f). In contrast, since evaporation is only observed in a small fraction of samples along the flank, these distributions are not systematically biased toward lower elevations (Figure 3.3ef). However, a trend in the residuals along the flank remains (Figure 3.3cd), where low (high) elevation catchments tend to have elevation predictions that are too high (low). We note two potential reasons for this relationship. First, prior climate modeling experiments have suggested that the isotopic lapse rate is not linear for all elevations, and varies in time and space due to variability in convective precipitation and entrainment of vapor from other vertical levels in the atmosphere [*Insel et al.*, 2012]. Second, low-elevation isotopic compositions at the eastern Andean flank are highly variable from year-to-year, and are closely related to convective and precipitation intensity over the Amazon Basin [e.g., *Fiorella et al.*, 2015]. Regardless, only the plateau catchments show substantial evidence of evaporation (Figure 3.6), lower d-excess values, higher δD_w and $\delta^{18}O_w$ values than anticipated for their elevation (Figure 3.5-6), and ultimately, a physical basis for elevation underestimation.

We find limited evidence for other potential explanations for the spatial pattern of evaporation on the plateau. For example, relationships between Altiplano $\delta^{18}O_w$ and catchment area ($r^2 = 0.02$), latitude ($r^2 = 0.16$), and longitude ($r^2 = 0.01$) are weak; thus, basin size and position are unlikely explanations for variability on the Altiplano (Table 3.6). Furthermore, the lower slope observed for Altiplano surface waters does not result from a few highly influential evaporated streams. Resampling of the Altiplano stream waters to remove the ten most evaporated streams yields a slope of 5.35 ± 0.25 (compared to 4.59 ± 0.11 with all streams), which is still much lower than the anticipated value of ~8 for unevaporated meteoric waters. Wide isotopic variations in Altiplano surface waters indicate variability in evaporative intensity. For example, the most evaporated surface waters exhibit isotopic compositions heavier than

measured Altiplano $\delta^{18}O_p$ by > 10 ‰ [*Fiorella et al.*, 2015], while stream waters that are less affected by evaporation may have isotopic compositions within 1 ‰ of $\delta^{18}O_p$.

3.6 Discussion

3.6.1 Evaporative Imprint on Proxy Materials and Elevation Reconstructions

Spatially variable evaporative intensity on the plateau provides the most direct explanation for the large range of Altiplano δ_w and the lower slope $\delta^{18}O$-δD relationship. The occurrence of large salt flats, such as the *Salar de Uyuni,* provide evidence for significant evaporation on the modern Altiplano. If evaporated surface waters propagate to proxy bearing soil horizons, proxies forming in equilibrium with these soil waters will record compositions heavier than precipitation. Interpretations from these proxy materials will be prone to underestimate elevation because of the heavier compositions recorded. Therefore, we consider lighter isotopic compositions to be stronger evidence for high elevations than heavier isotopic compositions are for low elevations.

Many, but not all, paleoaltimetry studies have sought to sample below 50 cm in paleosols based on theoretical and experimental observations that evaporation from the surface has minimal direct impact on soil water isotopes below this depth (Appendix 3C) [e.g., *Quade et al.*, 2007]. However, mixing of partially evaporated near-surface soil water with infiltrating precipitation promotes indirect enrichment of heavy isotopes in deeper soil waters [*Mathieu and Bariac*, 1996; *Breecker et al.*, 2009]. Observations in arid soils indicate that soil waters deeper than 50 cm can be up to ~7‰ heavier in $\delta^{18}O_w$ than annual mean $\delta^{18}O_p$ [*Hsieh et al.*, 1998; *Breecker et al.*, 2009]. Thus, soil waters below the 50 cm threshold may still exhibit evaporative bias relative to mean annual δ_p. Alternating 3-4 day periods of sun followed by convective rain are typical during the central Andes rainy season [*Garreaud et al.*, 2003]. This intermittent precipitation on the Altiplano during the rainy season allows for surficial waters to evaporate between storms. These evaporated surface waters may mix with subsequent rains, which would push partially evaporated waters to lower depths in the soil, and bias soil water isotopic compositions to heavier values than precipitation.

If we assume δ_w reflects the composition of surficial soil waters, we can make an order-of-magnitude estimate of the evaporative bias in deeper soil waters. We assume that the soil water in carbonate forming horizons is a mix of 70% unevaporated precipitation and 30%

shallow, evaporated soil waters. This partitioning is based on observations from African soils in a similar hydroclimate [*Mathieu and Bariac*, 1996]. For example, surface water shifts of 2.0 and 5.0‰ relative to precipitation would result in soil waters in carbonate forming horizons that are 0.6-1.5‰ more positive than $\delta^{18}O_p$. Based on modern precipitation lapse rates [*Gonfiantini et al.*, 2001; *Fiorella et al.*, 2015], carbonates forming from these soil waters would record compositions associated with ~1 km lower surface elevations due solely to the isotopic offset between precipitation and soil water. The magnitude of this bias depends on the fraction of surficial waters mixing with deeper soil waters, which in turn, depends on soil properties, climate, and vegetation [*Mathieu and Bariac*, 1996]. Soils where more (less) than 30% of total soil water in carbonate forming horizons from evaporated shallow soil waters will exhibit a larger (smaller) evaporative bias. Changes in soil properties through time may be difficult to determine, but paleoclimate model simulations can constrain changes in the net evaporation through time.

3.6.2 Intensity and Seasonality of Net Evaporation During Uplift

Several lines of geological evidence, in addition to climate model results, support arid conditions in the ancient central Andes. Evaporite sequences are observed in adjacent Atacama sediments from the end Triassic onward [e.g., *Clarke*, 2006]. In the Altiplano, evaporites are observed from ~15 Ma, and have been taken as evidence for the development of internal drainage [*Alonso et al.*, 1991; *Vandervoort et al.*, 1995]. The absence of evaporates prior to ~15 Ma may therefore reflect that the Altiplano was an externally drained basin, and does not necessarily suggest the region was less arid prior to this time. The central Andes lie in the dry subtropics, where moisture convergence and precipitation formation are inhibited by strong atmospheric subsidence. South America has not changed latitude significantly since the Triassic [e.g., *Gurnis et al.*, 2012], and therefore, the central Andes have been in a region of strong atmospheric subsidence throughout the Cenozoic. Andean uplift promotes the development and strengthening of the South American Low Level Jet, increasing moisture convergence and precipitation on the eastern flank of the central Andes, and resulting in less arid conditions [*Insel et al.*, 2010]. Ultimately, a higher E/P ratio early in the uplift of the Andes implies a larger magnitude evaporative bias in more ancient proxy materials.

Surface uplift also changes the seasonality of aridity, which we expect to change the seasonal timing of pedogenic carbonate formation (Figure 3.7) [e.g., *Peters et al.*, 2013]. This change in carbonate formation timing will influence both the $\delta^{18}O_{cc}$ value and the formation temperature inferred from clumped isotope thermometry (Δ_{47} compositions for pedogenic carbonates). Dry conditions that follow the rainy season in the central Andes during austral fall and winter likely instigate modern pedogenic carbonate formation. However, paleoclimate models suggest a later termination of the rainy season when the Andes are at low elevations (≤ 25% of modern), with evapotranspiration rates exceeding precipitation rates starting in May compared to April when the mountains are higher (Figure 3.7a). This result suggests that when plateau elevations were lower, carbonate formation was shifted later in the year. However, this effect was unlikely to be constant throughout the Altiplano, as the transition to an earlier onset of the dry season associated with uplift is less pronounced north of 17°S (Figure 3.7b), and more pronounced south of 17°S (Figure 3.7cd). As both soil temperature and $\delta^{18}O_w$ contribute to $\delta^{18}O_{cc}$, the shift to earlier carbonate formation would bias $\delta^{18}O_{cc}$ and Δ_{47} toward summer temperatures and $\delta^{18}O_w$.

Finally, the number of annual carbonate precipitation periods may have changed during Andean surface uplift. The modern evapotranspiration rate exceeds the precipitation amount for a single extended period (April-September). A similar pattern is observed when the Andes are at least 50% of their modern elevations (Figure 3.7a). Thus, pedogenic carbonates would form only during April-September when the Andes exceed 50% of modern elevations. In contrast, when the Andes are below 50% of their modern elevations, evapotranspiration exceeds precipitation both before (e.g., October-December) and after the rainy season (e.g., May-August), suggesting two distinct periods of possible carbonate growth. With two seasons of carbonate formation, the bulk carbonate composition would record a mixture of both dry and rainy season soil waters and soil temperatures. Modern precipitation during the dry season can exhibit $\delta^{18}O_p$ that is >5‰ more positive than rainy season $\delta^{18}O_p$ [*Gonfiantini et al.*, 2001; *Fiorella et al.*, 2015]. Using the same logic as above to estimate soil water $\delta^{18}O$, dry season soil waters would be >1.5‰ more positive than rainy season soil waters. Applying modern isotopic lapse rates to this difference in seasonal soil water compositions indicates that pedogenic carbonates forming in equilibrium with dry season soil waters would further underestimate elevations by ~1 km. Additionally, if carbonate precipitation occurs during both the summer and winter while elevations are low before

transitioning to winter-only formation when elevations are high, low elevation samples will be biased to lower Δ_{47} values, resulting in artificially warm temperatures. This reflects both the higher formation temperatures during the summer and due to non-linear effects in Δ_{47} values resulting from the homogenization of summer and winter carbonate values during analysis [*Defliese and Lohmann*, 2015].

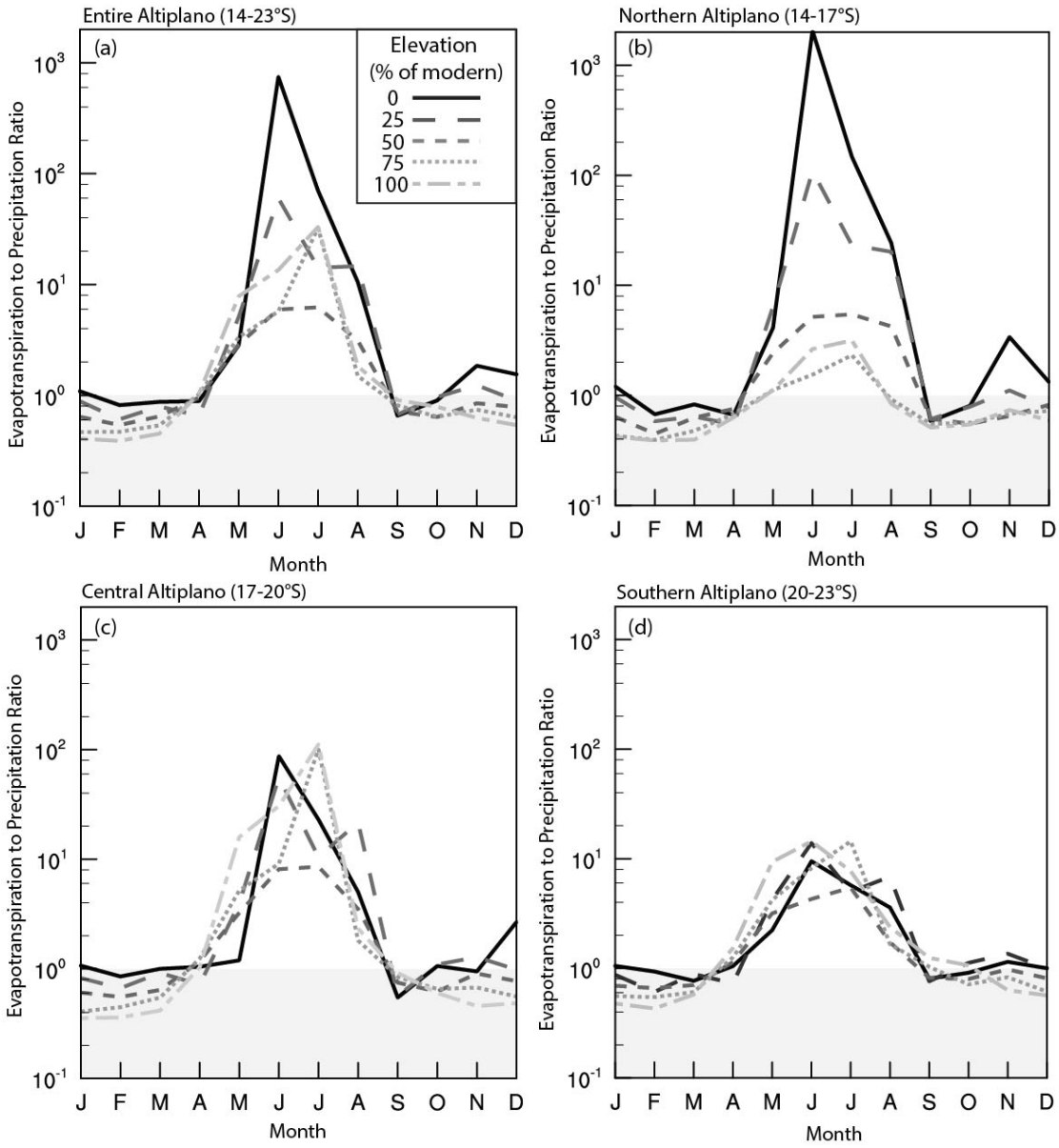

Figure 3.7. Monthly evapotranspiration to precipitation ratios for each climate model scenario for the entire Altiplano (a, 14-23°S), the northern Altiplano (b, 14-17°S), the central Altiplano (c, 17-20°S), and the southern Altiplano (d, 20-23°S). At higher elevations (>50%), evapotranspiration exceeds precipitation from April to September. In contrast, at lower elevations (<50%), evapotranspiration exceeds precipitation during two distinct periods (May-August, October-December). These changes in the annual hydrologic budget imply that the timing of pedogenic carbonate formation may have changed throughout the uplift and complicates direct comparison of $\delta^{18}O_{cc}$ values from different periods of Andes uplift.

3.6.3 Implications for central Andes paleoaltimetry

Stable isotope compositions of central Andes proxy materials have been used to support interpretations of rapid, punctuated, and spatially variable uplift, including uplift magnitudes of: (a) 2.2-3.7 km between 19-16 Ma for the Peruvian Western Cordillera [*Saylor and Horton*, 2014], (b) 2.5 ± 1.0 km between 10.3-6.8 Ma for the Bolivian Altiplano [*Garzione et al.*, 2006], and (c) 2.5-4.0 km since 29 Ma for the Eastern Cordillera [*Leier et al.*, 2013]. These high magnitudes and short durations of uplift stand in contrast with other lines of evidence including structural observations of: (a) crustal thicknesses of ~50-60 km for the Altiplano and Eastern Cordillera during the Oligocene [*McQuarrie*, 2002], (b) a strong association between crustal thickening and tectonic shortening at these latitudes (~17-21°S) [*Kley and Monaldi*, 1998], and (c) consistent regional shortening rates of 8-10 mm/yr from ~40 Ma [*Barnes and Ehlers*, 2009]. Furthermore, deformation in the Eastern Cordillera and Altiplano precedes apparent uplift by > 10 Ma [*Lamb and Hoke*, 1997; *Horton et al.*, 2001].

These differences between the surface uplift and deformation histories can be explained by isotopic fractionation associated with climate change during surface uplift [*Ehlers and Poulsen*, 2009; *Poulsen et al.*, 2010; *Poulsen and Jeffery*, 2011; *Insel et al.*, 2012]. Thus, proxy isotopic compositions may not only record changes in elevation, but also changes in climate. Proxy material isotopic compositions exhibit large variability within and between study sites [Figure 3.8, *Garzione et al.*, 2008; *Leier et al.*, 2013; *Garzione et al.*, 2014; *Saylor and Horton*, 2014]. Carbonates deposited from 6-7 Ma in the Corque Syncline show $\delta^{18}O_{cc}$ values ranging from -15.3 to -8.3‰ [Figure 3.8, *Garzione et al.*, 2006]. Likewise, though no values heavier than ~ -110‰ for δD occur in hydrated volcanic glass compositions after ~17 Ma in the Condoroma Basin in Peru [*Saylor and Horton*, 2014], isotopic compositions vary by at least ~70‰ in samples with overlapping dating uncertainty.

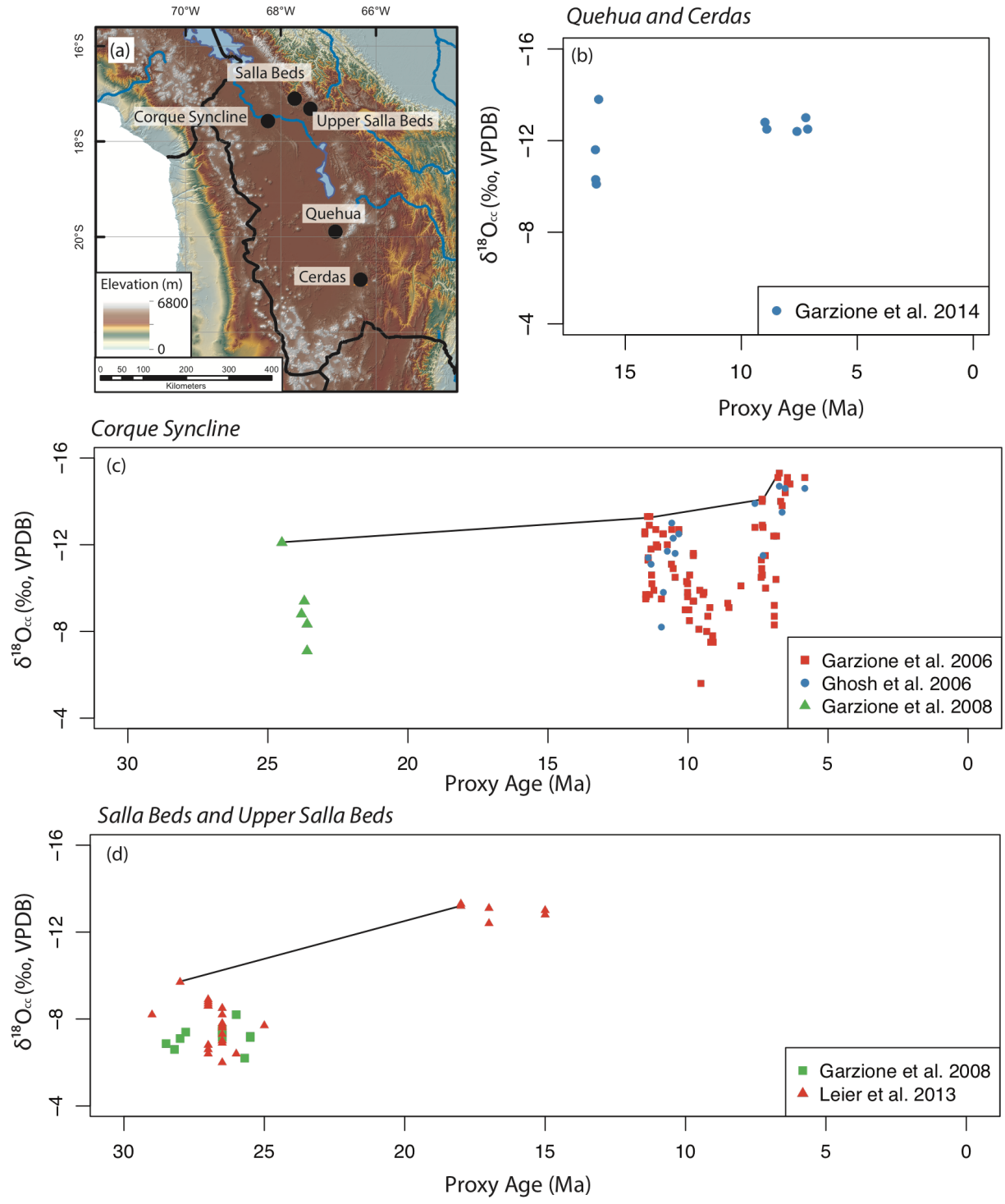

Figure 3.8. Proxy material sampling locations (a) and compilation of available proxy $\delta^{18}O_{cc}$ values from the central Andes plotted against proxy age for (b) Quehua and Cerdas [Garzione et al. 2014], (c) the Corque Syncline [Garzione et al. 2006; 2008, Ghosh et al. 2006] and (d) the Salla and Upper Salla Beds [Garzione et al. 2008, Leier et al. 2013]. Data points used in our proposed reconstruction using only the most negative carbonate values are connected in (c) and (d) with thin black lines.

Variability between these sites has been interpreted to reflect relative uplift between sites, perhaps by as much as multiple kilometers. Alternatively, this variability may represent changes in the spatial pattern of evaporation between sites. Proxy materials formed from evaporated waters would record heavier isotopic compositions associated with lower elevations. Based on climate modeling patterns of precipitation and evapotranspiration, this isotopic bias increases for more ancient proxy materials when elevations were lower. To minimize the impact of evaporative bias in paleoaltimetry studies, it has been suggested that only the lightest isotopic compositions should be used to reconstruct elevations [e.g., *Rowley and Currie*, 2006]. However, this maxim has been inconsistently applied to central Andes stable isotope paleoaltimetry studies.

Here, we reconsider the Bolivian Altiplano and Eastern Cordillera paleoaltimetry record using only the most negative isotopic compositions available. Starting with the Corque syncline on the Bolivian Altiplano, we identify four key carbonate compositions to construct a paleoelevation history based on the lightest isotopic compositions: -12.1‰ at 24.5 Ma, -13.3‰ at 11.45 Ma, -14.1‰ at 7.35 Ma, and -15.1‰ at 6.74 Ma (VPDB) [*Garzione et al.*, 2008]. The composition of meteoric water in equilibrium with these carbonates can be estimated by applying temperature constraints to the temperature-dependent fractionation of oxygen between calcite and water [*Kim and O'Neil*, 1997]. Assuming formation temperatures of 36°C, 28°C, 18°C, and 13°C based on clumped isotope paleothermometry [*Ghosh et al.*, 2006; *Leier et al.*, 2013], these carbonate compositions imply meteoric water compositions of -7.6‰ at 24.5 Ma, -10.3‰ at 11.45 Ma, -13.2‰ at 7.35 Ma, and -16.2‰ at 6.74 Ma (VSMOW). An annual mean $\delta^{18}O_p$ of -7.6 ‰ is inconsistent with near sea-level elevations, but is consistent with Andean elevations of ~25-50% of modern, or 1.0-2.0 km [*Insel et al.*, 2012]. Additionally, the $\delta^{18}O_p$ estimated for 6.74 Ma is consistent with modern observations [*Gonfiantini et al.*, 2001; *Fiorella et al.*, 2015], suggesting that modern elevations were reached by this time. This limits the total Altiplano uplift after 24.5 Ma to 1.7-3.0 km. Partitioning the 8.6‰ of estimated $\delta^{18}O_p$ change proportionally between these four points suggests uplift magnitudes of: 0.5-1.0 km from 24.5-11.45 Ma, 0.6-1.0 km from 11.45-7.35 Ma, and 0.6-1.0 km from 7.35-6.74 Ma. These uplift magnitudes would imply plateau elevations of 1.0-2.0 km at 24.5 Ma, and >1.5 km by 11.45 Ma and >2.1 km by 7.35 Ma (Figure 3.9a). Therefore, the total uplift of the Altiplano after 11.45 Ma cannot exceed ~2.2 km, and may have been as small as ~0.7 km. These estimates are substantially smaller than

previous interpretations of the isotopic data of 2.5±1.0 km of uplift after 11.45 Ma [e.g., *Garzione et al.*, 2008]. Further, our estimates represent maximum uplift magnitudes and place minimum bounds on past elevations, if the following two assumptions are correct: (1) the lightest isotopic compositions capture unevaporated meteoric water and (2) the isotopic composition of this proxy material represents the multi-year mean of the precipitation composition. In arid climates, compositions reflecting unevaporated water may not be preserved [*Quade et al.*, 2007], and therefore, elevations may be higher than suggested by the most negative proxy composition. Finally, we note that our assumption that clumped isotope compositions accurately record the proxy formation temperature is the more conservative approach to reinterpret the $\delta^{18}O_{cc}$ data with respect to the original interpretations. If RegCM surface temperatures were used instead, the estimated change in $\delta^{18}O_p$ would drop to a maximum of 7.7‰ instead of 8.6‰, which would also suggest a lower uplift magnitude. Furthermore, a formation temperature of 28°C from RegCM at 24.5 Ma implies a $\delta^{18}O_p$ of -9.1‰, and potentially higher paleoelevations than the 1-2 km estimated here.

Additionally, surface temperature histories inferred from clumped isotope compositions of pedogenic carbonates suggest that the southern Bolivian Altiplano was uplifted by 2.5±1.0 km between 16 and 13 Ma. In contrast, clumped isotope temperatures indicate the northern Bolivian Altiplano remained below 2 km until ~10 Ma, and experienced 2.5±1.0 km of uplift between 10 and 6 Ma [*Ghosh et al.*, 2006; *Garzione et al.*, 2014]. However, the most negative $\delta^{18}O$ compositions from the north and south halves of the Bolivian Altiplano do not show this discrepancy. The lightest isotopic compositions at the Cerdas and Quehua sites in the southern Altiplano are -13.8‰ at 16.15 Ma and -13.0‰ at 7.22 Ma respectively, while compositions of -12.1‰ at 24.5 Ma and -14.1‰ at 7.35 Ma are observed at the Corque Syncline (Figure 3.8). Therefore, $\delta^{18}O$ compositions would seem to suggest a spatially uniform uplift of the Bolivian Altiplano, in contrast to the heterogeneous uplift history previously inferred from Δ_{47} compositions. However, clumped isotope temperature estimates are highly uncertain for portions of the central Andes record. For example, carbonates within the Corque Syncline show a ~25°C range of temperature at 11 Ma and a ~20°C range of temperature at 6 Ma, while the Salla Beds also show a ~25°C range at 25 Ma [Appendix 3C, *Garzione et al.*, 2008; *Leier et al.*, 2013]. The RegCM temperature change between the 0% and 100% Andes simulations is ~22°C. Therefore, the temperature uncertainty for contemporaneously precipitated pedogenic carbonates

approaches the anticipated signal for the entire uplift of the Andes. As such, the clumped isotope record places weaker constraints on the paleoelevation history of the central Andes than do $\delta^{18}O$ compositions. As a result, our proposed Altiplano uplift scenario remains consistent with clumped isotope temperatures (Appendix 3C). This trend arises from the large Δ_{47} temperature variability as well as from uncertainties in the relationship between Δ_{47} formation temperatures and mean annual air temperatures (Appendix 3C).

Therefore, based on our prior assertion that more negative isotopic compositions are stronger evidence for high elevations than less negative compositions are for low elevations, we suggest that broadly synchronous uplift of the Bolivian Altiplano is consistent with the $\delta^{18}O_{cc}$ data (Appendix 3C). In addition, Δ_{47} temperatures also suggest a homogenous uplift of the Bolivian Altiplano when temperature estimates for Corque, Cerdas, and Quehua are estimated using the model of *Quade et al.* [2013]. Broadly synchronous uplift is also supported by evidence of similar deformation histories in the northern [*Lamb and Hoke*, 1997] and southern [*Elger et al.*, 2005] portions of the Bolivian Altiplano. Additionally, recent isotopic evidence suggests that the Puna plateau may have attained modern elevations at least as early as the mid-Miocene [e.g., *Quade et al.*, 2015], and perhaps as early as the Eocene [*Canavan et al.*, 2014]. Taken together, we suggest that a broadly uniform uplift of the entire central Andean plateau may yet be consistent with the isotopic data due to the strong hydrologic changes associated with uplift that may be reflected in proxy isotope compositions. Further, our proposed paleoelevation history is more consistent with crustal shortening records for the Altiplano [*Lamb and Hoke*, 1997; *Elger et al.*, 2005; *Oncken et al.*, 2006; *Eichelberger et al.*, 2015], and does not require massive, large-scale delamination.

In the Eastern Cordillera, the most negative $\delta^{18}O_{cc}$ value for the Salla Beds is -9.7‰ at 28.0 Ma, and -13.9‰ at 18.0 Ma for the Upper Salla Beds (VPDB) [*Leier et al.*, 2013]. Assuming formation temperatures (from Δ_{47}) of 36±4°C for the Salla Beds and 20±3°C for the Upper Salla Beds yields estimates of $\delta^{18}O_p$ of -5.0±0.7‰ and -12.5±0.6‰ for the Salla and Upper Salla Beds respectively (VSMOW). This estimate of $\delta^{18}O_p$ for the Salla Beds is slightly more negative than the estimation of *Leier et al.* [2013] of -4.0‰, but remains consistent with their interpretation of Salla Bed paleoelevations of 0-1.5 km (Figure 3.9b). In contrast, a value of -12.5±0.6‰ for $\delta^{18}O_p$ during deposition of the Upper Salla Beds suggests surface elevations >3 km (Figure 3.9b). Modern water isotope values more depleted than -12.0‰ are not observed in

precipitation and stream waters below 3 km [*Gonfiantini et al.*, 2001; *Bershaw et al.*, 2010; *Fiorella et al.*, 2015]. Furthermore, isotope tracking climate model experiments also indicate that $\delta^{18}O_p$ values less than -12.0‰ require elevations of > 3 km [*Insel et al.*, 2012]. Therefore, we suggest the Upper Salla Beds were deposited above 3 km. This is consistent with the estimate of 3.2±0.5 km in *Leier et al.* [2013] when all carbonate values are included, but inconsistent with their elevation estimate of ~2.5 km when the most negative carbonate value is treated as an outlier.

Finally, though we have considered evaporation in isolation, changes in Cenozoic climate have also likely impacted proxy isotopic compositions as well as evaporative intensity. Globally warmer conditions in the Paleogene relative to the Neogene may amplify evaporative bias [e.g., *Zachos et al.*, 2001]. Additionally, enhanced atmospheric subsidence would be expected over the central Andes region in a warmer climate. This atmospheric subsidence would transport heavier-than-anticipated vapor to the surface, and further bias proxy materials to lower elevations [*Poulsen and Jeffery*, 2011]. Unfortunately, the magnitude of evaporative bias is difficult to constrain throughout time in the absence of quantitative proxy-based estimates of net evaporation. We suggest that recent developments in ^{17}O-excess, an isotopic marker which records evaporative intensity when combined with $\delta^{18}O_{cc}$, may represent an important step forward to decoupling the contributions of climate and tectonic change to isotopic change [e.g., *Passey et al.*, 2014].

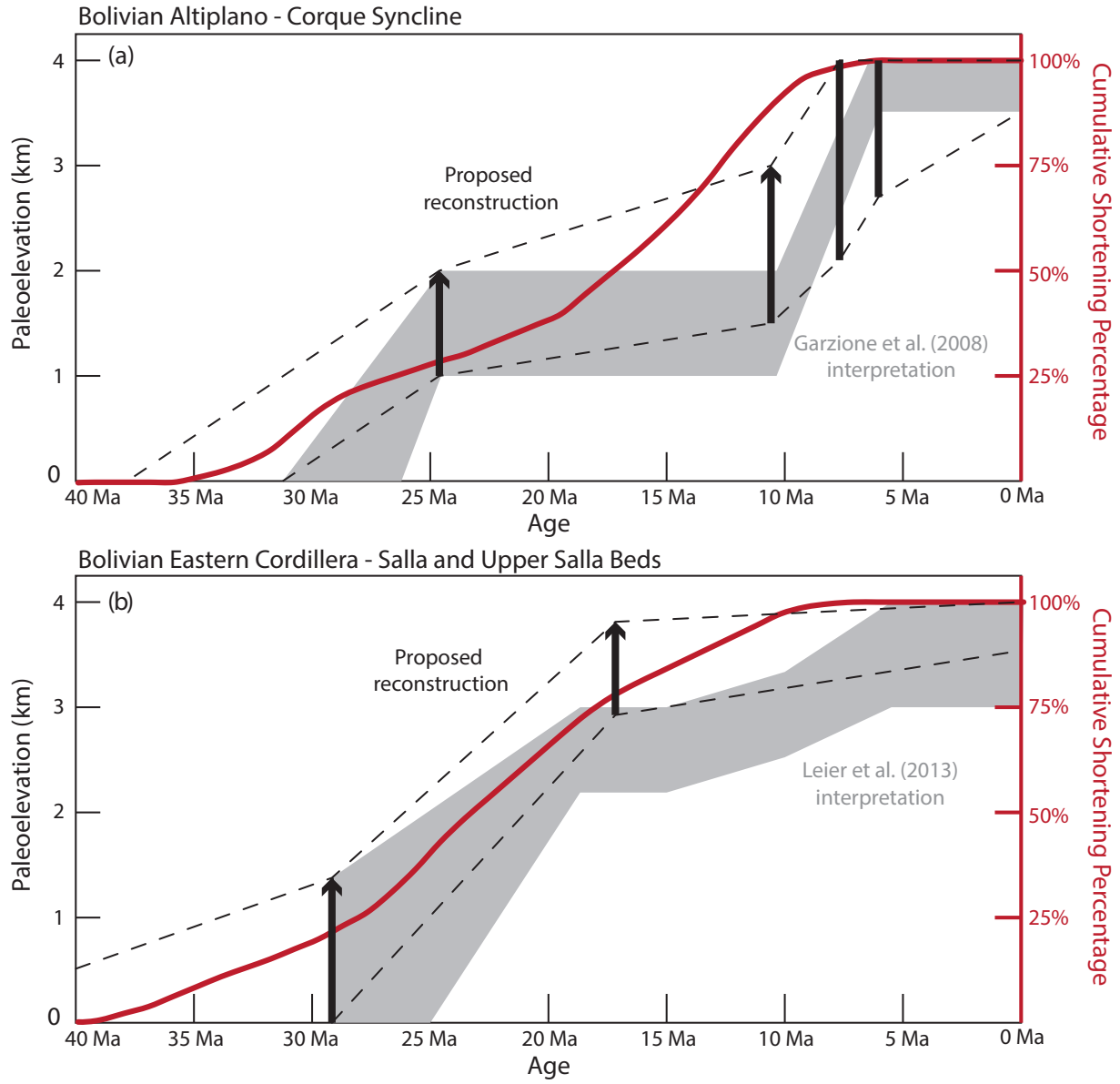

Figure 3.9. Schematic of the uplift of the Bolivian Altiplano (a) and Eastern Cordillera (b) proposed in this study. Key isotopic constraints identified in section 5.3 are shown in thick black lines, with arrows indicating that higher elevations are possible if a pedogenic carbonate in equilibrium with precipitation was not preserved. The range of elevations suggested by using only the lightest $\delta^{18}O_{cc}$ compositions in the proxy record is outlined in dashed black lines, though we note other uplift paths through the constraints identified are possible. Previous interpretations of the stable isotope data are shown in gray. Cumulative shortening after Oncken et al. [2006] is shown for each region as a red curve. For both regions, the proposed post-15 Ma uplift is reduced from the original interpretations, and provides a closer match between cumulative shortening and reconstructed elevations.

3.7 Conclusions

We provide a dataset of the isotopic composition of 249 central Andes streams collected over a 3.5-year period, constraining an important and previously missing aspect of the central Andes stable isotope system. The isotopic compositions of stream waters along the eastern Andean flank possess a δD-$\delta^{18}O$ that is similar to regional precipitation. In contrast, stream waters on the Altiplano exhibit a δD-$\delta^{18}O$ relationship with a shallower slope than that of regional precipitation, which we interpret as evidence of heavy isotope enrichment through evaporation. Propagation of this evaporative signal into soil waters that occurs during infiltration may result in soil water and carbonate compositions that underestimate modern elevations in modern soils. Paleoclimate model simulations indicate that the central Andes region has become progressively less arid through its uplift, and therefore, carbonates earlier in the uplift history may exhibit a greater bias. Cenozoic cooling and the increase in isotopic lapse rates inferred from climate modeling both amplify this bias [*Poulsen et al.*, 2010; *Poulsen and Jeffery*, 2011; *Insel et al.*, 2012; *Jeffery et al.*, 2012].

To avoid this bias, we propose paleoelevations for the Bolivian Altiplano of 1-2 km at 24.5 Ma, 1.5-3.0 km at ~11.45 Ma, and 2.7-4 km at 6 Ma based on the lightest isotopic compositions observed in proxy materials. Using the same logic, we estimate paleoelevations for the Eastern Cordillera of 0-1.5 km at ~28 Ma and >3 km at ~18 Ma. We draw three major conclusions from this reinterpretation of stable isotope proxy data: (1) mid-Miocene-to-modern elevation change on the Bolivian Altiplano was no greater than 2 km, which is less than prior stable isotope based estimates of 2.5 ± 1 km [e.g., *Garzione et al.*, 2008; 2014], (2) Bolivian Altiplano and Eastern Cordillera paleoelevations inferred in this study more closely match records of cumulative shortening (Figure 3.9) [e.g., *Oncken et al.*, 2006; *Barnes and Ehlers*, 2009] than do prior interpretations of stable isotope data, (3) when placed into a consistent framework, $\delta^{18}O$ and Δ_{47} compositions support a uniform, homogenous uplift of the Bolivian Altiplano. Therefore, central Andes surface uplift may be more spatially uniform and more closely linked to crustal shortening than suggested in previous interpretations of stable isotope paleoelevation proxies.

3.8 References

Alonso, R. N., T. E. Jordan, K. T. Tabbutt, and D. S. Vandervoort (1991), Giant Evaporite Belts of the Neogene Central Andes, *Geol*, *19*(4), 401–404, doi:10.1130/0091-7613(1991)019<0401:GEBOTN>2.3.CO;2.

Aravena, R., O. Suzuki, H. Pena, A. Pollastri, H. Fuenzalida, and A. Grilli (1999), Isotopic composition and origin of the precipitation in Northern Chile, *Applied Geochemistry*, *14*, 411–422, doi:10.1016/S0883-2927(98)00067-5.

Barnes, J. B., and T. A. Ehlers (2009), End member models for Andean Plateau uplift, *Earth-Science Reviews*, *97*(1-4), 105–132, doi:10.1016/j.earscirev.2009.08.003.

Bershaw, J., C. N. Garzione, P. Higgins, B. J. MacFadden, F. Anaya, and H. Alvarenga (2010), Spatial–temporal changes in Andean plateau climate and elevation from stable isotopes of mammal teeth, *Earth Planet Sc Lett*, *289*(3-4), 530–538, doi:10.1016/j.epsl.2009.11.047.

Bookhagen, B., and M. R. Strecker (2008), Orographic barriers, high-resolution TRMM rainfall, and relief variations along the eastern Andes, *Geophys Res Lett*, *35*(6), L06403, doi:10.1029/2007GL032011.

Breecker, D. O., Z. D. Sharp, and L. D. McFadden (2009), Seasonal bias in the formation and stable isotopic composition of pedogenic carbonate in modern soils from central New Mexico, USA, *Geological Society of America Bulletin*, *121*(3-4), 630–640, doi:10.1130/B26413.1.

Canavan, R. R., B. Carrapa, M. T. Clementz, J. Quade, P. G. DeCelles, and L. M. Schoenbohm (2014), Early Cenozoic uplift of the Puna Plateau, Central Andes, based on stable isotope paleoaltimetry of hydrated volcanic glass, *Geol*, *42*(5), 447–450, doi:10.1130/G35239.1.

Clarke, J. D. A. (2006), Antiquity of aridity in the Chilean Atacama Desert, *Geomorphology*, *73*(1-2), 101–114, doi:10.1016/j.geomorph.2005.06.008.

Coplen, T. B. (1996), New guidelines for reporting stable hydrogen, carbon, and oxygen isotope-ratio data, *Geochimica et Cosmochimica Acta*, *60*(17), 3359–3360, doi:10.1016/0016-7037(96)00263-3.

Defliese, W. F., and K. C. Lohmann (2015), Non-linear mixing effects on mass-47 CO_2 clumped isotope thermometry: Patterns and implications, *Rapid Commun. Mass Spectrom.*, 1–9, doi:10.1002/rcm.7175.

Ehlers, T. A., and C. J. Poulsen (2009), Influence of Andean uplift on climate and paleoaltimetry estimates, *Earth Planet Sc Lett*, *281*(3-4), 238–248, doi:10.1016/j.epsl.2009.02.026.

Eichelberger, N., N. McQuarrie, J. Ryan, B. Karimi, S. Beck, and G. Zandt (2015), Evolution of crustal thickening in the central Andes, Bolivia, *Earth Planet Sc Lett*, *426*(C), 191–203, doi:10.1016/j.epsl.2015.06.035.

Elger, K., O. Oncken, and J. Glodny (2005), Plateau-style accumulation of deformation: Southern Altiplano, *Tectonics*, *24*(4), n/a–n/a, doi:10.1029/2004TC001675.

Fiorella, R. P., C. J. Poulsen, R. S. Pillco Zolá, J. B. Barnes, C. R. Tabor, and T. A. Ehlers (2015), Spatiotemporal variability of modern precipitation $\delta^{18}O$ in the central Andes and implications for paleoclimate and paleoaltimetry estimates, *J Geophys Res-Atmos*, *120*(10), 4630–4656, doi:10.1002/2014JD022893.

Garreaud, R. D., M. Vuille, and A. Clement (2003), The climate of the Altiplano: observed current conditions and mechanisms of past changes, *Palaeogeography, Palaeoclimatology, Palaeoecology*, *194*(1-3), 5–22, doi:10.1016/S0031-0182(03)00269-4.

Garzione, C. N., D. J. Auerbach, J. J.-S. Smith, J. J. Rosario, B. H. Passey, T. E. Jordan, and J.

M. Eiler (2014), Clumped isotope evidence for diachronous surface cooling of the Altiplano and pulsed surface uplift of the Central Andes, *Earth Planet Sc Lett*, *393*(C), 173–181, doi:10.1016/j.epsl.2014.02.029.

Garzione, C. N., G. D. Hoke, J. C. Libarkin, S. Withers, B. J. MacFadden, J. M. Eiler, P. Ghosh, and A. Mulch (2008), Rise of the Andes, *Science*, *320*(5881), 1304–1307, doi:10.1126/science.1148615.

Garzione, C. N., P. Molnar, J. C. Libarkin, and B. J. MacFadden (2006), Rapid late Miocene rise of the Bolivian Altiplano: Evidence for removal of mantle lithosphere, *Earth Planet Sc Lett*, *241*(3-4), 543–556, doi:10.1016/j.epsl.2005.11.026.

Ghosh, P., C. N. Garzione, and J. M. Eiler (2006), Rapid uplift of the Altiplano revealed through 13C-18O bonds in paleosol carbonates, *Science*, *311*(5760), 511–515, doi:10.1126/science.1120792.

Gonfiantini, R., M. A. Roche, J. C. Olivry, J. C. Fontes, and G. M. Zuppi (2001), The altitude effect on the isotopic composition of tropical rains, *Chemical Geology*, *181*(1), 147–167.

Gurnis, M., M. Turner, S. Zahirovic, L. DiCaprio, S. Spasojevic, R. D. Müller, J. Boyden, M. Seton, V. C. Manea, and D. J. Bower (2012), Plate tectonic reconstructions with continuously closing plates, *Computers and Geosciences*, *38*(1), 35–42, doi:10.1016/j.cageo.2011.04.014.

Horton, B. K., B. A. Hampton, and G. L. Waanders (2001), Paleogene synorogenic sedimentation in the Altiplano plateau and implications for initial mountain building in the central Andes, *Geological Society of America Bulletin*, *113*(11), 1387–1400, doi:10.1130/0016-7606(2001)113<1387:PSSITA>2.0.CO;2.

Hsieh, J., O. A. Chadwick, E. F. Kelly, and S. M. Savin (1998), Oxygen isotopic composition of soil water: Quantifying evaporation and transpiration, *Geoderma*, *82*(1-3), 269–293.

Insel, N., C. J. Poulsen, and T. A. Ehlers (2010), Influence of the Andes Mountains on South American moisture transport, convection, and precipitation, *Climate Dynamics*, *35*(7-8), 1477–1492, doi:10.1007/s00382-009-0637-1.

Insel, N., C. J. Poulsen, T. A. Ehlers, and C. Sturm (2012), Response of meteoric $\delta^{18}O$ to surface uplift - Implications for Cenozoic Andean Plateau Growth, *Earth Planet Sc Lett*, *317-318*, 262–272, doi:10.1016/j.epsl.2011.11.039.

Isacks, B. L. (1988), Uplift of the Central Andean Plateau and Bending of the Bolivian Orocline, *J Geophys Res*, *93*, 3211–3231.

Jeffery, M. L., C. J. Poulsen, and T. A. Ehlers (2012), Impacts of Cenozoic global cooling, surface uplift, and an inland seaway on South American paleoclimate and precipitation $\delta^{18}O$, *Geological Society of America Bulletin*, *124*(3-4), 335–351, doi:10.1130/B30480.1.

Kendall, C., and T. B. Coplen (2001), Distribution of oxygen-18 and deuterium in river waters across the United States, *Hydrol. Process.*, *15*(7), 1363–1393, doi:10.1002/hyp.217.

Kim, S.-T., and J. R. O'Neil (1997), Equilibrium and nonequilibrium oxygen isotope effects in synthetic carbonates, *Geochimica et Cosmochimica Acta*, *61*(16), 3461–3475, doi:10.1016/S0016-7037(97)00169-5.

Kley, J., and C. R. Monaldi (1998), Tectonic shortening and crustal thickness in the Central Andes: How good is the correlation? *Geol*, *26*(8), 723–726, doi:10.1130/0091-7613(1998)026<0723:TSACTI>2.3.CO;2.

Lamb, S., and L. Hoke (1997), Origin of the high plateau in the Central Andes, Bolivia, South America, *Tectonics*, *16*(4), 623–649.

Leier, A., N. McQuarrie, C. Garzione, and J. Eiler (2013), Stable isotope evidence for multiple

pulses of rapid surface uplift in the Central Andes, Bolivia, *Earth Planet Sc Lett*, *371-372*(C), 49–58, doi:10.1016/j.epsl.2013.04.025.

Mathieu, R., and T. Bariac (1996), An isotopic study (^{2}H and ^{18}O) of water movements in clayey soils under a semiarid climate, *Water Resour Res*, *32*(4), 779–789.

McQuarrie, N. (2002), The kinematic history of the central Andean fold-thrust belt, Bolivia: Implications for building a high plateau, *Geological Society of America Bulletin*, *114*(8), 950–963, doi:10.1130/0016-7606(2002)114<0950:TKHOTC>2.0.CO;2.

McQuarrie, N., B. K. Horton, G. Zandt, S. Beck, and P. G. DeCelles (2005), Lithospheric evolution of the Andean fold–thrust belt, Bolivia, and the origin of the central Andean plateau, *Tectonophysics*, *399*(1-4), 15–37, doi:10.1016/j.tecto.2004.12.013.

Mulch, A., and C. P. Chamberlain (2007), Stable Isotope Paleoaltimetry in Orogenic Belts The Silicate Record in Surface and Crustal Geological Archives, in *Paleoaltimetry: geochemical and thermodynamic approaches*, vol. 66, edited by M. J. Kohn, pp. 89–118, Minerology Society of America.

Oncken, O., D. Hindle, J. Kley, K. Elger, P. Victor, and K. Schemmann (2006), Deformation of the Central Andean Upper Plate System - Facts, Fiction, and Constraints for Plateau Models, in *The Andes*, edited by O. Oncken, G. Chong, G. Franz, P. Giese, H.-J. Götze, V. A. Ramos, M. R. Strecker, and P. Wigger, pp. 3–27, Springer Berlin Heidelberg, Berlin.

Pal, J., F. Giorgi, X. Bi, N. Elguindi, F. Solmon, S. Rauscher, X. Gao, R. Francisco, A. Zakey, and J. Winter (2007), Regional climate modeling for the developing world: the ICTP RegCM3 and RegCNET, *Bulletin of the American Meteorological Society*, *88*(9), 1395–1409, doi:10.1175/BAMS-88-9-1395.

Passey, B. H., H. Hu, H. Ji, S. Montanari, S. Li, G. A. Henkes, and N. E. Levin (2014), Triple oxygen isotopes in biogenic and sedimentary carbonates, *Geochimica et Cosmochimica Acta*, *141*(C), 1–25, doi:10.1016/j.gca.2014.06.006.

Peters, N. A., K. W. Huntington, and G. D. Hoke (2013), Hot or not? Impact of seasonally variable soil carbonate formation on paleotemperature and O-isotope records from clumped isotope thermometry, *Earth Planet Sc Lett*, *361*, 208–218, doi:10.1016/j.epsl.2012.10.024.

Poulsen, C. J., and M. L. Jeffery (2011), Climate change imprinting on stable isotopic compositions of high-elevation meteoric water cloaks past surface elevations of major orogens, *Geol*, doi:10.1130/G32052.1.

Poulsen, C. J., T. A. Ehlers, and N. Insel (2010), Onset of Convective Rainfall During Gradual Late Miocene Rise of the Central Andes, *Science*, *328*(5977), 490–493, doi:10.1126/science.1185078.

Quade, J., C. N. Garzione, and J. M. Eiler (2007), Paleoelevation Reconstruction using Pedogenic Carbonates, *Reviews in Mineralogy and Geochemistry*, *66*(1), 53–87, doi:10.2138/rmg.2007.66.3.

Quade, J., J. M. Eiler, M. Daëron, and H. Achyuthan (2013), The clumped isotope geothermometer in soil and paleosol carbonate, *Geochimica et Cosmochimica Acta*, *105*(C), 92–107, doi:10.1016/j.gca.2012.11.031.

Quade, J., M. P. Dettinger, B. Carrapa, P. DeCelles, K. E. Murray, K. W. Huntington, A. Cartwright, R. R. Canavan, G. Gehrels, and M. Clementz (2015), The growth of the central Andes, 22°S–26°S, in *Geodynamics of a Cordilleran Orogenic System: The Central Andes of Argentina and Northern Chile*, vol. 212, pp. 277–308, Geological Society of America.

Rohrmann, A., M. R. Strecker, B. Bookhagen, A. Mulch, D. Sachse, H. Pingel, R. N. Alonso, T. F. Schildgen, and C. Montero (2014), Can stable isotopes ride out the storms? The role of

convection for water isotopes in models, records, and paleoaltimetry studies in the central Andes, *Earth Planet Sc Lett*, *407*, 187–195, doi:10.1016/j.epsl.2014.09.021.

Rowley, D. B. (2007), Stable Isotope-Based Paleoaltimetry: Theory and Validation, in *Paleoaltimetry: geochemical and thermodynamic approaches*, vol. 66, edited by M. J. Kohn, pp. 23–52, Minerology Society of America.

Rowley, D. B., and B. S. Currie (2006), Palaeo-altimetry of the late Eocene to Miocene Lunpola basin, central Tibet, *Nature*, *439*(7077), 677–681, doi:10.1038/nature04506.

Rozanski, K., L. Araguas-Araguas, and R. Gonfiantini (1993), Isotopic patterns in modern global precipitation, in *Climate Change in Continental Isotopic Records*, edited by P. K. Swart, K. C. Lohmann, J. Mckenzie, and S. M. Savin, pp. 1–36, American Geophysical Union.

Saylor, J. E., A. Mora, B. K. Horton, and J. Nie (2009), Controls on the isotopic composition of surface water and precipitation in the Northern Andes, Colombian Eastern Cordillera, *Geochimica et Cosmochimica Acta*, *73*(23), 6999–7018, doi:10.1016/j.gca.2009.08.030.

Saylor, J. E., and B. K. Horton (2014), Nonuniform surface uplift of the Andean plateau revealed by deuterium isotopes in Miocene volcanic glass from southern Peru, *Earth Planet Sc Lett*, *387*(C), 120–131, doi:10.1016/j.epsl.2013.11.015.

Vandervoort, D. S., T. E. Jordan, P. K. Zeitler, and R. N. Alonso (1995), Chronology of Internal Drainage Development and Uplift, Southern Puna Plateau, Argentine Central Andes, *Geol*, *23*(2), 145–148, doi:10.1130/0091-7613(1995)023<0145:COIDDA>2.3.CO;2.

Zachos, J., M. Pagani, L. C. Sloan, E. Thomas, and K. Billups (2001), Trends, rhythms, and aberrations in global climate 65 Ma to present, *Science*, *292*(5517), 686.

Appendix 3A. Central Andes stream catchment geographic parameters and isotopic data

Table 3.2. Geographic parameters of central Andes stream water catchments

ID	Collection Date	Latitude	Longitude	Mean Catchment Elevation (m)	Annual Precipitation Amount Weighted Mean Catchment Elevation (m)	Minimum Elevation (m)	Maximum Elevation (m)	Catchment Relief (m)	Catchment Area (sq. km)
ST001	8-Apr-09	-18.39	-66.98	4086	4085	3713	4664	951	107.2
ST002	8-Apr-09	-18.60	-66.91	4103	4116	3704	4771	1067	233.9
ST003	8-Apr-09	-19.03	-66.78	4434	4459	3730	5084	1354	87.9
ST004	8-Apr-09	-19.12	-66.77	4302	4286	3713	4907	1194	241.7
ST005	8-Apr-09	-19.39	-67.27	3805	3801	3708	4149	441	60.2
ST006A	8-Apr-09	-19.39	-67.27	3796	3800	3696	4069	373	177.4
ST006B	8-Apr-09	-19.39	-67.27	3796	3800	3696	4069	373	177.4
ST007	8-Apr-09	-19.64	-67.66	4125	4137	3706	4839	1133	12.1
ST008	10-Apr-09	-20.55	-66.68	3949	3973	3653	5222	1569	1933.1
ST009	10-Apr-09	-20.86	-66.54	4083	4054	3774	4777	1003	694.9
ST010	10-Apr-09	-20.93	-66.28	4002	4002	3808	4319	511	1.9
ST011	10-Apr-09	-20.93	-66.22	4064	4058	3645	4693	1048	358.9
ST012A	10-Apr-09	-21.05	-66.09	4038	4046	3966	4151	185	12.2
ST012B	10-Apr-09	-21.05	-66.09	4044	4046	3944	4244	300	19.1
ST013A	10-Apr-09	-21.11	-66.04	4108	4125	3960	4256	296	9.0
ST013B	10-Apr-09	-21.11	-66.04	4116	4123	3955	4358	403	12.0
ST014	10-Apr-09	-21.18	-65.90	4022	4022	3877	4241	364	0.6
ST015A	11-Apr-09	-21.74	-65.56	3641	3644	3395	4105	710	62.5
ST015B	11-Apr-09	-21.74	-65.56	3416	3416	3395	3466	71	0.2
ST016	11-Apr-09	-21.88	-65.40	3652	3618	2672	5046	2374	2848.8
ST017	11-Apr-09	-21.82	-65.18	4035	4035	3887	4198	311	0.9
ST018	11-Apr-09	-21.56	-65.05	3904	3905	3744	4284	540	1.5
ST019	11-Apr-09	-21.49	-64.97	3743	3758	3436	4411	975	2.6
ST020	11-Apr-09	-21.46	-64.87	3227	3227	3074	3347	273	0.1
ST021	11-Apr-09	-21.46	-64.83	2619	2616	2544	2729	185	0.6
ST022	11-Apr-09	-21.46	-64.84	2728	2720	2540	3076	536	3.9
ST023	11-Apr-09	-21.45	-64.29	2168	2168	1990	2286	296	0.1

ST024	11-Apr-09	-21.46	-64.75	2046	2046	1958	2268	310	2.5
ST025	11-Apr-09	-21.50	-64.76	2773	2713	1925	4236	2311	61.7
ST026	12-Apr-09	-21.55	-64.60	1921	1921	1894	1964	70	0.3
ST027	12-Apr-09	-21.52	-64.57	2377	2394	1934	3277	1343	250.6
ST028	12-Apr-09	-21.46	-64.50	2318	2318	2238	2434	196	0.9
ST029	12-Apr-09	-21.42	-64.41	2653	2653	2570	2783	213	0.5
ST030	12-Apr-09	-21.45	-64.36	2349	2349	2138	2494	356	0.1
ST031	12-Apr-09	-21.42	-64.31	2335	2331	2185	2509	324	0.3
ST032	12-Apr-09	-21.43	-64.27	1897	1905	1652	2095	443	0.2
ST033	12-Apr-09	-21.47	-64.21	1923	1923	1841	1980	139	0.1
ST034	12-Apr-09	-21.45	-64.08	1225	1235	1077	1458	381	0.2
ST035	12-Apr-09	-21.45	-64.07	1228	1228	1102	1312	210	0.6
ST036	12-Apr-09	-21.44	-64.01	1342	1380	953	2008	1055	45.5
ST037	12-Apr-09	-21.41	-63.82	1270	1295	773	2092	1319	68.5
ST038	12-Apr-09	-21.40	-63.66	1036	1031	698	1565	867	23.6
ST039A	12-Apr-09	-21.33	-63.62	959	1066	567	1648	1081	12.1
ST039B	12-Apr-09	-21.33	-63.62	1051	1071	557	1883	1326	411.9
ST040	13-Apr-09	-21.27	-63.52	855	836	380	1676	1296	48.3
ST041	13-Apr-09	-21.26	-63.55	825	825	424	1193	769	1.2
ST042	13-Apr-09	-21.24	-63.56	784	777	456	1264	808	2.5
ST043	13-Apr-09	-21.44	-64.04	1338	1353	1102	1659	557	13.1
ST045	13-Apr-09	-21.45	-64.33	2114	2114	2053	2193	140	0.1
ST046	14-Apr-09	-21.43	-64.79	2252	2265	2061	2438	377	2.3
ST047	14-Apr-09	-21.39	-64.98	3722	3724	3421	4327	906	11.8
ST048A	14-Apr-09	-20.97	-65.23	2412	2412	2272	2566	294	0.3
ST048B	14-Apr-09	-20.97	-65.23	3164	3047	2265	4341	2076	286.5
ST049	14-Apr-09	-20.53	-65.14	3203	3218	2859	3524	665	1.5
ST050	14-Apr-09	-20.24	-65.15	3402	3409	3356	3477	121	0.7
ST051	14-Apr-09	-19.87	-65.55	4301	4418	3404	4960	1556	21.7
ST052	15-Apr-09	-20.01	-66.86	4149	4181	3772	5380	1608	122.3
ST053	15-Apr-09	-19.52	-66.86	4118	4123	3772	4867	1095	218.4
ST054	15-Apr-09	-19.12	-66.77	4302	4286	3713	4907	1194	241.7
ST055	15-Apr-09	-18.39	-66.98	4086	4085	3713	4664	951	107.2
ST101	13-Apr-10	-18.16	-66.99	4219	4211	3722	4828	1106	683.0
ST102	13-Apr-10	-18.39	-66.98	4086	4085	3713	4664	951	107.2
ST103	13-Apr-10	-18.60	-66.91	4103	4116	3704	4771	1067	233.9
ST104	13-Apr-10	-19.12	-66.77	4302	4286	3713	4907	1194	241.7

ST105	13-Apr-10	-19.39	-67.27	3805	3801	3708	4149	441	60.2
ST106	13-Apr-10	-19.64	-67.66	4125	4137	3706	4839	1133	12.1
ST107	15-Apr-10	-20.63	-66.68	3949	3973	3653	5222	1569	1933.1
ST108	15-Apr-10	-20.86	-66.54	4083	4054	3774	4777	1003	694.9
ST109	15-Apr-10	-20.92	-66.28	4002	4002	3808	4319	511	1.9
ST110	15-Apr-10	-21.05	-66.09	4038	4046	3966	4151	185	12.2
ST111	15-Apr-10	-21.11	-66.04	4108	4125	3960	4256	296	9.0
ST112	15-Apr-10	-21.11	-66.04	4116	4123	3955	4358	403	12.0
ST113	15-Apr-10	-21.18	-65.90	4022	4022	3877	4241	364	0.6
ST114	16-Apr-10	-21.35	-65.49	3778	3778	3711	3871	160	2.0
ST115	16-Apr-10	-21.37	-65.49	3793	3791	3681	3982	301	8.9
ST116	16-Apr-10	-21.44	-65.42	4261	4239	4131	4354	223	0.3
ST117	16-Apr-10	-21.36	-65.18	3603	3425	2583	4353	1770	77.1
ST118	16-Apr-10	-21.22	-65.24	2450	2449	2378	2518	140	3.9
ST119	16-Apr-10	-21.21	-65.21	3296	3027	2326	4357	2031	962.4
ST120	16-Apr-10	-21.39	-64.98	3722	3724	3421	4327	906	11.8
ST121	16-Apr-10	-21.46	-64.87	3227	3227	3074	3347	273	0.1
ST122	16-Apr-10	-21.49	-64.76	2001	1997	1923	2238	315	2.8
ST123	17-Apr-10	-21.52	-64.57	2259	2267	1935	2781	846	37.7
ST124	17-Apr-10	-21.52	-64.57	2377	2394	1934	3277	1343	250.6
ST125	17-Apr-10	-21.46	-64.50	2318	2318	2238	2434	196	0.9
ST126	17-Apr-10	-21.45	-64.49	2416	2419	2247	2697	450	12.6
ST127	17-Apr-10	-21.42	-64.42	2686	2686	2620	2777	157	0.2
ST128	17-Apr-10	-21.42	-64.41	2653	2653	2570	2783	213	0.5
ST129	17-Apr-10	-21.45	-64.35	2349	2349	2138	2494	356	0.1
ST130	17-Apr-10	-21.45	-64.35	2631	2628	2136	3112	976	47.3
ST131	17-Apr-10	-21.42	-64.32	2324	2321	2212	2480	268	0.1
ST132	17-Apr-10	-21.33	-64.27	1897	1905	1652	2095	443	0.2
ST133	17-Apr-10	-21.47	-64.22	1879	1879	1768	1977	209	0.2
ST134	18-Apr-10	-21.53	-64.17	1111	1111	1050	1236	186	1.0
ST135	18-Apr-10	-21.42	-63.97	1413	1417	931	2093	1162	160.4
ST136	18-Apr-10	-21.41	-63.82	1270	1295	773	2092	1319	68.5
ST137	18-Apr-10	-21.30	-63.60	896	932	555	1498	943	8.9
ST139	18-Apr-10	-21.26	-63.55	895	873	428	1268	840	1.6
ST140	19-Apr-10	-17.01	-65.55	456	456	383	651	268	0.3
ST141	19-Apr-10	-17.06	-65.65	1236	1207	646	2050	1404	5.5
ST142	19-Apr-10	-17.14	-65.73	2119	2119	1864	2403	539	0.1

ST143	19-Apr-10	-17.21	-65.82	3480	3374	1887	4632	2745	121.2
ST144	19-Apr-10	-17.27	-65.88	3587	3587	3315	3940	625	17.0
ST145	19-Apr-10	-17.40	-65.86	3966	3966	3677	4150	473	2.1
ST146	20-Apr-10	-17.68	-66.43	3661	3661	3453	3803	350	0.3
ST147	20-Apr-10	-17.71	-66.58	4130	4125	3746	4448	702	124.4
ST148	20-Apr-10	-17.64	-66.87	4499	4499	4449	4563	114	0.3
ST201	5-Apr-11	-18.03	-67.15	3956	3974	3573	4809	1236	8784.1
ST202	5-Apr-11	-18.16	-66.99	4219	4211	3722	4828	1106	683.0
ST203	5-Apr-11	-18.39	-66.98	4086	4085	3713	4664	951	107.2
ST204	5-Apr-11	-18.60	-66.91	4103	4116	3704	4771	1067	233.9
ST205	5-Apr-11	-19.03	-66.78	4434	4459	3730	5084	1354	87.9
ST206	5-Apr-11	-19.12	-66.77	4302	4286	3713	4907	1194	241.7
ST207	5-Apr-11	-19.39	-67.27	3796	3800	3696	4069	373	177.4
ST208	6-Apr-11	-19.64	-67.66	4125	4137	3706	4839	1133	12.1
ST209	7-Apr-11	-20.96	-67.03	4160	4141	3653	5998	2345	12572.1
ST210	7-Apr-11	-20.61	-66.85	3883	3880	3607	5222	1615	6887.1
ST211	8-Apr-11	-20.63	-66.68	3949	3973	3653	5222	1569	1933.1
ST212	8-Apr-11	-20.92	-66.28	4002	4002	3808	4319	511	1.9
ST213	8-Apr-11	-21.05	-66.09	4044	4046	3944	4244	300	19.1
ST214	8-Apr-11	-21.11	-66.04	4108	4125	3960	4256	296	9.0
ST215	8-Apr-11	-21.11	-66.04	4116	4123	3955	4358	403	12.0
ST216	8-Apr-11	-21.18	-65.90	4022	4022	3877	4241	364	0.6
ST217	9-Apr-11	-21.35	-65.49	3778	3778	3711	3871	160	2.0
ST218	9-Apr-11	-21.37	-65.49	3793	3791	3681	3982	301	8.9
ST219	9-Apr-11	-21.36	-65.28	3603	3425	2583	4353	1770	77.1
ST220	9-Apr-11	-21.21	-65.21	3296	3027	2326	4357	2031	962.4
ST221	9-Apr-11	-21.39	-64.98	3722	3724	3421	4327	906	11.8
ST222	9-Apr-11	-21.49	-64.96	3863	3885	3430	4626	1196	175.6
ST223	9-Apr-11	-21.46	-64.87	3227	3227	3074	3347	273	0.1
ST224	9-Apr-11	-21.46	-64.83	2728	2720	2540	3076	536	3.9
ST225	9-Apr-11	-21.43	-64.79	2251	2265	2061	2438	377	2.3
ST226	9-Apr-11	-21.43	-64.79	2350	2369	2061	2596	535	8.8
ST227	9-Apr-11	-21.49	-64.76	2001	1997	1923	2238	315	2.8
ST228	10-Apr-11	-21.52	-64.57	2377	2394	1934	3277	1343	250.6
ST229	10-Apr-11	-21.46	-64.50	2318	2318	2238	2434	196	0.9
ST230	10-Apr-11	-21.42	-64.42	2686	2686	2620	2777	157	0.2
ST231	10-Apr-11	-21.42	-64.41	2641	2641	2478	2837	359	1.0

ST232	10-Apr-11	-21.45	-64.36	2349	2349	2138	2494	356	0.1
ST233	10-Apr-11	-21.43	-64.27	1897	1905	1652	2095	443	0.2
ST234	10-Apr-11	-21.47	-64.22	1879	1879	1768	1977	209	0.2
ST235	10-Apr-11	-21.45	-64.07	1327	1339	1077	1662	585	21.1
ST236	10-Apr-11	-21.44	-64.04	1337	1353	1104	1659	555	13.0
ST237	10-Apr-11	-21.44	-64.01	1342	1380	953	2008	1055	45.5
ST238	10-Apr-11	-21.41	-63.82	1270	1295	773	2092	1319	68.5
ST239	10-Apr-11	-21.33	-63.62	1051	1071	557	1883	1326	411.9
ST240	10-Apr-11	-21.30	-63.60	896	932	555	1498	943	8.9
ST241	10-Apr-11	-21.23	-63.56	716	715	439	1188	749	3.3
ST242	10-Apr-11	-21.26	-63.55	899	877	456	1268	812	1.6
ST243	10-Apr-11	-21.27	-63.52	606	608	390	1188	798	3.0
ST244	11-Apr-11	-20.10	-63.49	1146	1133	733	1883	1150	286.5
ST245	12-Apr-11	-17.64	-63.16	373	377	287	460	173	245.9
ST246	12-Apr-11	-17.47	-63.53	319	320	226	495	269	18.5
ST247	12-Apr-11	-17.00	-65.13	1592		195	3000	2805	1826.4
ST248	12-Apr-11	-17.06	-65.65	1236	1207	646	2050	1404	5.5
ST249	12-Apr-11	-17.14	-65.73	2178	2178	1720	2587	867	0.3
ST250	12-Apr-11	-17.21	-65.82	3480	3374	1887	4632	2745	121.2
ST251	12-Apr-11	-17.27	-65.88	3587	3587	3315	3940	625	17.0
ST252	12-Apr-11	-17.40	-65.86	3966	3966	3677	4150	473	2.1
ST253	12-Apr-11	-17.67	-66.43	3661	3661	3453	3803	350	0.3
ST254	13-Apr-11	-17.71	-66.58	4151	4142	3748	4337	589	10.0
ST255	13-Apr-11	-17.64	-66.87	4499	4499	4449	4563	114	0.3
ST301	10-Apr-12	-18.10	-67.27	4073	4039	3673	6401	2728	61840.0
ST302	10-Apr-12	-18.03	-67.15	3956	3974	3573	4809	1236	8784.1
ST303	10-Apr-12	-18.16	-66.99	4219	4211	3722	4828	1106	683.0
ST303B	10-Apr-12	-18.16	-66.96	4219	4211	3722	4828	1106	683.0
ST304	10-Apr-12	-18.39	-66.98	4086	4085	3713	4664	951	107.2
ST305	10-Apr-12	-18.60	-66.91	4103	4116	3704	4771	1067	233.9
ST306	10-Apr-12	-19.03	-66.78	4434	4459	3730	5084	1354	87.9
ST307	10-Apr-12	-19.12	-66.77	4302	4286	3713	4907	1194	241.7
ST308	10-Apr-12	-19.39	-67.27	3805	3801	3708	4149	441	60.2
ST309	10-Apr-12	-19.39	-67.27	3796	3800	3696	4069	373	177.4
ST310	11-Apr-12	-19.64	-67.66	4125	4137	3706	4839	1133	12.1
ST311	11-Apr-12	-19.26	-67.02	4139	4186	3642	5441	1799	2581.1
ST312	11-Apr-12	-19.22	-66.93	3750	3747	3669	4322	653	158.9

ST313	11-Apr-12	-19.52	-66.86	4118	4123	3772	4867	1095	218.4
ST314	11-Apr-12	-19.62	-66.80	4380	4460	3786	5195	1409	697.8
ST315	11-Apr-12	-20.07	-66.88	4153	4165	3760	5397	1637	234.3
ST317	12-Apr-12	-20.95	-67.03	4160	4141	3653	5998	2345	12572.1
ST318	12-Apr-12	-20.61	-66.85	3883	3880	3607	5222	1615	6887.1
ST319	13-Apr-12	-20.63	-66.68	3949	3973	3653	5222	1569	1933.1
ST320	13-Apr-12	-20.70	-66.64	3945	3939	3664	4672	1008	680.6
ST321	13-Apr-12	-20.86	-66.54	4083	4054	3774	4777	1003	694.9
ST322	13-Apr-12	-20.91	-66.27	4214	4185	3743	4675	932	41.7
ST323	13-Apr-12	-21.05	-66.09	4038	4046	3966	4151	185	12.2
ST324	13-Apr-12	-21.05	-66.09	4044	4046	3944	4244	300	19.1
ST325	13-Apr-12	-21.11	-66.04	4116	4123	3955	4358	403	12.0
ST326	13-Apr-12	-21.11	-66.04	4108	4125	3960	4256	296	9.0
ST327	13-Apr-12	-21.11	-65.99	4257	4257	4158	4361	203	0.5
ST328	13-Apr-12	-21.14	-65.97	4216	4220	4095	4381	286	6.2
ST329	13-Apr-12	-21.18	-65.90	4022	4022	3877	4241	364	0.6
ST330	14-Apr-12	-21.35	-65.49	3778	3778	3711	3871	160	2.0
ST331	14-Apr-12	-21.37	-65.49	3793	3791	3681	3982	301	8.9
ST332	14-Apr-12	-21.44	-65.42	4261	4239	4131	4354	223	0.3
ST333	14-Apr-12	-21.42	-65.38	4072	4072	4012	4109	97	0.0
ST334	14-Apr-12	-21.41	-65.37	3910	3910	3849	3973	124	0.0
ST335	14-Apr-12	-21.36	-65.28	3603	3425	2583	4353	1770	77.1
ST336	14-Apr-12	-21.32	-65.27	3294	3080	2535	4142	1607	29.9
ST337	14-Apr-12	-21.21	-65.21	3296	3027	2326	4357	2031	962.4
ST338	14-Apr-12	-21.39	-64.98	3720	3722	3418	4327	909	11.9
ST339	14-Apr-12	-21.49	-64.96	3863	3885	3430	4626	1196	175.6
ST340	14-Apr-12	-21.46	-64.87	3227	3227	3074	3347	273	0.1
ST341	14-Apr-12	-21.46	-64.83	2728	2720	2540	3076	536	3.9
ST342	14-Apr-12	-21.43	-64.79	2251	2265	2061	2438	377	2.3
ST343	14-Apr-12	-21.43	-64.79	2350	2369	2061	2596	535	8.8
ST344	14-Apr-12	-21.49	-64.76	2001	1997	1923	2238	315	2.8
ST345	15-Apr-12	-21.52	-64.57	2377	2394	1934	3277	1343	250.6
ST346	15-Apr-12	-21.46	-64.50	2318	2318	2238	2434	196	0.9
ST347	15-Apr-12	-21.42	-64.42	2686	2686	2620	2777	157	0.2
ST348	15-Apr-12	-21.42	-64.41	2641	2641	2478	2837	359	1.0
ST349	15-Apr-12	-21.45	-64.36	2349	2349	2138	2494	356	0.1
ST350	15-Apr-12	-21.45	-64.34	2239	2369	2095	2352	257	0.1

ST351	15-Apr-12	-21.41	-64.30	2100	2100	1973	2186	213	0.1
ST352	15-Apr-12	-21.43	-64.27	1897	1905	1652	2095	443	0.2
ST353	15-Apr-12	-21.47	-64.22	1879	1879	1768	1977	209	0.2
ST354	15-Apr-12	-21.48	-64.20	1809	1829	1620	1921	301	0.2
ST355	15-Apr-12	-21.45	-64.07	1327	1339	1077	1662	585	21.1
ST356	15-Apr-12	-21.44	-64.04	1337	1353	1104	1659	555	13.0
ST357	15-Apr-12	-21.44	-64.01	1342	1380	953	2008	1055	45.5
ST358	15-Apr-12	-21.41	-63.82	1270	1295	773	2092	1319	68.5
ST359	15-Apr-12	-21.30	-63.60	896	932	555	1498	943	8.9
ST360	15-Apr-12	-21.23	-63.56	717	717	438	1119	681	3.3
ST361	15-Apr-12	-21.26	-63.55	899	877	456	1268	812	1.6
ST362	15-Apr-12	-21.27	-63.52	606	608	390	1188	798	3.0
ST363	15-Apr-12	-20.10	-63.49	1146	1133	733	1883	1150	286.5
ST364	16-Apr-12	-17.22	-64.46	319	320	226	495	269	18.5
ST365	16-Apr-12	-17.02	-65.56	627	623	430	744	314	0.3
ST366	16-Apr-12	-17.07	-65.66	790	790	692	869	177	0.1
ST367	16-Apr-12	-17.12	-65.69	1673	1673	1015	2306	1291	3.1
ST368	16-Apr-12	-17.14	-65.73	2178	2178	1720	2587	867	0.3
ST369	16-Apr-12	-17.21	-65.82	3480	3374	1887	4632	2745	121.2
ST370	16-Apr-12	-17.27	-65.88	3587	3587	3315	3940	625	17.0
ST371	16-Apr-12	-17.40	-65.86	3966	3966	3677	4150	473	2.1
ST372	17-Apr-12	-17.68	-66.43	3661	3661	3453	3803	350	0.3
ST373	17-Apr-12	-17.71	-66.58	4130	4125	3746	4448	702	124.4
ST374	17-Apr-12	-17.71	-66.58	4151	4142	3748	4337	589	10.0
ST375	17-Apr-12	-17.64	-66.87	4499	4499	4449	4563	114	0.3
ST401	13-Oct-12	-18.39	-66.98	4086	4085	3713	4664	951	107.2
ST402	13-Oct-12	-19.12	-66.77	4302	4286	3713	4907	1194	241.7
ST403	13-Oct-12	-19.39	-67.27	3805	3801	3708	4149	441	60.2
ST404	13-Oct-12	-19.39	-67.27	3796	3800	3696	4069	373	177.4
ST405	14-Oct-12	-20.95	-67.03	4160	4141	3653	5998	2345	12572.1
ST406	14-Oct-12	-20.61	-66.85	3883	3880	3607	5222	1615	6887.1
ST407	15-Oct-12	-20.86	-66.54	4083	4054	3774	4777	1003	694.9
ST408	15-Oct-12	-20.63	-66.68	3949	3973	3653	5222	1569	1933.1
ST409	15-Oct-12	-20.07	-66.88	4153	4165	3760	5397	1637	234.3
ST410	15-Oct-12	-19.62	-66.80	4380	4460	3786	5195	1409	697.8
ST411	15-Oct-12	-19.12	-66.77	4302	4286	3713	4907	1194	241.7
ST412	15-Oct-12	-18.60	-66.91	4103	4116	3704	4771	1067	233.9

Table 3.3. Isotopic data and mean annual precipitation for central Andes stream water catchments

ID	Collection Date	$\delta^{18}O$ (‰, VSMOW)	δD (‰, VSMOW)	d-excess (‰)	$\delta^{18}O$ std error (‰, VSMOW)	δD std error (‰, VSMOW)	d-excess std error (‰)	Analysis Count	TRMM 3B43 Annual Precip. (m) (Bookhagen and Strecker 2008)
ST001	8-Apr-09	-13.40	-103.66	3.51	0.03	0.14	0.17	8	0.37
ST002	8-Apr-09	-13.50	-104.50	3.51	0.07	0.07	0.20	12	0.35
ST003	8-Apr-09	-14.08	-105.57	7.09	0.04	0.18	0.22	12	0.47
ST004	8-Apr-09	-13.64	-107.03	2.06	0.05	0.15	0.21	12	0.24
ST005	8-Apr-09	-11.56	-98.24	-5.75	0.05	0.06	0.16	8	0.30
ST006A	8-Apr-09	-10.85	-83.44	3.37	0.03	0.10	0.13	8	0.35
ST006B	8-Apr-09	-10.87	-83.30	3.70	0.02	0.15	0.17	12	0.35
ST007	8-Apr-09	-14.50	-109.43	6.57	0.03	0.12	0.14	12	0.36
ST008	10-Apr-09	-6.67	-73.07	-19.71	0.06	0.15	0.24	8	0.16
ST009	10-Apr-09	-11.97	-95.22	0.55	0.04	0.08	0.13	8	0.17
ST010	10-Apr-09	-13.95	-103.56	8.02	0.08	0.11	0.25	12	0.19
ST011	10-Apr-09	-13.31	-96.18	10.31	0.10	0.19	0.33	24	0.16
ST012A	10-Apr-09	-12.10	-89.22	7.59	0.05	0.12	0.19	12	0.19
ST012B	10-Apr-09	-15.82	-112.89	13.64	0.05	0.09	0.18	8	0.11
ST013A	10-Apr-09	-12.04	-79.94	16.39	0.09	0.19	0.33	16	0.22
ST013B	10-Apr-09	-12.97	-88.43	15.29	0.09	0.13	0.28	12	0.20
ST014	10-Apr-09	-10.09	-75.95	4.74	0.09	0.14	0.30	16	0.34
ST015A	11-Apr-09	-10.63	-71.49	13.59	0.09	0.17	0.30	16	0.36
ST015B	11-Apr-09	-11.69	-76.58	16.92	0.06	0.09	0.18	4	0.39
ST016	11-Apr-09	-9.08	-64.09	8.58	0.04	0.26	0.28	12	0.39
ST017	11-Apr-09	-11.25	-76.30	13.72	0.08	0.26	0.33	12	0.15
ST018	11-Apr-09	-9.80	-69.73	8.68	0.05	0.17	0.22	12	0.24
ST019	11-Apr-09	-10.82	-75.62	10.95	0.07	0.27	0.33	12	0.19
ST020	11-Apr-09	-7.00	-49.82	6.16	0.07	0.27	0.34	12	0.58
ST021	11-Apr-09	-7.46	-45.75	13.94	0.09	0.31	0.41	12	0.90
ST022	11-Apr-09	-7.49	-47.39	12.54	0.06	0.24	0.30	12	0.62
ST023	11-Apr-09	-5.90	-37.29	9.93	0.07	0.28	0.34	12	0.91
ST024	11-Apr-09	-7.81	-48.93	13.54	0.04	0.08	0.13	8	0.69
ST025	11-Apr-09	-7.85	-47.47	15.35	0.09	0.30	0.39	8	1.25
ST026	12-Apr-09	-5.59	-39.51	5.17	0.08	0.21	0.31	12	0.84

ST027	12-Apr-09	-6.76	-43.87	10.23	0.05	0.09	0.17	12	0.53
ST028	12-Apr-09	-6.23	-40.87	8.94	0.13	0.48	0.60	16	0.43
ST029	12-Apr-09	-7.30	-48.01	10.36	0.05	0.18	0.22	16	0.50
ST030	12-Apr-09	-7.69	-46.97	14.54	0.04	0.12	0.17	8	0.84
ST031	12-Apr-09	-7.38	-42.61	16.42	0.07	0.29	0.35	8	1.34
ST032	12-Apr-09	-6.81	-40.72	13.80	0.07	0.25	0.32	8	1.06
ST033	12-Apr-09	-7.47	-43.68	16.04	0.09	0.27	0.38	12	1.58
ST034	12-Apr-09	-6.63	-40.75	12.31	0.09	0.25	0.36	8	1.09
ST035	12-Apr-09	-6.15	-38.99	10.21	0.07	0.22	0.30	8	1.00
ST036	12-Apr-09	-5.78	-35.93	10.29	0.08	0.25	0.34	8	1.24
ST037	12-Apr-09	-6.34	-41.11	9.62	0.01	0.09	0.10	16	0.62
ST038	12-Apr-09	-6.32	-46.37	4.22	0.04	0.12	0.18	8	0.49
ST039A	12-Apr-09	-6.77	-44.98	9.21	0.04	0.06	0.12	8	0.50
ST039B	12-Apr-09	-6.53	-42.82	9.39	0.06	0.05	0.18	8	0.63
ST040	13-Apr-09	-6.50	-42.13	9.84	0.03	0.05	0.09	8	0.92
ST041	13-Apr-09	-6.89	-43.82	11.27	0.06	0.16	0.23	8	1.17
ST042	13-Apr-09	-6.77	-42.49	11.66	0.03	0.11	0.14	8	0.84
ST043	13-Apr-09	-5.89	-37.73	9.38	0.06	0.13	0.20	8	1.15
ST045	13-Apr-09	-6.61	-39.88	12.98	0.05	0.07	0.15	8	0.84
ST046	14-Apr-09	-7.14	-44.57	12.59	0.03	0.13	0.15	8	0.70
ST047	14-Apr-09	-9.94	-68.38	11.18	0.06	0.25	0.31	8	0.17
ST048A	14-Apr-09	-8.34	-60.82	5.87	0.06	0.18	0.24	8	0.61
ST048B	14-Apr-09	-10.11	-69.70	11.15	0.02	0.10	0.11	8	0.45
ST049	14-Apr-09	-11.06	-74.25	14.22	0.02	0.14	0.15	8	0.42
ST050	14-Apr-09	-9.41	-69.85	5.41	0.03	0.18	0.19	8	0.34
ST051	14-Apr-09	-9.10	-70.96	1.85	0.03	0.12	0.15	8	0.29
ST052	15-Apr-09	-12.66	-100.62	0.69	0.02	0.17	0.18	8	0.20
ST053	15-Apr-09	-13.98	-108.97	2.89	0.01	0.22	0.22	8	0.26
ST054	15-Apr-09	-13.91	-107.75	3.56	0.03	0.23	0.24	8	0.24
ST055	15-Apr-09	-13.09	-102.95	1.80	0.02	0.14	0.16	8	0.37
ST101	13-Apr-10	-11.94	-95.38	0.14	0.02	0.10	0.12	8	0.35
ST102	13-Apr-10	-12.70	-97.96	3.60	0.03	0.06	0.10	8	0.37
ST103	13-Apr-10	-11.56	-93.44	-0.97	0.03	0.07	0.11	8	0.35
ST104	13-Apr-10	-11.17	-93.59	-4.27	0.01	0.07	0.08	8	0.24
ST105	13-Apr-10	-8.77	-87.56	-17.41	0.03	0.08	0.11	8	0.30
ST106	13-Apr-10	-13.93	-107.89	3.57	0.03	0.05	0.10	12	0.36

ST107	15-Apr-10	-2.72	-55.28	-33.49	0.03	0.11	0.14	8	0.16
ST108	15-Apr-10	-11.16	-91.58	-2.33	0.03	0.06	0.10	8	0.17
ST109	15-Apr-10	-11.41	-90.85	0.45	0.02	0.05	0.07	8	0.19
ST110	15-Apr-10	-10.94	-80.80	6.69	0.03	0.05	0.11	8	0.19
ST111	15-Apr-10	-11.67	-79.16	14.21	0.02	0.06	0.09	8	0.22
ST112	15-Apr-10	-12.08	-84.57	12.03	0.03	0.12	0.15	8	0.20
ST113	15-Apr-10	-6.97	-60.63	-4.86	0.02	0.16	0.18	8	0.34
ST114	16-Apr-10	-8.91	-65.97	5.34	0.04	0.24	0.26	8	0.23
ST115	16-Apr-10	-7.97	-58.54	5.23	0.04	0.08	0.13	12	0.22
ST116	16-Apr-10	-10.69	-76.49	9.02	0.02	0.08	0.10	8	0.24
ST117	16-Apr-10	-7.11	-59.36	-2.49	0.01	0.08	0.09	8	0.23
ST118	16-Apr-10	-5.86	-47.03	-0.17	0.03	0.08	0.11	8	0.64
ST119	16-Apr-10	-7.74	-58.04	3.85	0.02	0.16	0.18	8	0.41
ST120	16-Apr-10	-9.93	-68.07	11.38	0.03	0.14	0.16	8	0.17
ST121	16-Apr-10	-7.99	-50.59	13.31	0.04	0.21	0.24	8	0.58
ST122	16-Apr-10	-7.57	-48.45	12.13	0.03	0.09	0.11	12	0.76
ST123	17-Apr-10	-4.90	-37.54	1.68	0.05	0.04	0.14	8	0.82
ST124	17-Apr-10	-3.35	-31.88	-5.08	0.03	0.10	0.14	8	0.53
ST125	17-Apr-10	-1.77	-24.25	-10.08	0.03	0.08	0.12	8	0.43
ST126	17-Apr-10	-5.43	-39.16	4.26	0.03	0.09	0.11	8	0.55
ST127	17-Apr-10	-7.28	-49.89	8.36	0.05	0.06	0.15	8	0.50
ST128	17-Apr-10	-6.23	-44.38	5.44	0.03	0.06	0.11	8	0.50
ST129	17-Apr-10	-6.97	-44.63	11.10	0.02	0.13	0.14	8	0.84
ST130	17-Apr-10	-7.16	-46.55	10.71	0.04	0.09	0.15	8	0.78
ST131	17-Apr-10	-6.82	-42.03	12.53	0.03	0.13	0.15	8	1.34
ST132	17-Apr-10	-6.76	-41.48	12.63	0.04	0.16	0.19	8	1.06
ST133	17-Apr-10	-4.38	-36.27	-1.21	0.08	0.26	0.35	16	1.58
ST134	18-Apr-10	-5.56	-34.52	9.95	0.09	0.32	0.42	16	1.10
ST135	18-Apr-10	-6.05	-37.22	11.20	0.07	0.37	0.43	8	1.11
ST136	18-Apr-10	-5.90	-38.42	8.77	0.07	0.29	0.35	8	0.62
ST137	18-Apr-10	-6.46	-43.73	7.98	0.04	0.22	0.25	8	0.64
ST139	18-Apr-10	-6.37	-41.13	9.83	0.03	0.22	0.24	8	1.01
ST140	19-Apr-10	-7.93	-50.30	13.14	0.02	0.09	0.10	8	4.49
ST141	19-Apr-10	-8.66	-54.82	14.49	0.04	0.20	0.23	8	3.00
ST142	19-Apr-10	-8.13	-52.93	12.11	0.04	0.13	0.18	8	1.47
ST143	19-Apr-10	-10.37	-71.57	11.39	0.04	0.25	0.28	8	0.28

ST144	19-Apr-10	-11.26	-80.11	9.94	0.03	0.16	0.18	8	0.22
ST145	19-Apr-10	-9.24	-81.06	-7.12	0.05	0.13	0.20	8	0.28
ST146	20-Apr-10	-12.55	-90.46	9.96	0.05	0.09	0.18	8	0.58
ST147	20-Apr-10	-11.42	-86.27	5.07	0.03	0.08	0.11	8	0.42
ST148	20-Apr-10	-9.80	-81.66	-3.29	0.05	0.08	0.16	8	0.39
ST201	5-Apr-11	-11.95	-105.26	-9.66	0.02	0.19	0.20	8	0.36
ST202	5-Apr-11	-15.60	-116.52	8.31	0.05	0.34	0.38	12	0.35
ST203	5-Apr-11	-15.00	-114.70	5.33	0.03	0.35	0.36	16	0.37
ST204	5-Apr-11	-15.18	-115.18	6.23	0.02	0.05	0.07	8	0.35
ST205	5-Apr-11	-16.13	-118.91	10.14	0.04	0.08	0.14	8	0.47
ST206	5-Apr-11	-14.02	-109.46	2.68	0.02	0.38	0.39	12	0.24
ST207	5-Apr-11	-13.56	-112.01	-3.55	0.05	0.29	0.32	12	0.35
ST208	6-Apr-11	-15.62	-117.49	7.50	0.10	0.24	0.36	8	0.36
ST209	7-Apr-11	-10.01	-86.22	-6.14	0.05	0.06	0.15	8	0.15
ST210	7-Apr-11	3.70	-24.21	-53.85	0.07	0.19	0.26	12	0.16
ST211	8-Apr-11	-5.48	-71.56	-27.73	0.05	0.15	0.21	8	0.16
ST212	8-Apr-11	-12.95	-98.36	5.23	0.02	0.16	0.17	8	0.19
ST213	8-Apr-11	-12.72	-90.61	11.14	0.03	0.27	0.28	12	0.11
ST214	8-Apr-11	-13.01	-86.67	17.42	0.04	0.25	0.28	12	0.22
ST215	8-Apr-11	-13.74	-95.80	14.11	0.02	0.08	0.09	8	0.20
ST216	8-Apr-11	-9.91	-76.42	2.88	0.01	0.20	0.20	8	0.34
ST217	9-Apr-11	-11.54	-78.76	13.54	0.02	0.25	0.25	16	0.23
ST218	9-Apr-11	-11.12	-74.64	14.30	0.02	0.19	0.20	12	0.22
ST219	9-Apr-11	-9.92	-70.51	8.81	0.02	0.14	0.15	8	0.23
ST220	9-Apr-11	-10.93	-73.13	14.33	0.07	0.18	0.27	12	0.41
ST221	9-Apr-11	-10.96	-74.05	13.61	0.05	0.23	0.27	12	0.17
ST222	9-Apr-11	-10.48	-68.12	15.74	0.04	0.22	0.25	12	0.20
ST223	9-Apr-11	-9.54	-58.26	18.06	0.03	0.21	0.23	12	0.58
ST224	9-Apr-11	-8.89	-54.43	16.72	0.05	0.20	0.24	12	0.62
ST225	9-Apr-11	-9.07	-57.21	15.35	0.03	0.19	0.21	12	0.70
ST226	9-Apr-11	-9.31	-58.77	15.69	0.02	0.07	0.10	12	0.83
ST227	9-Apr-11	-7.72	-49.90	11.83	0.02	0.23	0.24	8	0.76
ST228	10-Apr-11	-9.58	-61.75	14.91	0.07	0.27	0.32	12	0.53
ST229	10-Apr-11	-8.63	-61.04	7.99	0.07	0.34	0.40	12	0.43
ST230	10-Apr-11	-9.94	-66.48	13.07	0.05	0.17	0.22	8	0.50
ST231	10-Apr-11	-9.01	-58.25	13.84	0.04	0.22	0.25	8	0.50

ST232	10-Apr-11	-8.48	-51.71	16.10	0.02	0.11	0.13	12	0.84
ST233	10-Apr-11	-8.96	-55.46	16.18	0.02	0.10	0.12	12	1.06
ST234	10-Apr-11	-8.50	-49.88	18.12	0.05	0.22	0.26	12	1.58
ST235	10-Apr-11	-7.16	-45.50	11.80	0.05	0.20	0.24	12	1.15
ST236	10-Apr-11	-5.67	-40.44	4.94	0.02	0.08	0.10	12	1.15
ST237	10-Apr-11	-6.12	-41.08	7.91	0.03	0.19	0.21	8	1.24
ST238	10-Apr-11	-6.62	-43.47	9.48	0.03	0.11	0.15	8	0.62
ST239	10-Apr-11	-6.12	-43.05	5.93	0.03	0.53	0.54	8	0.63
ST240	10-Apr-11	-7.69	-47.87	13.65	0.05	0.23	0.27	12	0.64
ST241	10-Apr-11	-5.14	-36.53	4.56	0.06	0.17	0.24	12	0.74
ST242	10-Apr-11	-7.65	-47.97	13.24	0.06	0.36	0.40	8	1.01
ST243	10-Apr-11	-6.75	-41.71	12.26	0.06	0.30	0.34	8	1.16
ST244	11-Apr-11	-6.95	-45.71	9.91	0.04	0.17	0.20	12	0.78
ST245	12-Apr-11	-6.56	-41.62	10.83	0.04	0.17	0.21	12	1.38
ST246	12-Apr-11	-7.85	-48.11	14.67	0.03	0.07	0.10	12	3.08
ST247	12-Apr-11	-9.74	-61.46	16.48	0.04	0.38	0.40	8	0.00
ST248	12-Apr-11	-9.04	-55.59	16.70	0.04	0.22	0.25	12	3.00
ST249	12-Apr-11	-10.97	-70.06	17.71	0.05	0.38	0.41	8	1.47
ST250	12-Apr-11	-12.05	-78.55	17.83	0.04	0.16	0.20	12	0.28
ST251	12-Apr-11	-12.99	-90.20	13.74	0.04	0.25	0.28	12	0.22
ST252	12-Apr-11	-14.00	-103.49	8.50	0.06	0.16	0.24	8	0.28
ST253	12-Apr-11	-14.41	-102.72	12.55	0.02	0.12	0.13	8	0.58
ST254	13-Apr-11	-12.69	-97.75	3.77	0.03	0.22	0.23	20	0.48
ST255	13-Apr-11	-13.91	-106.91	4.36	0.03	0.17	0.19	8	0.39
ST301	10-Apr-12	-12.08	-100.91	-4.27	0.06	0.34	0.37	16	0.43
ST302	10-Apr-12	-11.95	-101.19	-5.60	0.06	0.35	0.39	16	0.36
ST303	10-Apr-12	-14.23	-108.30	5.54	0.06	0.29	0.33	16	0.35
ST303B	10-Apr-12	-14.36	-108.21	6.68	0.06	0.31	0.35	16	0.35
ST304	10-Apr-12	-14.24	-107.62	6.30	0.06	0.31	0.35	24	0.37
ST305	10-Apr-12	-13.64	-103.39	5.70	0.06	0.26	0.31	20	0.35
ST306	10-Apr-12	-15.31	-111.40	11.09	0.08	0.35	0.41	16	0.47
ST307	10-Apr-12	-13.96	-108.17	3.53	0.05	0.31	0.34	16	0.24
ST308	10-Apr-12	-11.42	-100.37	-9.04	0.06	0.27	0.31	16	0.30
ST309	10-Apr-12	-12.55	-105.90	-5.53	0.05	0.32	0.35	16	0.35
ST310	11-Apr-12	-15.69	-115.62	9.90	0.05	0.33	0.35	16	0.36
ST311	11-Apr-12	-12.43	-98.90	0.54	0.05	0.29	0.32	16	0.28

ST312	11-Apr-12	-13.25	-102.97	3.06	0.04	0.30	0.32	16	0.30
ST313	11-Apr-12	-13.54	-106.15	2.13	0.06	0.32	0.36	16	0.26
ST314	11-Apr-12	-13.84	-105.78	4.91	0.02	0.18	0.19	8	0.25
ST315	11-Apr-12	-11.31	-95.27	-4.83	0.05	0.35	0.37	8	0.27
ST317	12-Apr-12	-11.39	-94.96	-3.87	0.03	0.27	0.28	8	0.15
ST318	12-Apr-12	-7.65	-81.58	-20.39	0.06	0.29	0.33	8	0.16
ST319	13-Apr-12	-16.17	-119.81	9.58	0.05	0.36	0.39	16	0.16
ST320	13-Apr-12	-16.38	-123.60	7.46	0.04	0.16	0.19	8	0.12
ST321	13-Apr-12	-12.91	-101.58	1.68	0.06	0.30	0.35	12	0.17
ST322	13-Apr-12	-12.95	-101.32	2.28	0.05	0.27	0.31	16	0.14
ST323	13-Apr-12	-12.40	-90.37	8.84	0.06	0.35	0.40	8	0.19
ST324	13-Apr-12	-12.08	-88.14	8.48	0.05	0.28	0.31	12	0.11
ST325	13-Apr-12	-12.63	-88.28	12.72	0.07	0.37	0.41	12	0.20
ST326	13-Apr-12	-11.83	-81.74	12.89	0.04	0.35	0.36	12	0.22
ST327	13-Apr-12	-12.60	-95.37	5.46	0.05	0.34	0.37	12	0.25
ST328	13-Apr-12	-13.43	-96.88	10.59	0.03	0.32	0.33	12	0.25
ST329	13-Apr-12	-14.09	-104.88	7.81	0.07	0.25	0.31	12	0.34
ST330	14-Apr-12	-12.23	-87.39	10.49	0.07	0.32	0.38	8	0.23
ST331	14-Apr-12	-13.29	-97.16	9.17	0.09	0.29	0.39	8	0.22
ST332	14-Apr-12	-11.77	-82.67	11.48	0.07	0.24	0.32	12	0.24
ST333	14-Apr-12	-9.94	-70.69	8.85	0.07	0.19	0.28	12	0.12
ST334	14-Apr-12	-10.54	-72.13	12.18	0.10	0.23	0.36	8	0.12
ST335	14-Apr-12	-10.98	-77.26	10.59	0.07	0.20	0.29	8	0.23
ST336	14-Apr-12	-10.62	-72.79	12.19	0.08	0.17	0.28	8	0.21
ST337	14-Apr-12	-12.78	-90.16	12.09	0.09	0.37	0.45	8	0.41
ST338	14-Apr-12	-10.51	-71.45	12.62	0.07	0.21	0.28	12	0.17
ST339	14-Apr-12	-10.17	-67.10	14.26	0.07	0.17	0.25	8	0.20
ST340	14-Apr-12	-8.98	-56.83	15.03	0.06	0.31	0.35	12	0.58
ST341	14-Apr-12	-8.43	-53.02	14.42	0.02	0.11	0.12	8	0.62
ST342	14-Apr-12	-8.34	-55.53	11.19	0.07	0.18	0.27	8	0.70
ST343	14-Apr-12	-8.60	-57.69	11.15	0.08	0.17	0.29	8	0.83
ST344	14-Apr-12	-7.83	-49.21	13.47	0.03	0.08	0.12	8	0.76
ST345	15-Apr-12	-6.90	-51.64	3.53	0.02	0.08	0.10	8	0.53
ST346	15-Apr-12	-8.57	-57.40	11.14	0.03	0.14	0.16	8	0.43
ST347	15-Apr-12	-9.20	-61.48	12.13	0.02	0.13	0.14	8	0.50
ST348	15-Apr-12	-9.05	-58.64	13.78	0.05	0.10	0.16	8	0.50

ST349	15-Apr-12	-8.42	-51.74	15.62	0.03	0.05	0.10	8	0.84
ST350	15-Apr-12	-8.33	-50.73	15.88	0.05	0.07	0.15	8	0.84
ST351	15-Apr-12	-8.53	-53.81	14.41	0.05	0.09	0.15	8	1.40
ST352	15-Apr-12	-8.39	-52.72	14.42	0.05	0.07	0.15	8	1.06
ST353	15-Apr-12	-8.26	-49.32	16.76	0.05	0.04	0.15	7	1.58
ST354	15-Apr-12	-8.13	-50.14	14.94	0.05	0.23	0.27	16	1.41
ST355	15-Apr-12	-6.47	-41.99	9.77	0.07	0.33	0.38	8	1.15
ST356	15-Apr-12	-5.48	-39.05	4.79	0.09	0.31	0.40	8	1.15
ST357	15-Apr-12	-6.44	-40.37	11.15	0.08	0.28	0.35	8	1.24
ST358	15-Apr-12	-6.53	-42.37	9.84	0.08	0.27	0.35	8	0.62
ST359	15-Apr-12	-7.99	-50.57	13.31	0.05	0.19	0.24	8	0.64
ST360	15-Apr-12	-6.53	-43.86	8.38	0.08	0.04	0.22	8	0.74
ST361	15-Apr-12	-7.30	-46.02	12.41	0.05	0.12	0.18	8	1.01
ST362	15-Apr-12	-6.77	-43.46	10.71	0.05	0.07	0.16	8	1.16
ST363	15-Apr-12	-7.97	-54.07	9.68	0.06	0.06	0.17	8	0.78
ST364	16-Apr-12	-9.34	-62.69	12.07	0.09	0.21	0.32	8	3.08
ST365	16-Apr-12	-10.30	-68.15	14.22	0.08	0.21	0.31	8	4.44
ST366	16-Apr-12	-9.56	-61.56	14.90	0.08	0.17	0.29	8	3.04
ST367	16-Apr-12	-10.80	-70.42	15.98	0.06	0.16	0.24	8	2.03
ST368	16-Apr-12	-11.07	-74.16	14.38	0.03	0.18	0.20	8	1.47
ST369	16-Apr-12	-12.07	-81.24	15.31	0.04	0.08	0.15	8	0.28
ST370	16-Apr-12	-13.22	-93.18	12.58	0.03	0.13	0.15	8	0.22
ST371	16-Apr-12	-13.73	-100.02	9.80	0.06	0.16	0.23	8	0.28
ST372	17-Apr-12	-14.24	-100.94	12.95	0.03	0.13	0.16	8	0.58
ST373	17-Apr-12	-14.06	-104.89	7.62	0.04	0.16	0.19	8	0.42
ST374	17-Apr-12	-13.96	-100.96	10.73	0.05	0.12	0.18	8	0.48
ST375	17-Apr-12	-14.86	-110.87	8.03	0.07	0.12	0.23	8	0.39
ST401	13-Oct-12	-13.61	-105.55	3.33	0.03	0.11	0.13	8	0.37
ST402	13-Oct-12	-13.02	-103.73	0.40	0.02	0.08	0.10	8	0.24
ST403	13-Oct-12	-8.42	-89.12	-21.80	0.01	0.11	0.11	8	0.30
ST404	13-Oct-12	-11.40	-102.61	-11.40	0.02	0.09	0.11	8	0.35
ST405	14-Oct-12	-9.08	-81.66	-9.02	0.04	0.08	0.13	8	0.15
ST406	14-Oct-12	5.44	-18.73	-62.25	0.04	0.14	0.17	8	0.16
ST407	15-Oct-12	-11.52	-93.47	-1.28	0.02	0.14	0.16	8	0.17
ST408	15-Oct-12	-2.82	-60.44	-37.86	0.02	0.14	0.15	8	0.16
ST409	15-Oct-12	-11.73	-97.17	-3.29	0.02	0.10	0.12	8	0.27

ST410	15-Oct-12	-12.69	-101.09	0.45	0.03	0.09	0.13	8	0.25
ST411	15-Oct-12	-12.46	-101.98	-2.27	0.02	0.07	0.09	8	0.24
ST412	15-Oct-12	-11.84	-96.97	-2.24	0.04	0.07	0.14	8	0.35

Appendix 3B. Multivariate linear regression analysis of central Andes stream water compositions and analysis of uncertainty in the isotope-elevation relationship

Multivariate linear regression of central Andes stream water isotopic compositions

Many prior studies of the isotopic composition of precipitation and stream waters have constructed predictive multivariate linear models to understand the spatial distribution of water isotopologues [e.g., *Bowen and Wilkinson*, 2002; *Dutton et al.*, 2005; *Lechler and Niemi*, 2012; *Fiorella et al.*, 2015]. We constructed a hierarchical suite of multivariate linear model fits between the isotopic composition of stream waters ($\delta^{18}O_w$ and δD_w) with geographic (e.g., sampling latitude, sampling longitude, and mean catchment elevation) and climatic (e.g., mean annual precipitation) parameters. Models were constructed using all of the catchments at first, and then recalculated using only subsets of the data corresponding to: (a) only flank catchments or (b) only plateau catchments to determine if spatial relationships were regionally consistent. Results including all catchments are provided in Table 3.4, while results for flank catchments only or plateau catchments only are provided in Table 3.5 and Table 3.6 respectively.

The "best" multivariate linear model for each subset was chosen based on two different criteria. First, we rejected any models where two of the predictor variables (e.g., latitude, longitude, elevation, or annual precipitation) exhibited correlations stronger than $r = 0.5$. Multivariate linear regression assumes that the predictor variables are uncorrelated; inclusion of multiple correlated predictor variables can result in overfitting the model. Across the central Andes, for example, elevation can be strongly correlated with longitude or annual precipitation (Table 3.7). With the remaining set of models, we sought to minimize the Akaike Information Criterion [AIC; e.g., *Burnham and Anderson*, 2003]. The AIC seeks to optimize the trade-off between model complexity and fraction of variability explained; low AIC scores are associated with models that better fit the data.

Based on these model selection criteria, we determine that multivariate models using mean catchment elevation and sampling latitude best describe the isotopic compositions of stream waters for the entire dataset as well as the flank catchments only subset. In contrast, Altiplano catchment isotopic compositions are best described by a model retaining the mean catchment elevation and mean annual precipitation as predictor variables.

Table 3.4. Multivariate linear regressions between the isotopic compositions of all stream waters and environmental variables.

Models relating $\delta^{18}O$ and environmental variables						
Model	*Elevation (‰/m)*	*Latitude (‰/°)*	*Annual Precipitation (‰/m)*	*Intercept (‰)*	*r^2*	*AIC*
elev + lat + precip	*$-1.67x10^{-3}$*	*-0.671*	-0.318	*-18.20*	0.513	1127.3
elev + precip	*$-2.25x10^{-3}$*	N/A	*-1.41*	*-2.17*	0.447	1156.8
elev + lat	***$-1.54x10^{-3}$***	***-0.720***	***N/A***	***-19.78***	***0.511***	***1126.0***
lat + precip	N/A	*-1.18*	*2.17*	*-32.11*	0.369	1189.8
elev	*$-1.74x10^{-3}$*	N/A	N/A	*-4.55*	0.410	1170.0
lat	N/A	*-1.00*	N/A	*-30.21*	0.207	1244.6
precip	N/A	N/A	*1.61*	*-10.83*	0.093	1277.9
Models relating δD and environmental variables						
Model	*Elevation (‰/m)*	*Latitude (‰/°)*	*Annual Precipitation (‰/m)*	*Intercept (‰)*	*r^2*	*AIC*
elev + lat + precip	*$-1.49x10^{-2}$*	*-6.03*	0.668	*-149.6*	0.757	1972.6
elev + precip	*$-2.01x10^{-2}$*	N/A	*-9.14*	-5.36	0.668	2048.2
elev + lat	***$-1.52x10^{-2}$***	***-5.93***	**N/A**	***-146.2***	**0.756**	**1970.7**
lat + precip	N/A	*-10.57*	*22.87*	*-300.64*	0.564	2115.9
elev	*$-1.69x10^{-2}$*	N/A	N/A	*-20.82*	0.642	2065.0
lat	N/A	*-8.71*	N/A	*-249.0*	0.262	2244.9
precip	N/A	N/A	*17.91*	*-82.91*	0.193	2267.2

Table 3.5. Multivariate linear regressions between the isotopic compositions of flank stream waters and environmental variables.

Models relating flank $\delta^{18}O$ and environmental variables						
Model	*Elevation (‰/m)*	*Latitude (‰/°)*	*Annual Precipitation (‰/m)*	*Intercept (‰)*	*r^2*	*AIC*
elev + lat + precip	*$-1.64x10^{-3}$*	*-0.592*	-0.191	*-16.82*	0.673	665.2
elev + precip	*$-2.02x10^{-3}$*	N/A	*-1.07*	*-2.98*	0.582	707.4
elev + lat	***$-1.56x10^{-3}$***	***-0.624***	**N/A**	***-17.82***	**0.672**	**663.7**
lat + precip	N/A	*-0.991*	*1.97*	*-30.95*	0.407	770.2
elev	*$-1.61x10^{-3}$*	N/A	N/A	*-4.84*	0.537	723.7
lat	N/A	*-0.694*	N/A	*-23.41*	0.168	829.2
precip	N/A	N/A	*1.23*	*-9.99*	0.104	842.5
Models relating flank δD and environmental variables						
Model	*Elevation (‰/m)*	*Latitude (‰/°)*	*Annual Precipitation (‰/m)*	*Intercept (‰)*	*r^2*	*AIC*
elev + lat + precip	*$-1.30x10^{-2}$*	*-4.94*	-0.505	*-130.1*	0.770	1338.0
elev + precip	*$-1.61x10^{-2}$*	N/A	*-6.82*	*-14.74*	0.664	1404.3
elev + lat	***$-1.32x10^{-2}$***	***-4.85***	**N/A**	***-127.5***	**0.770**	**1336.1**
lat + precip	N/A	-8.09	17.62	-241.83	0.491	1478.6
elev	*$-1.35x10^{-2}$*	N/A	N/A	*-26.55*	0.633	1417.9
lat	N/A	*-5.44*	N/A	*-174.51*	0.173	1564.2
precip	N/A	N/A	*11.51*	*-70.67*	0.153	1568.4

Table 3.6. Multivariate linear regressions between the isotopic compositions of Altiplano stream waters and environmental variables.

Models relating Altiplano $\delta^{18}O$ and environmental variables							
Model	*Elevation (‰/m)*	*Latitude (‰/°)*	*Longitude (‰/°)*	*Annual Precipitation (‰/m)*	*Intercept (‰)*	r^2	*AIC*
elev + lat + lon + precip	*$-7.11x10^{-3}$*	$7.51x10^{-2}$	-0.962	*-19.53*	-40.27	0.326	368.7
elev + lat + lon	*$-7.96x10^{-3}$*	*-1.23*	0.703	N/A	43.57	0.271	372.1
elev + lat + precip	*$-7.66x10^{-3}$*	$6.70x10^{-2}$	N/A	*-17.47*	25.62	0.323	367.0
elev + lon + precip	*$-7.08x10^{-3}$*	N/A	-0.959	*-18.90*	-41.84	0.326	366.7
lat + lon + precip	N/A	-0.205	-2.80	*-23.00*	-196.90	0.244	374.6
elev + lat	*$-7.54x10^{-3}$*	*-1.34*	N/A	N/A	-7.43	0.269	370.3
elev + lon	*$-1.02x10^{-2}$*	N/A	2.60	N/A	*203.46*	0.209	375.7
elev + precip	***$-7.60x10^{-3}$***	**N/A**	**N/A**	***-16.92***	***24.02***	**0.322**	**365.0**
lat + lon	N/A	*-1.82*	-1.06	N/A	-118.46	0.167	379.3
lat + precip	N/A	-0.308	N/A	*-16.89*	-13.11	0.211	375.5
lon + precip	N/A	N/A	-2.83	*-24.80*	-194.56	0.244	374.6
elev	*$-9.20x10^{-3}$*	N/A	N/A	N/A	*25.68*	0.170	377.1
lat	N/A	*-1.67*	N/A	N/A	*-44.47*	0.161	377.8
lon	N/A	N/A	1.31	N/A	74.94	0.011	389.2
prec	N/A	N/A	N/A	*-19.49*	*-6.37*	0.210	373.7
Models relating Altiplano δD and environmental variables							
Model	*Elevation (‰/m)*	*Latitude (‰/°)*	*Longitude (‰/°)*	*Annual Precipitation (‰/m)*	*Intercept (‰)*	r^2	*AIC*
elev + lat + lon + precip	*$-3.01x10^{-2}$*	-1.27	-0.431	-73.09	-7.76	0.305	583.6
elev + lat + lon	*$-3.33x10^{-2}$*	*-6.16*	5.80	N/A	306.04	0.270	585.0
elev + lat + precip	*$-3.04x10^{-2}$*	-1.27	N/A	-72.17	21.78	0.305	581.6
elev + lon + precip	*$-3.07x10^{-2}$*	N/A	-0.484	*-83.70*	18.62	0.304	581.7
lat + lon + precip	N/A	-2.45	-8.23	*-87.82*	-671.90	0.238	588.0
elev + lat	*$-2.99x10^{-2}$*	*-7.12*	N/A	N/A	-114.72	0.264	583.6
elev + lon	*$-4.46x10^{-2}$*	N/A	*15.26*	N/A	*1104.99*	0.199	589.4
elev + precip	***$-3.10x10^{-2}$***	**N/A**	**N/A**	***-82.70***	**51.89**	**0.304**	**579.7**
lat + lon	N/A	*-8.62*	-1.59	N/A	-372.43	0.187	590.5
lat + precip	N/A	-2.75	N/A	-69.87	-131.80	0.225	587.1
lon + precip	N/A	N/A	-8.62	*-109.29*	-643.91	0.233	586.4
elev	*$-3.87x10^{-2}$*	N/A	N/A	N/A	59.98	0.137	592.6
lat	N/A	*-8.40*	N/A	N/A	*-261.54*	0.186	588.5
lon	N/A	N/A	9.65	N/A	548.25	0.026	600.9
prec	N/A	N/A	N/A	*-93.15*	*-71.50*	0.219	585.7

Table 3.7. Correlations between potential predictor variables.

All Streams			
	Latitude	Longitude	Annual Precipitation
Elevation	0.226	**-0.847**	**-0.693**
Latitude		**-0.539**	0.196
Longitude			0.402
All Flank Streams			
	Latitude	Longitude	Annual Precipitation
Elevation	0.058	**-0.825**	**-0.658**
Latitude		-0.475	0.337
Longitude			0.274
All Altiplano Streams			
	Latitude	Longitude	Annual Precipitation
Elevation	0.230	0.221	0.177
Latitude		-0.427	**0.826**
Longitude			**-0.559**

Table 3.8. Candidate empirical linear models of the isotope-elevation relationship in the central Andes

Model description		**Elevation coefficient (m/‰) (with ±1σ)**	**Intercept (m) (with ±1σ)**	**2σ Prediction Interval (m)**	**Number of streams included in model**	**r^2**
This study – all April streams		-269.1 ± 18.0	331.4 ± 186.3	1800	236	0.49
This study – all eastern flank streams		-333.2 ± 23.2	385.4 ± 219.6	1600	179	0.54
This study – separate regressions N/S of 20°S	North of 20°S	-366.6 ± 43.1	-939.7 ± 539.4	1660	79	0.48
	South of 20°S	-212.5 ± 24.0	941.7 ± 220.7	1900	168	0.32
This study – separate regressions for N/S transects	North Transect	-500.1 ± 73.0	-2849.6 ± 838.8	2000	31	0.61
	South Transect	-358.5 ± 23.9	-477.1 ± 214.1	1420	147	0.61
Bershaw et al. (2010) – transect at ~16°S		-536.4	-3201.7	1000	82	0.92

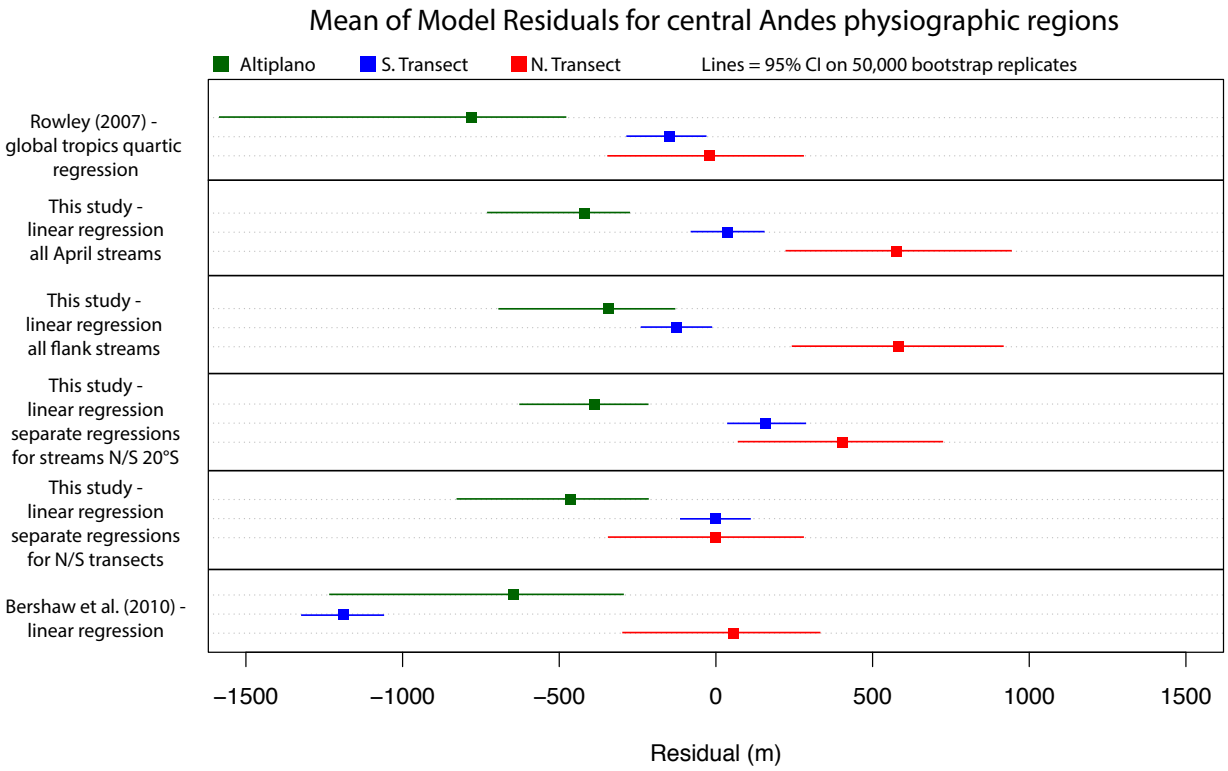

Figure 3.10. Mean residual for each physiographic region and model. Horizontal lines indicate the 95% confidence interval calculated from 50,000 bootstrap replicates with replacement.

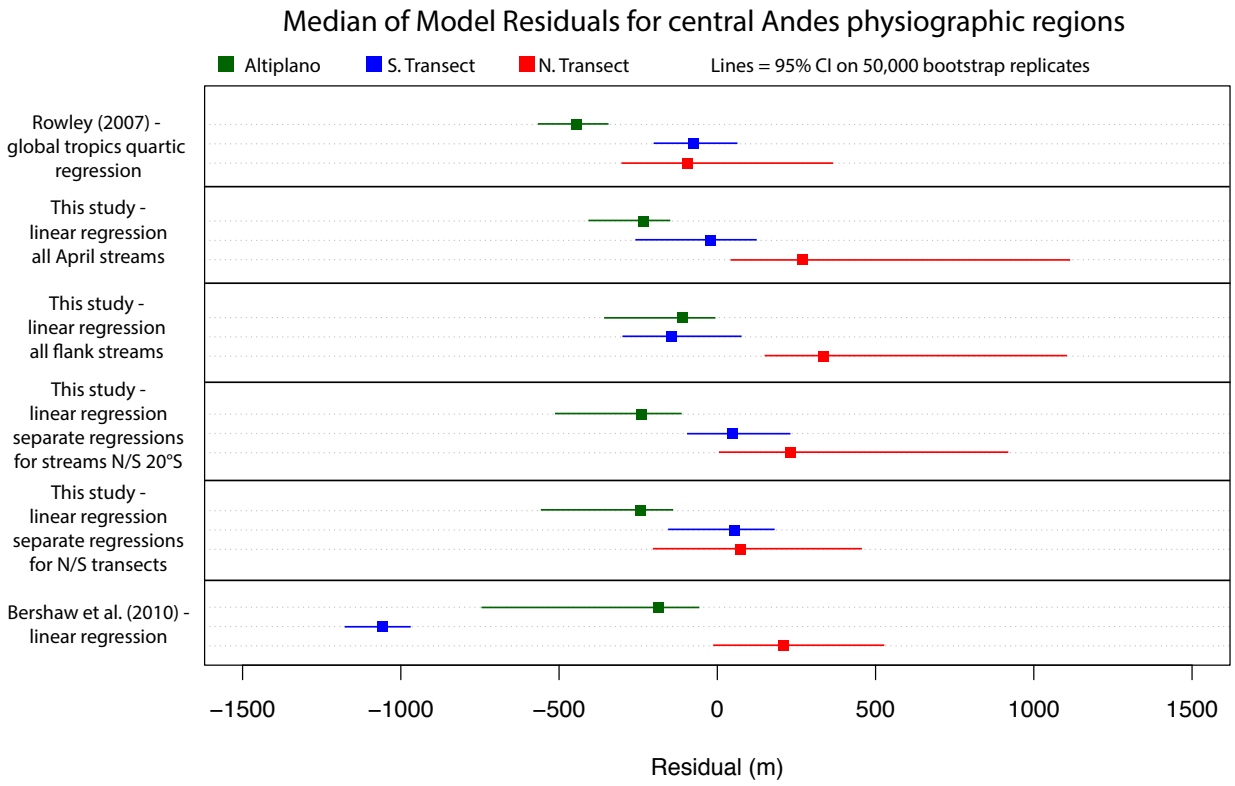

Figure 3.11. Median residual for each physiographic region and model. Horizontal lines indicate the 95% confidence interval calculated from 50,000 bootstrap replicates with replacement.

Alternate models of the isotope-elevation relationship of central Andes surface waters

The Mann-Whitney U test was used to determine if the mean residuals from the three physiographic regions follow the same distribution. We determined if the mean residual for the distributions from the three physiographic regions tested were statistically distinguishable from each other using the Mann-Whitney U test. We considered each set of physiographic regions pairwise (N. vs. S. Transect, N. Transect vs. Altiplano, S. Transect vs. Altiplano) for the Rowley (2007) model and our linear regressions. These tests show that mean residuals for the Altiplano were distinct from the flanks, while flank mean residuals were not statistically distinguishable from each other (Table 3.9).

Table 3.9. Mann-Whitney U test results for each model and pair of physiographic regions. Values indicate the probability that the mean residual for the two distributions being compared are equal.

Model	Altiplano vs N. Transect	Altiplano vs S. Transect	N. Transect vs S. Transect
Rowley (2007) – global quartic regression	3.9×10^{-3}	1.2×10^{-4}	0.61
This study – all April streams	2.7×10^{-5}	3.9×10^{-3}	3.9×10^{-3}
This study – all eastern flank streams	8.0×10^{-5}	0.56	3.9×10^{-3}
This study – separate regressions N/S of 20°S	1.1×10^{-4}	3.9×10^{-3}	0.093
This study – separate regressions for N/S transects	0.028	3.9×10^{-3}	0.70

References

Bowen, G. J., and B. Wilkinson (2002), Spatial distribution of $\delta^{18}O$ in meteoric precipitation, *Geology*, *30*(4), 315, doi:10.1130/0091-7613(2002)030<0315:sdooim>2.0.co;2.

Burnham, K. P., and D. R. Anderson (2003), *Model Selection and Multimodel Inference*, edited by K. P. Burnham and D. R. Anderson, Springer Science & Business Media, New York, NY.

Dutton, A., B. H. Wilkinson, J. M. Welker, G. J. Bowen, and K. C. Lohmann (2005), Spatial distribution and seasonal variation in $^{18}O/^{16}O$ of modern precipitation and river water across the conterminous USA, *Hydrol. Process.*, *19*(20), 4121–4146, doi:10.1002/hyp.5876.

Fiorella, R. P., C. J. Poulsen, R. S. Pillco Zolá, J. B. Barnes, C. R. Tabor, and T. A. Ehlers (2015), Spatiotemporal variability of modern precipitation $\delta^{18}O$ in the central Andes and implications for paleoclimate and paleoaltimetry estimates, *Journal of Geophysical Research: Atmospheres*, *120*(10), 4630–4656, doi:10.1002/2014JD022893.

Lechler, A. R., and N. A. Niemi (2012), Controls on the Spatial Variability of Modern Meteoric ^{18}O: Empirical Constraints from the Western U.S. and East Asia and Implications for Stable Isotope Studies, *American Journal of Science*, *311*(8), 664–700, doi:10.2475/08.2011.02.

Rowley, D. B. (2007), Stable Isotope-Based Paleoaltimetry: Theory and Validation, in *Paleoaltimetry: geochemical and thermodynamic approaches*, vol. 66, edited by M. J. Kohn, pp. 23–52, Minerology Society of America.

Appendix 3C. Compilation of central Andes clumped isotope records and comparison to climate model simulations

Methods

A fundamental limitation associated with using pedogenic carbonates to reconstruct paleoenvironments is that the $\delta^{18}O$ or δD compositions recorded depend on both the environmental $\delta^{18}O$ or δD compositions as well as the temperature at which the carbonate formed. The clumped isotope paleothermometer has been suggested as a way to independently constrain formation temperature, as the abundance of a multiply substituted isotopologue containing a ^{13}C-^{18}O bond is dependent on temperature, but not the isotopic composition of the water the carbonate forms in equilibrium with [*Ghosh et al.*, 2006b; *Eiler*, 2007]. As a result, the clumped isotope compositions of carbonates in the central Andes have been used in several studies to estimate paleoelevations indsaependent of $\delta^{18}O$ lapse rates by using temperature lapse rates [*Ghosh et al.*, 2006a; *Garzione et al.*, 2008; *Leier et al.*, 2013; *Garzione et al.*, 2014]. Additionally, clumped isotopes have been preferred in the region to address concerns that $\delta^{18}O_{cc}$ compositions may be evaporatively biased, particularly for the more arid Southern Altiplano [*Garzione et al.*, 2007; 2014].

Here, we have compiled the Δ_{47} temperatures and compare them to simulated model temperatures to reevaluate the paleoelevation interpretations. Since the first interpretations of Δ_{47} temperatures in the central Andes were published in 2006 [*Ghosh et al.*, 2006a], our understanding of the relationship between Δ_{47} temperatures and mean annual air temperatures has been refined significantly. First, Δ_{47} temperatures are thought to reflect soil temperatures at the time of carbonate formation [*Passey et al.*, 2010], and not air temperatures directly. Second, carbonate formation is likely more seasonal than previously assumed, with carbonate precipitation occurring during the driest portions of the year [e.g., *Breecker et al.*, 2009]. As a result, the $\delta^{18}O$, $\delta^{13}C$, and Δ_{47} compositions of pedogenic carbonate may reflect seasonal and not annual conditions [e.g., *Breecker et al.*, 2009; *Peters et al.*, 2013]. Third, if the timing of formation can be constrained, empirical transfer functions relating soil temperatures at the carbonate-bearing depths to mean annual air temperatures can be developed [e.g., *Quade et al.*, 2013]. Additionally, comparisons of Δ_{47} compositions from different laboratories have shown that there is an additional instrument-specific fractionation due to variability in the ionizing source and environmental lab conditions. *Dennis et al.* [2011] developed an 'absolute' reference

frame (ARF) to report Δ_{47} compositions in order to facilitate interlaboratory comparisons that account for instrument-specific effects. In light of these developments, we estimate past surface air temperatures from the Δ_{47} using a series of assumptions reflecting the evolution of clumped isotope methods: (1) Temperatures from Δ_{47} values as originally published reflect surface air temperatures, (2) Temperatures from Δ_{47} values reflect surface air temperatures, if first converted to a standard ARF that is not instrument-dependent [*Dennis et al.*, 2011], (3) Temperatures from Δ_{47} values reflect soil temperatures, but mean annual air temperatures (MAAT) can be estimated via the empirical relationship of *Quade et al.* [2013, equation 3]. As the clumped isotope data for the central Andes was collected prior to the development of the ARF, an indirect transfer function to estimate compositions within the ARF must be used. All of the published clumped isotope data for the central Andes were generated on a ThermoFisher MAT 253 isotope ratio mass spectrometer at the California Institute of Technology. Three transfer functions have been published relating Δ_{47} compositions from this instrument to the ARF [*Dennis et al.*, 2011; *Leier et al.*, 2013; *Quade et al.*, 2015], though the differences between these calibrations relative to the difference between measured Δ_{47} compositions and estimated ARF Δ_{47} compositions is negligible. Therefore, we present results using the *Quade et al.* [2015] transfer function only.

Clumped Isotope Results

Paleoelevations inferred from comparing modeled simulated temperatures to Δ_{47} temperatures are highly sensitive to the method used to relate Δ_{47} temperatures to surface air temperatures (Figure 3C.1). When the temperatures are calculated using the *Ghosh et al.* [2006a] calibration, paleoelevations for the Corque syncline are < 0-25 % of modern elevations at ~11 Ma, and 25- >100% of modern elevations at 6 Ma (Figure 3C.1a). At Cerdas and Quehua (Figure 3C.1b), paleoelevations are < 0 % of modern elevations at 16 Ma and 0-25% of modern elevations at 8 Ma. At the Salla and Upper Salla beds (Figure 3C.1c), paleoelevations are < 0 - ~25% of modern elevations at 25 Ma and 25-50% at 15 Ma. Similar results are obtained when temperatures are calculated by estimating equivalent compositions in the ARF and calculating the formation temperature using the calibration of *Dennis and Schrag* [Figure 3C.1d-f, 2010], though these temperatures tend to be ~3°C warmer across the dataset.

Air temperatures calculated using the *Quade et al.* [2013] linear regression, following the method as implemented in *Garzione et al.* [2014], suggest cooler temperatures and higher

elevations. Air temperatures from the Corque syncline suggest elevations of ~50-100% of modern elevations at ~11 Ma, and > 100% of modern elevations at ~6 Ma (Figure 3C.1g). Temperatures from southern Altiplano sites suggest elevations of 25-50% of modern at ~16 Ma, and >100% at ~8 Ma (Figure 3C.1h). Finally, air temperatures at the Salla and Upper Salla Beds imply elevations of < 0-100% of modern elevations at 25 Ma, and >100% of modern elevations at ~15 Ma (Figure 3C.1i). In contrast to the interpretations in *Garzione et al.* [2014], the elevation reconstructions for the northern and southern halves of the Altiplano are generally consistent when both sections are converted to mean annual air temperature estimates.

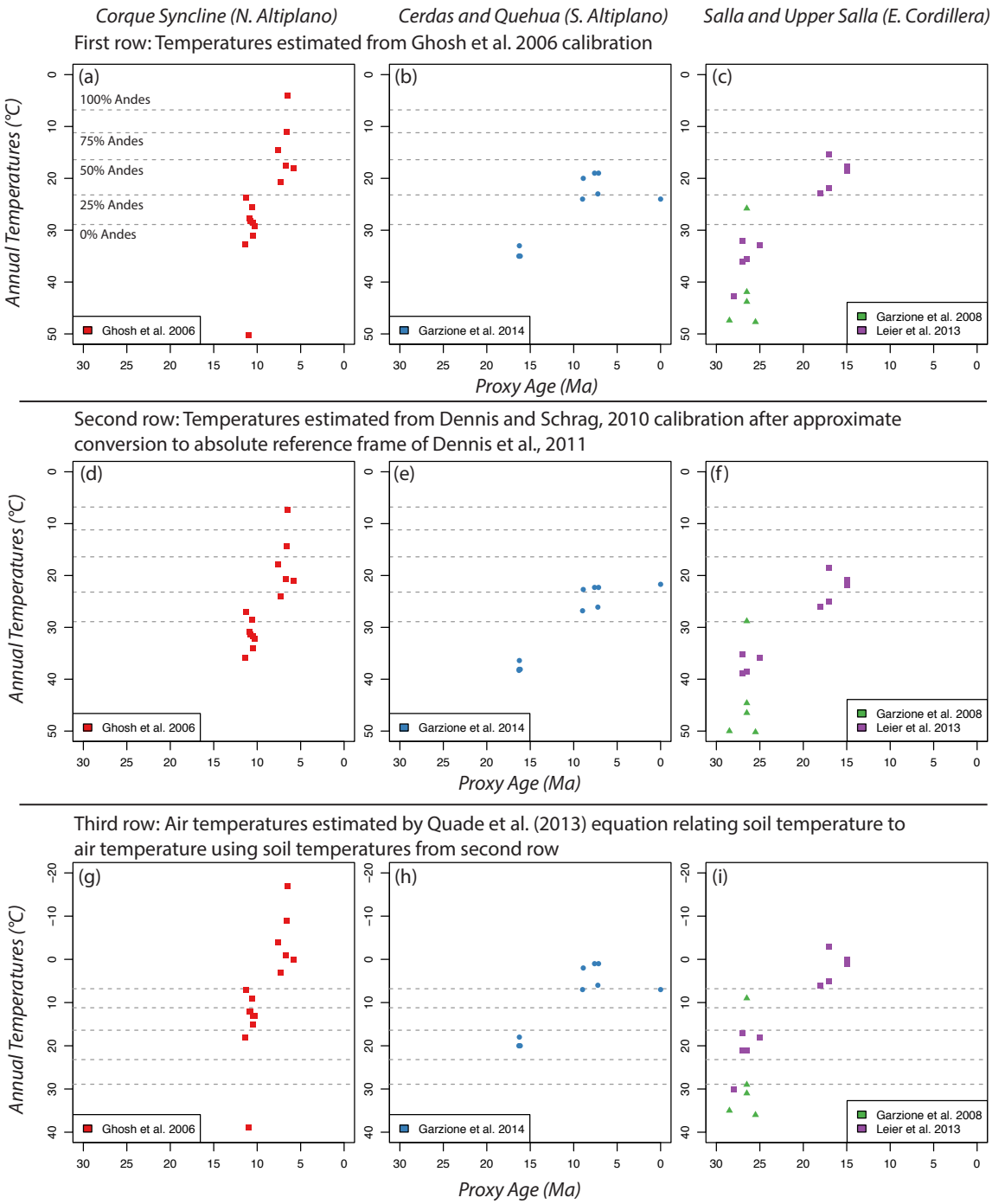

Figure 3.12. $T(\Delta_{47})$ (°C) against proxy age (Ma). Mean annual temperatures from the RegCM model simulations are shown as grey dashed lines as a function of elevation. Temperatures are estimated from Δ_{47} compositions in three different ways: the Ghosh et al. [2006b] calibration (top row), the Dennis and Schrag [2010] calibration following approximate conversion into the reference frame of Dennis et al. [2011] (middle row), and using the linear regression between soil temperature and air temperature from Quade et al. [2013] (bottom row). Proxy records from the Corque Syncline (N. Altiplano), Cerdas and Quehua (S. Altiplano), and the Salla and Upper Salla Beds (Eastern Cordillera) are shown in the left, middle, and right columns respectively.

There are several caveats to both the proxy and climate modeling components presented here that complicate the comparison between Δ_{47} and GCM model temperatures. The GCM simulations of *Ehlers and Poulsen* [2009] used in this study assume a uniform uplift of the entire Andean range. In reality, some variability in uplift along and across strike is likely [e.g., *Allmendinger et al.*, 1997; *Barnes and Ehlers*, 2009; *Quade et al.*, 2015]. Additionally, these simulations held CO_2 concentrations fixed at 355 ppmv. Atmospheric pCO_2 was likely higher during periods of the Cenozoic, and therefore, temperatures likely warmer than simulated here during periods of elevated CO_2. Therefore, these simulations likely underestimate the temperature range that would be associated with uplift of the Andes to their modern elevations by perhaps as much as ~4-8°C [e.g., *Jeffery et al.*, 2012].

Table 3.10. Sampling depths for clumped isotope paleoaltimetry in the central Andes.

Study	***Geologic Unit***	***Sampling Depths***
Ghosh et al. 2006	Corque Syncline	~25-80 cm
Garzione et al. 2008	Corque Syncline	17-40 cm
Garzione et al. 2008	Salla Beds	below 30-50 cm
Leier et al. 2013	Salla and Upper Salla Beds	> 50 cm, typically 100 cm
Garzione et al. 2014	Cerdas and Quehua	~20-200 cm

There are several additional considerations for interpreting the Δ_{47} compositions for the central Andes as well. First, the depth of the paleosol horizons sampled varies greatly amongst the studies (Table 3.10). Depth within the soil column of the pedogenic carbonate has strong implications for the temperature of the surrounding environment during carbonate formation. Soil temperatures are typically modeled as sinusoidal variations from an average air temperature [e.g., *Hillel*, 1980]. The variability in soil temperature associated with variability in air temperatures decays with depth. Damping depths (i.e., the e-folding depth) for the model soil in *Quade et al.* [2013] on diurnal and annual timescales are 8 cm and 153 cm, respectively. As a result, the shallowest pedogenic carbonates in these studies (20 cm) experience ~10% of the diurnal and ~88% of the annual temperature range. Therefore, constraints on the timing of pedogenic carbonate formation is critically important to evaluate the relationship of recorded temperatures to mean annual air temperatures, particularly for the shallowest carbonates sampled. Second, the *Quade et al.* [2013] linear regression may be inappropriate to use for central Andes paleosols if our suggestion that pedogenic carbonates are forming largely during

austral winter is correct. This relationship was developed for soils where the warm and dry seasons coincided, and as a result, all of the soil temperatures used to generate this regression were above the mean annual air temperature. In contrast, pedogenic carbonates forming during winter would record temperatures equal to or more likely, below, the mean annual value. Formation temperatures matching mean annual temperatures instead of annual maximum temperatures were observed in high-elevation pedogenic carbonates at ~33°S, south of our study site [*Peters et al.*, 2013]. In this case, application of the *Quade et al.* [2013] relationship to estimate central Andean MAAT would result in temperature estimates that are too low and paleoelevation estimates that are too high. This trend is consistent with our observation of MAAT estimates that are colder than modern for a significant portion of the pedogenic carbonates in the central Andes (Figure 3C.1g-i). Finally, central Andes temperatures from Δ_{47} compositions show considerable variability within single geologic units. For example, carbonates within the Corque Syncline show a ~25°C range of temperature at 11 Ma and a ~20°C range of temperature at 6 Ma, while the Salla Beds also show a ~25°C range at 25 Ma. In contrast, the temperature change between the 0% and 100% Andes GCM simulations is ~22°C. Therefore, the uncertainty at certain periods approaches the magnitude of the signal of the entire Andean uplift. The hottest temperatures recorded are potentially affected by post-formation diagenetic alteration [*Ghosh et al.*, 2006a; *Garzione et al.*, 2008]. Burial of paleosols to a few kilometers depth can promote the solid-state reordering of C-O bonds [*Henkes et al.*, 2014], and alter the temperature to partially overprint the surface temperature with the temperature at depth. However, even ignoring the warmest temperatures in these sections that may be diagenetically altered, temperature ranges in these units still remains near ~15°C, limiting paleoelevation estimation precision to > 2 km.

References

Allmendinger, R. W., T. E. Jordan, S. M. Kay, and B. L. Isacks (1997), The evolution of the Altiplano-Puna plateau of the Central Andes, *Annu. Rev. Earth Planet. Sci.*, *25*(1), 139–174, doi:10.1146/annurev.earth.25.1.139.

Barnes, J. B., and T. A. Ehlers (2009), End member models for Andean Plateau uplift, *Earth-Science Reviews*, *97*(1-4), 105–132, doi:10.1016/j.earscirev.2009.08.003.

Breecker, D. O., Z. D. Sharp, and L. D. McFadden (2009), Seasonal bias in the formation and stable isotopic composition of pedogenic carbonate in modern soils from central New Mexico, USA, *Geological Society of America Bulletin*, *121*(3-4), 630–640, doi:10.1130/B26413.1.

Dennis, K. J., and D. P. Schrag (2010), Clumped isotope thermometry of carbonatites as an indicator of diagenetic alteration, *Geochimica et Cosmochimica Acta*, *74*(14), 4110–4122, doi:10.1016/j.gca.2010.04.005.

Dennis, K. J., H. P. Affek, B. H. Passey, D. P. Schrag, and J. M. Eiler (2011), Defining an absolute reference frame for "clumped" isotope studies of CO_2, *Geochimica et Cosmochimica Acta*, *75*(22), 7117–7131, doi:10.1016/j.gca.2011.09.025.

Ehlers, T. A., and C. J. Poulsen (2009), Influence of Andean uplift on climate and paleoaltimetry estimates, *Earth Planet Sc Lett*, *281*(3-4), 238–248, doi:10.1016/j.epsl.2009.02.026.

Eiler, J. M. (2007), "Clumped-isotope" geochemistry—The study of naturally-occurring, multiply-substituted isotopologues, *Earth Planet Sc Lett*, *262*(3-4), 309–327, doi:10.1016/j.epsl.2007.08.020.

Garzione, C. N., D. J. Auerbach, J. J.-S. Smith, J. J. Rosario, B. H. Passey, T. E. Jordan, and J. M. Eiler (2014), Clumped isotope evidence for diachronous surface cooling of the Altiplano and pulsed surface uplift of the Central Andes, *Earth Planet Sc Lett*, *393*(C), 173–181, doi:10.1016/j.epsl.2014.02.029.

Garzione, C. N., G. D. Hoke, J. C. Libarkin, S. Withers, B. J. MacFadden, J. M. Eiler, P. Ghosh, and A. Mulch (2008), Rise of the Andes, *Science*, *320*(5881), 1304–1307, doi:10.1126/science.1148615.

Garzione, C. N., P. Molnar, J. C. Libarkin, and B. J. MacFadden (2007), Reply to Comment on "Rapid late Miocene rise of the Bolivian Altiplano: Evidence for removal of mantle lithosphere" by Garzione et al. (2006), Earth Planet. Sci. Lett. 241 (2006) 543–556, *Earth Planet Sc Lett*, *259*(3-4), 630–633, doi:10.1016/j.epsl.2007.04.054.

Ghosh, P., C. N. Garzione, and J. M. Eiler (2006a), Rapid uplift of the Altiplano revealed through ^{13}C-^{18}O bonds in paleosol carbonates, *Science*, *311*(5760), 511–515, doi:10.1126/science.1120792.

Ghosh, P., J. Adkins, H. Affek, B. Balta, W. Guo, E. Schauble, D. P. Schrag, and J. M. Eiler (2006b), ^{13}C–^{18}O bonds in carbonate minerals: A new kind of paleothermometer, *Geochimica et Cosmochimica Acta*, *70*(6), 1439–1456, doi:10.1016/j.gca.2005.11.014.

Henkes, G. A., B. H. Passey, E. L. Grossman, B. J. Shenton, A. Perez-Huerta, and T. E. Yancey (2014), Temperature limits for preservation of primary calcite clumped isotope paleotemperatures, *Geochimica et Cosmochimica Acta*, *139*(C), 362–382, doi:10.1016/j.gca.2014.04.040.

Hillel, D. (1980), *Fundamentals of soil physics*, Academic Press, New York.

Jeffery, M. L., C. J. Poulsen, and T. A. Ehlers (2012), Impacts of Cenozoic global cooling, surface uplift, and an inland seaway on South American paleoclimate and precipitation $\delta^{18}O$, *Geological Society of America Bulletin*, *124*(3-4), 335–351, doi:10.1130/B30480.1.

Leier, A., N. McQuarrie, C. Garzione, and J. Eiler (2013), Stable isotope evidence for multiple pulses of rapid surface uplift in the Central Andes, Bolivia, *Earth Planet Sc Lett*, *371-372*(C), 49–58, doi:10.1016/j.epsl.2013.04.025.

Passey, B. H., N. E. Levin, T. E. Cerling, F. H. Brown, and J. M. Eiler (2010), High-temperature environments of human evolution in East Africa based on bond ordering in paleosol carbonates, *Proceedings of the National Academy of Sciences*, *107*(25), 11245–11249, doi:10.1073/pnas.1001824107.

Peters, N. A., K. W. Huntington, and G. D. Hoke (2013), Hot or not? Impact of seasonally variable soil carbonate formation on paleotemperature and O-isotope records from clumped isotope thermometry, *Earth Planet Sc Lett*, *361*, 208–218, doi:10.1016/j.epsl.2012.10.024.

Quade, J., J. M. Eiler, M. Daëron, and H. Achyuthan (2013), The clumped isotope geothermometer in soil and paleosol carbonate, *Geochimica et Cosmochimica Acta*, *105*(C), 92–107, doi:10.1016/j.gca.2012.11.031.

Quade, J., M. P. Dettinger, B. Carrapa, P. DeCelles, K. E. Murray, K. W. Huntington, A. Cartwright, R. R. Canavan, G. Gehrels, and M. Clementz (2015), The growth of the central Andes, 22°S–26°S, in *Geodynamics of a Cordilleran Orogenic System: The Central Andes of Argentina and Northern Chile*, vol. 212, pp. 277–308, Geological Society of America.

Chapter 4. Seasonal patterns of water vapor cycling in a deep, continental mountain valley

4.1 Abstract

The water cycle within high-elevation continental interiors remains poorly understood. We present sub-hourly measurements of the isotopic composition of summer and winter water vapor from a deep mountain valley in northwestern Wyoming. Isotope measurements are paired with local meteorological measurements, and local transpiration fluxes are estimated using sap flux measurements. Relationships between local vapor isotopic compositions and large-scale air transport are explored by calculating atmospheric back trajectories. Isotopic compositions exhibit pronounced seasonal, diurnal, and synoptic-scale variations. The summer diurnal cycle results from transpiration and boundary layer development and decay, which are more prominent during summer than winter. The most prominent summer isotopic diurnal cycle is observed in deuterium excess ($d = \delta D - 8\delta^{18}O$), which increases during the morning, peaks in the afternoon, and decreases in the evening, often to negative values. We suggest that the strong cycle in deuterium excess is likely driven by non-steady state transpiration. Local isotopic compositions show a stronger dependence on air transport pathway during the winter than during the summer. These results suggest that isotopic characteristics of vapor transported to the continental interior are overprinted by local transpiration and boundary layer mixing during the summer. In contrast, the isotopic composition of the air source is preserved in the winter. Continued monitoring of the isotopic composition of near-surface vapor in continental settings may help detect changes in regional moisture convergence and the local evapotranspiration flux, as well as assess meso-to-regional scale ecohydrologic responses to hydrologic variability.

4.2 Introduction

Recycling of water over continents is a critical component of the terrestrial water cycle and the surface energy balance. Continental precipitation is nearly three times greater than the mass of water advected over the continents from the oceans on an annual basis [*Trenberth et al.*,

2007]. The evapotranspiration (ET) flux from the land surface provides the water vapor necessary to maintain these elevated precipitation amounts. Water is cycled over the continents, perhaps several times, before returning to the ocean through runoff [*Brubaker et al.*, 1993; *Gimeno et al.*, 2010; *van der Ent et al.*, 2010].

Continental water cycling, especially in high-elevation environments in the Western US, is changing in response to anthropogenic warming. Winter snowfall provides an important source of water for ecosystems and communities as it melts during spring and summer [*Bales et al.*, 2006; *Hunter et al.*, 2006]. In recent decades, the mass of the Western US snowpack has been decreasing [*Mote et al.*, 2005; *Kalra et al.*, 2008], as has the fraction of annual precipitation falling as snow [*Knowles et al.*, 2006]. These changes in montane hydrology have led to earlier peak snowmelt [*Cayan et al.*, 2001], decreased summer stream flow [*Rood et al.*, 2008], and increased risk of forest mortality [*Anderegg et al.*, 2012; 2013] and wildfires [*Westerling et al.*, 2006] resulting from drier summer conditions. Improved understanding of how water cycles through high elevation environments, and how these processes relate to local (e.g., valley-to-ridge scale) and remote (e.g., meso- to synoptic scales) changes to meteorology and atmospheric circulation, will be critical to managing water resources and assessing regional forest drought susceptibility.

Stable isotopes of hydrogen and oxygen can be used as tracers of water transport processes. Phase transitions partition the heavy (e.g., ^{18}O, ^{17}O, and ^{2}H or D) and light isotopes (^{16}O and ^{1}H) of oxygen and hydrogen in water unequally, with the heavier isotopes preferentially remaining in or entering the condensed phase [*Gat*, 1996]. At equilibrium, this isotopic fractionation between two phases is temperature dependent [*Majoube*, 1971; *Horita and Wesolowski*, 1994]. Condensation of water from an air parcel reduces the concentration of heavy isotopes in the remaining vapor. Turbulent transport in the atmosphere and from the land or ocean surface, particularly during evaporation, often prevents isotopic equilibrium from being attained, resulting in an additional kinetic fractionation arising from the different diffusivities of each water isotopologue [*Craig and Gordon*, 1965; *Merlivat and Jouzel*, 1979; *Cappa et al.*, 2003; *Luz et al.*, 2009]. Therefore, the degree of isotope partitioning reflects both equilibrium and kinetic fractionation processes.

Water vapor isotopes reflect the integrated moisture history of an air parcel, including their evaporative source, mixing between air masses and with surface sources of water vapor,

and through condensation and partial evaporation during precipitation processes. Unlike isotope tracers in precipitation, which are sampled during discrete events, water vapor isotope measurements can be monitored continuously. Prior to the proliferation of laser-based spectrometers, measurements of the isotopic composition of water vapor were difficult and relatively rare [*Rozanski and Sonntag*, 1982; *White and Gedzelman*, 1984; *Helliker et al.*, 2002; *Ehhalt et al.*, 2005]. Continuous, high-resolution (e.g., ~0.1-1 Hz) measurements of water vapor isotopic composition have shown that large-scale changes in atmospheric transport influence water vapor isotopic composition, including moisture source directions [*Galewsky and Samuels-Crow*, 2015; *Larsen et al.*, 2015], upwind convective intensity [*Brown et al.*, 2008; *Crow et al.*, 2014], passage of frontal systems [*Lee et al.*, 2006; *Aemisegger et al.*, 2015], and cloud microphysical properties [*Galewsky et al.*, 2011; *Bailey et al.*, 2015]. The isotopic composition of near-surface water vapor also records information on local processes, such as boundary layer development and entrainment of free tropospheric vapor [*He and Smith*, 1999; *Lai and Ehleringer*, 2010; *Noone et al.*, 2011; *Bailey et al.*, 2013], evapotranspiration [*Moreira et al.*, 1997; *Yepez et al.*, 2003; *Welp et al.*, 2008; *Aemisegger et al.*, 2014; *Good et al.*, 2014], and dewfall or frost [*Wen et al.*, 2012; *Noone et al.*, 2013]. These studies have established that water vapor isotopic compositions are useful for understanding atmospheric moisture transport and land-atmosphere exchanges across a variety of time scales, and provide an integrated picture of moisture transport from the ocean surface to continental interiors.

In this study, we present and analyze the isotopic composition of near-surface water vapor in a deep, continental mountain valley from two summers and one winter measurement period. We seek to understand how regional atmospheric circulation, boundary layer entrainment of free tropospheric vapor, and the local ET flux influence the near-surface isotopic composition of water vapor at the seasonal and diurnal time scales. Our isotopic measurements are augmented with local meteorological measurements and atmospheric back trajectory analysis using reanalysis data. To estimate the local transpiration flux, we measured sap flux in dominant local tree species during one of the summer measurement campaigns. Combining these measurements, we find that winter isotopic compositions are closely related to synoptic-scale atmospheric circulations, but that local effects progressively overprint information about the remote transport pathway during the summer. Both transpiration and boundary layer entrainment and mixing contribute to a prominent diurnal cycle observed during summer, but not winter.

4.3 Theory: Diurnal Circulation in a Mountain Valley

Several processes scale with or depend on the diurnal cycle, such as boundary layer development and decay and the evapotranspiration flux. Individual fluxes of moisture into or out of the near-surface layer have characteristic influences on boundary layer water vapor amount and isotopic composition. Free tropospheric air under clear conditions has lower humidity than air near the surface, due to condensation as that air was lifted from the surface and cooled. Therefore, the vapor in free tropospheric air is typically more depleted in heavy isotopes [e.g., *Gedzelman*, 1988]. Daytime entrainment of free tropospheric air into the mixed boundary layer tends to reduce the humidity and heavy isotopic composition of near-surface vapor. Evaporation of water from soils also adds isotopically light water to the near-surface vapor, but soils are very dry at the CDFS during the summer. Therefore, the soil evaporation flux at the CDFS is expected to be negligible except immediately following precipitation events.

The influence of transpiration on near-surface vapor isotopic compositions is more complicated. Plants do not fractionate water during root uptake [*Ehleringer and Dawson*, 1992], and mass balance requires that on long timescales the isotopic composition of transpired vapor equals the source water, at which point it is considered to be in 'steady-state.' However, diurnal changes in temperature and RH cause substantial changes in fractionation factors at the site of evaporation within leaves. As a result, transpiration may only approach steady-state during prolonged periods (e.g., hours) of steady temperature and RH [*Harwood et al.*, 1998; 1999; *Simonin et al.*, 2013a]. In either case, leaf water undergoes a well-known isotopic enrichment during the day due to preferential loss of lighter isotopes during evaporation from the leaf. This enrichment is typically lost overnight through nocturnal transpiration, leaf water recharge from the xylem, and equilibration of leaf water with atmospheric water vapor [*Cernusak et al.*, 2002; *Farquhar and Cernusak*, 2005]. Effective fractionation factors increase more rapidly for oxygen than hydrogen with decreases in RH, as the diffusivity difference between $H_2{}^{18}O$ and $H_2{}^{16}O$ is greater than between $HD^{16}O$ and $H_2{}^{16}O$ [*Merlivat*, 1978; *Cappa et al.*, 2003]. As a result, evaporation from the leaf during periods of rapidly decreasing (increasing) RH are expected to contribute to the boundary layer more light (heavy) oxygen than light (heavy) hydrogen [*Simonin et al.*, 2013b]. Due to these diurnal changes in fractionation factors and the requirement of mass balance on longer timescales, it is expected that in an environment with rapidly changing RH throughout the day, such as the CDFS, morning transpiration would increase the d-excess of

near-surface vapor while late afternoon and evening transpiration would decrease the d-excess of near-surface vapor. Assuming a sensitivity of d-excess during evaporation of -0.53‰/% RH [e.g., *Pfahl and Wernli*, 2008] implies a maximum change of ~32‰ if the amplitude of the diurnal cycle in RH is 60%.

The location of the CDFS within a deep mountain valley introduces several additional processes that modify the cycle of boundary layer development and decay. Nocturnal capping inversions inhibit mixing between near-surface vapor with the atmosphere above and slow the development of the mixed layer in the morning. Anabatic valley winds transport warm air at the surface upslope, while cold air from the inversion core sinks to replace it, which limits the height of the mixed layer while the inversion core persists [*McNider and Pielke*, 1981; *Whiteman*, 1982]. When the inversion core is eliminated, the height of the mixed layer can increase rapidly with a corresponding increase in turbulent kinetic energy [*Banta*, 1985; *Whiteman et al.*, 2004]. At sunset, the inversion develops again, with cold surface katabatic winds entering the valley, beneath a warmer residual layer aloft [*McNider and Pielke*, 1981]. Based on these processes, we would expect to capture in our isotopic and meteorological measurements: (a) a strong signal of transpiration fluxes after sunrise, but before development of a deep boundary layer and substantial entrainment of free tropospheric air, and (b) a rapid collapse of vertical mixing and development of katabatic mountain winds near sunset as the inversion develops.

4.4 Methods

4.4.1 Site description

The Camp Davis Rocky Mountain field station (CDFS, Figure 4.1, 43.283°N, 110.659°W) is located at 1860 m elevation in a NW-SE trending mountain valley that is ~10 km long and ~2 km wide at its widest point. The surrounding mountain peaks range from 2100-3000+ m. The valley is bisected by US Highway 191/189/89/26. The field station occupies 48.6 ha near the SW valley wall south of the highway. The Bridger-Teton National Forest bounds the valley on all sides.

Long-term climatological records are not available for the CDFS, but the nearby NOAA climate station in Bondurant, WY (20 km ESE) reports a mean annual temperature of 1.5°C and mean annual precipitation of ~480 mm (NCDC 1981-2010 climate normals). A NOAA climate station in Jackson, WY (25 km NNW) has a similar annual climatology (4.1°C and ~430 mm).

Precipitation is evenly distributed throughout the year without a distinct rainy season, though winter tends to have slightly more precipitation. Winter precipitation is typically associated with extratropical cyclones, with vapor transported from the northwest, while summer precipitation is associated with moisture transport from the west and the southwest [*Despain*, 1987]. The Hoback River runs through the valley and is ~200 m away from the collection site at its closest point. Nocturnal temperature inversions in the valley are common throughout the year and are similar to temperature inversions observed in other deep valleys in the Rocky Mountains [*Whiteman*, 1982; *Whiteman et al.*, 2004; *Bailey et al.*, 2011].

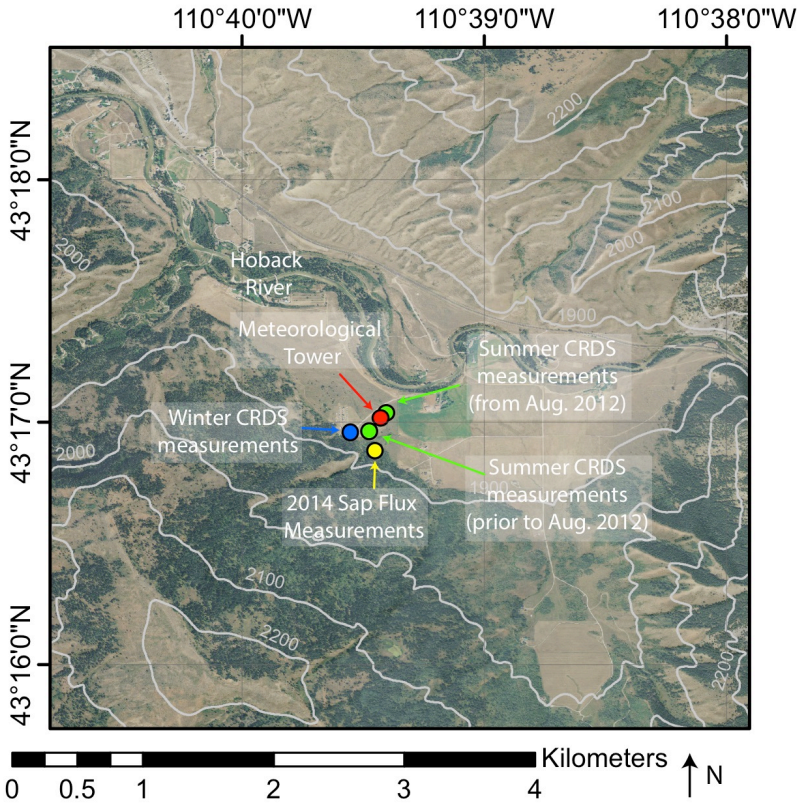

Figure 4.1. Aerial map of the Camp Davis field station location (CDFS). Summer CRDS deployment locations are shown as green circles and the winter CRDS deployment location is shown as a blue circle. The red circle denotes the location of the meteorological measurements, and the yellow circle indicates the location of the forest where we measured sap flux. The CDFS is within a deep mountain valley bounded on all sides by higher peaks, with the Hoback river running through the valley from east to west. Topography is shown in gray contour lines in 100 m elevation intervals.

The valley near the collection site and the southern-facing slopes bounding the valley are shrublands dominated by big sagebrush (*Artemisia tridentata*) and rabbitbrush (*Ericameria nauseosa*). Northern-facing slopes are forested mainly by lodgepole pine (*Pinus contorta*), trembling aspen (*Populus tremuloides*), and Douglas fir (*Psuedotsuga menziesii*), with

occasional subalpine fir (*Abies lasiocarpa*) and narrowleaf cottonwood (*Populus angustifolia*) also present.

4.4.2 Meteorological measurements

Meteorological data were collected at a 10 m tower in the valley (Figure 4.1). Measurements included 2- and 10-m temperature and relative humidity (RH) (CS500, Campbell Scientific/Vaisala), 10-m wind speed and direction (05103, R.M. Young), barometric pressure (CS100, Campbell Scientific/Setra), solar insolation (LI200S, LI-COR Biosciences), and precipitation amount (TE525WS, Texas Electronics). Sensor data were recorded every minute by a Campbell Scientific data logger (CR10X), and averaged to 15-minute time intervals. A power outage and equipment failure led to the loss of a portion of the 2012 meteorological data (Table 4.1).

Table 4.1. CDFS data availability summary

Measurement Period	Number of days	Meteorology (%)	Isotope (%)	Sap Flux (%)
June 12-September 2, 2012	82	88.7	71.1	N/A
January 12-February 4, 2013	23	100	87.5	N/A
June 30-July 16, 2014	17	100	69.8	88.3

4.4.3 Vapor isotope measurements

We deployed a Picarro L2120-i cavity ring-down spectrometer (CRDS) in a protected shelter at the field station. The CRDS was operated for three periods: 12 June-2 September, 2012 (DOY 164-246); 12 January-2 February, 2013 (DOY 12-33); and 30 June-15 July, 2014 (DOY 181-196). Two liquid water standards were analyzed every 12 hours to convert measured vapor values to the VSMOW scale [*Coplen*, 1996] and to monitor for instrumental drift. Typical instrumental drift on the Picarro CRDS is less than 0.6‰ for $\delta^{18}O$ and 1.8‰ for δD over a 24-hour period, while analytical precision exceeds 0.1‰ for $\delta^{18}O$ and 0.4‰ for δD. CRDS measurements also exhibit a small degree of water vapor concentration dependence; we estimate that this may introduce up to 2.0‰ uncertainty in both isotope systems spread across the range of humidity in these field experiments (~0.14‰ / mmol H_2O / mol air, or ~ 2.0‰ across a range of 14 g/kg in specific humidity). The CRDS collected measurements of $\delta^{18}O$ (‰), δD (‰), and specific humidity (q) (ppm) at ~1-2 second intervals. Isotope data presented here are fifteen-

minute average values. Deuterium excess (d-excess) is calculated after *Dansgaard* (1964, $d = \delta D - 8\delta^{18}O$), and reflects the degree of kinetic fractionation recorded in the vapor.

For the 2012 and 2013 campaigns, standards were introduced using an autosampler, while in the 2014 campaign, the Picarro Standard Delivery Module was used. The location of the CRDS analyzer within the field station changed throughout the campaigns due to operational constraints for different seasons, but was always located within non-forested clearings (Figure 4.1). During summer 2012, the analyzer was first deployed in a cabin ~300 m south of the field station meteorological tower, and then moved into a small temperature-controlled shed constructed 15 m away from the meteorological tower. All subsequent summer isotope measurements were collected at the meteorological tower. Winter measurements were made in a building further south, and closer to the wall of the valley (Figure 4.1).

Atmospheric vapor was introduced to the CRDS through either 1/8" stainless steel tubing (during winter 2013 and prior to construction of the temperature-controlled shed in summer 2012), or through Bev-A-Line IV plastic tubing. Prior studies have indicated that isotopic fractionation caused by adsorption of water vapor to tubing walls of these materials is minimal [*Tremoy et al.*, 2011; *Simonin et al.*, 2013a]. In both setups, the sampling height was approximately 3 m above the ground. A partial vacuum was maintained in the sampling lines to reduce the likelihood of water condensation in the tubing. Sampling lines were not heated in this setup, though no evidence of condensation within the sampling lines was observed at this location due to the low relative humidities typical in NW Wyoming. Gaps in the isotope data were caused by hardware failure, and several shorter periods of missing data resulted from software crashes (Table 4.1).

4.4.4 Process-based isotope modeling

The isotopic composition of water vapor provides insights into the processes that moisten or dry the atmosphere [e.g., *Gat*, 1996; *Dessler and Sherwood*, 2003; *Galewsky and Hurley*, 2010; *Noone*, 2012]. Evaporation, condensation, and air-mass mixing possess characteristic patterns of isotopic change with respect to changes in humidity. We consider isotopic box-models for condensation and air-mass mixing below.

The evolution of the water isotopic composition in a condensing air parcel depends on whether the air parcel acts as an open or closed system. The canonical Rayleigh distillation

equation describes a fully open system, where all of the condensed liquid is immediately removed from the air parcel [*Gat*, 1996]. The isotopic composition of water vapor in a condensing air mass following Rayleigh distillation will be proportional to the natural logarithm of specific humidity [*Dansgaard*, 1964; *Gat*, 1996]:

$$\ln\left(\frac{q}{q_0}\right)(\alpha - 1) = \ln\left(\frac{R}{R_0}\right) \approx \delta - \delta_0 \qquad \text{(Eqn. 1)}$$

where q is the specific humidity, R is the heavy-to-light isotope ratio, δ is the isotopic composition in per-mil deviation from a standard R (for water, VSMOW, [*Coplen*, 1996]), and α the effective isotope fractionation factor. A subscript 0 refers to the parcel's initial properties prior to condensation. The effective isotope fractionation factor may be altered by temperature-dependent changes in the equilibrium fractionation factor [*Majoube*, 1971; *Horita and Wesolowski*, 1994] or by changes in the kinetic fractionation factor, which are affected by changes in environmental conditions such as wind speed and RH. Strictly speaking, equation 1 represents an integrated form of the Rayleigh equation and assumes constant α throughout condensation; this assumption may be relaxed when this equation is solved numerically with variable α for small changes in q/q_0 [e.g., *Noone*, 2012].

For a closed air parcel, all of the condensate remains within the air parcel. The total water content of the air parcel remains unchanged throughout the condensation. In this case, isotopic composition of water vapor in an air parcel will be linearly proportional to the specific humidity [*Jouzel*, 1986; *Noone*, 2012]:

$$\left(\frac{q}{q_0} - 1\right)(\alpha - 1) \approx \delta - \delta_0 \qquad \text{(Eqn. 2)}$$

Condensation processes with a partial loss of condensate will follow a trajectory between these two end-member models.

Finally, the mixing of two or more air masses with distinct specific humidities and isotopic compositions can be modeled from mass balance. Writing separate mass balance equations for the light and heavy isotopes, the measured quantities of specific humidity can be expressed as the sum of a background value and the net flux into or out of the parcel:

$$(1 - R_{obs})q_{obs} = (1 - R_{bg})q_{bg} + (1 - R_f)q_f \quad \text{(light isotope mass balance)} \qquad \text{(Eqn. 3)}$$

$$R_{obs}q_{obs} = R_{bg}q_{bg} + R_f q_f \quad \text{(heavy isotope mass balance)} \qquad \text{(Eqn. 4)}$$

where subscripts *obs*, *bg*, and *f* refer to the observed, background, and flux properties respectively. The "flux" in these equations represents the net properties of all component fluxes.

These equations can be simplified by noting that R << 1 for all three components, and that the heavy isotope mass balance equation can be written in delta notation equivalently within 0.01‰ (Hayes 1982):

$$q_{obs} = q_{bg} + q_f \qquad \text{(Eqn. 5)}$$

$$\delta_{obs} q_{obs} = \delta_{bg} q_{bg} + \delta_f q_f \qquad \text{(Eqn. 6)}$$

Substituting one of these mass balance equations into the other yields an equation for the observed isotopic composition of water vapor of:

$$\delta_{obs} = \frac{q_{bg}}{q_{obs}} \left(\delta_{bg} - \delta_f \right) + \delta_f \qquad \text{(Eqn. 7)}$$

Therefore, an air mass that has undergone mixing will have an observed isotopic composition proportional to $1/q$, and trace a hyperbolic shape in q-δ space. This equation can be rearranged to yield an equivalent linear form where mixing can be identified by a linear relationship between $q\delta$ and q:

$$\delta_{obs} q_{obs} = \delta_f \left(q_{obs} - q_{bg} \right) + \delta_{bg} q_{bg} \qquad \text{(Eqn. 8)}$$

This model is analogous to the Keeling plots used to discriminate sources and sinks of CO_2 to the atmosphere [*Keeling*, 1958; 1961; *Miller and Tans*, 2003; *Pataki et al.*, 2003], and has been previously extended to atmospheric water vapor to investigate mixing of atmospheric air masses [*Gedzelman*, 1988; *Dessler and Sherwood*, 2003; *Galewsky and Hurley*, 2010; *Noone et al.*, 2011] and to constrain surface fluxes from natural [*He and Smith*, 1999; *Noone et al.*, 2013] and agricultural ecosystems [*Brunel et al.*, 1992; *Welp et al.*, 2008].

We applied each of these isotope models to the isotopic and meteorological time series collected at the Camp Davis field station by calculating moving correlations between δD or $\delta^{18}O$ and q, ln(q), and $q\delta$. Each correlation was calculated over a 96-point moving window, corresponding to 24 hours of data. We divided the data into three classes: (1) periods dominated by air-mass mixing, (2) periods dominated by condensation processes, and (3) periods dominated by neither process. A process was considered "dominant" when the coefficient of determination (e.g., r^2) was greater than both 0.8 and greater than the r^2 for alternate process models [after *Noone et al.*, 2011]. We assumed no process was dominant when the r^2 was less than 0.8 for all process models.

4.4.5 Atmospheric back trajectory modeling

Ten-day atmospheric back trajectories were calculated to investigate large-scale changes in moisture advection to NW Wyoming. We used the HYbrid coordinate Single Parcel Lagrangian Integrated Trajectory model (HYSPLIT, [*Draxler and Hess*, 1998]) to calculate back-trajectories from NCEP/NCAR reanalysis derived wind fields [*Kalnay et al.*, 1996]. Trajectories were initiated from five locations (the lat/lon coordinates of Camp Davis, and points displaced 0.25° in each cardinal direction) at 250, 500, and 1000 m above the ground surface, resulting in 15 trajectories calculated at each time. Trajectories were initiated every six hours during the measurement periods. Characteristic air source regions were identified for each season. Four source regions were identified from visual inspection of the trajectories through time for the summer 2012 and winter 2013 measurement periods, while two were identified from the summer 2014 data. As 15 trajectories were calculated for each specific time, individual time windows often exhibited advection from more than one characteristic pathway. For analysis purposes, the source region for these points was assigned based on which pathway the majority of trajectories followed. Finally, trajectories that did not follow any of these characteristic regions were excluded from this analysis; this occurred commonly when advection was changing from one region to another. After all of the time windows had been assigned to a region or excluded, back trajectory locations were binned on a 0.75° horizontal grid to determine how frequently air parcels within that group passed through specific locations [as in *Fiorella et al.*, 2015].

Isotope and meteorological fields were extracted over the time periods corresponding to each air trajectory region and treated as clusters to determine if distinct patterns were observable locally at the CDFS. Mean cluster q and $\delta^{18}O$ values were determined in addition to the range corresponding to the 95% confidence interval (e.g., the 2.5-97.5 percentiles). We calculated the silhouette width, a measure of how close a given data point is to the centroid of its cluster relative to the centroid of the other clusters [*Rousseeuw*, 1987], for each point within each cluster to assess how distinct each cluster was. A positive silhouette width indicates a data point is closer to the centroid of its own cluster than to the centroid of any other cluster, indicating that regional characteristics are borne out in the data. In contrast, a negative silhouette width indicates a data point is closer to the centroid of a different cluster than to the centroid of its assigned cluster, indicating that the region assignments poorly describe the structure of the data.

4.4.6 Time series analysis

Isotopic and meteorological time series exhibited variability on a range of temporal scales. The Pearson correlation coefficient was calculated between pairs of time series of isotopic and meteorological variables; p-values were provided only when greater than 0.05. The most prominent high-frequency variability has a period of one day, and reflects the diurnal cycle. We applied a moving-average filter with a span of one day to isolate the lower frequency (e.g., seasonal and synoptic) variability from the diurnal cycle. In order to apply the moving-average filter across the full time series and avoid large, non-physical responses around gaps in the data, missing data were imputed using a simple linear interpolation between the last non-missing data points. After the filter was applied, the imputed data was once again set as missing and removed from subsequent analysis. The mean diurnal cycle is then calculated as the mean residual for each time window between the observed time series and the filtered time series. Where the deviation from the 24-hour running mean is used in the results, a capital delta (Δ) is used to distinguish these quantities from measured isotopic compositions, δ. When characterizing the summer diurnal cycle, we exclude days where at least 1.0 mm of rainfall was recorded at the meteorological station, corresponding to 19 and 4 days in summer 2012 and summer 2014, respectively. Precipitation results in large, rapid changes in humidity and isotopic composition that are unrelated to the underlying diurnal fluxes [e.g., *Berkelhammer et al.*, 2013]. Lacking estimates of winter precipitation amounts, all 23 winter days during our observation period are included in the diurnal cycle composites.

4.4.7 Transpiration estimates

We estimated the stand-level transpiration flux by measuring sap flux in dominant local tree species. Sap flux was monitored via Granier-style [1987] thermal dissipation probes from 27 June-16 July 2014 in the three most abundant species at the site, trembling aspen (n=15), lodgepole pine (n=14), and Douglas fir (n = 7). Trees were selected to capture a variety of sizes and canopy positions (Table 4.2). Tree height, diameter at breast height (DBH), and projected crown area were measured for each instrumented individual. Two 20 mm long probes were inserted one above the other into the sapwood at breast height, and the upper probe was continuously supplied with heating power. Sap flux is proportional to the voltage difference measured between thermocouples located in the two probes. Voltage differences were monitored

and recorded every minute and averaged to half hourly time steps. The *Clearwater et al.* [1999] correction was applied to all data for trees where sapwood depth was less than 2 cm, to correct for biases due to sensor penetration into heartwood. A baseline procedure was used to convert raw data to sap flow with respect to the maximal nocturnal temperature for each sensor to account for variation between sensors. Maximum temperature baselines were developed for times when the two-hour average *VPD* was below 0.5 kPa to allow for nightly recharge flow [*Oishi et al.*, 2008]. Processed data were converted to sap flux density ($gH_2O\ m^{-2}_{sapwood}\ s^{-1}$) following the equations presented in *Granier* [1987].

Sap flux density was converted to sap flow ($g\ s^{-1}$) by multiplying sap flux density by the sapwood area of the individual tree. Sapwood depth was determined through the use of species-specific allometric equations relating sapwood area and diameter at breast height. These relationships were developed from a staining assay using 2% tetrazolium chloride to distinguish hydroactive xylem following *Bovard et al.* [2005]. Cores were harvested at breast height from 20 trembling aspen, 11 lodgepole pine, and 9 Douglas fir that were not instrumented with sap flow sensors, but were representative of the entire range of stem diameters present in the sap flux group. Sapwood area, A_s, was then calculated using Equation 9 in conjunction with empirically-determined species-specific fit parameters (β_1, β_2, β_3, Table 4.3):

$$A_s = \beta_1 + \beta_2(DBH)^{\beta_3} \qquad \text{(Eqn. 9)}$$

We converted our sap flux measurements into a stand-level transpiration estimate by weighting each the mean sap flux of each species by its stand basal area fraction. Censuses of DBH and species composition were conducted in three separate forested areas representing various aspects and elevation. The surveyed areas covered 6,011 m^2 and encompassed 144 individuals of diameter > 4 cm. On the basis of census data, tree-level sap flux was statistically scaled to the plot level following *Matheny et al.* [2014]. In brief, the method assumes that trees of similar species and size (e.g., DBH) will transpire similarly. Thus, the sap flux for each individual of a species-size class is assumed to equal the mean of the measured sap flux for that same species-size class. Finally, sap flux often lags transpiration, as some transpiration must occur to generate the hydraulic gradient within the tree that causes water to flow up the xylem [*Granier and Loustau*, 1994]. The length of the time lag between transpiration and sap flux typically ranges between 0.5-2 hours [*Granier and Loustau*, 1994]. We analyze the cross-correlation between sap flux and incident solar irradiance ($W\ m^{-2}$) at the CDFS to estimate this time lag. The highest

correlation between these two time series occurs when sap flux lags solar irradiance by one hour. Therefore, we account for this lag when discussing net transpiration fluxes by shifting the sap flux time series accordingly.

Table 4.2. Tree size data for sap flux trees are presented as mean ± standard deviation. Crown area was approximated as an ellipse using measured ground projections of the perpendicular major and minor diameters for each crown. Leaf area index (LAI) was not measured as a part of this study; references for species-specific LAI data are provided.

Control	n	DBH (cm)	Height (m)	Crown area (m^2)	LAI (m^2/m^2)
T. aspen	15	18.9 ± 5.5	21.0 ± 7.3	14.5 ± 5.8	1.4 [*Hogg and Hurdle*, 1997]
L. pine	14	23.4 ± 7.5	27.0 ± 7.1	23.4 ± 22.2	3.4 [*Sampson and Allen*, 1995]
D. fir	7	27.8 ± 13.2	25.9 ± 11.1	33.9 ± 21.3	6.9 [*Phillips et al.*, 2002]

Table 4.3. Species-specific variables to determine sapwood area (cm^2) from diameter at breast height (cm) (equation 9)

Species	n	β_1	β_2	β_3	R^2
T. aspen	20	0	1.37	1.7207	0.94
L. pine	11	0	0.77	1.9025	0.93
D. fir	9	-233.5	22.4	1	0.94

4.4.8 Diurnal processes and relationship to diurnal isotopic cycle

Based on the theoretical framework outlined in section 4.3, an isotopic box model is used to estimate the magnitude and timing of these individual flux components throughout the diurnal cycle. The observed specific humidity represents the background specific humidity plus the sum of all of the humidity fluxes:

$$q_{obs}(t) = q_{bg}(t) + q_{mixing}(t) + q_{transpiration}(t) + q_{dew}(t) + q_{evaporation}(t) \quad \text{(Eqn. 10)}$$

Based on the semi-arid location of the CDFS and dry soil conditions during the summer, we assume that $q_{evaporation}$ is negligible. Further, we assume that q_{dew} is also negligible. We did not measure leaf wetness, but if we estimate dew formation as likely when nocturnal 2-m RH exceeds 90%, this only occurs on 22% (17 of 75) of rain-free summer days. If this mass balance equation is applied to the isolated diurnal cycles, $q_{bg}(t)$ reduces to zero, and the mass balance equation can be expressed in simplified form for the diurnal cycle based on the above assumptions:

$$\Delta q_{obs} = \Delta q_{mixing} + \Delta q_{transpiration} \quad \text{(Eqn. 11)}$$

Following the same procedure as in section 2.4, an isotopic version of this mass balance equation can be written:

$$(\Delta_{obs})\Delta q_{obs} = (\Delta_{mixing})\Delta q_{mixing} + (\Delta_{transpiration})\Delta q_{transpiration} \quad \text{(Eqn. 12)}$$

where Δ indicates that we are considering the departures from the 24 hour moving average. Δ_{obs} and q_{obs} are directly measured by the CRDS, while the remaining parameters must be inferred. We estimate $\Delta q_{transpiration}$ by developing a linear transfer function using early morning Δq_{obs} and our sap flux-based estimates of transpiration from summer 2014. Calibrating this relationship using data in the early morning is advantageous because atmospheric mixing is at a minimum while the valley is capped by a thermal inversion. Additionally, we exclude days where the nighttime maximum 2-m RH exceeded 90% to reduce the influence of dew on our calibration. Seven mornings from the summer 2014 observation period remained to train the linear regression model after excluding days with more than 1.0 mm precipitation and a maximum 2-m RH value exceeding 90%. From each of these seven days, we extracted the two-hour period that had the greatest correlation between the transpiration flux and observed specific humidity rise observed between 6 am and 10 am. We then fit a linear mixed model constrained to pass through the origin to estimate the multiplicative factor to translate our composite transpiration estimates into a specific humidity change. The best-fit linear mixed model yields a transfer function between our transpiration flux estimates and its effect on specific humidity:

$$\Delta q_{transpiration} = (0.0318 \pm 0.0040)\mathrm{Tr} \quad \text{(Eqn. 13)}$$

where Tr represents the transpiration estimate taken from time-adjusted sap flux estimates (W/m^2). The mean diurnal cycle of $\Delta q_{transpiration}$ was determined by averaging across all of the days with less than 1.0 mm of rain. The magnitude of the mixing flux is then calculated as the residual between the observed Δq and $\Delta q_{transpiration}$. Estimates of the isotopic composition of the transpiration fluxes are made using equation 12 and holding either $\Delta_{transpiration}$ or Δ_{mixing} constant.

4.5 Results

4.5.1 General features of the isotopic datasets

Isotopic compositions of near-surface vapor and temperature, RH, and q at the CDFS are shown for summer 2012, winter 2013, and summer 2014, respectively (Figures 4.2-4.4). The isotopic and meteorological time series show variability across a broad range of timescales from

diurnal (high frequency) to multiple days to weeks (low frequency). Isotopic compositions are generally lower during the winter period than during the summer, consistent with the colder temperatures and lower *q* values observed during winter. Vapor isotopic compositions range from −30.3 ‰ (−231.0 ‰) to −9.6 ‰ (−82.4 ‰) for $\delta^{18}O$ (δD) in summer 2012, −24.2 ‰ (−199.6 ‰) to −14.6 ‰ (−130.3 ‰) in summer 2014, and −42.6 ‰ (−326.3 ‰) to −25.8 ‰ (−193.5 ‰) in winter 2013 (Table 4.4). Both mean isotopic compositions and meteorological variables are similar for the two summer periods sampled.

Table 4.4. Measurement period mean isotopic compositions and meteorological conditions

Measurement Period	Mean $\delta^{18}O$ (‰ VSMOW)	Mean δD (‰ VSMOW)	mean d-excess (‰ VSMOW)	mean 2-m *q* (g/kg)	mean 2-m temperature (°C)	Total precipitation (mm)
June 12-September 2, 2012	-19.9	-157.2	1.8	6.7	17.4	42.3
January 12-February 4, 2013	-35.4	-268.3	14.8	1.9	-10.3	N/A – bucket not heated
June 30-July 16, 2014	-20.2	-165.5	-3.9	7.5	17.2	16.2

Oxygen and hydrogen isotope ratios in water vapor correlate (e.g., $|r| > 0.5$) with 2- and 10-m *q* and dew point temperature during both seasons (Table 4.5). Correlations between isotopic composition and other meteorological variables exhibit a more complicated structure. Winter vapor $\delta^{18}O$ and δD strongly correlate with 2- and 10-m temperature ($r > 0.7$) (Table 4.5). Summer vapor $\delta^{18}O$ (2012 and 2014) and summer 2012 vapor δD are not correlated with 2- and 10-m temperature ($|r| < 0.2$), but 2014 summer vapor δD is (Table 4.5). Summer vapor $\delta^{18}O$ is correlated with 2- and 10-m RH, but both $\delta^{18}O$ and δD are uncorrelated with RH during the winter. In contrast to $\delta^{18}O$ and δD, vapor d-excess is most strongly correlated with summer 2- and 10-m temperature ($r = 0.755$ and 0.714 respectively) and summer 2- and 10-m RH ($r = −0.590$ and −0.492 respectively). During the winter, vapor d-excess is uncorrelated with temperature, but is weakly correlated with 2- and 10-m RH ($r = −0.328$ and −0.363 respectively). Furthermore, *q* and dew point temperature, which are highly correlated with $\delta^{18}O$ and δD, are uncorrelated with d-excess.

Seasonal differences in the relationship between $\delta^{18}O$ and δD are also apparent (Figure 4.5). The summer data occupy a broad region at less negative isotopic compositions, with the

majority of the data points plotting below the global meteoric water line (GMWL). Data from summer 2012 and summer 2014 plot in similar isotopic space, though the range of compositions observed in summer 2014 is much smaller than in 2012, which is likely the result of the shorter measurement period. In contrast, the winter data occupy a narrow band close to the GMWL, with most of the points above the line.

Table 4.5. Correlations between isotopic composition and meteorological variables[1]

Correlations	Summer 2012	Winter 2013	Summer 2014	All Summer data	Summer data overlapping
2 m q, $\delta^{18}O$	0.830	0.783	0.636	0.770	0.619
2 m q, δD	0.800	0.801	0.568	0.715	0.519
2 m q, d-excess	0.088	-0.210	-0.014 (p = 0.65)	0.031	-0.104
2 m RH, $\delta^{18}O$	0.507	0.077	0.404	0.475	0.396
2 m RH, δD	0.237	0.043 (p = 0.06)	-0.247	0.167	-0.026 (p = 0.21)
2 m RH, d-excess	-0.553	-0.328	-0.726	-0.590	-0.724
2 m T, $\delta^{18}O$	-0.063	0.779	-0.130	-0.069	-0.157
2 m T, δD	0.259	0.809	0.551	0.277	0.288
2 m T, d-excess	0.767	-0.103	0.788	0.755	0.798
2 m T_d, $\delta^{18}O$	0.839	0.809	0.633	0.782	0.639
2 m T_d, δD	0.792	0.832	0.561	0.711	0.523
2 m T_d, d-excess	0.050	-0.181	-0.023 (p = 0.45)	-0.003 (p = 0.84)	-0.130
10 m q, $\delta^{18}O$	0.834	0.794	0.647	0.779	0.644
10 m q, δD	0.808	0.810	0.543	0.726	0.532
10 m q, d-excess	0.010	-0.226	-0.059 (p > 0.05)	0.036	-0.123
10 m RH, $\delta^{18}O$	0.542	0.052	0.376	0.504	0.411
10 m RH, δD	0.311	0.012 (p = 0.59)	-0.192	0.237	0.035 (p = 0.09)
10 m RH, d-excess	-0.452	-0.363	-0.631	-0.492	-0.639
10 m T, $\delta^{18}O$	-0.067	0.775	-0.097	-0.069	-0.155
10 m T, δD	0.238	0.807	0.543	0.258	0.272
10 m T, d-excess	0.725	-0.088	0.744	0.714	0.765
$\delta^{18}O$, δD	0.908	0.995	0.610	0.891	0.843
$\delta^{18}O$, d-excess	-0.055	-0.504	-0.361	-0.073	-0.161
δD, d-excess	0.368	-0.414	0.520	0.387	0.395

1: p-values shown only when greater than 0.05.

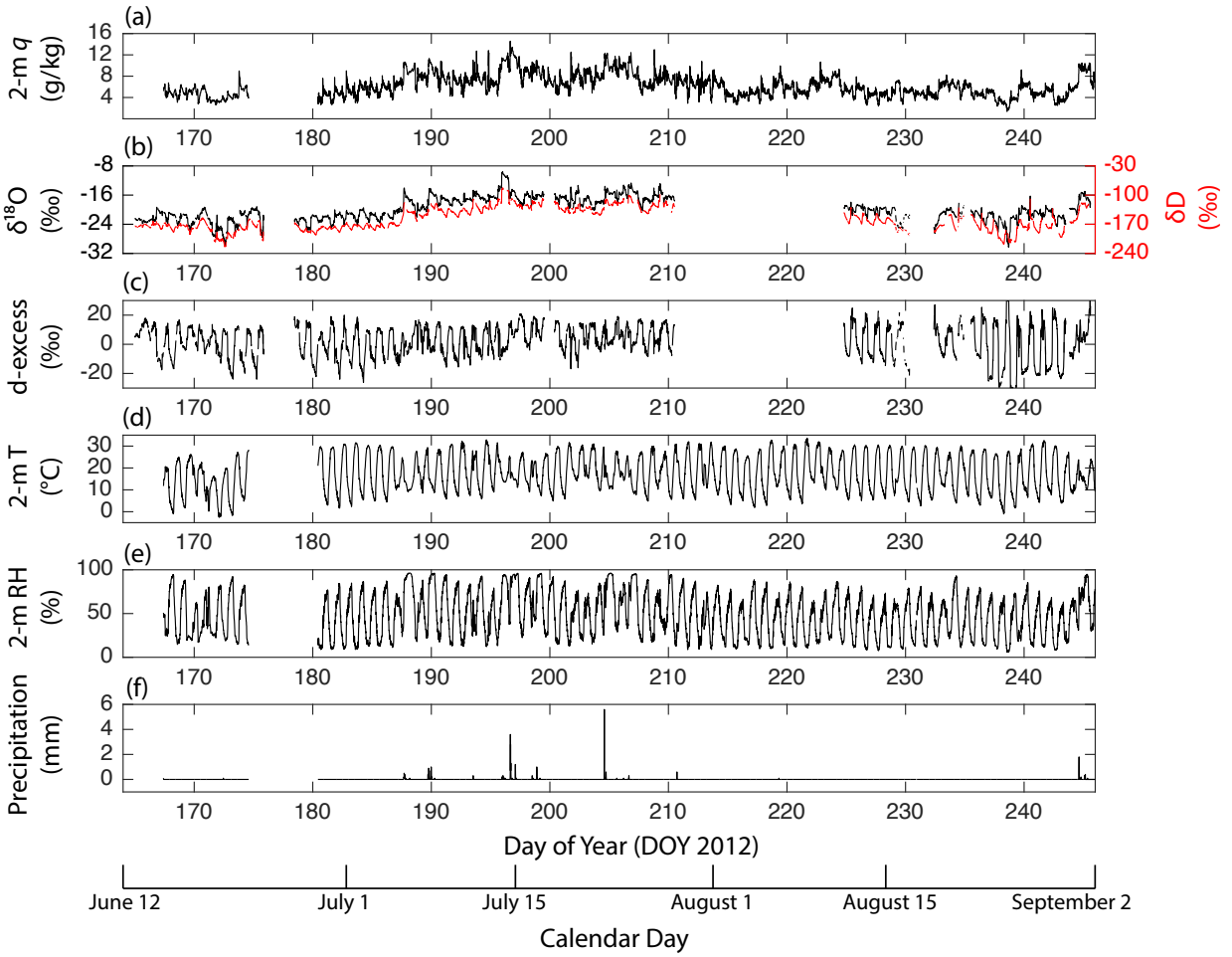

Figure 4.2. Time series of summer 2012 isotopic and meteorological data (DOY 164-246). (a) Specific humidity, q (2-m, g/kg), (b) $\delta^{18}O$ (black) and δD (red) (‰ VSMOW), (c) d-excess (‰ VSMOW), (d) temperature (2-m, °C), (e) relative humidity (2-m, %), and (f) precipitation amount (mm).

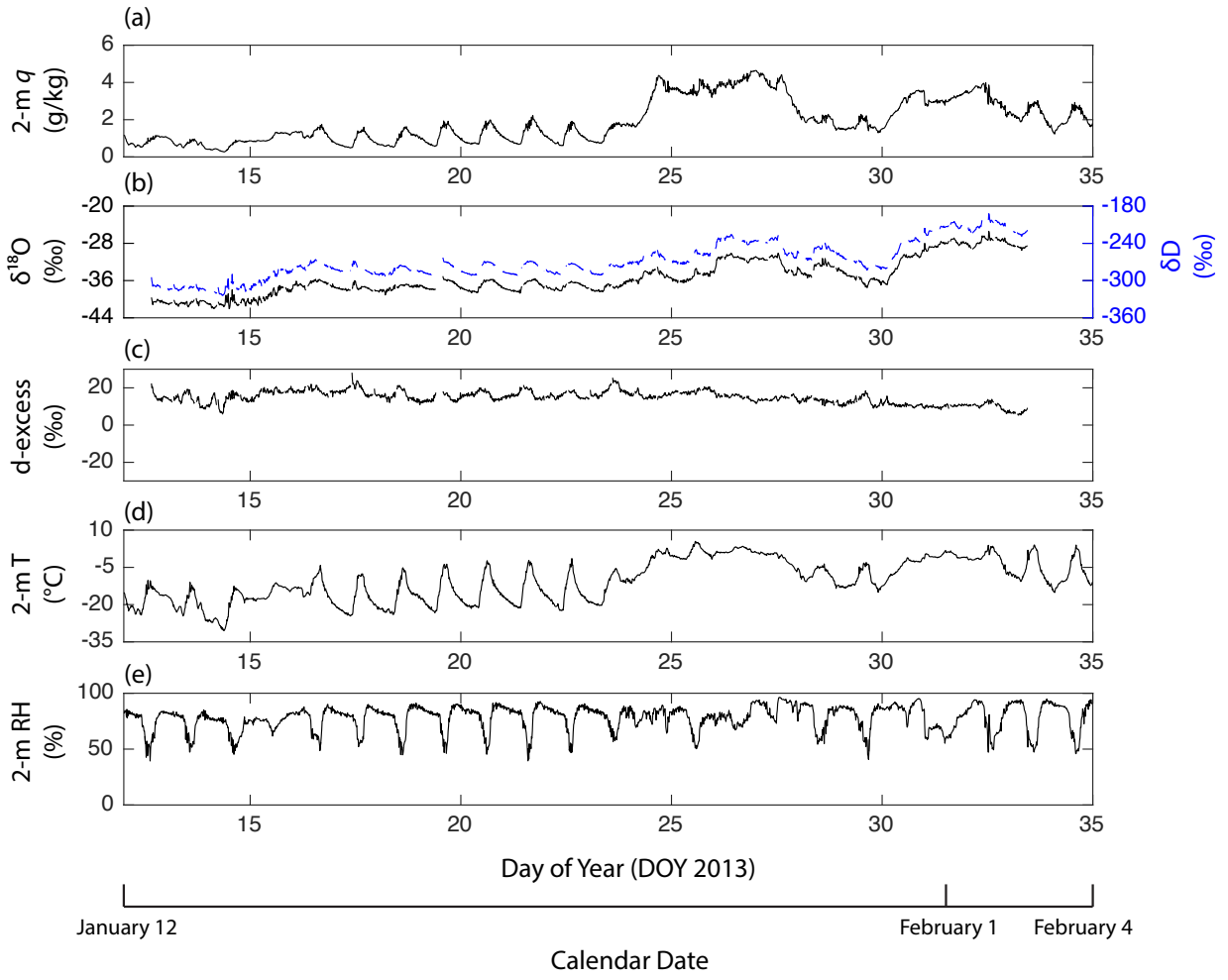

Figure 4.3. Time series of winter 2013 isotopic and meteorological data (DOY 10-35). (a) Specific humidity, q (2-m, g/kg), (b) $\delta^{18}O$ (solid black) and δD (dashed blue) (‰ VSMOW), (c) d-excess (‰ VSMOW), (d) temperature (2-m, °C), and (e) relative humidity (2-m, %). Camp Davis precipitation data not available during the winter as the precipitation gauge was unheated.

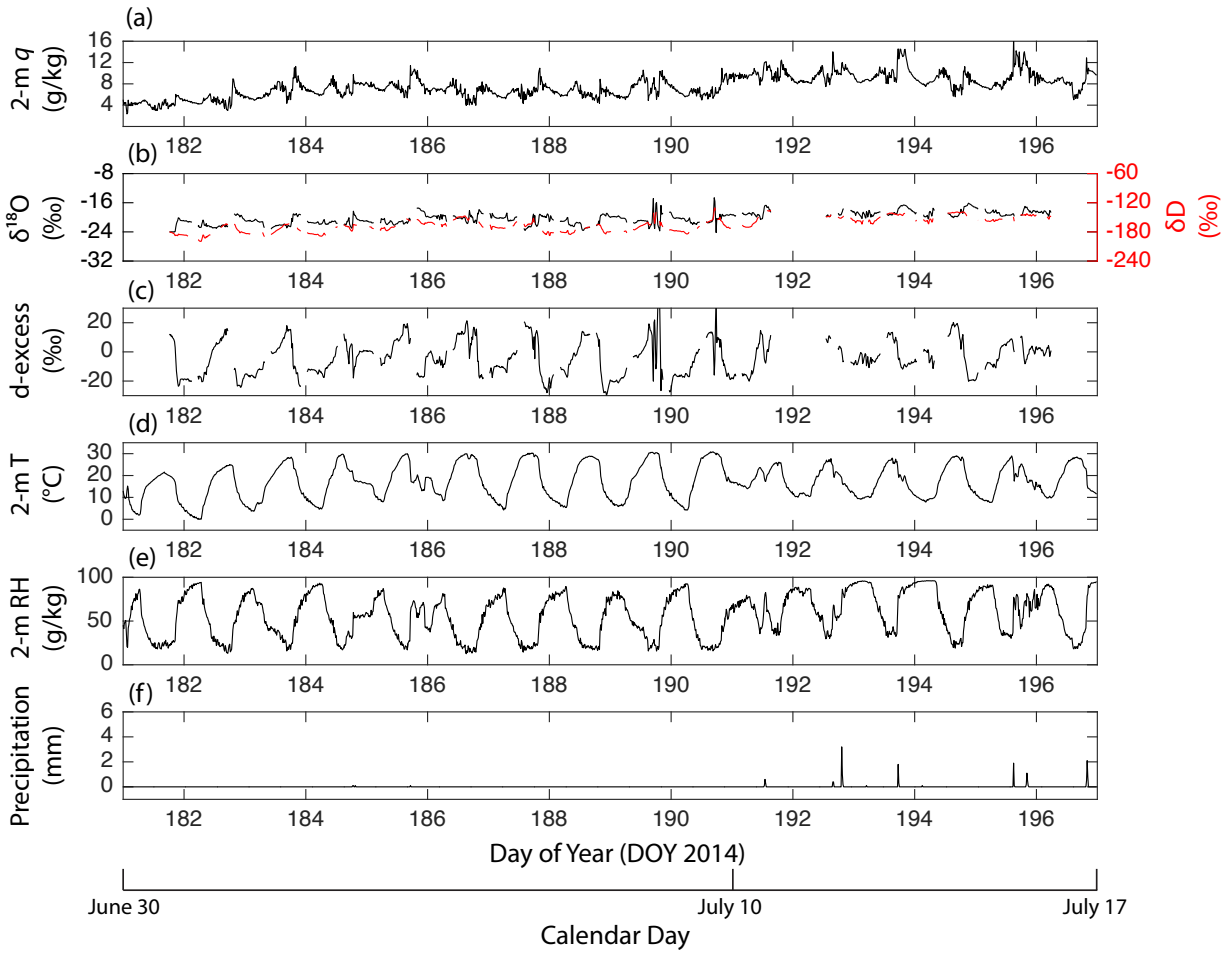

Figure 4.4. Time series of summer 2014 isotopic and meteorological data (DOY 181-197). (a) Specific humidity, q (2-m, g/kg), (b) $\delta^{18}O$ (black) and δD (red) (‰, VSMOW), (c) d-excess (‰ VSMOW), (d) temperature (2-m, °C), (e) relative humidity (2-m, %), and (f) precipitation amount (mm).

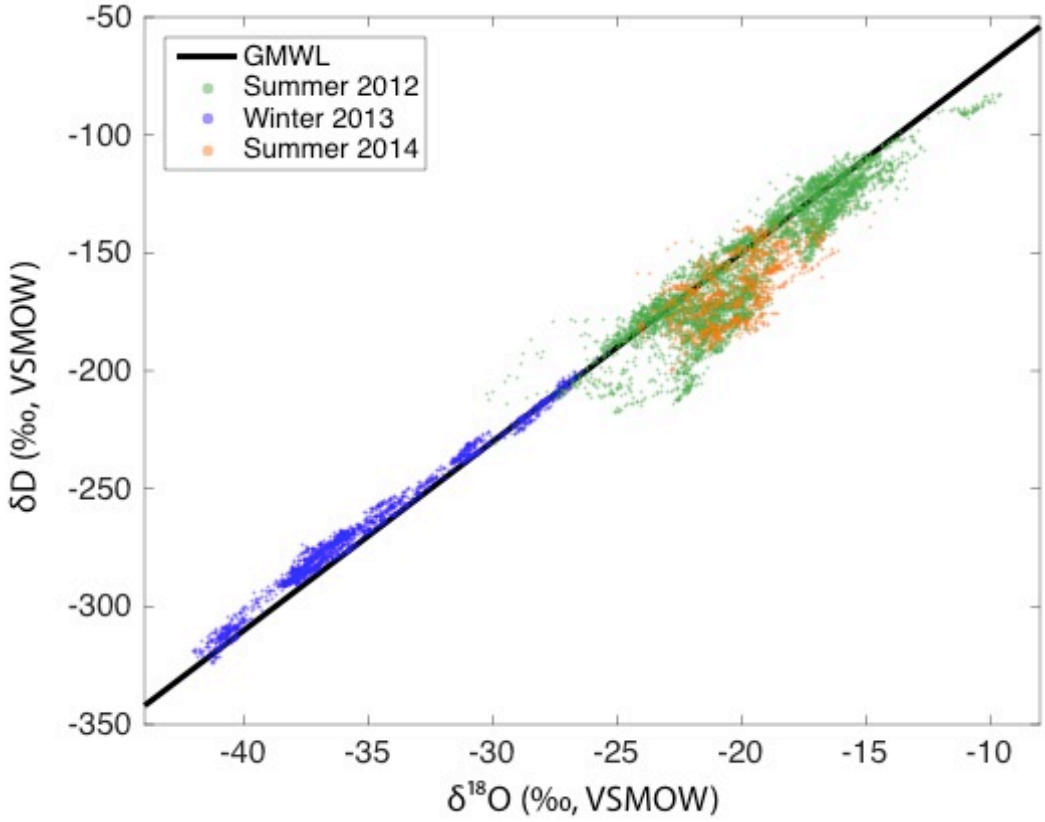

Figure 4.5. The δD vs $\delta^{18}O$ relationship at CDFS. Summer 2012, winter 2013, and summer 2014 data are shown as green, purple, and orange dots respectively. The global meteoric water line (GMWL) suggested by Dansgaard [1964] is shown a solid black line. Data from winter 2013 plot in a narrow envelope surrounding the GMWL, while the summer data exhibits a much larger range of variability about the GMWL.

4.5.2 Seasonal relationships between specific humidity and isotopic composition

Clear seasonal contrasts emerge in the relationship between $\delta^{18}O$ (Figure 4.6a,c) or δD (Figure 4.6b,d) and q for all three of our measurement periods. The isotopic composition of an air-mass is modeled with two initial moisture source conditions typical of the northern (10°C, 85% RH, blue lines) and subtropical Pacific ocean (20°C, 85% RH, red lines) [after *Noone*, 2012]. Predictions are made for both open-system or Rayleigh condensation (solid lines) and closed-system condensation (dashed lines). These conditions broadly reflect the range of summer oceanic moisture sources to the Rocky Mountains and are provided primarily for reference.

Near-surface air during the summer (Figure 4.5, 2012 – green dots, 2014 – orange dots) is moister and is less depleted in heavy isotopes than near-surface air during the winter (Figure 4.5, 2013 – blue dots). For both seasons, no single condensation pathway can explain the q-δ

distributions (Figure 4.6). Values that fall between two different condensation lines may result from upwind mixing of two distinct air-masses, or from precipitation processes that lie between open and closed end members. In contrast, many observations exhibit isotopic compositions too depleted or too moist to be explained by a 20°C, 85% RH ocean vapor source undergoing open-system condensation, and plot below the warm source Rayleigh line (Figure 4.6, Table 4.6). These observations are best explained by either a yet warmer ocean source or vapor recycling over the continent. Back trajectory analysis does suggest air transport from the Gulf of Mexico on rare occasions (see section 3.4), but not frequently enough to explain the fraction of moist but highly depleted observations. Local or upwind partial evaporation of falling raindrops and evapotranspiration can preferentially return light water isotopologues to the atmosphere, causing isotopic compositions to be lower than predicted from Rayleigh condensation. For example, analysis of North American Regional Reanalysis data suggests that ~15-25% of the vapor associated with the North American Monsoon is recycled [*Dominguez et al.*, 2008]. A greater fraction of observations from summer 2014 (85%) than 2012 (45.6%) fall below the 20°C open condensation line (Table 4.6, Figure 4.6). This relationship is most likely due to stronger continental recycling during the 2014 observational period than in 2012.

Winter q-δ relationships demonstrate similar features as summer. Water vapor in winter air exhibits q values too moist and too dry and isotopic compositions above and below the Rayleigh prediction lines for both modeled ocean sources (Table 4.6). As during the summer, data with isotopic compositions above Rayleigh predictions are best explained by partially closed precipitation processes where not all of the condensed vapor is removed from the cloud, or by mixing with a dry, isotopically light air mass.

A second layer of information about the long-term processes influencing local isotopic variability can be recovered from a moving correlation analysis of q relative to δ [*He and Smith*, 1999; *Noone et al.*, 2011]. Using a 96-point window corresponding to one day of data, mixing of multiple water sources is identified as the dominant process affecting the isotopic composition of near-surface water vapor for nearly the entire observational period (>90%, Table 4.7). In contrast, open or closed system condensation models provide the best explanation for no more than 6% of the data. The periods where condensation processes are the best model, or where no model provides the best explanation, are closely associated with precipitation events.

Table 4.6. Relationship between isotopic composition and predicted Rayleigh values

	Too moist for source	Too depleted for source	Too enriched for source
Summer 2012 – 20°C source	0.7%	45.6%	53.7%
Summer 2012 – 10°C source	41.5%	54.3%	4.3%
Winter 2013 – 20°C source	0%	23.8%	76.2%
Winter 2013 – 10°C source	0%	52.5%	47.5%
Summer 2014 – 20°C source	2.1%	85.0%	12.8%
Summer 2014 – 10°C source	68.6%	31.2%	0.2%

Table 4.7. Atmospheric process breakdown

	Measurement Period		
δD	**Summer 2012**	**Winter 2013**	**Summer 2014**
Air Mass Mixing	92.2%	97.4%	96.7%
Condensation (open/Rayleigh or closed)	5.1%	0%	0%
Neither process dominant	2.2%	2.6%	3.3%
$\delta^{18}O$	**Summer 2012**	**Winter 2013**	**Summer 2014**
Air Mass Mixing	89.2%	97.3%	98.2%
Condensation (open/Rayleigh or closed)	6.9%	0%	<0.1%
Neither process dominant	3.6%	2.7%	1.6%

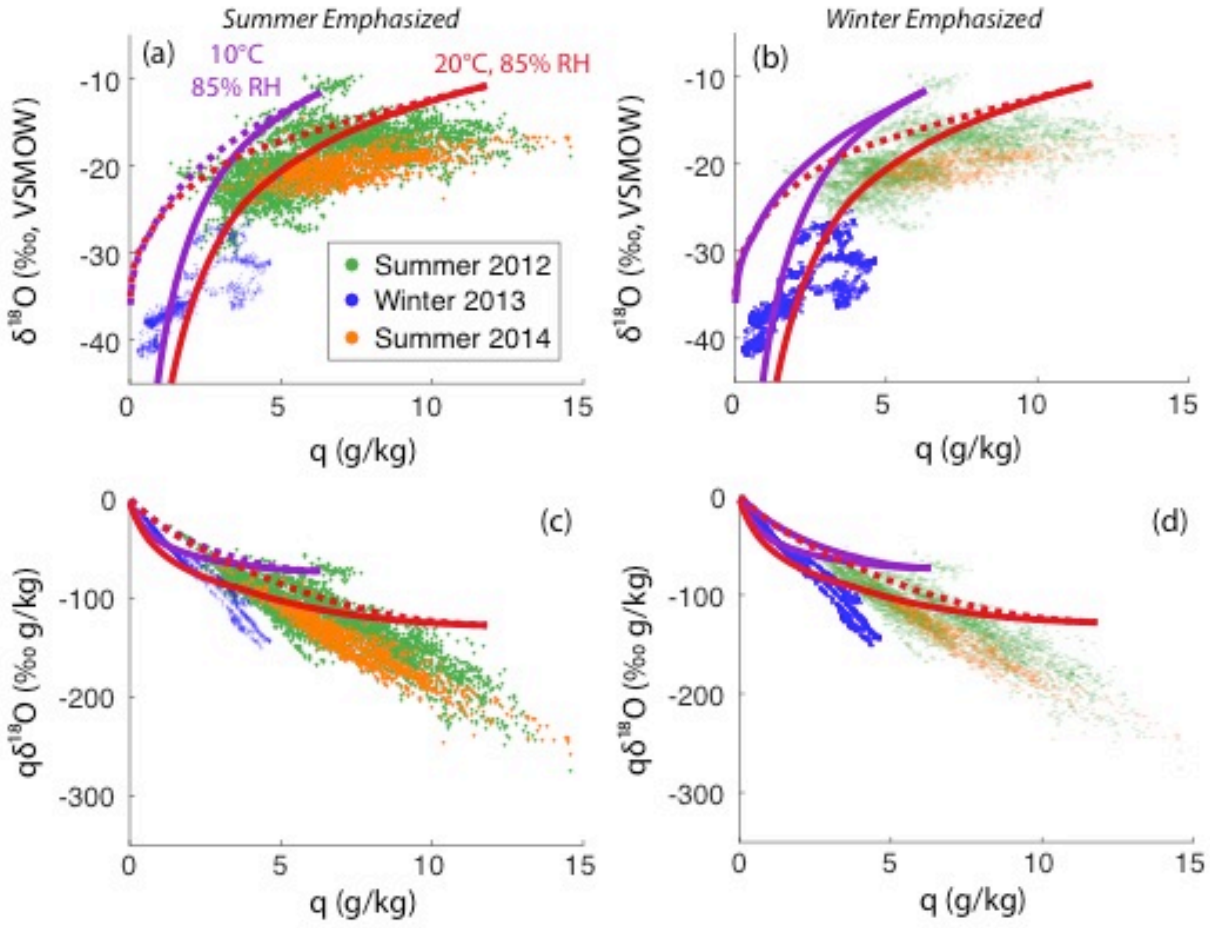

Figure 4.6. Scatterplots of specific humidity (q, g/kg) vs $\delta^{18}O$ (a,b) and the product of vapor pressure and isotopic composition ($q\delta^{18}O$) vs $\delta^{18}O$ (c,d). The left (right) column emphasizes the summer (winter) data by reducing the transparency of the other season. Summer 2012 (2014) data are shown as green (orange) dots, and winter 2013 data as blue dots. Modeled isotopic compositions as water vapor is condensed from an air parcel based on open (solid lines) or closed system (dashed lines) behavior as water vapor is removed from an air parcel. Initial conditions are calculated assuming 85% relative humidity and temperatures of 20°C (red) or 10°C (purple), and isotopic compositions of 0‰ VSMOW at the initial oceanic evaporation source.

4.5.3 High-frequency variability and the diurnal cycle

4.5.3.1 Seasonal changes in the diurnal cycle

We isolated diurnal scale variability as the residual between the measured data series and the 24-hour-filtered time series. Clear but distinct diurnal cycles emerge in both summer and winter datasets. In summer 2012, q increases between sunrise and 10 am, decreases from 10 am to 2 pm, remains steady between 2 pm and ~5 pm, increases rapidly at 6 pm, and then decreases slowly over night (Figure 4.7a). The morning increase in Δq is associated with large (10-30‰) increases in ΔD and Δd-excess and with little change in $\Delta^{18}O$ (< 1‰) (Figure 4.7b-d). As Δq begins to decrease after 10 am, $\Delta^{18}O$ begins to decrease along with ΔD, while d-excess continues

to increase. At 2 pm, when Δq stabilizes, $\Delta^{18}O$, ΔD, and Δd-excess also stabilize. After 5 pm until ~8 pm, Δq and $\Delta^{18}O$ increase rapidly, but ΔD remains fairly constant, driving a rapid decrease in Δd-excess. Strong daily cycles are also present in temperature, RH, vapor pressure deficit (VPD), and 10-m wind speed (Figure 4.7e-h). Daily temperature varies by ~20°C (Figure 4.7e). RH varies inversely with temperature and by up to 90%, with minimum values between noon and 6 pm, and maximum values just before dawn (Figure 4.7f). As a result of these temperature and RH patterns, VPD reaches a maximum value of > 3 kPa on average during the afternoon (~1 pm to 5 pm) before dropping rapidly after sunset (Figure 4.7g). Finally, wind speeds tend to be low (< 1 m s^{-1}) at night, rise gradually between sunrise and ~3 pm, and then decrease rapidly after sunset (Figure 4.7h). Nights with high wind speeds are associated with frontal systems and often preceded or lagged large precipitation events by several hours to a day.

Patterns for summer 2014 are qualitatively similar to summer 2012 (Figure 4.8). The 2014 dataset only includes 12 days, while the 2012 dataset includes 63. As a result, slight changes in the timing of the development and decay of the boundary layer introduce high-frequency features into the mean diurnal cycle that would disappear by averaging over a longer measurement period (e.g., dusk in Figure 4.8b).

The diurnal cycle in winter is far simpler than in the summer. Specific humidity rises in the morning and decreases in the afternoon and overnight (Figure 4.9a), with a diurnal amplitude that is only ~30% of the summer amplitude. In contrast to the summer, both $\Delta^{18}O$ and ΔD tend to track Δq (Figure 4.9bc), and as a result, the Δd-excess cycle is much smaller (< 5‰, Figure 4.9d). Diurnal amplitudes in temperature, RH, and VPD are also smaller than their summer counterparts (Figure 4.9efg). Mean afternoon VPD is less than 7% of its summer value. Finally, the diurnal cycle in 10-m wind speeds is muted during the winter, likely due to a more permanent inversion in the valley during the winter than during the summer.

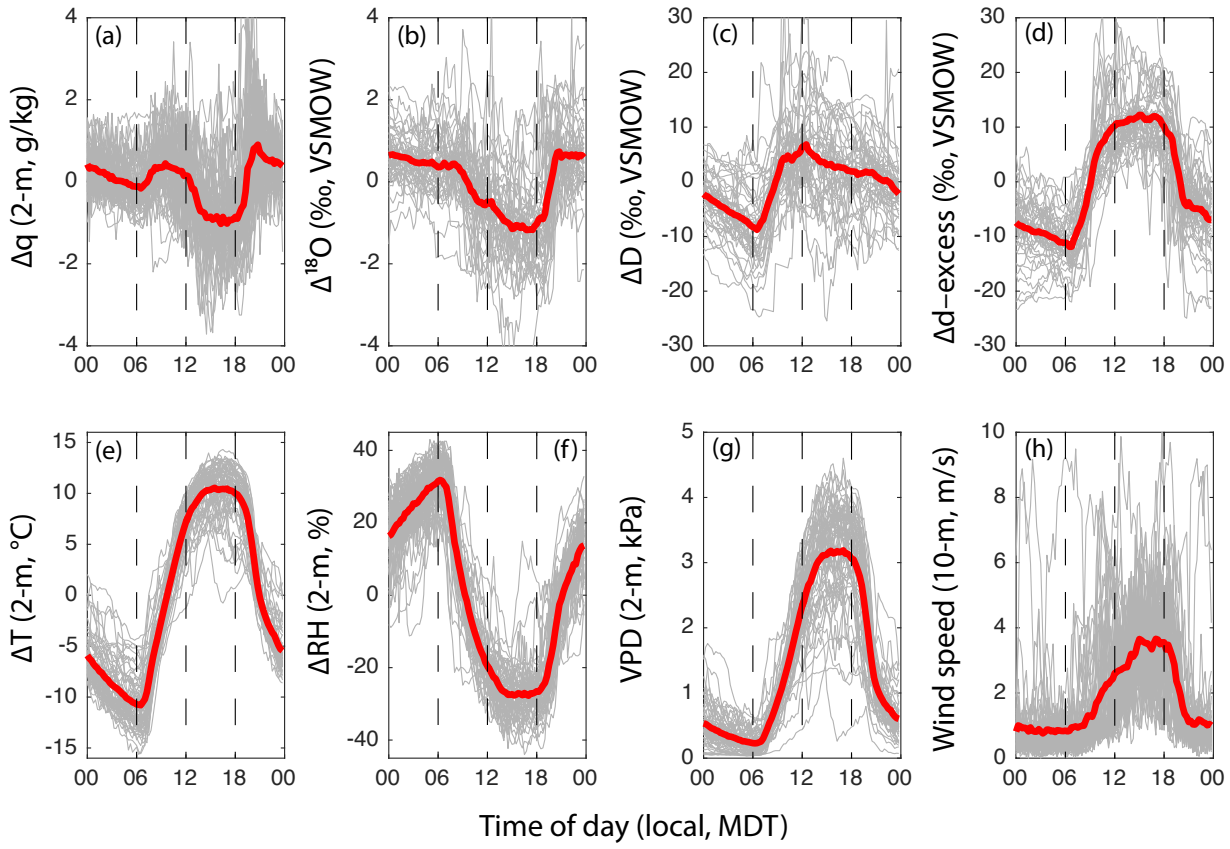

Figure 4.7. Summer 2012 diurnal cycles of (a) 2-m specific humidity, Δq (g/kg), (b) $\Delta^{18}O$ (‰ VSMOW), (c) ΔD (‰ VSMOW), (d) Δd-excess (‰ VSMOW), (e) 2-m temperature (ΔT, °C), (f) 2-m relative humidity (ΔRH, %), (g) 2-m vapor pressure deficit (kPa), and (h) 10-m wind speed (m/s). Data in (a)-(f) are residuals from the 24-h moving average, while (g) and (h) are the measured values. The solid red line is the multiday mean diurnal cycle.

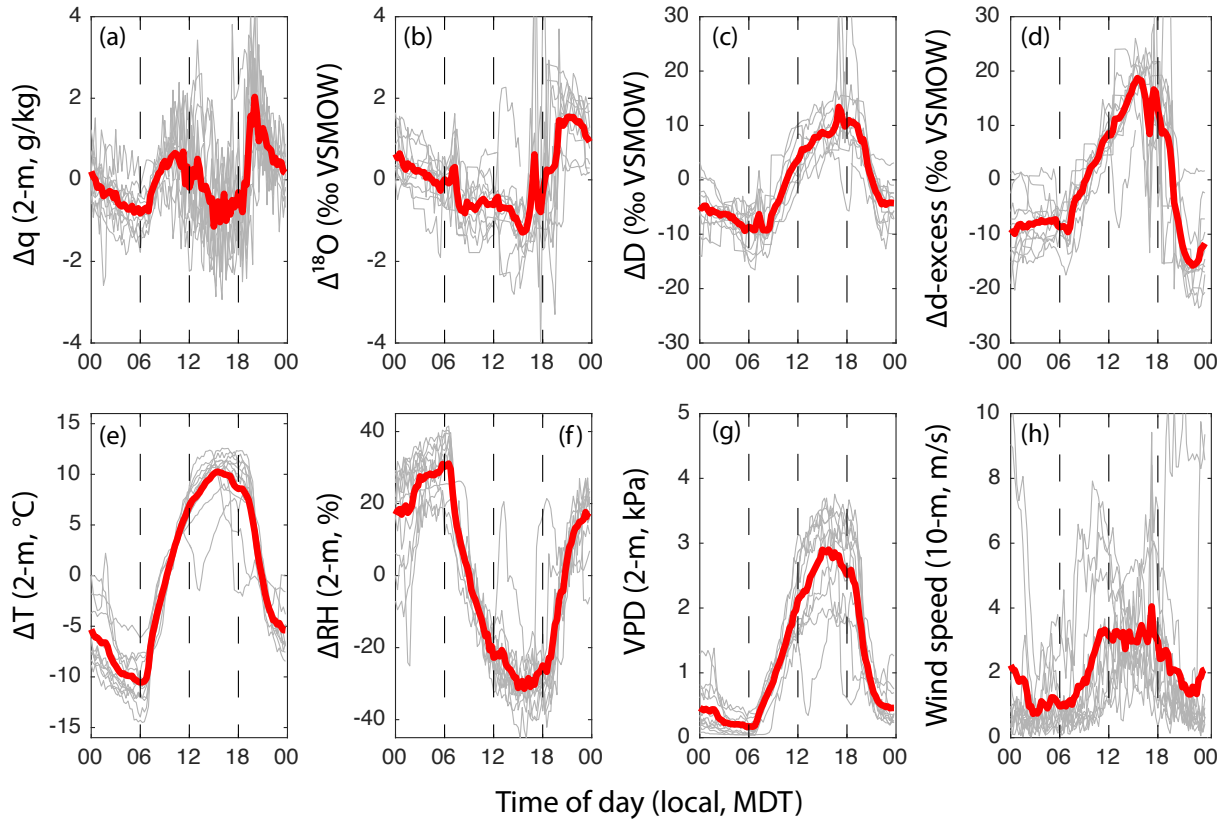

Figure 4.8. Summer 2014 diurnal cycles of (a) 2-m specific humidity, Δq (g/kg), (b) $\Delta^{18}O$ (‰ VSMOW), (c) ΔD (‰ VSMOW), (d) Δd-excess (‰ VSMOW), (e) 2-m temperature (ΔT, °C), (f) 2-m relative humidity (ΔRH, %), (g) 2-m vapor pressure deficit (kPa), and (h) 10-m wind speed (m/s). Data in (a)-(f) are residuals from the 24-h moving average, while (g) and (h) are the measured values. The solid red line is the multiday mean diurnal cycle.

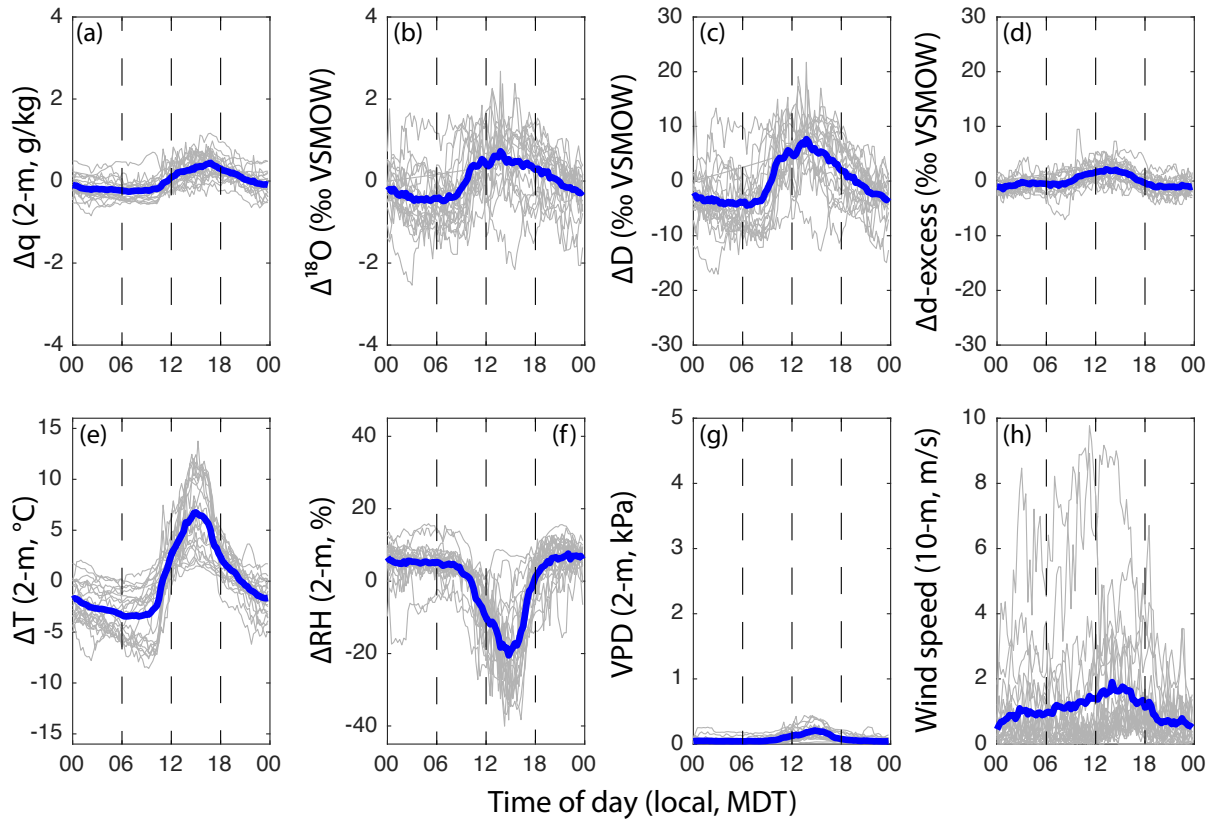

Figure 4.9. Winter 2013 diurnal cycles of (a) specific humidity, Δq (g/kg), (b) $\Delta^{18}O$ (‰ VSMOW), (c) ΔD (‰ VSMOW), (d) Δd-excess (‰ VSMOW), (e) 2-m temperature (ΔT, °C), (f) 2-m relative humidity (ΔRH, %), (g) 2-m vapor pressure deficit (kPa), and (h) 10-m wind speed (m/s). Data in (a)-(f) are residuals from the 24-h moving average, while (g) and (h) are the measured values. The solid blue line is the multiday mean diurnal cycle.

4.5.3.2 Integrating sap flux with isotope measurements to understand summer diurnal water cycling

Estimates of the transpiration flux combined with specific humidity measurements provide an approximation of the magnitude and timing of the transpiration water flux into the near-surface layer, as well as its export from the near-surface layer by atmospheric mixing. Transpiration fluxes are a source of near-surface humidity throughout the day and decrease to near zero at night (Figure 4.10). Mixing, calculated as the residual of the specific humidity and transpiration, removes near-surface humidity from the surface throughout the day, only acting as a source of humidity around and immediately after dusk (Figure 4.10).

Lacking additional constraints on the isotopic composition of either flux, the isotopic composition of the mixing flux required to balance a range of transpiration isotopic fluxes can be calculated from mass-balance (equation 12). For simplicity, four cases are considered here where

either the mixing or the transpiration flux is assumed to be isotopically invariant with respect to $\Delta^{18}O$ throughout the day, and positive or negative (Figure 4.11). If the isotopically fixed flux is negative, the isoforcing (i.e., the product of the humidity and isotopic fluxes) by mixing is positive throughout the day, while the isoforcing by transpiration is negative (Figure 4.11a-b). Though the signs of the isoforcing differ during the day, the isotopic compositions of the transpiration and mixing fluxes are both negative during the day, but the flux allowed to vary becomes positive overnight (Figure 4.11c-d). If the isotopically fixed flux is positive instead, the opposite trends hold (Figure 4.11e-h). In cases where $\Delta^{18}O_{transpiration}$ is held constant, the sign of the isoforcing of each flux does not change throughout the day (Figure 4.11a,e), and the magnitude of the daytime $\Delta^{18}O_{mixing}$ forcing reaches a maximum in late morning before decaying throughout the afternoon until near sunset (Figure 4.11c,g). At sunset, the inferred $\Delta^{18}O_{mixing}$ appears to change rapidly as Δq_{mixing} approaches zero. In contrast, when $\Delta^{18}O_{mixing}$ is held constant, the sign of the isoforcing for both fluxes changes at dusk (Figure 4.11b,f), and the inferred isotopic magnitude of the transpiration flux increases throughout the day, reaching a maximum in late afternoon, and changes sign into the evening (Figure 4.11d,h).

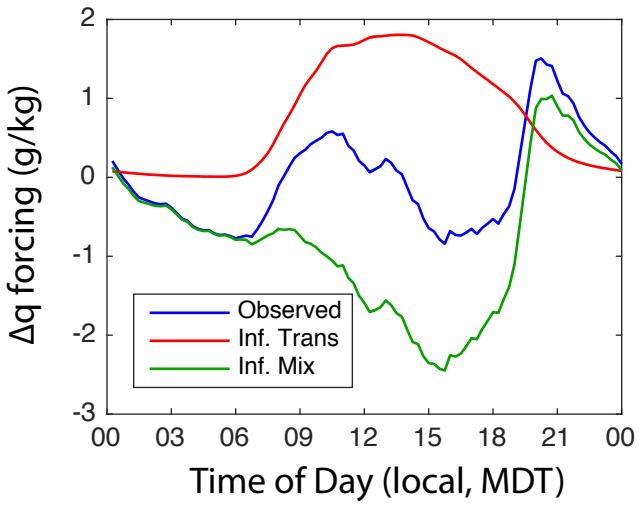

Figure 4.10. Observed diurnal cycle of Δq and inferred components. Observed Δq was smoothed with a 5 point moving average filter to reduce high frequency variability. Inferred $\Delta q_{transpiration}$ was calculated using equation 14. Inferred Δq_{mixing} was estimated as the residual between $\Delta q_{transpiration}$ and the observed Δq.

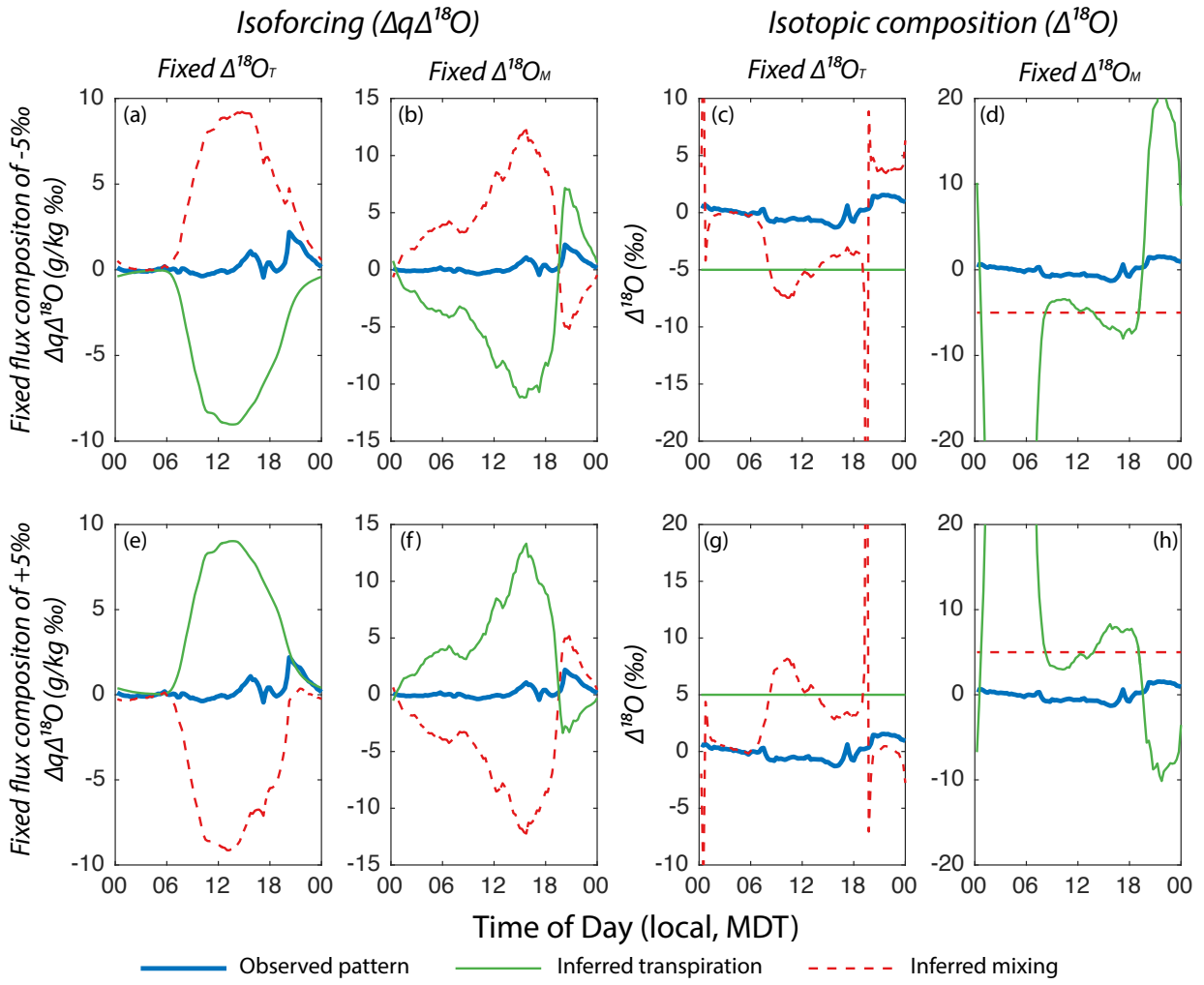

Figure 4.11. Isoforcing and isotopic compositions required to match observations if one of the component fluxes is assumed to be isotopically invariant. The top row (a-d) fixes one of the isotopic fluxes at -5‰, while the bottom row (e-h) fixes the isotopic fluxes at +5‰. The left two columns are the required isoforcings ($\Delta q\Delta^{18}O$) to match the observed isoforcing for a fixed $\Delta^{18}O_T$ (first column) or a fixed $\Delta^{18}O_M$ (second column). The right two columns calculate the isotopic composition of the variable flux required to balance a fixed $\Delta^{18}O_T$ (third column) or a fixed $\Delta^{18}O_M$ (fourth column). Observed values are shown as thick, solid blue lines, inferred transpiration values as thin, solid green lines, and inferred mixing values as thin, dashed red lines.

4.5.4 Relationships between weather patterns and low-frequency isotopic and meteorological variability

We isolate the low-frequency isotopic and meteorological variability from our time series by applying a 24-hour moving average filter to remove the diurnal cycle (Figure 4.12). Both summer and winter data show evidence of synoptic changes reflected in specific humidity and isotopic composition. To first order, these changes in low-frequency isotopic compositions reflect changes in moisture transport to NW Wyoming.

Back trajectories during summer 2012 fall into four broad groups. Two of these groups brought air parcels from north of the CDFS, either up the Snake-Columbia River valleys (SCR, Figure 4.13a) or from Canada, typically east of the Coast Ranges in British Columbia (CAN, Figure 4.13b). The other two trajectories transport air parcels from the south from the North American Monsoon region and are Pacific-derived (NAM, Figure 4.13c) or from the central US, ultimately from the Gulfs of California and Mexico (CUS, Figure 4.13d). Northerly air parcels tend to be drier and more depleted in heavy isotopes than air parcels of southern origin (Table 4.8, Figure 4.13e). Moist air parcels arriving from the south were associated with 69% of summer precipitation during the summer despite comprising only 41% of the trajectories, indicating that large-scale moisture convergence is important in triggering precipitation events (Table 4.8, Figure 4.13e). However, the mean silhouette width was negative for summer 2012 clusters (Table 4.8), consistent with the substantial overlap observed between clusters in a plot of q and $\delta^{18}O$ (Figure 4.13e, Table 4.8). The distributions of observed d-excess during these periods are quite similar for all four trajectory clusters, suggesting that the d-excess of the original moisture source has been overprinted by continental recycling and mixing (Figure 4.13f). As a result, the d-excess of near-surface vapor likely no longer represents the oceanic moisture source, but instead, represents a mixture of the d-excess of oceanic and terrestrial moisture sources [*Welp et al.*, 2012; *Aemisegger et al.*, 2014].

Back trajectories during summer 2014 fall into two distinct clusters (Figure 4.14a-b, Table 4.8). The most common back trajectory pattern (89%) is the SRC pathway observed in 2012 (Figure 4.14a). A pattern of advection from the southwest (Figure 4.14b), comprised the remaining 11% of trajectories and is similar to the NAM pathway observed in 2012. In contrast to 2012, the SRC pathway was associated with almost all of the precipitation during the 2014 observation period (99%), while the NAM pathway contributed almost no rainfall (1%). No separation of these trajectory pathways was observed in the relationship between q and $\delta^{18}O$ (Figure 4.14c), indicating that no evidence of distinct properties resulting from shifts in regional air transport are apparent in summer 2014 either. However, the distribution of observed d-excess was skewed toward more negative values for the SRC pathway than the NAM pathway, potentially reflecting a stronger influence of evaporated, low d-excess leaf waters on near-surface humidity (Figure 4.14d).

Trajectories during the winter 2013 observation period also split into four distinct regions (WT1-4, "winter trajectory"). Air transport for the first ten days of the measurement period was from the north and along the Snake River Plain (WT1, Figure 4.15a). Following this period, two successive snowstorms occurred at the CDFS. The first was driven by a large low-pressure system that moved into NW Wyoming on DOY 23, bringing moist air derived from the North Pacific (Figure 4.15b). At DOY 28, the low-pressure system was cut-off from its oceanic moisture source (Figure 4.15c), resulting in drier conditions at CDFS. Finally, at DOY 30, a second snowstorm entered the region, with strong air advection from the Pacific over Oregon and up the Snake River Plain (Figure 4.15d). In contrast to the summer data, the four trajectory pathways identified form unique clusters of q versus $\delta^{18}O$ (Figure 4.15e), as indicated by a positive mean silhouette width (Table 4.8). The driest periods associated with the lowest isotopic composition occur when air advection is from the far north (Figure 4.15a). The two snowstorm periods (Figure 4.15b,d) are the most humid, and also show distinct isotopic compositions (Figure 4.15e). The period between the two snowstorms (Figure 4.15c) shows a drying trend, associated with the removal of an oceanic moisture source as the low moves onto the continent. Also in contrast to the summer, the observed distributions of d-excess are all above zero during the winter and show some separation between air transport pathways (Figure 4.15f).

Table 4.8. Vapor Source Mean Characteristics and Average Silhouette Widths

SUMMER					
Source Pathway (Year)	**Mean $\delta^{18}O$ (‰)**	**5/95th percentile $\delta^{18}O$ (‰)**	**Mean *q* (g/kg)**	**5/95th percentile *q* (g/kg)**	**Average hours over land**
ST1 (2012)	-21.44	-26.49/-15.04	5.64	3.07/9.83	126
ST2 (2012)	-21.40	-24.79/-19.42	5.49	3.82/7.10	191
ST3 (2012)	-19.06	-23.20/-14.85	6.85	3.56/10.97	140
ST4 (2012)	-16.78	-18.89/-15.69	7.35	4.73/9.98	235
ST5 (2014)	-20.19	-22.77/-17.51	7.55	4.27/11.02	148
ST6 (2014)	-20.23	-21.82/-17.60	7.18	4.63/9.64	139
Mean Summer 2012 Silhouette Width (4 clusters)			-0.281		
Mean Summer 2014 Silhouette Width (2 clusters)			-0.093		
Mean Summer Silhouette Width (both years, 6 clusters)			-0.287		
WINTER					
Source Pathway (Year)	**Mean $\delta^{18}O$ (‰)**	**5/95th percentile $\delta^{18}O$ (‰)**	**Mean *q* (g/kg)**	**5/95th percentile *q* (g/kg)**	**Average hours over land**
WT1 (2013)	-38.29	-41.12/-35.99	1.00	0.44/1.71	132
WT2 (2013)	-34.04	-37.56/-30.73	3.24	1.20/4.48	163
WT3 (2013)	-34.70	-36.87/-32.32	1.77	1.43/2.20	220
WT4 (2013)	-28.49	-30.92/-26.80	2.75	1.65/3.71	72
Mean Winter 2013 Silhouette Width (4 clusters)			0.299		

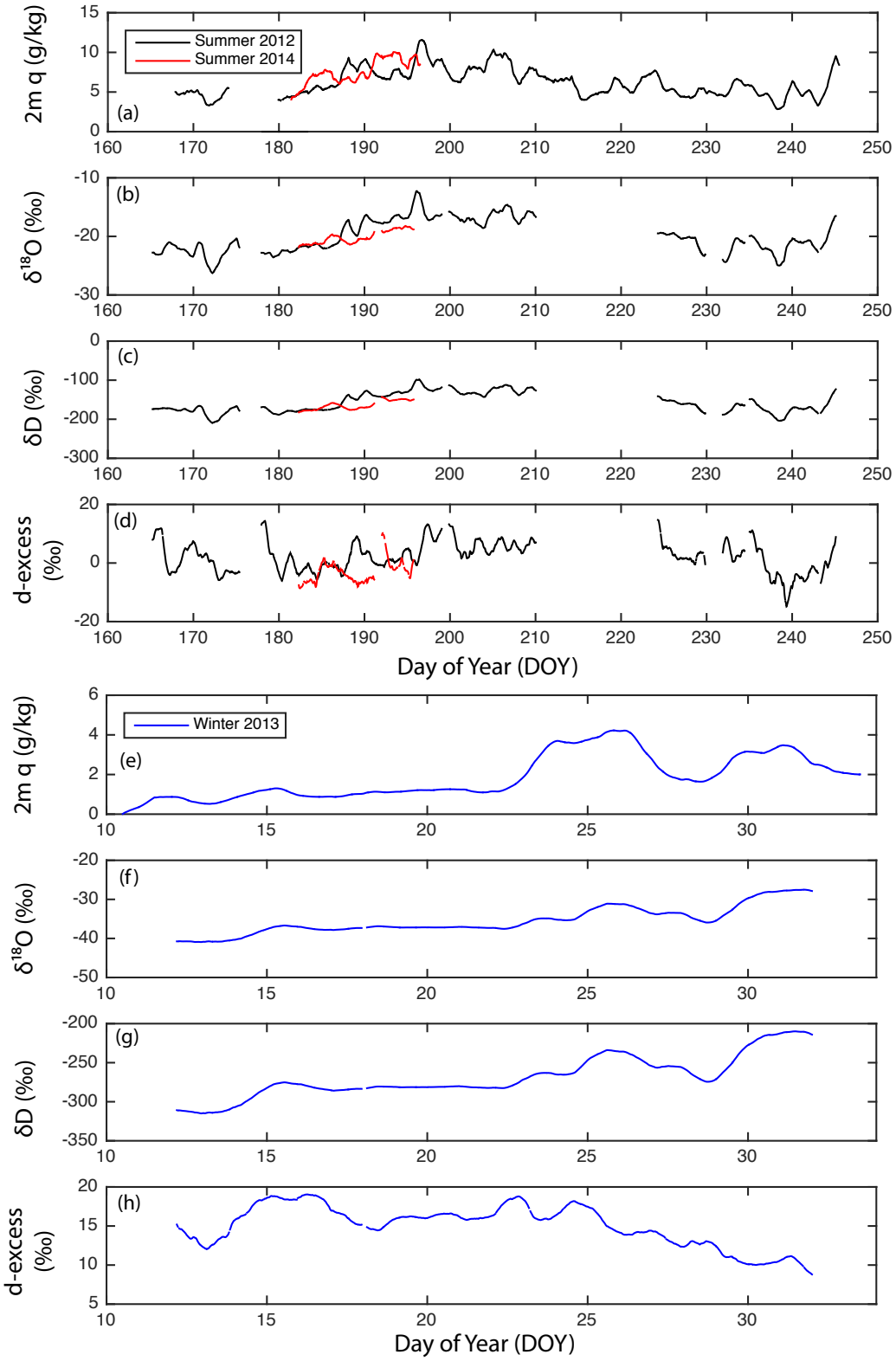

Figure 4.12. Comparison of summer (upper half) and winter (lower half) low-frequency variability. Data in this figure are the same as in Figures 1-3, but filtered with a 24-hour moving average. (a,e) Specific humidity, q (g/kg), (b,f) $\delta^{18}O$ (‰ VSMOW), (c,g) δD (‰ VSMOW), and (d,h) d-excess (‰ VSMOW).

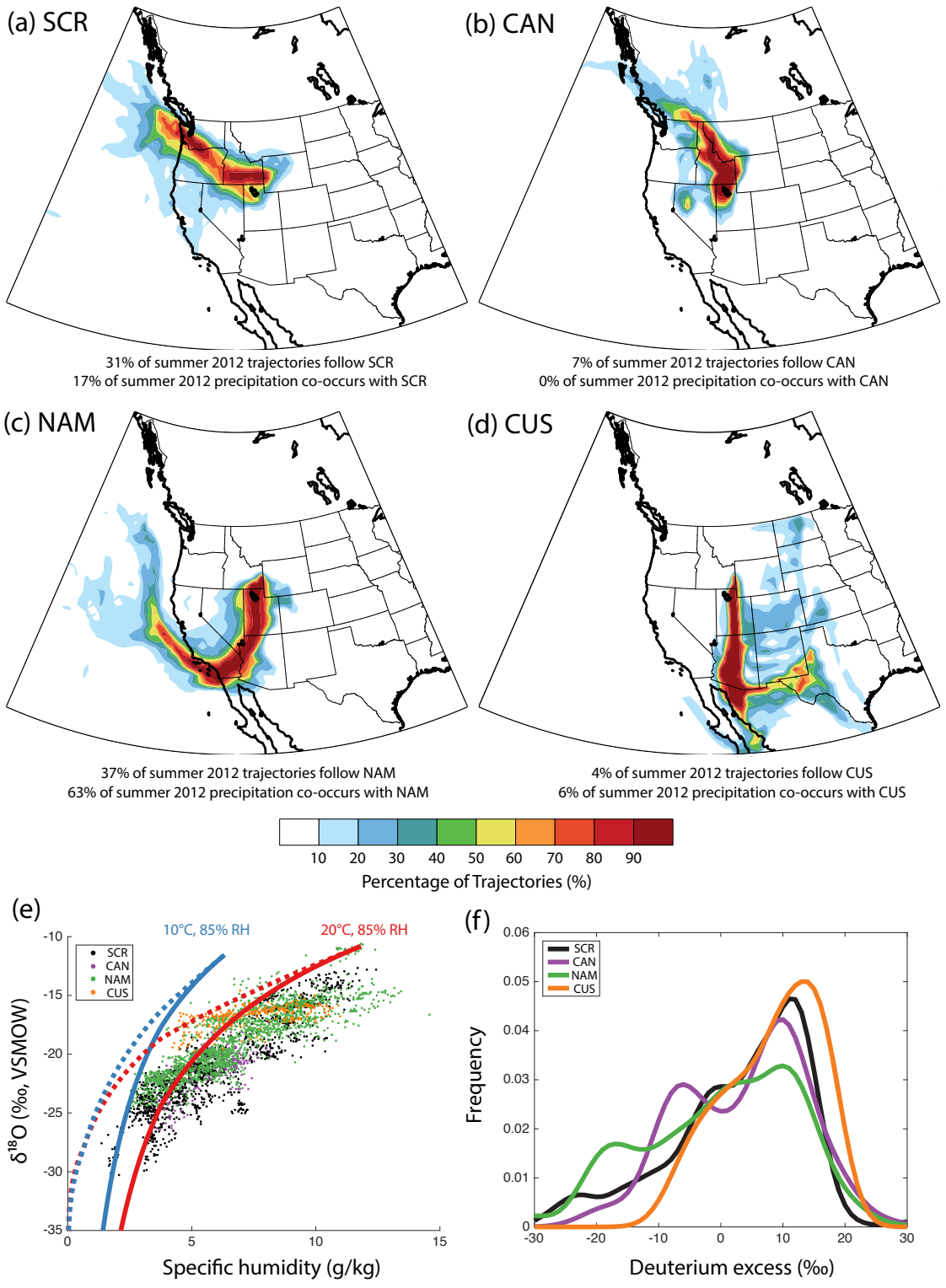

Figure 4.13. Back trajectory pathway clusters and isotopic compositions for summer 2012. The four back trajectory regions identified are shown in (a)-(d). Contours show the percentage of back trajectories that fall through each 0.75° grid cell. (e) Relationship of q with $\delta^{18}O$ and (f) probability density functions of measured d-excess by trajectory cluster.

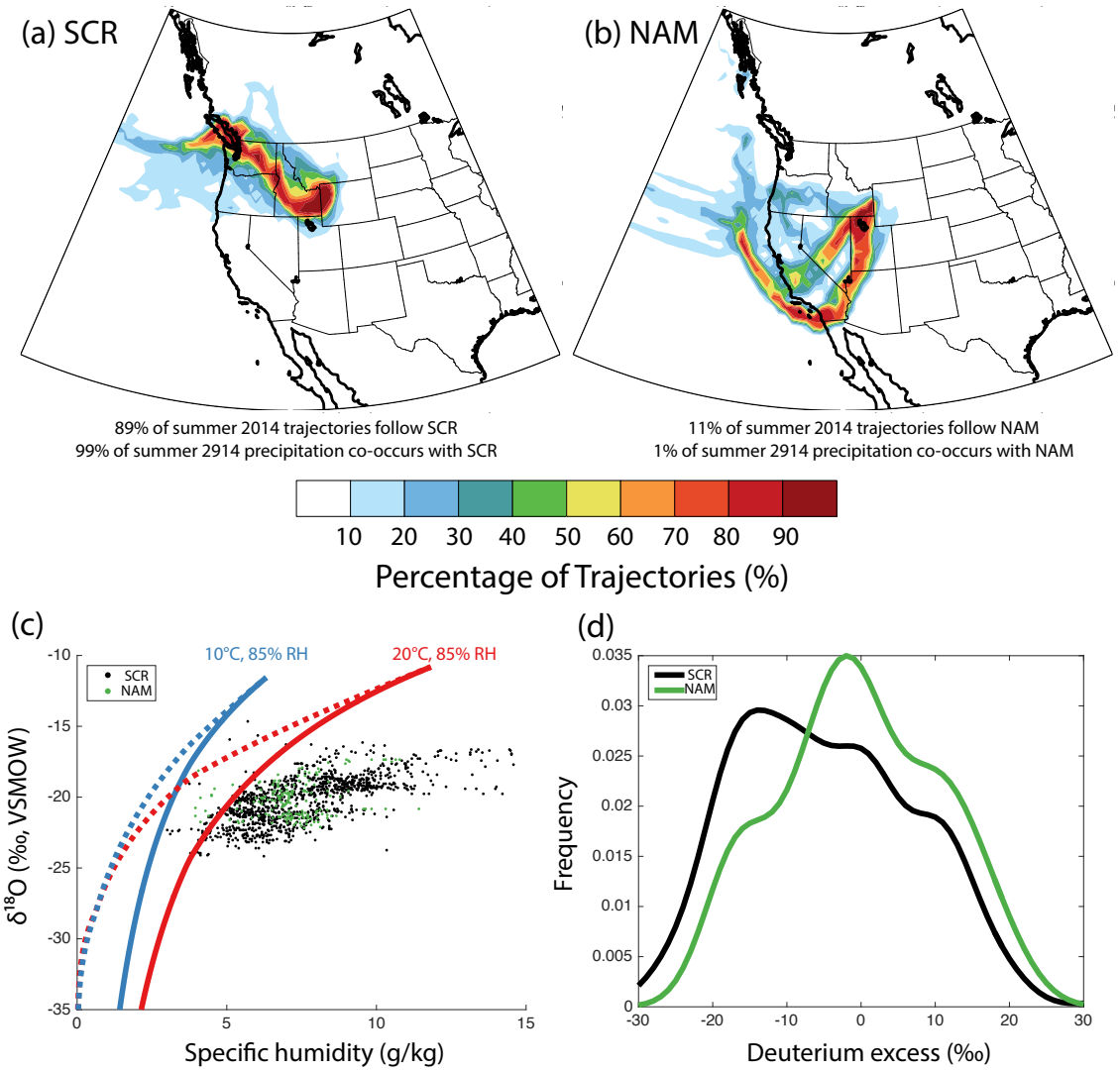

Figure 4.14. Back trajectory pathway clusters and isotopic compositions for summer 2014. The back trajectory clusters identified are shown in (a)-(b). Contours show the percentage of back trajectories that fall through each 0.75° grid cell. (c) Relationship of q with $\delta^{18}O$ and (d) probability density functions of measured d-excess by trajectory cluster.

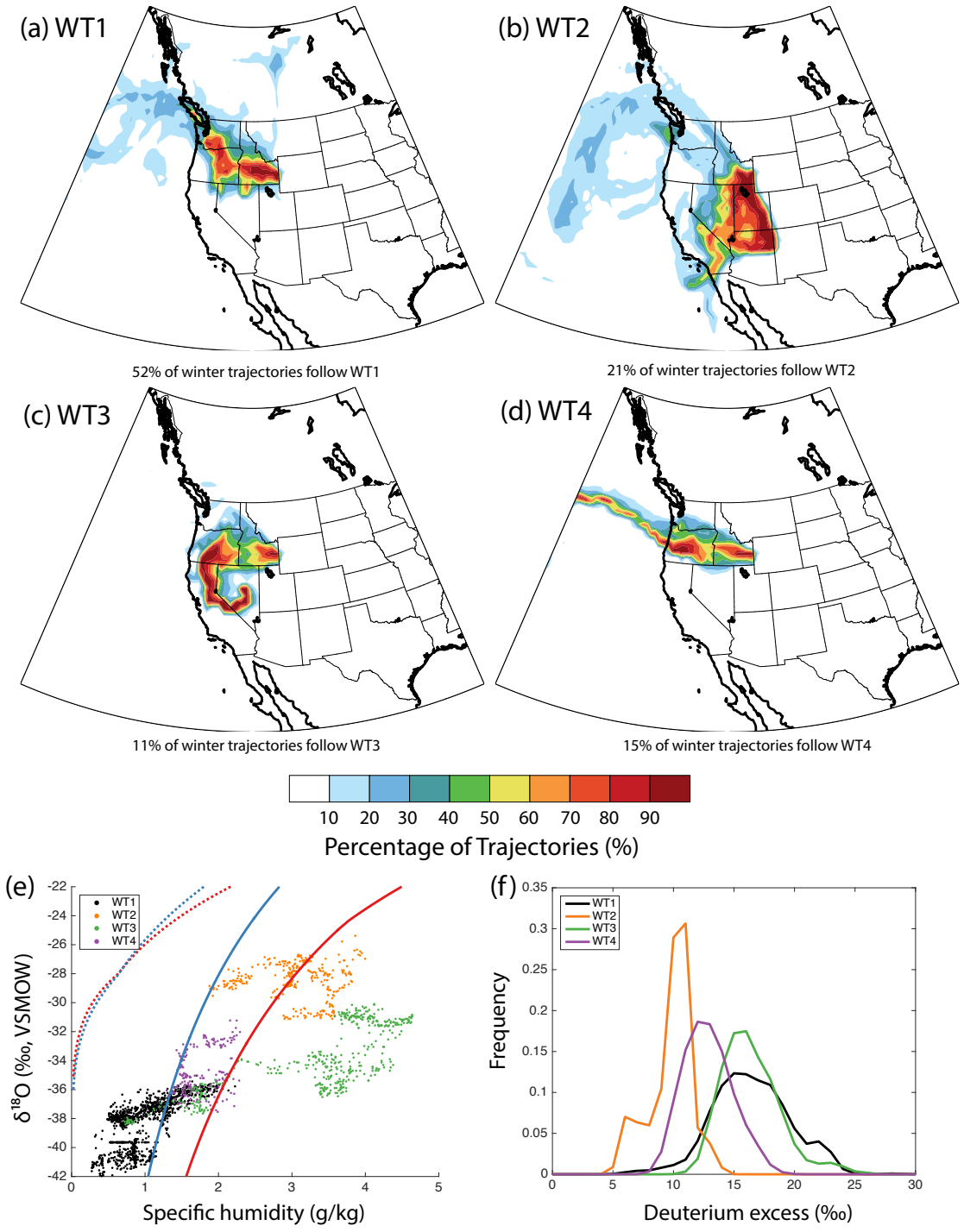

Figure 4.15. Back trajectory pathway clusters and isotopic compositions for winter 2013. The four back trajectory clusters identified, WT1-WT4 are shown in (a)-(d). Contours show the percentage of back trajectories that fall through each 0.75° grid cell. (e) Relationship of q with $\delta^{18}O$ and (f) probability density functions of measured d-excess by trajectory cluster.

4.6 Discussion

4.6.1 Low frequency variability in isotopic composition dominated by seasonal patterns of moisture transport and synoptic-scale events

Long-term changes (days to weeks) in the isotopic composition of near-surface vapor are associated with seasonal changes in vapor transport to NW Wyoming. Summer air masses source predominantly from the Pacific between 25-40°N and the Gulfs of California and Mexico (Figures 4.13-4.14), while winter air masses tend to originate in the North Pacific (north of 40°N) and from continental Canada (Figure 4.15). Conditions in the winter source regions are colder, resulting in the arrival of dry, cold air that has already lost most of its vapor content upstream, and hence, is highly depleted in heavy isotopes (Figure 4.15). Additionally, local conditions at CDFS during winter were very cold, and the average RH during the winter (Figure 4.3) was significantly higher than during the summer (Figures 4.2, 4.4). In contrast, summer air masses originated from warmer regions and were almost always moister than winter air masses (Figure 4.5). As a result, summer isotopic compositions tend to be more enriched in heavy isotopes than winter isotopic compositions, which matches expectations from changes in large-scale atmospheric moisture transport across the seasons.

Individual weather systems can have a dramatic impact on the isotopic composition of near-surface vapor. For example, the first two weeks of winter measurements were dominated by a high-pressure system that resulted in dry, clear, and cold conditions. As a result, isotopic compositions were at their most negative due to air advection from the dry, cold north combined with local conditions that were very cold. For the final week of winter observation, a low-pressure system brought moisture from the south to the field station, resulting in warmer and wetter conditions and higher isotopic compositions. Abrupt changes in summer isotopic composition are also observed near precipitation events (e.g., Figures 4.2, 4.4). Large precipitation events on DOY 187, 189, 196, and 245 in summer 2012 all resulted in rapid increases in specific humidity and isotopic composition (Figures 4.2, 4.4). These cases are consistent with subcloud evaporation of precipitation [*Lee and Fung*, 2007; *Risi et al.*, 2008]. The effects of these precipitation fluxes on local humidity and isotopic composition are short

lived, however, due to the high evaporative demand during summer in northwestern Wyoming, and efficient mixing of near-surface vapor aloft during the daytime.

Connections to vapor transport pathways are identified in both seasons, but the influence of air source is seasonally dependent. Winter data form distinct clusters between isotopic composition and humidity. In contrast, more vigorous continental recycling and local transpiration fluxes and atmospheric vertical mixing during the summer act to dampen the effect of changing air sources by overprinting the initial attributes of the air parcel. This hints that source effects may dominate during the winter, but that summer isotopic compositions may have significant contributions from both local and remote processes through enhanced continental recycling via evapotranspiration and boundary layer exchanges.

4.6.2 High frequency variability in isotopic composition dominated by diurnal processes

4.6.2.1 Summer diurnal cycle

During the summer, the morning increase in humidity is most likely associated with the onset of transpiration (Figures 4.7, 4.8), as shown by rapid increases in morning sap flux (Figure 4.10). Atmospheric entrainment and mixing associated with boundary layer development is likely minimal prior to the breakup of the valley-capping inversion. We also note that air mixing down from aloft would likely be drier than near-surface air, and thus, we would expect to see a decrease in near-surface specific humidity if atmospheric mixing were influencing near-surface humidity in the early morning. Furthermore, the weak surface winds in the morning are directed up-valley [*Whiteman*, 1982], transporting air and moisture laterally upslope, and away from the valley floor.

At midday, the surface specific humidity begins to decrease despite transpiration fluxes reaching a maximum. This pattern is best explained by the breakup of the valley inversion and the onset of strong vertical mixing. Vertical mixing reduces the moisture gradient between the humid surface layer and dry air aloft. The midday stabilization of near-surface humidity likely reflects the development of equilibrium between vertical mixing and evapotranspiration. Near sunset, vertical mixing ceases and the lower atmosphere begins to stratify again. Humidity continues to build near the surface as transpiration continues but is no longer removed from the near-surface layer by mixing. Near-surface humidity stabilizes overnight, or decreases slightly when the dew point is approached.

These diurnal changes in specific humidity coincide with marked changes in vapor isotopic composition, consistent with expectations from the interplay between transpiration and vertical atmospheric mixing. The morning increase in specific humidity co-occurs with rapid increases in ΔD and Δd-excess, while $\Delta^{18}O$ decreases slightly (Figures 4.7, 4.8). Several prior studies of near-surface vapor have also observed similar patterns in morning isotopic compositions and concluded that boundary layer entrainment of free tropospheric air from aloft was the dominant factor contributing to morning isotopic change [*Lai et al.*, 2006; *Lee et al.*, 2007; *Welp et al.*, 2008]. Based on their site descriptions, these measurements were carried out in areas with more homogenous topography and would not have had the delay in atmospheric entrainment observed at CDFS. Instead, we interpret this pattern to be consistent with a changing isotopic composition of transpired vapor associated with rapid morning changes in temperature and RH. Based on the Craig-Gordon evaporation model, fractionation at the leaf evaporation sites would increase more with increased temperature and decreased RH for $\delta^{18}O$ than δD for two reasons. First, the ratio of equilibrium fractionation factors between D/H and $^{18}O/^{16}O$ decreases with increasing temperature, which results in a higher d-excess of vapor in equilibrium with leaf water [*Simonin et al.*, 2013b]. Second, decreasing RH increases the degree of kinetic fractionation during evaporation and favors the loss of the ^{16}O relative to ^{18}O more than H to D, due to the higher diffusivity difference between isotopes of oxygen [*Merlivat*, 1978; *Cappa et al.*, 2003; *Luz et al.*, 2009]. Both of these factors favor an increasing d-excess of transpired vapor during the morning. The sensitivity of d-excess to changes in temperature and RH has been estimated to be ~ +0.3‰/K and ~ -0.4‰/% RH [*Jouzel and Merlivat*, 1984; *Pfahl and Wernli*, 2009; *Benetti et al.*, 2014]. Further, to maintain plant-level isotope mass balance on longer time scales, this implies an isostorage of low d-excess water that must later enter the atmosphere through transpiration or equilibration between leaf water and atmospheric water vapor.

Onset of strong vertical mixing in the late morning is associated with a decrease in $\delta^{18}O$, continued increase of d-excess, and constant δD (Figures 4.7, 4.8). The midday and afternoon minimum in humidity coincides with daily minimum values $\delta^{18}O$, daily maximum values of d-excess (Fig. 7-8), and daily maximum values of sap flux (Figure 4.10). As vertical mixing stops at dusk and specific humidity rises, $\delta^{18}O$ rises again and d-excess decreases rapidly (Fig. 7-8). Environmental conditions during the late afternoon and early evening are the opposite of the early morning, with rapidly increasing RH and decreasing temperature, both of which would

favor a decreasing d-excess of the transpiration flux following the above logic. Additionally, transpiration fluxes decrease slowly following dusk (Figure 4.10). While a portion of this transpiration flux likely reflects refilling of the trees' internal storage, recent observations have demonstrated that up to ~10-20% of plant water loss may occur at night [*Caird et al.*, 2007; *Dawson et al.*, 2007; *Fisher et al.*, 2007]. During the evening, katabatic winds increase the forested area represented in valley water vapor as the nocturnal inversion begins to form [*McNider and Pielke*, 1981; *Whiteman et al.*, 2004], and therefore could augment the rate and magnitude of isotopic and meteorological change. Overnight, Δd-excess and ΔD tend to decrease while $\Delta^{18}O$ remains comparatively stable. In fact, d-excess becomes negative over most nights (Figures 4.2, 4.4), which is inconsistent with expectations of water vapor from an oceanic source [*Craig and Gordon*, 1965; *Uemura et al.*, 2008; *Benetti et al.*, 2014]. The negative d-excess values and decreasing δD are explained by equilibration of leaf water and atmospheric water vapor and loss of leaf water enrichment throughout the night [*Cernusak et al.*, 2002; *Farquhar and Cernusak*, 2005]. Due to midday isotopic enrichment and the preferential loss of the light isotopes of oxygen relative to hydrogen, leaf water would be expected to have low d-excess by the late afternoon. During the evening, when evaporation of water from the stomata would occur closer to equilibrium, this isostorage of low d-excess leaf water would be released. Additionally, if stomata remain open overnight, exchange between the leaves and the atmosphere would bring the two water pools toward equilibrium [*Farquhar et al.*, 2006; *Simonin et al.*, 2013b]. We observe these processes in the anti-symmetry of morning and late afternoon isotopic fluxes: morning increases in Δd-excess are driven predominantly by the strong increase in ΔD and a slight decrease in $\Delta^{18}O$, while evening decreases in Δd-excess are driven predominantly by strong increases in $\Delta^{18}O$ and a slight decrease in ΔD. The long timescale over which d-excess continues to change overnight suggests that there is a water turnover lag in the leaves, consistent with observations in *P. menziesii* of non-steady state transpiration by *Lai et al.* [2006]. Finally, the d-excess of the xylem source water may also contribute to the observed negative nocturnal d-excess. While we did not measure xylem water in this study, it is likely that shallow soil waters during dry summers have a negative d-excess as a result of strong soil drying and evaporative loss [*Allison et al.*, 1985]. Therefore, even after the isostorage of low d-excess water in leaves is exhausted, transpiration of vapor under conditions with a small kinetic fractionation may still

result in transpiration of water with a negative d-excess values, further promoting low atmospheric d-excess values.

This pattern of transpiration suggests that though plants do not fractionate water during uptake into the roots [e.g., *Ehleringer and Dawson*, 1992], they may fractionate water from the perspective of atmospheric moisture transport [e.g., *Gat and Matsui*, 1991; *Gat*, 2000]. Fractionation occurs in this case because the mixing of water vapor into the free troposphere from the surface only occurs during the day, when d-excess of transpired vapor is high. This pattern is also consistent with contributions from transpired air associated with boundary layer mixing upwind of CDFS, which would have increased the d-excess of free tropospheric air. As a result, the assumption that evapotranspiration can be partitioned into evaporation and transpiration components by assuming that plants do not fractionate water may be invalid in regions and across time periods where steady-state transpiration is unlikely to occur.

4.6.2.2 Winter diurnal cycle

The winter diurnal cycle is more muted than the summer diurnal cycle (compare Figure 4.9 to Figures 4.7, 4.8), as both local transpiration and atmospheric mixing are subdued in the winter relative to the summer. Transpiration in Rocky Mountain forests decreases rapidly in fall when night time temperatures consistently drop below 0°C [*Fahey*, 1979; *Smith et al.*, 1984], and stomata typically remain closed during extended periods of below freezing temperatures to prevent cavitation [*Tranquillini*, 1982]. During our observation period, temperatures were often below -10°C, and fell as low as -30°C. Therefore, the rise in morning specific humidity is unlikely to be due to transpiration. Likewise, boundary layer mixing is greatly reduced in the winter due to both decreased solar insolation and a more reflective surface, both of which reduce surface heating and ultimately limit boundary layer development [e.g., *Garratt*, 1994]. In contrast to the summer, the valley inversion is unlikely to break every day, and may persist for several days. As a result, atmospheric boundary layer heights are lower at the field site in the winter, and the column affected by atmospheric mixing is much shallower.

Instead, the diurnal cycle of specific humidity and isotopic composition is likely driven by sublimation and deposition of snow in the valley. As temperatures rise and insolation increases in the morning, a portion of the snow likely sublimates and then is redeposited in the

evening when the temperatures decrease again. As a result of this cycling, the isotopic change in $\Delta^{18}O$ mirrors that of ΔD, and thus, there is no diurnal cycle in d-excess.

4.6.3 Implications for studies of current and future moisture transport

The stable isotopic composition of near-surface water vapor at Camp Davis shows characteristic imprints of both local and upstream fractionation processes and sources. On timescales longer than a day, water vapor characteristics can be linked to synoptic-scale circulation. As both remote and local processes are recorded in our measurements, long-term monitoring of near-surface isotopic composition combined with meteorological data can potentially be used to understand changes in catchment-to-regional scale moisture balance [*Henderson-Sellers et al.*, 2004]. In particular, the relative contributions of remote moisture transport through meso-to-synoptic scale weather patterns compared to the local ET flux can be constrained. Model studies [*Lee et al.*, 2012; *Swann et al.*, 2012; *Risi et al.*, 2013] and satellite data [*Spracklen et al.*, 2012] suggest that transpiration is an important component in both triggering precipitation and minimizing risk of extreme hydroclimatic events. Our results suggest that long-term isotopic monitoring of water inputs and losses to a region can faithfully document the factors contributing to hydrologic variability and change. Additionally, these records provide the basis for another dimension with which to evaluate simulated water fluxes in atmosphere-land surface models.

4.6.4 Implications for paleoclimate proxies

Deuterium excess has been used as a tracer for oceanic moisture source conditions in precipitation [*Rozanski et al.*, 1993] and ice core records [e.g., *Jouzel et al.*, 1982; *Vimeux et al.*, 1999; *Masson-Delmotte et al.*, 2005]. Our results suggest that vapor d-excess is not a conservative tracer of ocean moisture source in continental interiors, consistent with conclusions of prior studies [e.g., *Welp et al.*, 2012]. If reflected in precipitation, precipitation d-excess would also fail to capture the signal of the oceanic moisture source. Instead, precipitation d-excess will reflect a mixture of oceanic and terrestrial water sources. Additionally, the influence of continental moisture recycling will likely vary by environment both because the amplitude of the diurnal cycles of temperature, RH, and VPD are highly variable through different climates and seasons, and the partitioning of transpiration and evaporation in the total ET flux varies by

ecosystem and by time. On an annual basis, transpiration is the largest component of the surface ET flux [*Jasechko et al.*, 2013; *Schlesinger and Jasechko*, 2014; *Good et al.*, 2015], but these ratios are highly variable and time dependent at any particular location [e.g., *Ferretti et al.*, 2003; *Aemisegger et al.*, 2014]. As a result, the contributions of evaporation, transpiration, and atmospheric entrainment will have different influences across space and time, and therefore, deviations from ocean moisture source d-excess will also be variable.

In addition to precipitation and ice cores, improved knowledge of the spatiotemporal controls on the isotopic composition of near-surface water vapor may help improve confidence in interpretations of isotope ratios of tree ring records. Leaf water isotopic composition largely determines the oxygen and hydrogen isotopic compositions of organic matter generated during photosynthesis [*Gray and Thompson*, 1976; *White et al.*, 1985; *Roden et al.*, 2000; *Barbour et al.*, 2004]. Additionally, the degree of isotopic enrichment in leaf water depends on the isotopic gradient between leaf and atmospheric water [*Dongmann et al.*, 1974; *Farquhar and Cernusak*, 2005]. *Farquhar and Cernusak* [2005] further suggest that after accounting for both fluxes into and out of the leaf instead of just the net flux of water, atmospheric water may be more important to leaf water status than water delivered from the roots. As a result, tree ring records may be influenced by long-term changes in atmospheric moisture transport, independent of changes in growing season precipitation, for example. Long-term records of leaf and atmospheric water isotopic compositions represent an important data source.

4.7 Conclusions

We present the isotopic compositions of near-surface vapor in a deep mountain valley in NW Wyoming during both summer and winter conditions. Water vapor is more depleted in heavy isotopes in the winter than the summer, consistent with the lower specific humidities and colder source regions observed during the winter. On a process-based level, we determine that air mass mixing is the dominant process influencing near-surface humidity across multiple days to seasonal timescales.

Imprints of both local and synoptic scale processes are apparent in vapor isotopic compositions. Isotopic composition of CDFS near-surface vapor is more closely related to moisture source direction during the winter than during the summer. Local processes, including transpiration and vertical mixing associated with boundary layer development, are most

prominent during the summer. Transpiration and vertical mixing both contribute to a clear diurnal cycle in d-excess of lower surface vapor. This strong diurnal cycle suggests that d-excess cannot be taken as a reliable indicator of oceanic moisture source, which is consistent with other observations of vapor d-excess in continental environments [*Lai and Ehleringer*, 2010; *Welp et al.*, 2012].

Our results suggest that continued monitoring of the isotopic composition of near-surface vapor in continental settings may help detect changes in the relative importance of regional moisture convergence and the local evapotranspiration flux as sources of water vapor to the lower troposphere. The strong summer coupling of water vapor isotopic composition with local processes on diurnal cycles during the summer suggests that isotopic monitoring can be used to assess meso-to-regional scale ecohydrologic responses to hydrologic variability.

4.8 References

Aemisegger, F., J. K. Spiegel, S. Pfahl, H. Sodemann, W. Eugster, and H. Wernli (2015), Isotope meteorology of cold front passages: A case study combining observations and modeling, *Geophys. Res. Lett.*, *42*(13), 5652–5660, doi:10.1002/2015gl063988.

Aemisegger, F., S. Pfahl, H. Sodemann, I. Lehner, S. I. Seneviratne, and H. Wernli (2014), Deuterium excess as a proxy for continental moisture recycling and plant transpiration, *Atmos. Chem. Phys.*, *14*(8), 4029–4054, doi:10.5194/acp-14-4029-2014.

Allison, G. B., J. R. Gat, and F. W. J. Leaney (1985), The relationship between deuterium and oxygen-18 delta values in leaf water, *Chemical Geology: Isotope Geoscience section*, *58*(1-2), 145–156, doi:10.1016/0168-9622(85)90035-1.

Anderegg, W. R. L., J. M. Kane, and L. D. L. Anderegg (2012), Consequences of widespread tree mortality triggered by drought and temperature stress, *Nature Climate Change*, *3*(1), 1–7, doi:10.1038/nclimate1635.

Anderegg, W. R. L., L. Plavcová, L. D. L. Anderegg, U. G. Hacke, J. A. Berry, and C. B. Field (2013), Drought's legacy: multiyear hydraulic deterioration underlies widespread aspen forest die-off and portends increased future risk, *Global Change Biology*, *19*(4), 1188–1196, doi:10.1111/gcb.12100.

Bailey, A., D. Toohey, and D. Noone (2013), Characterizing moisture exchange between the Hawaiian convective boundary layer and free troposphere using stable isotopes in water, *J Geophys Res-Atmos*, *118*(15), 8208–8221, doi:10.1002/jgrd.50639.

Bailey, A., J. Nusbaumer, and D. Noone (2015), Precipitation efficiency derived from isotope ratios in water vapor distinguishes dynamical and microphysical influences on subtropical atmospheric constituents, *J Geophys Res-Atmos*, 1–19, doi:10.1002/(ISSN)2169-8996.

Bailey, A., T. N. Chase, J. J. Cassano, and D. Noone (2011), Changing Temperature Inversion Characteristics in the U.S. Southwest and Relationships to Large-Scale Atmospheric Circulation, *J. Appl. Meteor. Climatol.*, *50*(6), 1307–1323, doi:10.1175/2011JAMC2584.1.

Bales, R. C., N. P. Molotch, T. H. Painter, M. D. Dettinger, R. Rice, and J. Dozier (2006), Mountain hydrology of the western United States, *Water Resources Research*, *42*(8), doi:10.1029/2005WR004387.

Banta, R. M. (1985), Late-morning jump in TKE in the mixed layer over a mountain basin, *Journal of the Atmospheric Sciences*, *42*(4), 407–411, doi:10.1175/1520-0469(1985)042<0407:lmjiti>2.0.co;2.

Barbour, M. M., J. S. Roden, G. D. Farquhar, and J. R. Ehleringer (2004), Expressing leaf water and cellulose oxygen isotope ratios as enrichment above source water reveals evidence of a Péclet effect, *Oecologia*, *138*(3), 426–435, doi:10.1007/s00442-003-1449-3.

Benetti, M., G. Reverdin, C. Pierre, C. Risi, H. C. Steen-Larsen, and F. Vimeux (2014), Deuterium excess in marine water vapor: Dependency on relative humidity and surface wind speed during evaporation, *Journal of Geophysical Research: Atmospheres*, *119*(2), 584–593, doi:10.1002/2013jd020535.

Berkelhammer, M., J. Hu, A. Bailey, D. C. Noone, C. J. Still, H. Barnard, D. Gochis, G. S. Hsiao, T. Rahn, and A. Turnipseed (2013), The nocturnal water cycle in an open-canopy forest, *Journal of Geophysical Research: Atmospheres*, *118*(17), 10,225–10,242, doi:10.1002/jgrd.50701.

Bovard, B. D., P. S. Curtis, C. S. Vogel, H. B. Su, and H. P. Schmid (2005), Environmental controls on sap flow in a northern hardwood forest, *Tree Physiology*, *25*(1), 31–38,

doi:10.1093/treephys/25.1.31.
Brown, D., J. Worden, and D. Noone (2008), Comparison of atmospheric hydrology over convective continental regions using water vapor isotope measurements from space, *Journal of Geophysical Research*, *113*(D15), D15124–17, doi:10.1029/2007JD009676.
Brubaker, K. L., D. Entekhabi, and P. S. Eagleson (1993), Estimation of Continental Precipitation Recycling, *J. Climate*, *6*(6), 1077–1089, doi:10.1175/1520-0442(1993)006<1077:EOCPR>2.0.CO;2.
Brunel, J. P., H. J. Simpson, A. L. Herczeg, R. Whitehead, and G. R. Walker (1992), Stable isotope composition of water vapor as an indicator of transpiration fluxes from rice crops, *Water Resources Research*, *28*(5), 1407–1416, doi:10.1029/91WR03148.
Caird, M. A., J. H. Richards, and T. C. Hsiao (2007), Significant transpirational water loss occurs throughout the night in field-grown tomato, *Functional Plant Biol.*, *34*(3), 172–6, doi:10.1071/FP06264.
Cappa, C. D., M. B. Hendricks, D. J. DePaolo, and R. C. Cohen (2003), Isotopic fractionation of water during evaporation, *Journal of Geophysical Research*, *108*(D16), doi:10.1029/2003jd003597.
Cayan, D. R., M. D. Dettinger, S. A. Kammerdiener, J. M. Caprio, and D. H. Peterson (2001), Changes in the Onset of Spring in the Western United States, *Bull. Amer. Meteor. Soc.*, *82*(3), 399–415, doi:10.1175/1520-0477(2001)082<0399:citoos>2.3.co;2.
Cernusak, L. A., J. S. Pate, and G. D. Farquhar (2002), Diurnal variation in the stable isotope composition of water and dry matter in fruiting Lupinus angustifolius under field conditions, *Plant, Cell and Environment*, *25*(7), 893–907, doi:10.1046/j.1365-3040.2002.00875.x.
Clearwater, M. J., F. C. Meinzer, J. L. Andrade, G. Goldstein, and N. M. Holbrook (1999), Potential errors in measurement of nonuniform sap flow using heat dissipation probes, *Tree Physiology*, *19*(10), 681–687.
Coplen, T. B. (1996), New guidelines for reporting stable hydrogen, carbon, and oxygen isotope-ratio data, *Geochimica et Cosmochimica Acta*, *60*(17), 3359–3360, doi:10.1016/0016-7037(96)00263-3.
Craig, H., and L. I. Gordon (1965), Deuterium and oxygen 18 variations in the ocean and the marine atmosphere, in *Stable Isotopes in Oceanographic Studies and Paleotemperatures*, edited by E. Tongiorgi.
Crow, K. S., J. Galewsky, D. R. Hardy, Z. D. Sharp, J. Worden, and C. Braun (2014), Upwind convective influences on the isotopic composition of atmospheric water vapor over the tropical Andes, *J Geophys Res-Atmos*, doi:10.1002/(ISSN)2169-8996.
Dansgaard, W. (1964), Stable isotopes in precipitation, *Tellus A*, 436–468, doi:10.3402/tellusa.v16i4.8993.
Dawson, T. E., S. S. O. Burgess, K. P. Tu, R. S. Oliveira, L. S. Santiago, J. B. Fisher, K. A. Simonin, and A. R. Ambrose (2007), Nighttime transpiration in woody plants from contrasting ecosystems, *Tree Physiology*, *27*(4), 561–575, doi:10.1093/treephys/27.4.561.
Despain, D. G. (1987), *The two climates of Yellowstone National Park*, Proceedings of the Montana Academy of Science.
Dessler, A. E., and S. C. Sherwood (2003), A model of HDO in the tropical tropopause layer, *Atmos. Chem. Phys.*, *3*(6), 2173–2181, doi:10.5194/acp-3-2173-2003.
Dominguez, F., P. Kumar, and E. R. Vivoni (2008), Precipitation Recycling Variability and Ecoclimatological Stability—A Study Using NARR Data. Part II: North American Monsoon Region, *J. Climate*, *21*(20), 5187–5203, doi:10.1175/2008JCLI1760.1.

Dongmann, G., H. W. Nürnberg, H. Förstel, and K. Wagener (1974), On the enrichment of $H_2{}^{18}O$ in the leaves of transpiring plants, *Radiation and Environmental Biophysics*, *11*(1), 41–52, doi:10.1007/BF01323099.

Draxler, R. R., and G. D. Hess (1998), An overview of the HYSPLIT_4 modelling system for trajectories, dispersion and deposition, *Australian Meteorological Magazine*, *47*(4), 295–308.

Ehhalt, D. H., F. Rohrer, and A. Fried (2005), Vertical profiles of HDO/H_2O in the troposphere, *Journal of Geophysical Research*, *110*(D13), D13301–13, doi:10.1029/2004JD005569.

Ehleringer, J. R., and T. E. Dawson (1992), Water uptake by plants: perspectives from stable isotope composition, *Plant, Cell and Environment*, *15*(9), 1073–1082, doi:10.1111/j.1365-3040.1992.tb01657.x.

Fahey, F. T. (1979), The effect of night frost on the transpiration of Pinus contorta ssp. latifolia [Wyoming], *Oecologia Plantarum*.

Farquhar, G. D., and L. A. Cernusak (2005), On the isotopic composition of leaf water in the non-steady state, *Functional Plant Biol.*, *32*(4), 293–11, doi:10.1071/FP04232.

Farquhar, G. D., L. A. Cernusak, and B. Barnes (2006), Heavy Water Fractionation during Transpiration, *Plant Physiology*, *143*(1), 11–18, doi:10.1104/pp.106.093278.

Ferretti, D. F., E. Pendall, J. A. Morgan, J. A. Nelson, D. Lecain, and A. R. Mosier (2003), Partitioning evapotranspiration fluxes from a Colorado grassland using stable isotopes: Seasonal variations and ecosystem implications of elevated atmospheric CO_2, *Plant and Soil*, *254*(2), 291–303, doi:10.1023/A:1025511618571.

Fiorella, R. P., C. J. Poulsen, R. S. Pillco Zolá, J. B. Barnes, C. R. Tabor, and T. A. Ehlers (2015), Spatiotemporal variability of modern precipitation $\delta^{18}O$ in the central Andes and implications for paleoclimate and paleoaltimetry estimates, *Journal of Geophysical Research: Atmospheres*, *120*(10), 4630–4656, doi:10.1002/2014JD022893.

Fisher, J. B., D. D. Baldocchi, L. Misson, T. E. Dawson, and A. H. Goldstein (2007), What the towers don't see at night: nocturnal sap flow in trees and shrubs at two AmeriFlux sites in California, *Tree Physiology*, *27*(4), 597–610, doi:10.1093/treephys/27.4.597.

Galewsky, J., and J. V. Hurley (2010), An advection-condensation model for subtropical water vapor isotopic ratios, *Journal of Geophysical Research*, *115*(D16), D16116–10, doi:10.1029/2009JD013651.

Galewsky, J., and K. Samuels-Crow (2015), Summertime Moisture Transport to the Southern South American Altiplano: Constraints from In Situ Measurements of Water Vapor Isotopic Composition, *J. Climate*, *28*(7), 2635–2649, doi:10.1175/JCLI-D-14-00511.1.

Galewsky, J., C. Rella, Z. Sharp, K. Samuels, and D. Ward (2011), Surface measurements of upper tropospheric water vapor isotopic composition on the Chajnantor Plateau, Chile, *Geophys. Res. Lett.*, *38*(17), n/a–n/a, doi:10.1029/2011GL048557.

Garratt, J. R. (1994), Review: the atmospheric boundary layer, *Earth Science Reviews*, *37*(1-2), 89–134, doi:10.1016/0012-8252(94)90026-4.

Gat, J. R. (1996), Oxygen and Hydrogen Isotopes in the Hydrologic Cycle, *Annu. Rev. Earth Planet. Sci.*, *24*(1), 225–262, doi:10.1146/annurev.earth.24.1.225.

Gat, J. R. (2000), Atmospheric water balance—the isotopic perspective, *Hydrol. Process.*, *14*(8), 1357–1369, doi:10.1002/1099-1085(20000615)14:8<1357::AID-HYP986>3.0.CO;2-7.

Gat, J. R., and E. Matsui (1991), Atmospheric water balance in the Amazon basin: An isotopic evapotranspiration model, *Journal of Geophysical Research*, *96*(D7), 13179–13188, doi:10.1029/91JD00054.

Gedzelman, S. D. (1988), Deuterium in water vapor above the atmospheric boundary layer, *Tellus B*, *40B*(2), 134–147, doi:10.1111/j.1600-0889.1988.tb00217.x.

Gimeno, L., A. Drumond, R. Nieto, R. M. Trigo, and A. Stohl (2010), On the origin of continental precipitation, *Geophys. Res. Lett.*, *37*(13), n/a–n/a, doi:10.1029/2010GL043712.

Good, S. P., D. Noone, and G. Bowen (2015), Hydrologic connectivity constrains partitioning of global terrestrial water fluxes, *Science*, *349*(6244), 175–177, doi:10.1126/science.aaa5931.

Good, S. P., K. Soderberg, K. Guan, E. G. King, T. M. Scanlon, and K. K. Caylor (2014), δ^2H isotopic flux partitioning of evapotranspiration over a grass field following a water pulse and subsequent dry down, *Water Resources Research*, *50*(2), 1410–1432, doi:10.1002/2013WR014333.

Granier, A. (1987), Evaluation of transpiration in a Douglas-fir stand by means of sap flow measurements, *Tree Physiology*, *3*(4), 309–320, doi:10.1093/treephys/3.4.309.

Granier, A., and D. Loustau (1994), Measuring and modeling the transpiration of a maritime pine canopy from sap-flow data, *Agricultural and Forest Meteorology*, *71*(1-2), 61–81, doi:10.1016/0168-1923(94)90100-7.

Gray, J., and P. Thompson (1976), Climatic Information From $^{18}O/^{16}O$ Ratios of Cellulose in Tree Rings, *Nature*, *262*(5568), 481–482, doi:10.1038/262481a0.

Harwood, K. G., J. S. Gillon, A. Roberts, and H. Griffiths (1999), Determinants of isotopic coupling of CO_2 and water vapour within a Quercus petraea forest canopy, *Oecologia*, *119*(1), 109–119, doi:10.1007/s004420050766.

Harwood, K. G., J. S. Gillon, H. Griffiths, and M. S. J. Broadmeadow (1998), Diurnal variation of $\Delta^{13}CO_2$, $\Delta C^{18}O^{16}O$ and evaporative site enrichment of $\delta H_2{}^{18}O$ in Piper aduncum under field conditions in Trinidad, *Plant Cell Environ*, *21*(3), 269–283, doi:10.1046/j.1365-3040.1998.00276.x.

He, H., and R. B. Smith (1999), Stable isotope composition of water vapor in the atmospheric boundary layer above the forests of New England, *Journal of Geophysical Research*, *104*(D9), 11657–11673, doi:10.1029/1999JD900080.

Helliker, B. R., J. S. Roden, C. Cook, and J. R. Ehleringer (2002), A rapid and precise method for sampling and determining the oxygen isotope ratio of atmospheric water vapor, *Rapid Commun. Mass Spectrom.*, *16*(10), 929–932, doi:10.1002/rcm.659.

Henderson-Sellers, A., K. McGuffie, D. Noone, and P. Irannejad (2004), Using stable water isotopes to evaluate basin-scale simulations of surface water budgets, *J Geophys Res-Atmos*, *5*(5), 805–822, doi:10.1175/1525-7541(2004)005<0805:USWITE>2.0.CO;2.

Hogg, E. H., and P. A. Hurdle (1997), Sap flow in trembling aspen: implications for stomatal responses to vapor pressure deficit, *Tree Physiology*, *17*(8-9), 501–509, doi:10.1093/treephys/17.8-9.501.

Horita, J., and D. J. Wesolowski (1994), Liquid-vapor fractionation of oxygen and hydrogen isotopes of water from the freezing to the critical temperature, *Geochimica et Cosmochimica Acta*, *58*(16), 3425–3437, doi:10.1016/0016-7037(94)90096-5.

Hunter, T., G. Tootle, and T. Piechota (2006), Oceanic-atmospheric variability and western U.S. snowfall, *Geophys. Res. Lett.*, *33*(13), L13706–5, doi:10.1029/2006GL026600.

Jasechko, S., Z. D. Sharp, J. J. Gibson, S. J. Birks, Y. Yi, and P. J. Fawcett (2013), Terrestrial water fluxes dominated by transpiration, *Nature*, *496*(7445), 347–350, doi:10.1038/nature11983.

Jouzel, J., and L. Merlivat (1984), Deuterium and oxygen 18 in precipitation: Modeling of the isotopic effects during snow formation, *Journal of Geophysical Research*, *89*(D7), 11749–

11757, doi:10.1029/JD089iD07p11749.
Jouzel, J., L. Merlivat, and C. Lorius (1982), Deuterium excess in an East Antarctic ice core suggests higher relative humidity at the oceanic surface during the last glacial maximum, *Nature*, *299*(5885), 688–691, doi:10.1038/299688a0.
Kalnay, E. et al. (1996), The NCEP/NCAR 40-Year Reanalysis Project, *Bull. Amer. Meteor. Soc.*, *77*(3), 437–471, doi:10.1175/1520-0477(1996)077<0437:tnyrp>2.0.co;2.
Kalra, A., T. C. Piechota, R. Davies, and G. A. Tootle (2008), Changes in U.S. Streamflow and Western U.S. Snowpack, *Journal of Hydrologic Engineering*, *13*(3), 156–163, doi:10.1061/(asce)1084-0699(2008)13:3(156).
Keeling, C. D. (1958), The Concentration and Isotopic Abundances of Atmospheric Carbon Dioxide in Rural Areas, *Geochimica et Cosmochimica Acta*, *13*(4), 322–334.
Keeling, C. D. (1961), The Concentration and Isotopic Abundances of Carbon Dioxide in Rural and Marine Air, *Geochimica et Cosmochimica Acta*, *24*(3-4), 277–298, doi:10.1016/0016-7037(58)90033-4.
Knowles, N., M. D. Dettinger, and D. R. Cayan (2006), Trends in snowfall versus rainfall in the Western United States, *J. Climate*, *19*(18), 4545–4559, doi:10.1175/JCLI3850.1.
Lai, C.-T., and J. R. Ehleringer (2010), Deuterium excess reveals diurnal sources of water vapor in forest air, *Oecologia*, *165*(1), 213–223, doi:10.1007/s00442-010-1721-2.
Lai, C.-T., J. R. Ehleringer, B. J. Bond, and K. T. Paw U (2006), Contributions of evaporation, isotopic non-steady state transpiration and atmospheric mixing on the $\delta^{18}O$ of water vapour in Pacific Northwest coniferous forests, *Plant, Cell and Environment*, *29*(1), 77–94, doi:10.1111/j.1365-3040.2005.01402.x.
Larsen, H. S., A. E. Sveinbjörnsdottir, T. Jonsson, F. Ritter, J.-L. Bonne, V. Masson-Delmotte, H. Sodemann, T. Blunier, D. Dahl-Jensen, and B. M. Vinther (2015), Moisture sources and synoptic to seasonal variability of North Atlantic water vapor isotopic composition, *J Geophys Res-Atmos*, doi:10.1002/(ISSN)2169-8996.
Lee, J.-E. et al. (2012), Reduction of tropical land region precipitation variability via transpiration, *Geophys. Res. Lett.*, *39*(19), doi:10.1029/2012GL053417.
Lee, J.-E., and I. Fung (2007), "Amount effect" of water isotopes and quantitative analysis of post-condensation processes, *Hydrol. Process.*, *22*(1), 1–8, doi:10.1002/hyp.6637.
Lee, X., K. Kim, and R. Smith (2007), Temporal variations of the $^{18}O/^{16}O$ signal of the whole-canopy transpiration in a temperate forest, *Global Biogeochem. Cycles*, *21*(3), doi:10.1029/2006GB002871.
Lee, X., R. Smith, and J. Williams (2006), Water vapour $^{18}O/^{16}O$ isotope ratio in surface air in New England, USA, *Tellus B*, *58*(4), 293–304, doi:10.1111/j.1600-0889.2006.00191.x.
Luz, B., E. Barkan, R. Yam, and A. Shemesh (2009), Fractionation of oxygen and hydrogen isotopes in evaporating water, *Geochimica et Cosmochimica Acta*, *73*(22), 6697–6703, doi:10.1016/j.gca.2009.08.008.
Majoube, M. (1971), *Fractionnement en oxygène 18 entre la glace et la vapeur d'eau*, J. Chem. Phys.
Masson-Delmotte, V., J. Jouzel, A. Landais, and M. Stievenard (2005), GRIP deuterium excess reveals rapid and orbital-scale changes in Greenland moisture origin, *Science*, *309*(5731), 118–121, doi:10.1126/science.1108575.
Matheny, A. M. et al. (2014), Species-specific transpiration responses to intermediate disturbance in a northern hardwood forest, *Journal of Geophysical Research Biogeosciences*, 1–20, doi:10.1002/(ISSN)2169-8961.

McNider, R. T., and R. A. Pielke (1981), Diurnal boundary-layer development over sloping terrain, *Journal of the Atmospheric Sciences*, *38*(10), 2198–2212, doi:10.1175/1520-0469(1981)038<2198:DBLDOS>2.0.CO;2.

Merlivat, L. (1978), Molecular diffusivities of $H_2{}^{16}O$, $HD^{16}O$, and $H_2{}^{18}O$ in gases, *Journal of Chemical Physics*, *69*(6), 2864–2871, doi:10.1063/1.436884.

Merlivat, L., and J. Jouzel (1979), Global climatic interpretation of the deuterium-oxygen 18 relationship for precipitation, *Journal of Geophysical Research*.

Miller, J. B., and P. P. Tans (2003), Calculating isotopic fractionation from atmospheric measurements at various scales, *Tellus B*, *55*(2), 207–214, doi:10.3402/tellusb.v55i2.16697.

Moreira, M. Z., L. D. S. L. Sternberg, L. A. Martinelli, R. L. Victoria, E. M. Barbosa, L. C. M. Bonates, and D. C. Nepstad (1997), Contribution of transpiration to forest ambient vapour based on isotopic measurements, *Global Change Biology*, *3*(5), 439–450, doi:10.1046/j.1365-2486.1997.00082.x.

Mote, P. W., A. F. Hamlet, M. P. Clark, and D. P. Lettenmaier (2005), Declining mountain snowpack in western North America, *Bull. Amer. Meteor. Soc.*, *86*(1), 39–49, doi:10.1175/BAMS-86-1-39.

Noone, D. (2012), Pairing Measurements of the Water Vapor Isotope Ratio with Humidity to Deduce Atmospheric Moistening and Dehydration in the Tropical Midtroposphere, *J. Climate*, *25*(13), 4476–4494, doi:10.1175/JCLI-D-11-00582.1.

Noone, D. et al. (2013), Determining water sources in the boundary layer from tall tower profiles of water vapor and surface water isotope ratios after a snowstorm in Colorado, *Atmos. Chem. Phys.*, *13*(3), 1607–1623, doi:10.5194/acp-13-1607-2013.

Noone, D. et al. (2011), Properties of air mass mixing and humidity in the subtropics from measurements of the D/H isotope ratio of water vapor at the Mauna Loa Observatory, *Journal of Geophysical Research: Atmospheres*, *116*(D22), doi:10.1029/2011JD015773.

Oishi, A. C., R. Oren, and P. C. Stoy (2008), Estimating components of forest evapotranspiration: A footprint approach for scaling sap flux measurements, *Agricultural and Forest Meteorology*, *148*(11), 1719–1732, doi:10.1016/j.agrformet.2008.06.013.

Pataki, D. E., J. R. Ehleringer, L. B. Flanagan, D. Yakir, D. R. Bowling, C. J. Still, N. Buchmann, J. O. Kaplan, and J. A. Berry (2003), The application and interpretation of Keeling plots in terrestrial carbon cycle research, *Global Biogeochem. Cycles*, *17*(1), doi:10.1029/2001GB001850.

Pfahl, S., and H. Wernli (2008), Air parcel trajectory analysis of stable isotopes in water vapor in the eastern Mediterranean, *Journal of Geophysical Research*, *113*(D20), D20104–16, doi:10.1029/2008JD009839.

Pfahl, S., and H. Wernli (2009), Lagrangian simulations of stable isotopes in water vapor: An evaluation of nonequilibrium fractionation in the Craig-Gordon model, *Journal of Geophysical Research*, *114*(D20), D20108–12, doi:10.1029/2009JD012054.

Phillips, N., B. J. Bond, N. G. McDowell, and M. G. Ryan (2002), Canopy and hydraulic conductance in young, mature and old Douglas-fir trees, *Tree Physiology*, *22*(2-3), 205–211, doi:10.1093/treephys/22.2-3.205.

Risi, C., D. Noone, C. Frankenberg, and J. Worden (2013), Role of continental recycling in intraseasonal variations of continental moisture as deduced from model simulations and water vapor isotopic measurements, *Water Resources Research*, *49*(7), 4136–4156, doi:10.1002/wrcr.20312.

Risi, C., S. Bony, and F. Vimeux (2008), Influence of convective processes on the isotopic

composition ($\delta^{18}O$ and δD) of precipitation and water vapor in the tropics: 2. Physical interpretation of the amount effect, *Journal of Geophysical Research*, *113*(D19), D19306–12, doi:10.1029/2008JD009943.

Roden, J. S., G. G. Lin, and J. R. Ehleringer (2000), A mechanistic model for interpretation of hydrogen and oxygen isotope ratios in tree-ring cellulose, *Geochimica et Cosmochimica Acta*, *64*(1), 21–35, doi:10.1016/S0016-7037(99)00195-7.

Rood, S. B., J. Pan, K. M. Gill, C. G. Franks, G. M. Samuelson, and A. Shepherd (2008), Declining summer flows of Rocky Mountain rivers: Changing seasonal hydrology and probable impacts on floodplain forests, *J Hyrdol*, *349*(3-4), 397–410, doi:10.1016/j.jhydrol.2007.11.012.

Rousseeuw, P. J. (1987), Silhouettes - a Graphical Aid to the Interpretation and Validation of Cluster-Analysis, *Journal of Computational and Applied Mathematics*, *20*, 53–65, doi:10.1016/0377-0427(87)90125-7.

Rozanski, K., and C. Sonntag (1982), Vertical-Distribution of Deuterium in Atmospheric Water-Vapor, *Tellus*, *34*(2), 135–141.

Rozanski, K., L. Araguás-Araguás, and R. Gonfiantini (1993), *Isotopic Patterns in Modern Global Precipitation*, Geophysical Monograph Series, American Geophysical Union, Washington, D. C.

Sampson, D. A., and H. L. Allen (1995), Direct and Indirect Estimates of Leaf-Area Index (LAI) for Lodgepole and Loblolly-Pine Stands, *Trees*, *9*(3), 119–122, doi:10.1007/BF02418200.

Schlesinger, W. H., and S. Jasechko (2014), Transpiration in the global water cycle, *Agricultural and Forest Meteorology*, *189-190*, 115–117, doi:10.1016/j.agrformet.2014.01.011.

Simonin, K. A., A. B. Roddy, P. Link, R. Apodaca, K. P. Tu, J. Hu, T. E. Dawson, and M. M. Barbour (2013a), Isotopic composition of transpiration and rates of change in leaf water isotopologue storage in response to environmental variables, *Plant Cell Environ*, *36*(12), 2190–2206, doi:10.1111/pce.12129.

Simonin, K. A., P. Link, D. Rempe, S. Miller, J. Oshun, C. Bode, W. E. Dietrich, I. Fung, and T. E. Dawson (2013b), Vegetation induced changes in the stable isotope composition of near surface humidity, *Ecohydrol.*, *7*(3), 936–949, doi:10.1002/eco.1420.

Smith, W. K., D. R. Young, G. A. Carter, J. L. Hadley, and G. M. McNaughton (1984), Autumn stomatal closure in six conifer species of the Central Rocky Mountains, *Oecologia*, *63*(2), 237–242, doi:10.1007/BF00379883.

Spracklen, D. V., S. R. Arnold, and C. M. Taylor (2012), Observations of increased tropical rainfall preceded by air passage over forests, *Nature*, *489*(7415), 282–285, doi:10.1038/nature11390.

Swann, A. L. S., I. Y. Fung, and J. C. H. Chiang (2012), Mid-latitude afforestation shifts general circulation and tropical precipitation, *Proc Natl Acad Sci USA*, *109*(3), 712–716, doi:10.1073/pnas.1116706108.

Tranquillini, W. (1982), Frost-Drought and Its Ecological Significance, in *Physiological Plant Ecology II*, edited by O. L. Lange, P. S. Nobel, C. B. Osmond, and H. Ziegler, pp. 379–400, Springer Berlin Heidelberg, Berlin, Heidelberg.

Tremoy, G., F. Vimeux, O. Cattani, S. Mayaki, I. Souley, and G. Favreau (2011), Measurements of water vapor isotope ratios with wavelength-scanned cavity ring-down spectroscopy technology: new insights and important caveats for deuterium excess measurements in tropical areas in comparison with isotope-ratio mass spectrometry, *Rapid Commun. Mass Spectrom.*, *25*(23), 3469–3480, doi:10.1002/rcm.5252.

Trenberth, K. E., L. Smith, T. Qian, A. Dai, and J. Fasullo (2007), Estimates of the Global Water Budget and Its Annual Cycle Using Observational and Model Data, *J. Hydrometeor*, *8*(4), 758–769, doi:10.1175/JHM600.1.

Uemura, R., Y. Matsui, K. Yoshimura, H. Motoyama, and N. Yoshida (2008), Evidence of deuterium excess in water vapor as an indicator of ocean surface conditions, *Journal of Geophysical Research*, *113*(D19), D19114–10, doi:10.1029/2008JD010209.

van der Ent, R. J., H. H. G. Savenije, B. Schaefli, and S. C. Steele-Dunne (2010), Origin and fate of atmospheric moisture over continents, *Water Resources Research*, *46*(9), doi:10.1029/2010WR009127.

Vimeux, F., V. Masson, J. Jouzel, M. Stievenard, and J. R. Petit (1999), Glacial–interglacial changes in ocean surface conditions in the Southern Hemisphere, *Nature*.

Welp, L. R., X. Lee, K. Kim, T. J. Griffis, K. A. Billmark, and J. M. Baker (2008), $\delta^{18}O$ of water vapour, evapotranspiration and the sites of leaf water evaporation in a soybean canopy, *Plant Cell Environ*, *31*(9), 1214–1228, doi:10.1111/j.1365-3040.2008.01826.x.

Welp, L. R., X. Lee, T. J. Griffis, X.-F. Wen, W. Xiao, S. Li, X. Sun, Z. Hu, M. Val Martin, and J. Huang (2012), A meta-analysis of water vapor deuterium-excess in the midlatitude atmospheric surface layer, *Global Biogeochem. Cycles*, *26*(3), doi:10.1029/2011GB004246.

Wen, X.-F., X. Lee, X.-M. Sun, J.-L. Wang, Z.-M. Hu, S.-G. Li, and G.-R. Yu (2012), Dew water isotopic ratios and their relationships to ecosystem water pools and fluxes in a cropland and a grassland in China, *Oecologia*, *168*(2), 549–561, doi:10.1007/s00442-011-2091-0.

Westerling, A. L., H. G. Hidalgo, D. R. Cayan, and T. W. Swetnam (2006), Warming and earlier spring increase western US forest wildfire activity, *Science*, *313*(5789), 940–943, doi:10.1126/science.1128834.

White, J. W. C., and S. D. Gedzelman (1984), The Isotopic Composition of Atmospheric Water-Vapor and the Concurrent Meteorological Conditions, *Journal of Geophysical Research: Atmospheres*, *89*(ND3), 4937–4939, doi:10.1029/JD089iD03p04937.

White, J. W. C., E. R. Cook, J. R. Lawrence, and W. S. Broecker (1985), The D/H ratios of sap in trees: Implications for water sources and tree ring D/H ratios, *Geochimica et Cosmochimica Acta*, *49*(1), 237–246, doi:10.1016/0016-7037(85)90207-8.

Whiteman, C. D. (1982), Breakup of temperature inversions in deep mountain valleys: Part I. Observations, *Journal of Applied Meteorology*, *21*(3), 270–289, doi:10.1175/1520-0450(1982)021<0270:botiid>2.0.co;2.

Whiteman, C. D., B. Pospichal, S. Eisenbach, P. Weihs, C. B. Clements, R. Stenacker, E. Mursch-Radlgruber, and M. Dorninger (2004), Inversion breakup in small Rocky Mountain and Alpine basins, *Journal of Applied Meteorology*, *43*(8), 1069–1082, doi:10.1175/1520-0450(2004)043<1069:ibisrm>2.0.co;2.

Yepez, E. A., D. G. Williams, R. L. Scott, and G. Lin (2003), Partitioning overstory and understory evapotranspiration in a semiarid savanna woodland from the isotopic composition of water vapor, *Agricultural and Forest Meteorology*, *119*(1-2), 53–68, doi:10.1016/S0168-1923(03)00116-3.

Chapter 5. Using stable water isotopes to examine the influence of moderate disturbance on canopy water cycling and forest-atmosphere water exchange

5.1 Abstract

Forest structure, age, and species composition modulate fluxes of carbon and water between the land surface and the atmosphere. The response of forests to intermediate disturbances such as ecological succession, species-specific insect invasion, or selective logging that disrupt the canopy but do not promote complete stand replacement, shape how these fluxes evolve through time. We investigate the impact of an intermediate disturbance to water cycling processes by comparing vertical profiles of stable water isotopes in two closely located forest canopies in the northern lower peninsula of Michigan. In one of the canopies, an intermediate disturbance was prescribed in 2008 by inducing mortality in all canopy-dominant early successional species. Isotopic compositions of atmospheric water vapor are measured at six heights during two time periods (summer and early fall) at two flux towers and compared with local meteorology and calculated atmospheric back-trajectories. Disturbance has little impact on low-frequency changes in isotopic composition (e.g., >1 day); at these timescales, isotopic composition is strongly related to large-scale moisture transport. In contrast, disturbance has substantial impacts on the vertical distribution of water isotopes throughout the canopy when transpiration rates are high during the summer, but impact is muted during early fall. Sub-diurnal differences in canopy water vapor cycling are likely related to differences in species composition and response to disturbance and changes in canopy structure. Predictions of transpiration fluxes by land-surface models that do not account species-specific relationships and canopy structure are unlikely to capture these relationships, but addition of stable isotopes to land surface models may provide a useful parameter for evaluating these predictions.

5.2 Introduction

The evapotranspiration (ET) flux from the land surface joins the surface water, carbon, and energy cycles together. The terrestrial latent heat flux associated with ET may represent as much as 50% of the absorbed solar insolation [*Trenberth et al.*, 2009]. Further, water availability is a major control on gross photosynthetic productivity, and hence, carbon uptake by terrestrial plants [e.g., *Baldocchi et al.*, 2002; *Law et al.*, 2002]. Partitioning of the ET flux between transpiration (T) and evaporation (E) is biased toward transpiration, with estimates suggesting that 60->80% of the total ET flux is due to plant transpiration [*Jasechko et al.*, 2013; *Good et al.*, 2015]. Therefore, understanding the spatial, temporal, and plant physiological controls on transpiration is critical to predicting how forests may respond to long-term changes in hydroclimate forced by anthropogenic carbon emissions.

Forest canopy structure is dynamic and is influenced by season, species composition, stand age, and the magnitude and duration of past environmental disturbances. In turn, forest structure is a dominant control on the exchanges of CO_2 and water between the land and the atmosphere [*Baldocchi et al.*, 2002; *Law et al.*, 2002]. Disturbances of forest canopies therefore can alter the ecosystem carbon uptake [e.g., *Pan et al.*, 2011b], and induce changes to biogeochemical cycling of water and nitrogen, for example. Intermediate canopy disturbances, or disturbances that are not severe enough to trigger total stand replacement, can occur naturally due to forest ecological succession [*Gough et al.*, 2013; *Hardiman et al.*, 2013b], species-specific pest invasion [*Kurz et al.*, 2008; *Herms and McCullough*, 2014], or due to extreme weather events such as storms or droughts [*Canham and Loucks*, 1984; *Foster*, 1988; *McDowell et al.*, 2008; *Anderegg et al.*, 2013]. Intermediate disturbances can also be anthropogenically-driven by selective logging [*Asner et al.*, 2004; *Harrod et al.*, 2009] or prescribed fires or fire suppression [*Parsons and DeBenedetti*, 1979; *Nowacki and Abrams*, 2008]. These disturbances will alter the amount of solar energy reaching different heights in the forest canopy [*Hardiman et al.*, 2013b], and in turn, influence canopy microclimate via changes in soil heating, air temperature, vapor pressure deficit, and wind speeds and structures.

In this study, we compare water cycling in two closely located forest stands at the University of Michigan Biological Station in Northern Michigan. One of the forest stands has experienced an induced but rapid intermediate disturbance, where the early successional species were girdled in 2008, resulting in tree death within a few years. The girdling treatment induced

rapid changes in both nitrogen [*Nave et al.*, 2011] and carbon cycling [*Gough et al.*, 2013], but full recovery to pre-treatment values were observed within a few years. In contrast, differences in forest canopy structure and water cycling have persisted between the sites. Forced senescence of canopy-dominant early successional species resulted in a more complex canopy structure marked by increased canopy openness and light penetration into the canopy [*Hardiman et al.*, 2013a; 2013b]. These changes in canopy structure have promoted an increase in soil water content as decreases in precipitation interception and transpiration are greater than the increased surface evaporation associated with more light reaching the surface [*He et al.*, 2013]. Transpiration between the sites has also changed, both due to changes in species composition between the sites and species-specific responses to changes in canopy structure and soil moisture [*Matheny et al.*, 2014].

We seek to further elucidate differences in water vapor cycling between the two forest canopies using stable water isotopes in atmospheric water vapor. Stable isotopes of water are useful tracers of environmental water transport. Phase changes of water impart an unequal partitioning of the heavy and light isotopologues of water, with the heavy isotopologues preferentially entering or remaining in the liquid or solid phase (relative to gas or liquid). This partitioning is a temperature dependent process at equilibrium, with lower temperatures promoting a higher degree of partitioning [*Horita and Wesolowski*, 1994]. When the two phases are unable to reach equilibrium, such as during evaporation, an additional kinetic fractionation occurs due to differences in diffusivities among isotopologues. During evaporation, the diffusivity difference between D/H is larger than that between $^{18}O/^{16}O$, resulting in a stronger kinetic effect observed between hydrogen isotopes than oxygen isotopes [*Merlivat*, 1978; *Cappa et al.*, 2003; *Luz et al.*, 2009]. As a result, the degree of kinetic fractionation is commonly examined through the deuterium excess (d-excess, $d = \delta D - 8\delta^{18}O$, [*Dansgaard*, 1964]), which relates the oxygen and hydrogen isotopic compositions. Fluxes that act to moisten or dry the atmospheric boundary layer leave characteristic isotopic signals. Evaporation of soil water adds vapor that is relatively depleted in heavy isotopes, associated with equilibrium and kinetic fractionations at the soil surface [*Barnes and Allison*, 1984]. Vapor derived from soil evaporation tends to be high in d-excess due to the high degree of kinetic fractionation associated with evaporation. Under clear conditions, entrainment of atmospheric vapor typically injects drier air that has more isotopically depleted water vapor than the near surface air it replaces.

The influence of transpiration fluxes on canopy water vapor depend on the timescale, microclimate, and vegetation of interest. Because there is no fractionation of water during root uptake [*Ehleringer and Dawson*, 1992], the isotopic composition of transpiration must approach the isotopic composition of water taken up by the roots on long time scales. On short time scales, however, the isotopic composition of transpired vapor can deviate from the source water substantially, particularly when environmental conditions are changing rapidly [e.g., *Harwood et al.*, 1998; *Cernusak et al.*, 2002; *Simonin et al.*, 2013].

Here, we integrate profile measurements of the isotopic composition of water vapor with local meteorological variables between two forest canopies: a control site that is representative of most forests in the Great Lakes region, and a disturbed site where all early successional species were removed. The two sites show substantially different diurnal patterns of water cycling through the isotopic composition of water vapor, which we relate to differences in canopy structure and species composition. In contrast, long-term (e.g., >1 day) changes in isotopic composition are closely related to atmospheric moisture transport patterns. Our results suggest that stable water isotopes are valuable tracers of forest processes and can be used to improve the representation of ecological succession and changes in surface fluxes in land surface models.

5.3 Methods

5.3.1 Site Description

The University of Michigan Biological Station (UMBS) is located within a temperate hardwood forest at the northern tip of Michigan's lower peninsula. UMBS forests were extensively logged during the early twentieth century before entering protection, resulting in forests that are approximately 80-90 years old [e.g., *Pan et al.*, 2011a]. UMBS receives 805 mm of mean annual precipitation and has a mean annual temperature of 6.8°C [*Matheny et al.*, 2014]. UMBS soils are part of the Rubicon, Blue Lake, or Cheboygan series of well-drained Haplorthods, and are 95% sand and 5% silt [*Nave et al.*, 2011]. Despite over 800 mm of annual precipitation, summer soil water content tends to be very low due to the high sand content of the soils [*He et al.*, 2013]. As a result, UMBS forests often experience water stressed conditions during the summer.

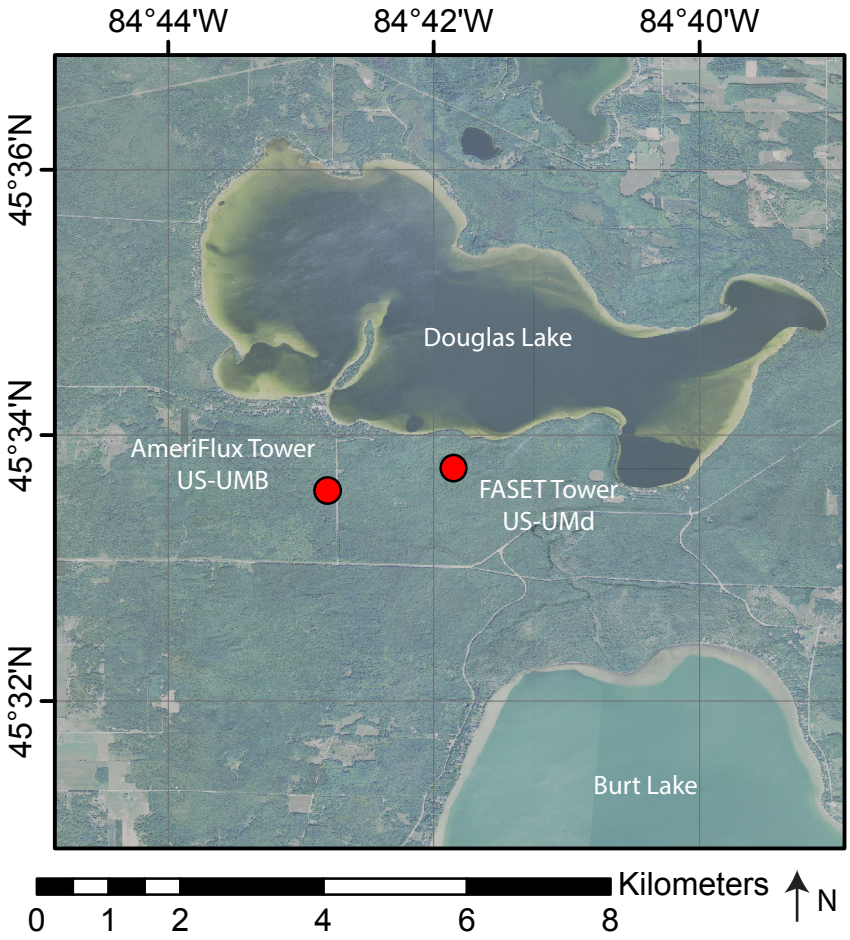

Figure 5.1. Map of the region surrounding the University of Michigan Biological Station with the locations of the two flux towers noted. The flux towers are located in the northern lower peninsula of Michigan between Douglas and Burt Lakes.

We measured the isotopic composition of water vapor along vertical profiles at two eddy covariance flux towers located at UMBS associated with the AmeriFlux network. A full description of the tower and plot setup is provided in [*Gough et al.*, 2013], but essential details are provided here. The two towers are located ~2 km apart and have near identical meteorological conditions at tower top. The forest surrounding one of the towers, hereafter the control tower (AmeriFlux station US-UMB), has been undisturbed since the land entered protection. The forest surrounding this tower is currently transitioning from one dominated by early successional bigtooth aspen (*Populus grandidentata*) and paper birch (*Betula papyrifera*) to one dominated by mid-successional red oak (*Quercus rubra*), red maple (*Acer rubra*), white pine (*Pinus strobus*), American beech (*Fagus grandifolia*), and sugar maple (*Acer saccharum*). The mean canopy height is 25 m. The second tower (AmeriFlux station US-UMd) is surrounded by

the Forest Accelerated Succession ExperimenT (FASET) plot. Within the 39-ha FASET plot, the early successional aspen and birch species were stem-girdled in 2008. The stem girdling had induced mortality or defoliation in 97% of affected trees by 2011 [*Gough et al.*, 2013]. Before stem girdling, forest composition and structure and meteorological conditions were similar at both sites. As a result, we assume that all of the differences in meteorology and isotopic composition at the sites are due to the girdling treatment.

5.3.2 Vapor Isotope Measurements

We deployed cavity ring-down spectrometers (CRDS) at each eddy covariance tower starting on April 30, 2015. A Picarro L2130-i CRDS was installed at the tower in the control plot (AmeriFlux), and a Picarro L2120-i CRDS was installed at the experimental plot (FASET). Standards were introduced at the control plot by a CTC PAL autosampler, and by the Picarro Standard Delivery Module (SDM) at the experimental plot. In both setups, two internal laboratory liquid standards were measured approximately every 12 hours to monitor for drift, and to calibrate isotopic data to the VSMOW scale [*Coplen*, 1996]. Samples introduced by the autosampler are injected into a vaporization module maintained at 110°C under vacuum. Water pulses are delivered as discrete injections, with six injections of two standards. In contrast, standards delivered by the SDM enter the vaporization module maintained at 140°C at ambient pressure, and standards are delivered using a continuous stream of water. Dry carrier air for standards analysis is provided to the analyzer by running ambient air through a drying column filled with anhydrous calcium sulfate with a cobalt chloride redox indicator (Drierite, 26800). No trend was found in standard compositions on diurnal-seasonal timescales, and therefore, no drift corrections or adjustments due to diurnal temperature changes in the instrument trailer are necessary.

Prior studies have demonstrated that CRDS instruments exhibit an instrument-specific water vapor concentration bias in measurements of isotopic composition [e.g., *Tremoy et al.*, 2011; *Steen-Larsen et al.*, 2013]. To account for this bias, we measured our laboratory standards at water vapor concentrations between 10,000 and 30,000 ppmv using the same standard introduction system on each analyzer as was used in the field. Within this concentration range, we found a small concentration correction was necessary for the L2120-i with the SDM, but found no robust evidence to require a correction on the L2130-i with the autosampler. Measured

isotopic values on the L2120-i were corrected by -0.1‰ for $\delta^{18}O$ and -1.0‰ for δD for every 10,000 ppmv deviation from 20,000 ppmv. Our concentration corrections are smaller than those in *Steen-Larsen et al.* [2013], but our environmental conditions are not as dry and our analyzers are a newer generation with improved concentration stability.

Each tower was equipped with a vapor sampling manifold to enable sampling at six heights. Both towers had sampling ports at 2, 5, 10, 15, and 20 m. The highest port was 32 m at FASET and 34 m at the AmeriFlux tower, and was set to be collocated with temperature, relative humidity, and 3D wind measurements collected on each tower.

A multi-position valve controlled by the CRDS was used to switch between the ports (VICI/Valco EMT2SD6MWE). The manifold was maintained at sub-atmospheric pressure by a diaphragm pump operating at 5 L/min to maintain constant airflow through the sampling manifold, and to ensure air in the sampling lines corresponded to current conditions and to minimize latency and memory effects when switching between inlets. Each port was measured for 5 minutes, enabling collection of one vertical profile every half hour. Data from the first 3 minutes of each measurement were omitted as a result of memory associated with switching port sources. Data presented here represent mean values from the last 2 minutes of each measurement, and then are interpolated to a standard half-hour time step in order to facilitate analysis [after *Berkelhammer et al.*, 2013].

Both isotope analyzers were deployed from April 30 until October 23, 2015. The first several weeks of data collection exhibited evidence of water condensation in the sampling lines, and we excluded this period of data from further analysis. Insulation and heating wire was installed on the sampling lines and manifolds at both towers in late May to minimize condensation. Additionally, a solenoid valve failed at the AmeriFlux analyzer that inhibited vapor measurements for three weeks. From the remaining data, we identified two extended periods where both analyzers were functioning well: July 8-August 13, 2015 (summer, DOY 189-225), and September 5-29, 2015 (early fall, DOY 248-272). We focus our analyses on these two periods.

5.3.3 Meteorological Measurements

A suite of meteorological measurements was collected at both flux towers. Additional measurements included 3D wind speeds (Campbell Scientific CSAT3), temperature and relative

humidity (Rotronic), CO2 and H2O concentrations (LiCOR Infrared Gas Analyzer, LI-6262), precipitation amount (Thies Clima Optical Precipitation Sensor 5.4013.20.041, and a Texas Instruments 525MM tipping bucket rain gauge) at 34 m at the control-plot tower and at 32 m at the disturbed-plot tower. The relative humidity sensor at 32 m at the disturbed-plot tower failed at DOY 110 and was replaced around DOY 225. Periods of faulty RH measurements were removed from subsequent analysis. Tower measurements were collected as 10-minute means.

To better resolve the vertical gradient of temperature and humidity, additional temperature and relative humidity measurements were made using HOBO data loggers (Onset Computer Corporation, U23 Pro V2) during 2015. Sensors were installed at 2, 10, 20, and 34 m at the control tower, and 2 and 20 m at the disturbed-plot tower. Data were collected as 15-minute averages.

5.3.4 Data Processing Methods

All data were processed to a common 30-minute time step to facilitate comparison of isotopic and meteorological data. To accomplish this, meteorological data were averaged from 1-, 10-, or 15-minute averages to 30-minute averages. For isotopic measurements, the 2-minute average from each port collected during each 30-minute profile was assumed to represent the entire 30-minute period. From this method, we generate 48 vertical profiles per day.

Correlations between variables were determined using the Pearson coefficient, with p values provided when greater than 0.05. We separated the time series into low frequency (period longer than a day) and high frequency (period less than a day) by applying a 48-point moving average filter to the data. The low frequency data corresponds to the averaged data, while the high frequency data corresponds to the difference between the raw data and the 24-hour moving average. To apply the filter, missing data were imputed using a linear interpolation between the nearest non-missing points. After the residual between the raw and low frequency time series was calculated, the time periods corresponding to the missing data were specified as missing once again. For clarity, when discussing the diurnal cycle deviation from the long-term mean, we use a capital delta (Δ) to indicate that these are isotopic differences from the long-term mean.

5.3.5 Back Trajectory Modeling

We calculated atmospheric back-trajectories to investigate the relationship between air source pathways and local isotopic composition. Ten-day back-trajectories were calculated using the HYbrid Single Parcel Lagrangian Integrated Transport model (HYSPLIT). A full description of the algorithms used in the HYSPLIT model are available in *Draxler and Hess* [1998]. Back trajectories were calculated using NCEP/NCAR Reanalysis Data as an input [*Kalnay et al.*, 1996]. Air parcel vertical velocity was determined by using reanalysis vertical velocities.

The relationship between air sourcing and local vapor isotopic composition was explored by comparing the low frequency $\delta^{18}O$ signal to calculated back-trajectories. The histogram of the low frequency $\delta^{18}O$ vapor time series for the 34m port at AmeriFlux was used to identify natural groupings. The same minimum values are observed in the histograms for both seasons and are around -22.0‰ and -18.0‰ $\delta^{18}O$. These groupings (e.g., < -22.0‰, > -18.0‰, and values in between) are used to generate three sets of back-trajectory frequency composites using calculations from the times represented by each grouping. If the low-frequency isotope composition at the UMBS sites are strongly influenced by the isotopic composition of moisture advected by the large-scale flow, these frequency composites should show distinct patterns from one another. Frequency composites were generated by binning hourly back-trajectory data into a 0.75° grid and normalizing by the number of trajectories [as in *Fiorella et al.*, 2015].

5.4 Results

5.4.1 Mean Conditions at the AmeriFlux and FASET flux towers

5.4.1.1 Summer

Isotopic and meteorological conditions were similar at both stations when considering the long-term mean (Table 5.1, Figures 5.2-5.3). Both stations exhibit a long-term gradient in isotopic composition, with AmeriFlux exhibiting slightly lower heavy isotope compositions than FASET as a whole. Isotopic compositions were least depleted in heavy isotopes at the surface at AmeriFlux (-20.37 ‰ $\delta^{18}O$, -146.11‰ δD at 2 m), with the heavy isotope content decreasing with height to the canopy top (-21.04 ‰ $\delta^{18}O$, -148.83 ‰ δD at 20 m) (Figure 5.2a-c). In contrast, isotopic compositions at FASET are most enriched in heavy isotopes at 10 m (-19.44 ‰ $\delta^{18}O$, -142.71 ‰ δD), with decreasing heavy isotope content toward the surface and toward the

canopy top and above (Figure 5.3a-c, Table 5.1). Isotopic compositions at both stations varied on multiple timescales, ranging from a few hours to a week. AmeriFlux summer $\delta^{18}O/\delta D$ values ranged from -29.86 ‰ / -208.88 ‰ (observed at 5 m) to -11.43 ‰ / -72.82 ‰ (observed at 10 m) (Figure 5.2a-c), while FASET $\delta^{18}O/\delta D$ values ranged from -26.85 ‰ / -192.74 ‰ (observed at 32 m) to - 9.15 ‰ (observed at 10 m) / -102.81 ‰ (observed at 32 m) (Figure 5.3a-c).

Specific humidity measured by the HOBO data loggers and the Rotronic Temp/RH sensor decreased from 2-20 m at AmeriFlux, but were greater than 20 m at 34 m (Figure 5.2d-e, Figure 5.3d-e). At FASET, 20 m specific humidity was greater than 2 m specific humidity. Mean water vapor mixing ratios measured by the CRDS decreased with height at both stations. Mixing ratios vary from 16.5 mmol/mol at 2 m to 16.2 mmol/mol at 34 m at AmeriFlux, and 18.0 mmol/mol at 2 m to 17.7 mmol/mol at 32 m at FASET (Figure 5.2f, Figure 5.3f, Table 5.1). For both sets of measurements, FASET was more humid than AmeriFlux in the long-term mean.

Temperature, relative humidity, water vapor mixing ratio, specific humidity, and dew point temperature correlate with $\delta^{18}O$ and δD at nearly all heights and at both stations (Table 5.2). Correlations are strongest between isotopic composition and vapor mixing ratio, specific humidity, and dew point temperature ($r > 0.6$). Isotopic composition is more weakly correlated with temperature and relative humidity at both stations ($r < 0.5$). At AmeriFlux, correlation strength between $\delta^{18}O$ and δD increased with height for most meteorological variables, reaching a maximum value above the canopy at 34 m (Table 5.2). In contrast, correlations between $\delta^{18}O$ and δD and meteorological variables at FASET were often weakest at 10 m within the canopy, and increased toward the surface and the canopy top (Table 5.2).

Deuterium excess exhibits markedly different relationships with meteorological variables than $\delta^{18}O$ and δD. At both stations, the d-excess is most strongly correlated with relative humidity (Table 5.2). RH correlates most strongly with d-excess near the surface, with the relationship becoming weaker with height at both towers (Table 5.2). Water vapor mixing ratio is most strongly correlated with d-excess at the canopy top and above at AmeriFlux (20 and 34 m), and near the surface (2 m) and above the canopy (32 m) at FASET. The sign of the correlation changes from negative to positive within the canopy at FASET (10, 15, and 20m sampling heights), but not at AmeriFlux. Deuterium excess correlates significantly but weakly with temperature within the canopy at both towers, but is uncorrelated with temperature above the canopy (Table 5.2). Finally, specific humidity and dew point temperature are uncorrelated with

d-excess below the canopy top at AmeriFlux, but are negatively correlated at the canopy top and above. At FASET, specific humidity and dew point temperature are both negatively and weakly correlated with d-excess, but the correlation is stronger at 2 m than it is at 20 m.

Table 5.1. Summer mean water vapor concentrations and isotopic compositions

AmeriFlux Tower				
Height	**Specific humidity (g/kg)**	**Vapor Mixing Ratio (ppm)**	**$\delta^{18}O$ (‰ VSMOW)**	**δD (‰ VSMOW)**
2 m	12.66	16536	-20.37	-146.11
5 m	no sensor	16413	-20.55	-147.11
10 m	12.43	16382	-20.70	-147.71
15 m	no sensor	16333	-20.87	-148.30
20 m	12.18	16293	-21.04	-148.83
34 m	12.53	16169	-21.06	-148.62
FASET Tower				
Height	**Specific humidity (g/kg)**	**Vapor Mixing Ratio (ppm)**	**$\delta^{18}O$ (‰ VSMOW)**	**δD (‰ VSMOW)**
2 m	13.37	17995	-19.65	-143.17
5 m	no sensor	17903	-19.51	-142.64
10 m	no sensor	17849	-19.44	-142.71
15 m	no sensor	17849	-19.57	-143.08
20 m	13.49	17770	-19.68	-143.72
32 m	sensor malfunction	17712	-20.09	-145.00

Table 5.2. Summer correlations between isotopic compositions and meteorological variables.

AmeriFlux Tower						
$\delta^{18}O$	**2 m**	**5 m**	**10 m**	**15 m**	**20 m**	**34 m**
Temperature	0.165		0.190		0.293	0.364
Relative Humidity	0.409		0.376		0.307	0.347
Vapor Mixing Ratio	0.826	0.827	0.830	0.847	0.860	0.865
Specific Humidity	0.700		0.715		0.780	0.861
Dew Point	0.685		0.699		0.771	0.853
δD	**2 m**	**5 m**	**10 m**	**15 m**	**20 m**	**34 m**
Temperature	0.293		0.300		0.350	0.398
Relative Humidity	0.278		0.262		0.232	0.286
Vapor Mixing Ratio	0.828	0.829	0.830	0.834	0.837	0.831
Specific Humidity	0.757		0.763		0.788	0.838
Dew Point	0.741		0.746		0.776	0.825
d-excess	**2 m**	**5 m**	**10 m**	**15 m**	**20 m**	**34 m**
Temperature	0.462		0.457		0.247	0.038 (p=0.12)
Relative Humidity	-0.700		-0.670		-0.596	-0.583
Vapor Mixing Ratio	-0.314	-0.285	-0.288	-0.384	-0.492	-0.673
Specific Humidity	-0.040 (p=0.10)		-0.020 (p=0.41)		-0.256	-0.517
Dew Point	-0.039 (p=0.11)		0.508		-0.269	-0.627
FASET Tower						
$\delta^{18}O$	**2 m**	**5 m**	**10 m**	**15 m**	**20 m**	**32 m**
Temperature	0.248				0.379	0.392
Relative Humidity	0.287				0.121	
Vapor Mixing Ratio	0.782	0.646	0.489	0.543	0.534	0.824
Specific Humidity	0.670				0.646	
Dew Point	0.656				0.638	
δD	**2 m**	**5 m**	**10 m**	**15 m**	**20 m**	**32 m**
Temperature	0.368				0.476	0.437
Relative Humidity	0.151				0.043 (p=0.16)	
Vapor Mixing Ratio	0.779	0.734	0.658	0.685	0.684	0.800
Specific Humidity	0.721				0.726	
Dew Point	0.706				0.716	
d-excess	**2 m**	**5 m**	**10 m**	**15 m**	**20 m**	**32 m**
Temperature	0.235				0.068	-0.048 (p=0.11)
Relative Humidity	-0.595				-0.228	
Vapor Mixing Ratio	-0.466	-0.057 (p=0.06)	0.195	0.099	0.122	-0.647
Specific Humidity	-0.228				-0.082	
Dew Point	-0.225				-0.082	

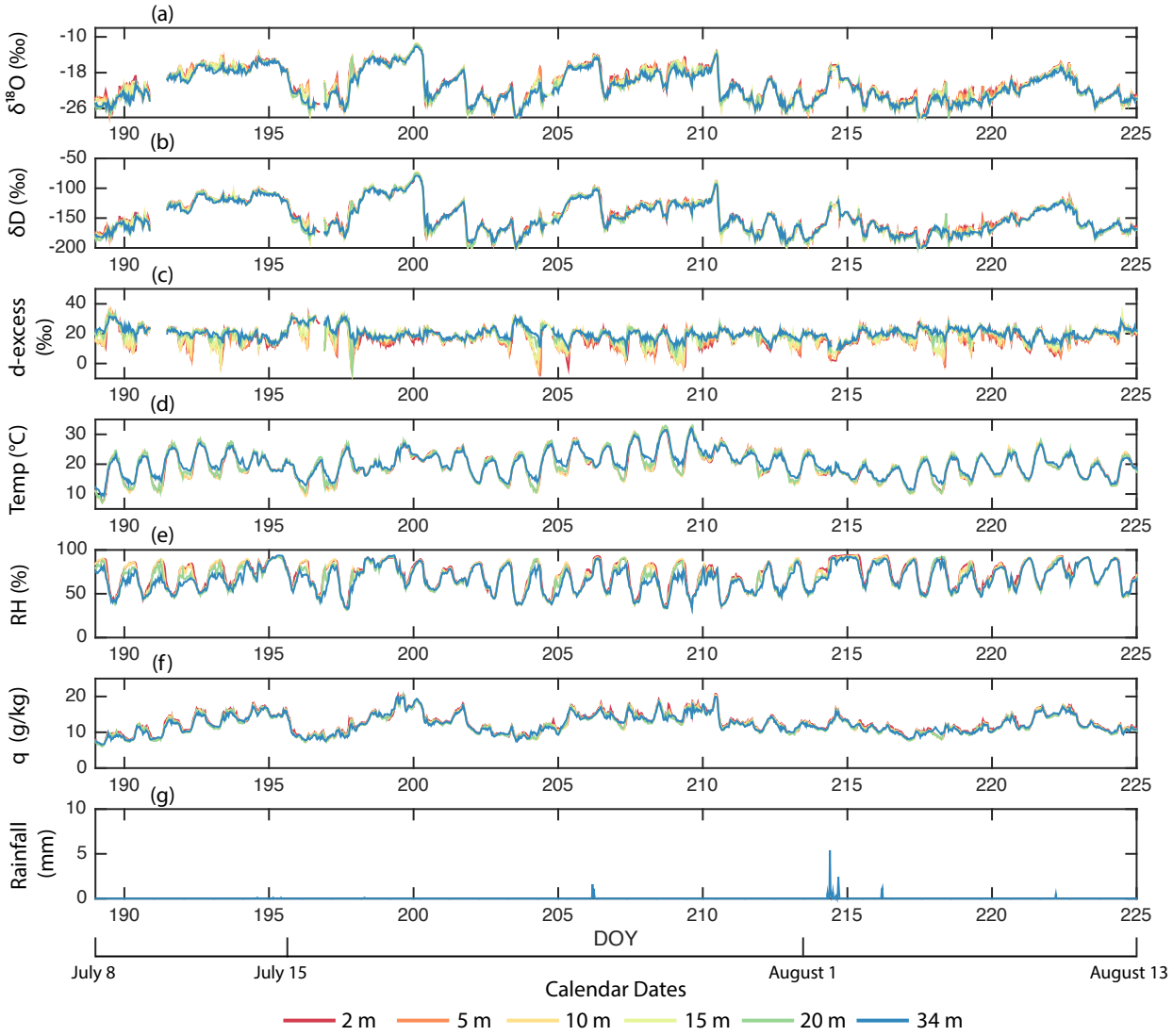

Figure 5.2. Time series of the summer (DOY 188-225, July 8-August 13, 2015) isotopic and meteorological data at the AmeriFlux (control) tower. (a) Vapor $\delta^{18}O$ (‰, VSMOW), (b) δD (‰, VSMOW), (c) d-excess (‰, VSMOW), (d) temperature (°C), (e) relative humidity (RH, %), (f) specific humidity (q, g/kg), and (g) rainfall amount (mm). Data are shown for every height available as a different color along a spectrum from red (canopy floor, 2 m) to blue (above canopy, 34 m).

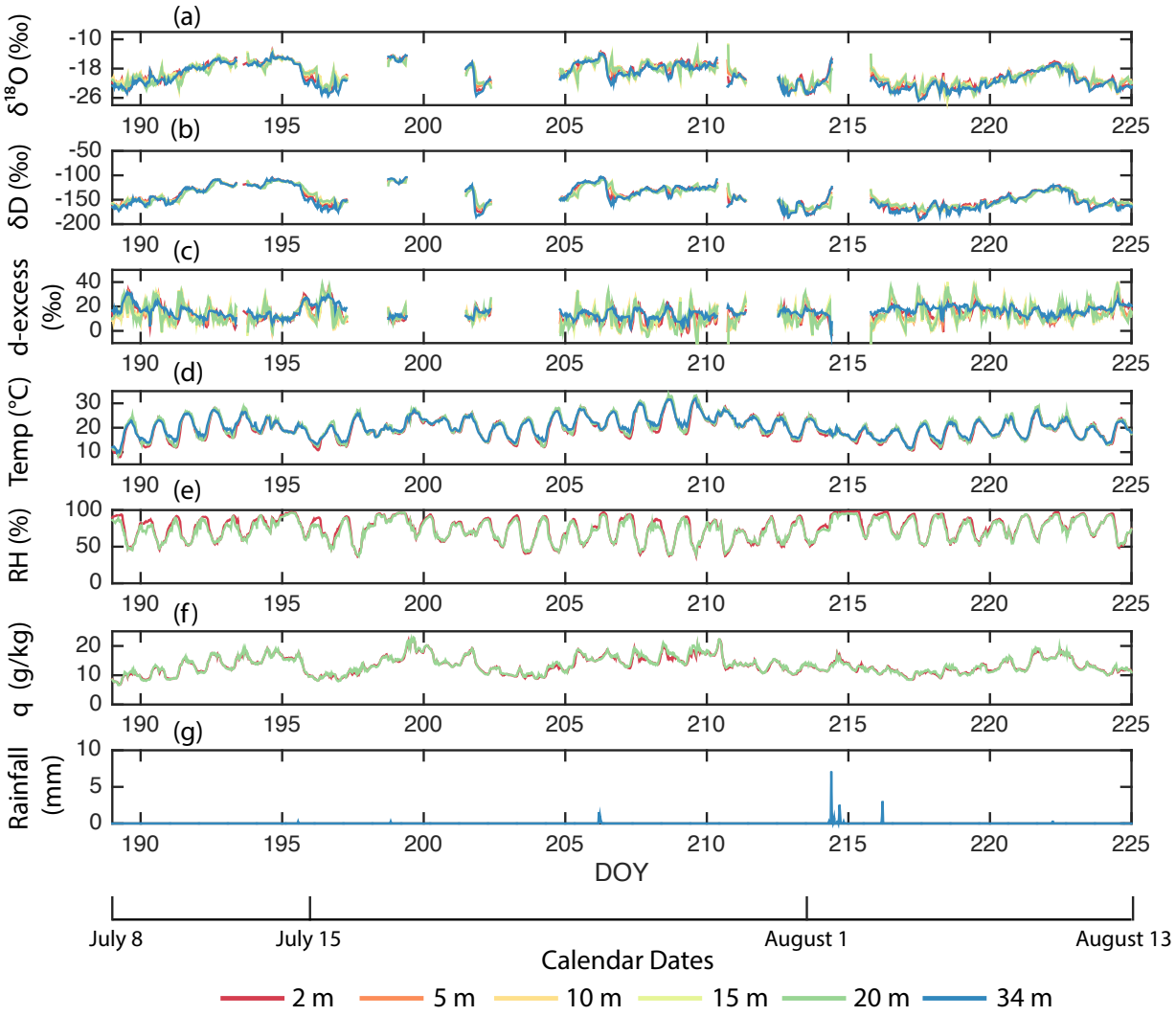

Figure 5.3. Time series of the summer (DOY 188-225, July 8-August 13, 2015) isotopic and meteorological data at the FASET (disturbed) tower. (a) Vapor $\delta^{18}O$ (‰, VSMOW), (b) δD (‰, VSMOW), (c) d-excess (‰, VSMOW), (d) temperature (°C), (e) relative humidity (RH, %), (f) specific humidity (q, g/kg), and (g) rainfall amount (mm). Data are shown for every height available as a different color along a spectrum from red (canopy floor, 2 m) to blue (above canopy, 32 m).

5.4.1.2 Early fall

Mean specific humidity and water vapor mixing ratios were similar in early fall to their summer values, but isotopic compositions were generally less negative (Table 5.3). Mean water vapor mixing ratios decreased from 16.3 mmol/mol at 2 m to 15.7 mmol/mol at 34 m at AmeriFlux, and from 17.9 mmol/mol at 2 m to 17.2 mmol/mol at 32 m at FASET (Table 5.3). As during the summer, FASET was consistently more humid than AmeriFlux. Vertical trends in isotopic composition are similar to summer, though the entire column is less depleted in heavy isotopes at both sites. Mean $\delta^{18}O$ and δD values decreased throughout the column at AmeriFlux (Figure 5.4), but reached a maximum at 10 m at FASET while decreasing toward the surface and toward and above the canopy top (Figure 5.5). The range of isotopic compositions observed during early fall was similar to that observed during the summer. Early fall $\delta^{18}O$ / δD values at AmeriFlux ranged from -28.18 ‰ / -194.69 ‰ (both at 20 m) to -10.55 ‰ / -59.88 ‰ (both at 34 m) (Figure 5.4, Table 5.3). FASET $\delta^{18}O$ / δD values ranged from -26.81 ‰ / -187.40 ‰ (both at 32 m) to -9.15 ‰ (10 m) / -71.49 ‰ (32 m) (Figure 5.5, Table 5.3).

As during summer, $\delta^{18}O$ and δD correlate strongly ($r > 0.7$) with water vapor mixing ratio, vapor pressure, and dew point temperature in early fall at both towers. The magnitude of the correlations between $\delta^{18}O$, δD and temperature and relative humidity change substantially in early fall, however. Temperature emerges as a strong positive covariate with $\delta^{18}O$ and δD during the early fall, with r values typically greater than 0.7 (Table 5.4). During the summer, r values between temperature and $\delta^{18}O$ or δD were below 0.5. In contrast, relative humidity exhibits a much weaker and often insignificant correlation with $\delta^{18}O$ or δD during early fall. Summer r values between relative humidity and $\delta^{18}O$ and δD were typically above |0.1|, but are generally below |0.1| during the early fall.

Correlations between meteorological variables and d-excess also exhibit differences between summer and early fall. As during summer, d-excess correlates most strongly with relative humidity during early fall. No trend in the strength of the relationship between RH and d-excess with height was observed at AmeriFlux, but the negative correlation between d-excess and RH was stronger at 2 m than 20 m at FASET (Table 5.4). As during the summer, vapor mixing ratio is most strongly correlated at and above the canopy top (20 and 34 m) at AmeriFlux, but near the surface and above the canopy (2 and 32 m) at FASET (Table 5.4).

Table 5.3. Early fall mean water vapor concentrations and isotopic compositions

AmeriFlux Tower				
Height	**Specific Humidity (g/kg)**	**Vapor Mixing Ratio (ppm)**	**$\delta^{18}O$ (‰ VSMOW)**	**δD (‰ VSMOW)**
2 m	12.20	16260	-18.04	-123.54
5 m	no sensor	16051	-18.15	-124.21
10 m	11.79	15886	-18.33	-124.97
15 m	no sensor	15791	-18.52	-125.82
20 m	11.62	15692	-18.72	-126.69
34 m	11.98	15670	-18.73	-126.55
FASET Tower				
Height	**Specific Humidity (g/kg)**	**Vapor Mixing Ratio (ppm)**	**$\delta^{18}O$ (‰ VSMOW)**	**δD (‰ VSMOW)**
2 m	12.77	17850	-17.64	-124.54
5 m	no sensor	17893	-17.53	-123.40
10 m	no sensor	18016	-17.49	-122.98
15 m	no sensor	17911	-17.66	-123.58
20 m	12.63	17831	-17.73	-124.10
32 m	sensor malfunction	17206	-18.07	-126.93

Table 5.4. Early fall correlations between isotopic composition and meteorological variables

AmeriFlux Tower						
$\delta^{18}O$	**2 m**	**5 m**	**10 m**	**15 m**	**20 m**	**34 m**
Temperature	0.700		0.700		0.734	0.793
Relative Humidity	0.095		0.037 (p=0.21)		-0.009 (p=0.77)	0.092
Vapor Mixing Ratio	0.831	0.821	0.815	0.820	0.823	0.834
Specific Humidity	0.821		0.820		0.838	0.850
Dew Point	0.829		0.828		0.852	0.881
δD	**2 m**	**5 m**	**10 m**	**15 m**	**20 m**	**34 m**
Temperature	0.781		0.770		0.770	0.818
Relative Humidity	-0.041 (p=0.16)		-0.091		-0.104	0.006 (p=0.83)
Vapor Mixing Ratio	0.822	0.807	0.794	0.789	0.782	0.793
Specific Humidity	0.844		0.831		0.824	0.820
Dew Point	0.854		0.840		0.837	0.839
d-excess	**2 m**	**5 m**	**10 m**	**15 m**	**20 m**	**34 m**
Temperature	0.241		0.309		0.102	-0.146
Relative Humidity	-0.687		-0.699		-0.677	-0.653
Vapor Mixing Ratio	-0.233	-0.216	-0.217	-0.332	-0.469	-0.640
Specific Humidity	-0.072		-0.047 (p=0.11)		-0.291	-0.523
Dew Point	-0.069		-0.039 (p=0.19)		-0.296	-0.565
FASET Tower						
$\delta^{18}O$	**2 m**	**5 m**	**10 m**	**15 m**	**20 m**	**32 m**
Temperature	0.711				0.674	0.786
Relative Humidity	0.101				0.132	
Vapor Mixing Ratio	0.838	0.787	0.715	0.738	0.727	0.826
Specific Humidity	0.832				0.813	
Dew Point	0.841				0.822	
δD	**2 m**	**5 m**	**10 m**	**15 m**	**20 m**	**32 m**
Temperature	0.782				0.793	0.810
Relative Humidity	-0.028 (p=0.34)				-0.011 (p=0.70)	
Vapor Mixing Ratio	0.816	0.816	0.784	0.789	0.788	0.778
Specific Humidity	0.845				0.864	
Dew Point	0.855				0.878	
d-excess	**2 m**	**5 m**	**10 m**	**15 m**	**20 m**	**32 m**
Temperature	-0.091				0.002 (p = 0.95)	-0.364
Relative Humidity	-0.619				-0.452	
Vapor Mixing Ratio	-0.563	-0.314	-0.156	-0.224	-0.181	-0.806
Specific Humidity	-0.405				-0.247	
Dew Point	-0.408				-0.240	

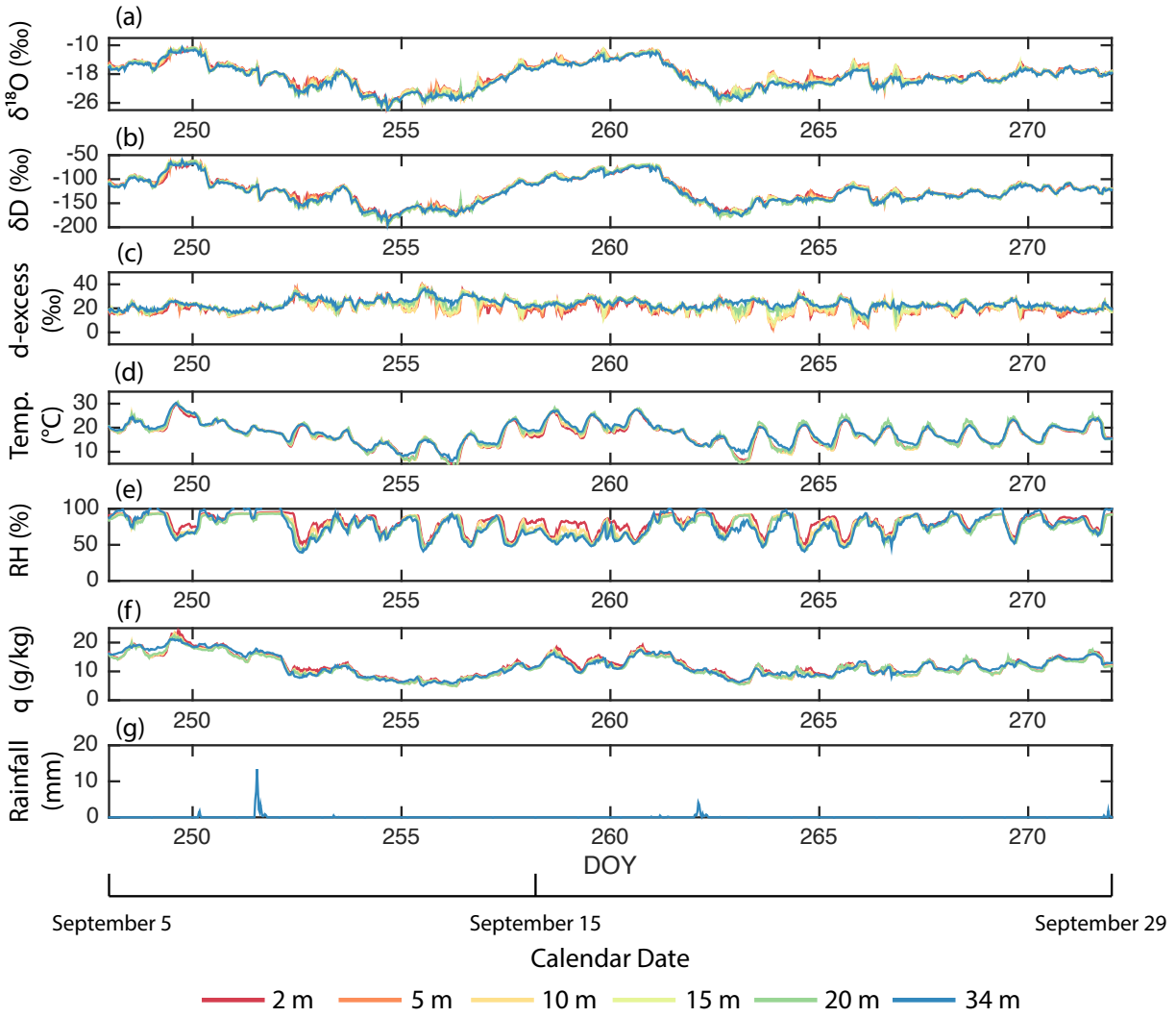

Figure 5.4. Time series of the early fall (DOY 248-272, September 5-29, 2015) isotopic and meteorological data at the AmeriFlux (control) tower. (a) Vapor $\delta^{18}O$ (‰, VSMOW), (b) δD (‰, VSMOW), (c) d-excess (‰, VSMOW), (d) temperature (°C), (e) relative humidity (RH, %), (f) specific humidity (q, g/kg), and (g) rainfall amount (mm). Data are shown for every height available as a different color along a spectrum from red (canopy floor, 2 m) to blue (above canopy, 34 m).

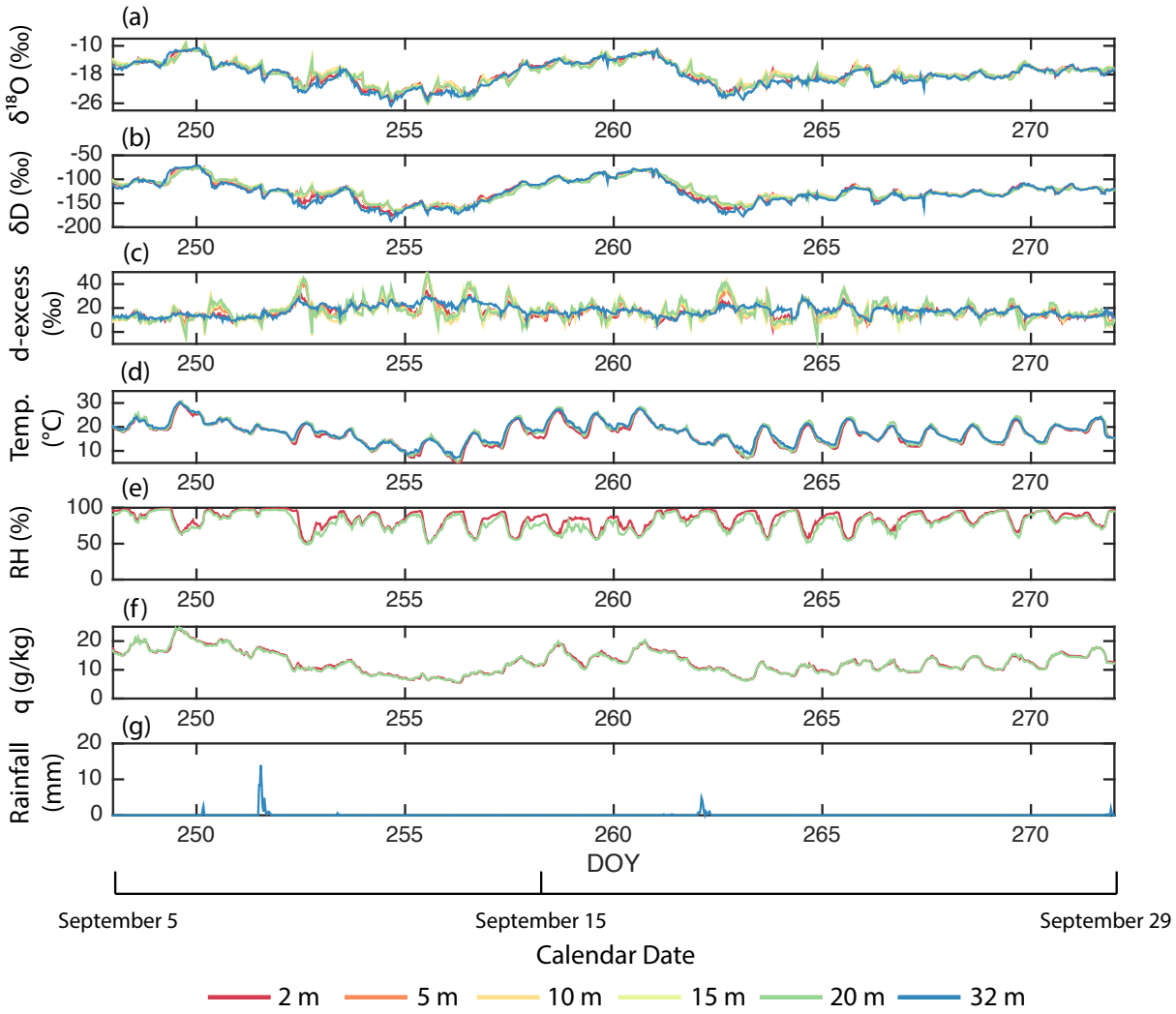

Figure 5.5. Time series of the early fall (DOY 248-272, September 5-29, 2015) isotopic and meteorological data at the FASET (disturbed) tower. (a) Vapor $\delta^{18}O$ (‰, VSMOW), (b) δD (‰, VSMOW), (c) d-excess (‰, VSMOW), (d) temperature (°C), (e) relative humidity (RH, %), (f) specific humidity (q, g/kg), and (g) rainfall amount (mm). Data are shown for every height available as a different color along a spectrum from red (canopy floor, 2 m) to blue (above canopy, 32 m).

5.4.2 The Diurnal Cycle

5.4.2.1 Summer

Strong diurnal cycles in isotopic compositions occur at both towers, though different patterns are observed at each site. At AmeriFlux, the magnitude of the diurnal isotopic cycle is inversely proportional to height, with the largest isotopic change observed at 2 and 5 m. $\Delta^{18}O$ and ΔD both increase from midnight until 8-9 am (Figure 5.6ab). During this period, d-excess decreases slowly between midnight and 6 am, before decreasing rapidly between 6 and 8-9 am (Figure 5.6c). After 9 am, $\Delta^{18}O$ and ΔD decrease rapidly until 2-3 pm (Figure 5.6ab). During this period, d-excess increases rapidly from 9 am until noon, before leveling off or decreasing slightly after 1-2 pm (Figure 5.6c). Vertical isotope gradients are small at AmeriFlux between 11 am and ~3 pm (Figure 5.6a-c). After 3 pm, $\Delta^{18}O$ increases rapidly until midnight, while ΔD increases rapidly until about 6 pm, and more slowly between 6 pm and midnight (Figure 5.6ab). Concurrently, d-excess values decrease from their daily maximum values from 6 pm onward (Figure 5.6c). These changes promote the reestablishment of an isotopic gradient throughout the profile. However, despite differences in the magnitude of these changes at different heights, the timing of isotopic change is coherent throughout the profile.

Diurnal cycles of $\Delta^{18}O$ and ΔD are similar at FASET compared to AmeriFlux at 2 m and at the highest port (34 or 32 m respectively) (Figure 5.6d), but FASET observations diverge from AmeriFlux observations at all other heights. At 5 m, FASET $\Delta^{18}O$ is stable between midnight and 6 am, decreases rapidly between 6 am and noon, increases rapidly between noon and 4 pm, and then remains steady from 4 pm until midnight (Figure 5.6d). FASET ΔD at 5m decreases from midnight to 6 am, increases between 6 am and 6 pm, and then decreases from 6 pm to midnight (Figure 5.6e). Daytime patterns (e.g., between 6 am and 6 pm) are similar to observations at 5m at the 10, 15, and 20 m sampling heights (Figure 5.6d,e), but diverge during the night. At 10-20 m, $\Delta^{18}O$ decreases from 6 pm until 6 am, while little change is observed during this time period at 5 m (Figure 5.6d). FASET ΔD at 10-20 m exhibits a similar pattern as observed at 5 m, but the magnitude of ΔD decrease between 6 pm to 6 am is larger (Figure 5.6e). FASET Δd-excess patterns are also distinct from observations at AmeriFlux, apart from at the tower top (Figure 5.6f). Between 10 and 20 m, d-excess values rise rapidly between 7 and 11 am, before decreasing from 11 am to 6 pm (Figure 5.6f). At 5 m, d-excess values are intermediate to values observed at 2 m and from 10-20 m; this trend likely represents mixing between water at

those levels. Also in contrast to patterns observed at AmeriFlux, the isotope gradient is large throughout the day at FASET. In the morning, $\Delta^{18}O$ and ΔD decrease while d-excess increases from 2-20 m, while the opposite trend holds in the afternoon. There is no extended period in the long-term composite of the diurnal cycle where isotopic compositions appear well mixed (Figure 5.6d-f).

Despite the large differences in diurnal cycles of isotopic composition between the AmeriFlux and FASET locations, diurnal cycles of meteorological variables are nearly identical between each location (Figure 5.7). During the summer, each site exhibits a ~10°C cycle in temperature (Figure 5.7ae), a 2-3 g/kg cycle in specific humidity (Figure 5.7df), a ~40% cycle in relative humidity (Figure 5.7cg), and maximum VPD values of ~2 kPa during the mid afternoon (Figure 5.7dh). The magnitude of each cycle is comparable with increasing height or decreases slightly at both stations. The similarity in meteorology between the two flux towers suggests that it is unlikely to be driving the differences in water vapor cycling observed in the isotopic compositions.

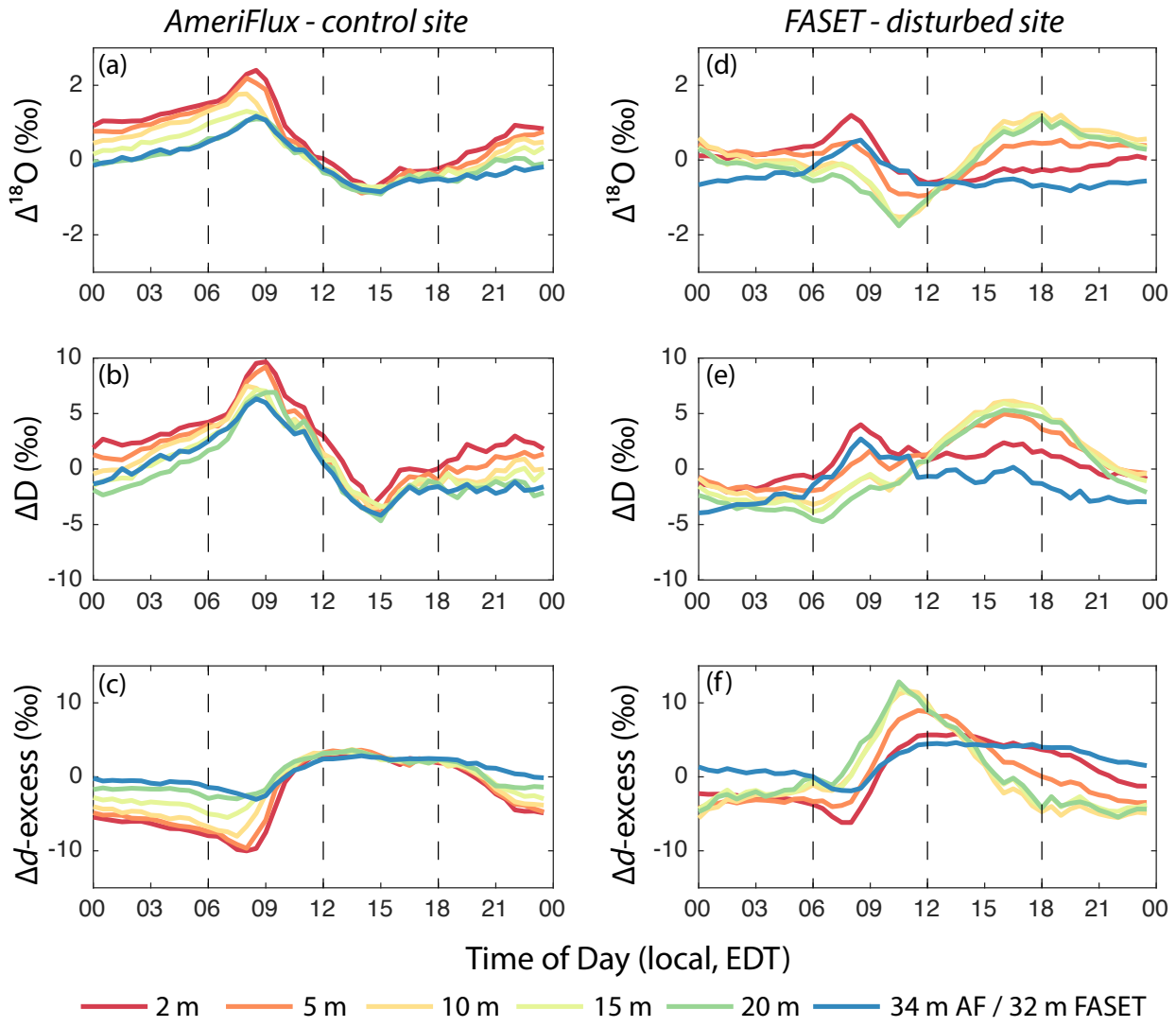

Figure 5.6. Composites of the isotopic diurnal cycle at each sampling height for the summer period at AmeriFlux (left column, a-c) and FASET (right column, d-f). $\Delta^{18}O$ (a,d), ΔD (b,e), and Δd-excess (c,f) are expressed as deviations from the 24-hour running mean of that variable at 20-m.

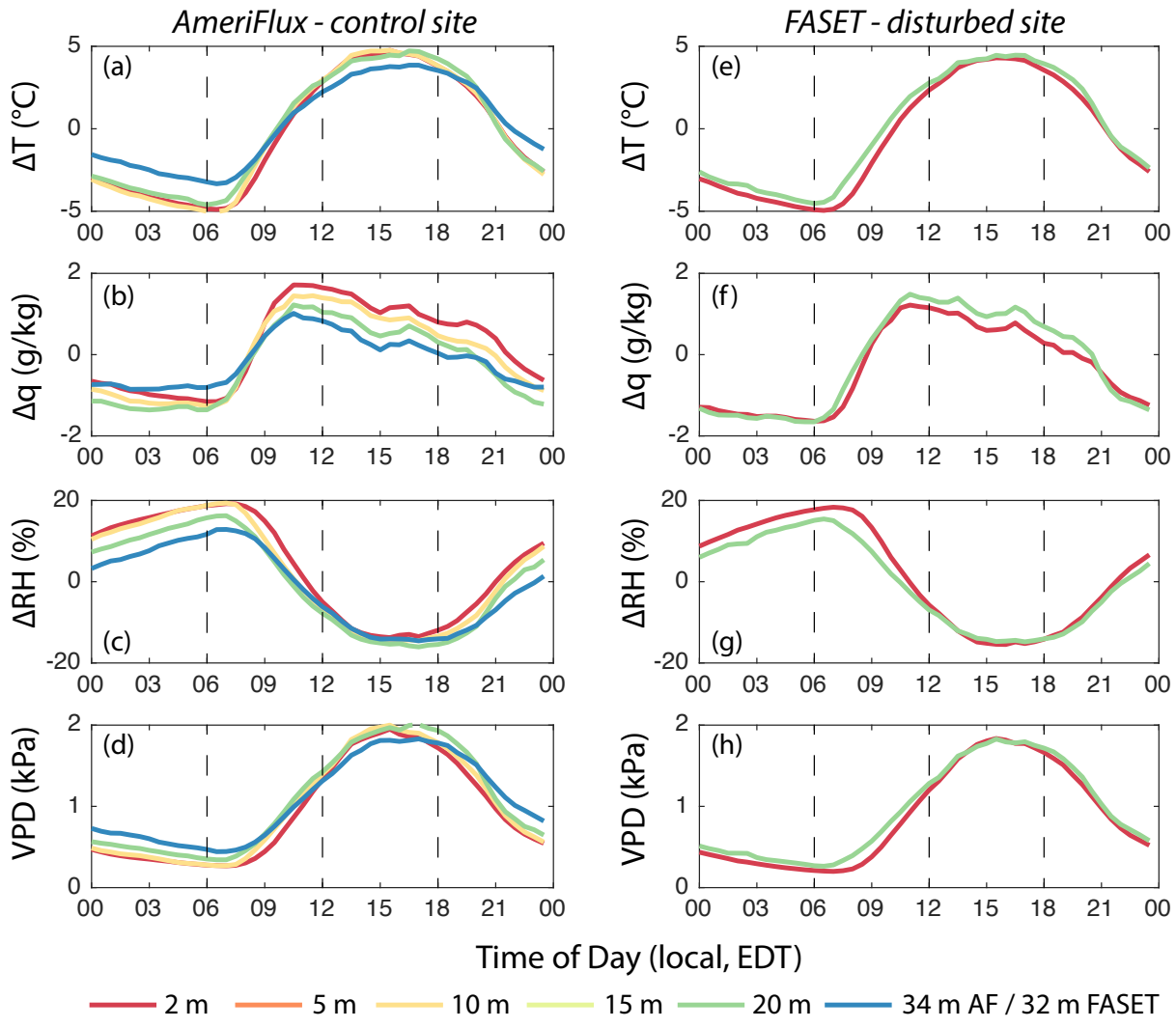

Figure 5.7. Composites of the meteorological diurnal cycle at each sampling height for the summer period at AmeriFlux (left column, a-d) and FASET (right column, e-h). Temperature (ΔT, °C) (a,e), specific humidity (Δq, g/kg) (b,f), and relative humidity (ΔRH, %) (c,g) are shown as deviations from the 24-hour running mean at 20-m. Vapor pressure deficit (VPD, kPa) is expressed as its measured value (d,h).

5.4.2.2 Early fall

The diurnal cycles in isotopic composition are different at both sites in the early fall, but are more consistent with each other than during the summer. At AmeriFlux, $\Delta^{18}O$ decreases slightly for all heights between midnight and 7 am, before rising at all heights between 7 and 9 am (Figure 5.8). From 9 until 11 am, $\Delta^{18}O$ values decrease at 20 m and below, but remain steady at 34 m (Figure 5.8a). As a result, the vertical gradient observed in $\Delta^{18}O$ decreases in the late morning. $\Delta^{18}O$ values increase at all heights between 11 am and 6 pm, but more rapidly at lower heights (Figure 5.8a). After 6 pm, $\Delta^{18}O$ values increase more rapidly until 9 pm, with the greatest

rates of change occurring at the lowest levels. From 9 pm until midnight, $\Delta^{18}O$ values decrease by 0.5-1‰ (Figure 5.8a). AmeriFlux ΔD values follow the same trend as $\Delta^{18}O$ between 7 pm and 7 am, but exhibit a slightly different pattern during the day (Figure 5.8b). Between 7 am and ~2 pm, ΔD increases before stabilizing until ~6 pm (Figure 5.8b). Early fall d-excess exhibits a similar trend as during the summer (compare Figure 5.6c to 5.8c), though the magnitude of the diurnal cycle is smaller in early fall than summer. As during the summer, the magnitude of the d-excess cycle is largest near the surface and decreases with height. As during the summer, the vertical d-excess gradient is small during the day, and larger at night (Figure 5.8c). Additionally, early fall Δd-excess trends diverge from summer trends at dawn and dusk (compare Figure 5.6c to 5.8c). Early fall Δd-excess values at AmeriFlux reach their diurnal minimum typically after dusk between 8-9 pm, while summer d-excess values reach their daily minimum values at dawn.

At FASET, the early fall diurnal cycle is similar to AmeriFlux in ΔD and $\Delta^{18}O$ for most of the day, however, the vertical gradient between 2 and 20 m is usually smaller at FASET than at AmeriFlux (Figure 5.8de). Additionally, the largest amplitude diurnal cycles in $\Delta^{18}O$ and ΔD are observed at 2 m at AmeriFlux, but are observed from 10-20 m at FASET. The cycle in Δd-excess is distinct during the day however, with Δd-excess values increasing ~10‰ above the 32 m value at 10-20 m height between 11 am and 1 pm. After 1 pm, Δd-excess values decrease rapidly between 10-20 m until ~ 9 pm (Figure 5.8f). As for $\Delta^{18}O$ and ΔD, the largest amplitude diurnal changes in Δd-excess are observed from 10-20 m at FASET (Figure 5.8f), but from 2-5 m at AmeriFlux (Figure 5.8c).

As during the summer, diurnal cycles between meteorological variables are nearly identical between the two sites (Figure 5.9). During the early fall, each site exhibits a ~10°C in temperature (Figure 5.9ae), a 2-3 g/kg cycle in specific humidity (Figure 5.9df), a ~40% cycle in relative humidity (Figure 5.9cg), and maximum VPD values of ~1.2 kPa during the mid afternoon (Figure 5.9dh). Peak specific humidity occurs later in the day in the early fall than during the summer (between noon and 6 pm, and between 10-11 am respectively; compare Figures 5.7 and 5.9). VPD is ~40% lower during the early fall than during the summer. As during the summer measurement period, however, there is little difference in meteorology between sites to suggest that meteorological conditions are responsible for the observed difference in isotopic compositions (Figure 5.9).

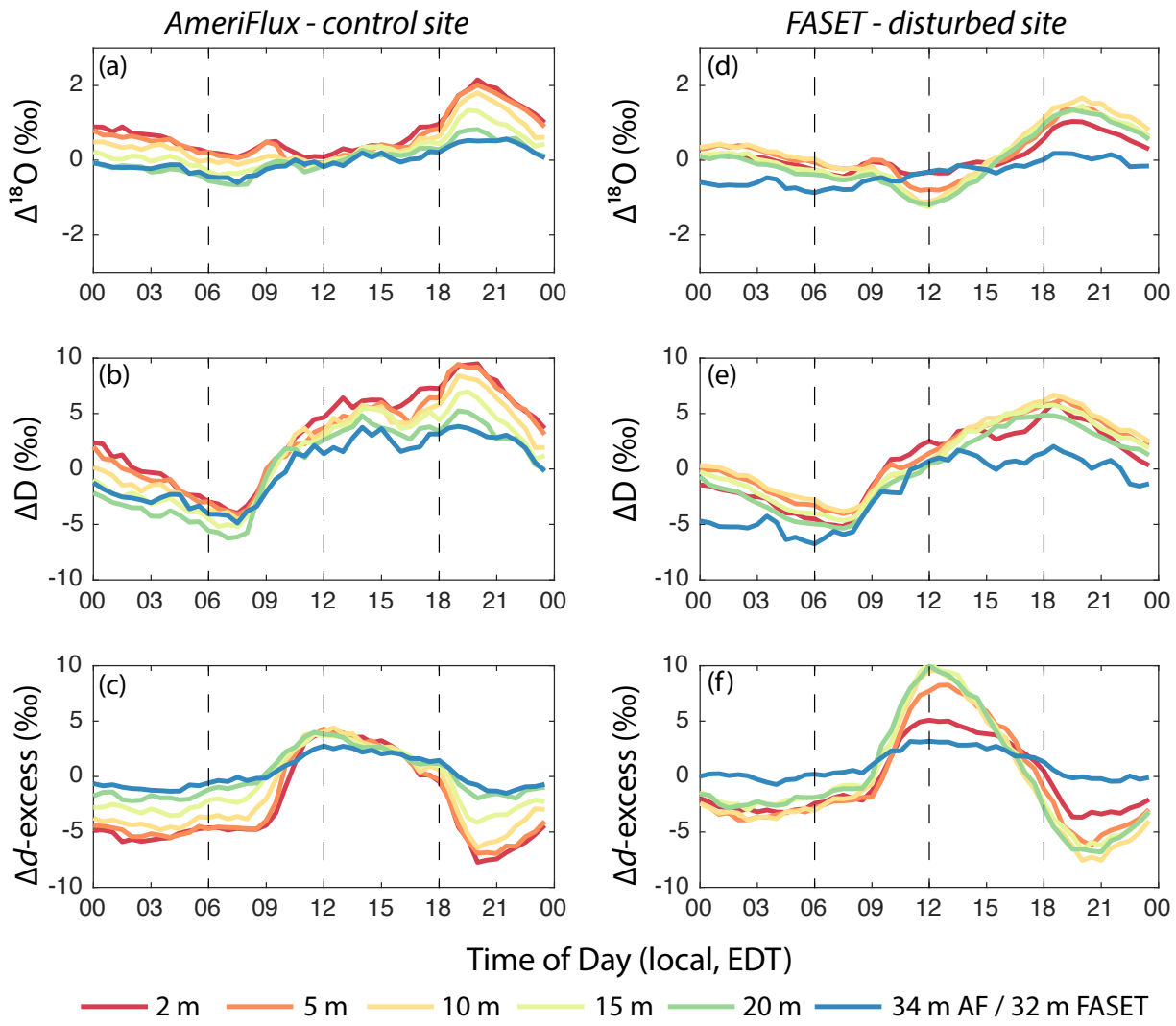

Figure 5.8. Composites of the isotopic diurnal cycle at each sampling height for the early fall period at AmeriFlux (left column, a-c) and FASET (right column, d-f). Δ18O (a,d), ΔD (b,e), and Δd-excess (c,f) are expressed as deviations from the 24-hour running mean at 20-m.

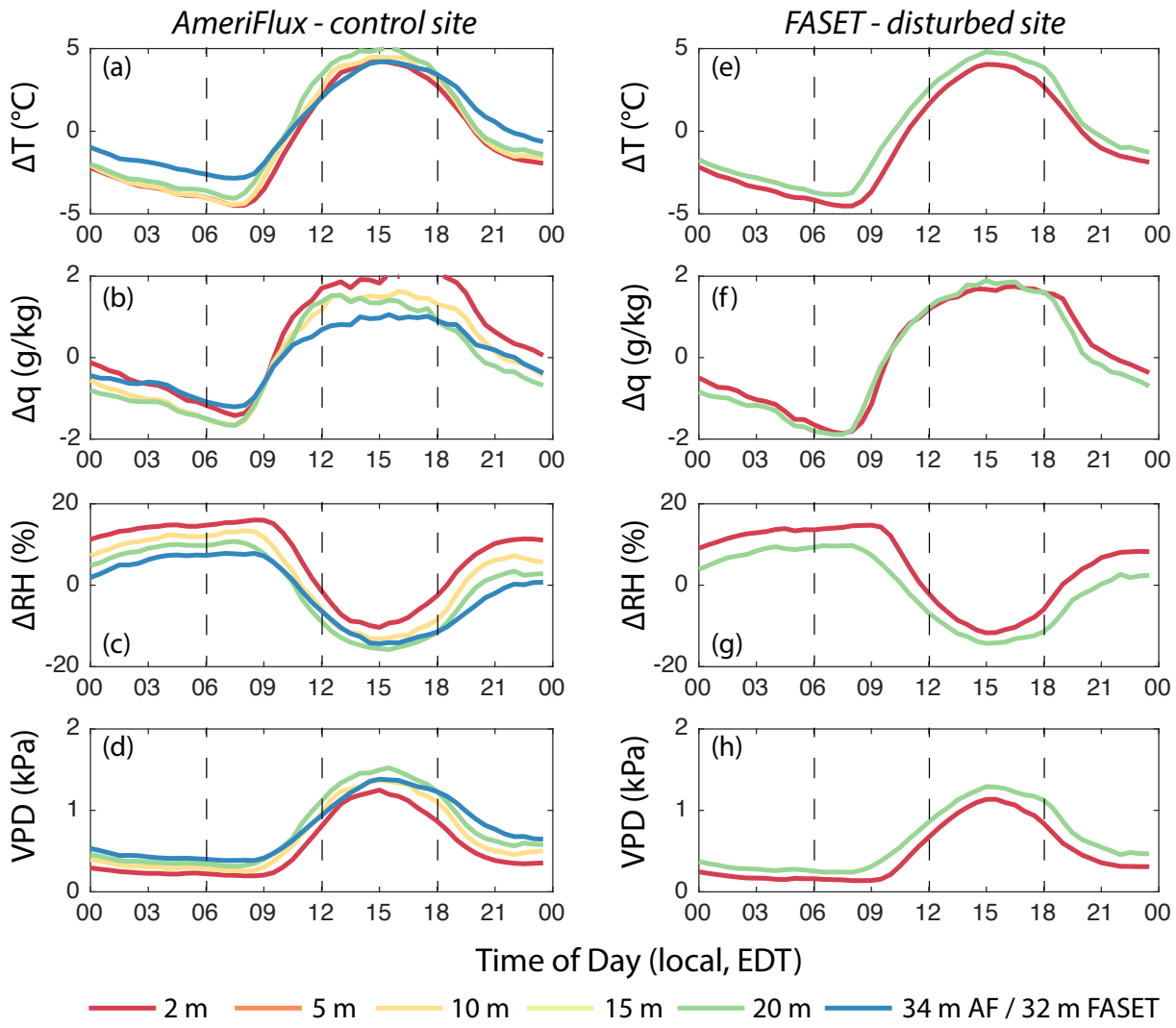

Figure 5.9. Composites of the meteorological diurnal cycle at each sampling height for the early fall period at AmeriFlux (left column, a-d) and FASET (right column, e-h). Temperature (ΔT, °C) (a,e), specific humidity (Δq, g/kg) (b,f), and relative humidity (ΔRH, %) (c,g) are shown as deviations from the 24-hour running mean at 20-m. Vapor pressure deficit (VPD, kPa) is expressed as its measured value (d,h).

5.4.3 Variability in the vertical isotope gradient

Vertical gradients in isotopic composition show variability on timescales of a few days (Figures 5.2-5.5). For example, d-excess shows a large gradient on several days in Figure 5.2 that is nearly absent on other days (e.g., DOY 198-203). These observations appear to be closely related to local wind speeds (Figures 5.10-5.11), though the two flux towers exhibit different relationships in different portions of the canopy, or between day and night. The relationship between wind speed and the vertical isotopic gradient does not change based on the season. Nocturnal isotope gradients between 2 and 32/34 m show no dependence on above-canopy wind

speed (at 34 or 32 m, depending on the tower) for $\delta^{18}O$, δD, or d-excess (Figure 5.10a-c). Above-canopy wind speeds are nearly always below 4 m/s. Vertical isotopic gradients tend to be smaller during the day than at night, but show different relationships when above-canopy wind speeds exceed 4 m/s during the day (Figure 5.10d-f). When winds are high, the vertical isotope gradient between 2 and 32/34 m for d-excess (Figure 5.10f) and $\delta^{18}O$ (Figure 5.10d) are smaller than when winds are low, though wind speeds appear to have little influence on the δD gradient (Figure 5.10e). These trends likely reflect the tendency of higher wind speeds to drive more complete mixing of lower atmospheric air, preventing large isotopic gradients from developing.

Within the canopies, different relationships between the isotopic gradient and wind speeds hold and site-specific behavior emerges (Figure 5.11). At both sites, the nocturnal vertical isotopic gradient between 2 and 15 m can be positive or negative for $\delta^{18}O$, δD, or d-excess (Figure 5.11a-c). Gradient magnitudes appear independent of wind speed. During the day, however, the magnitude of the isotopic gradient between 2 and 15 m increases at FASET for all three isotopic species, but decreases at AmeriFlux (Figure 5.11d-f). Above-canopy wind speeds do not influence the 2-15 m isotopic gradient at FASET (Figure 5.11d-f), but high wind speeds appear to decrease the d-excess gradient at AmeriFlux (Figure 5.11f).

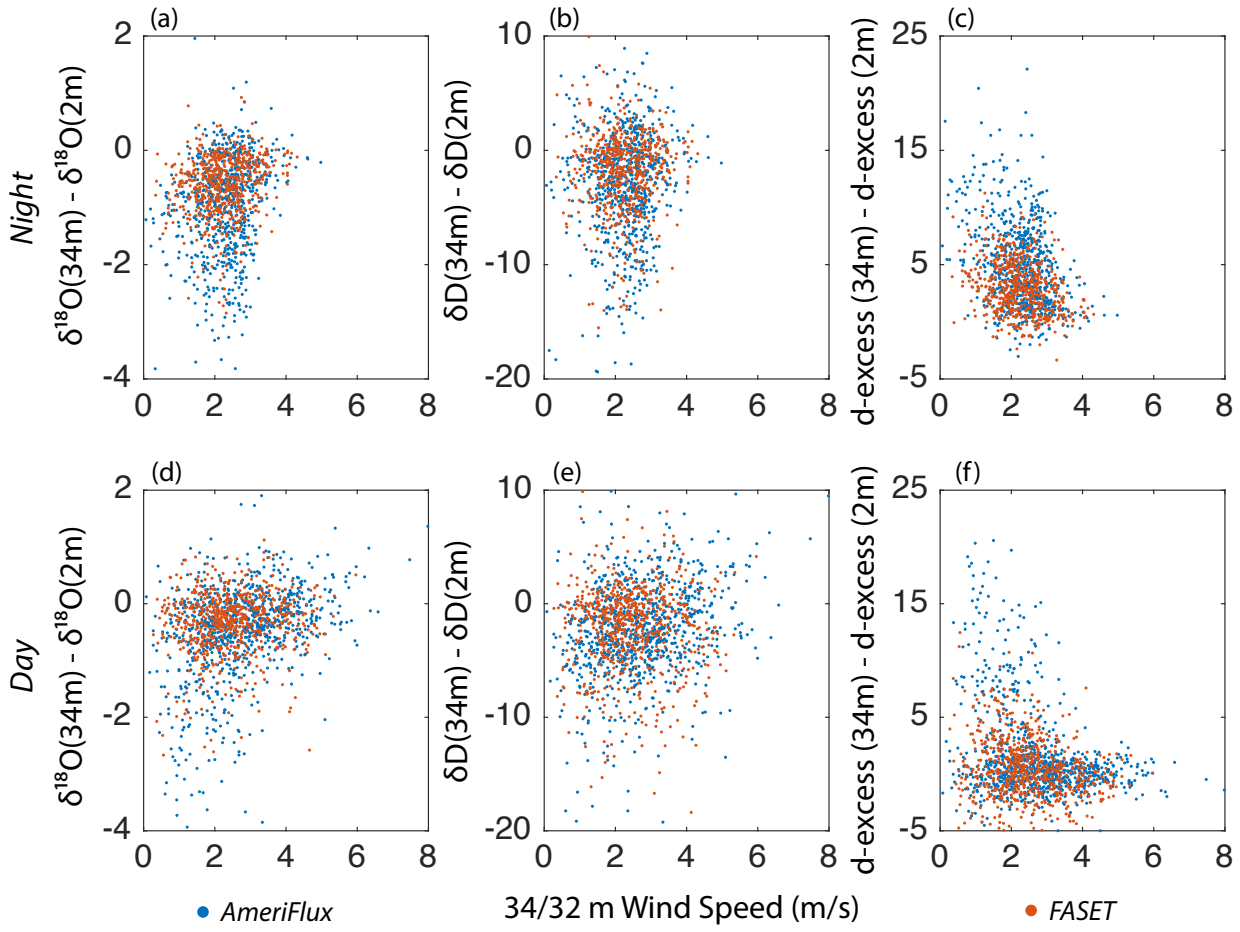

Figure 5.10. Scatter plots of the isotopic gradient between 2 m and 32/34 m as a function of above-canopy wind speed (m/s) for the summer measurement period. The top row shows values at night, while the bottom row shows daytime data. Night and day were determined based on whether a pyranometer at 46 m at the AmeriFlux tower recorded less or more than 25 W/m^2. The left column shows data for $\delta^{18}O$, the middle column shows data for δD, and the right column shows data for d-excess. Data from AmeriFlux are plotted as blue circles, while data from FASET are plotted as red circles.

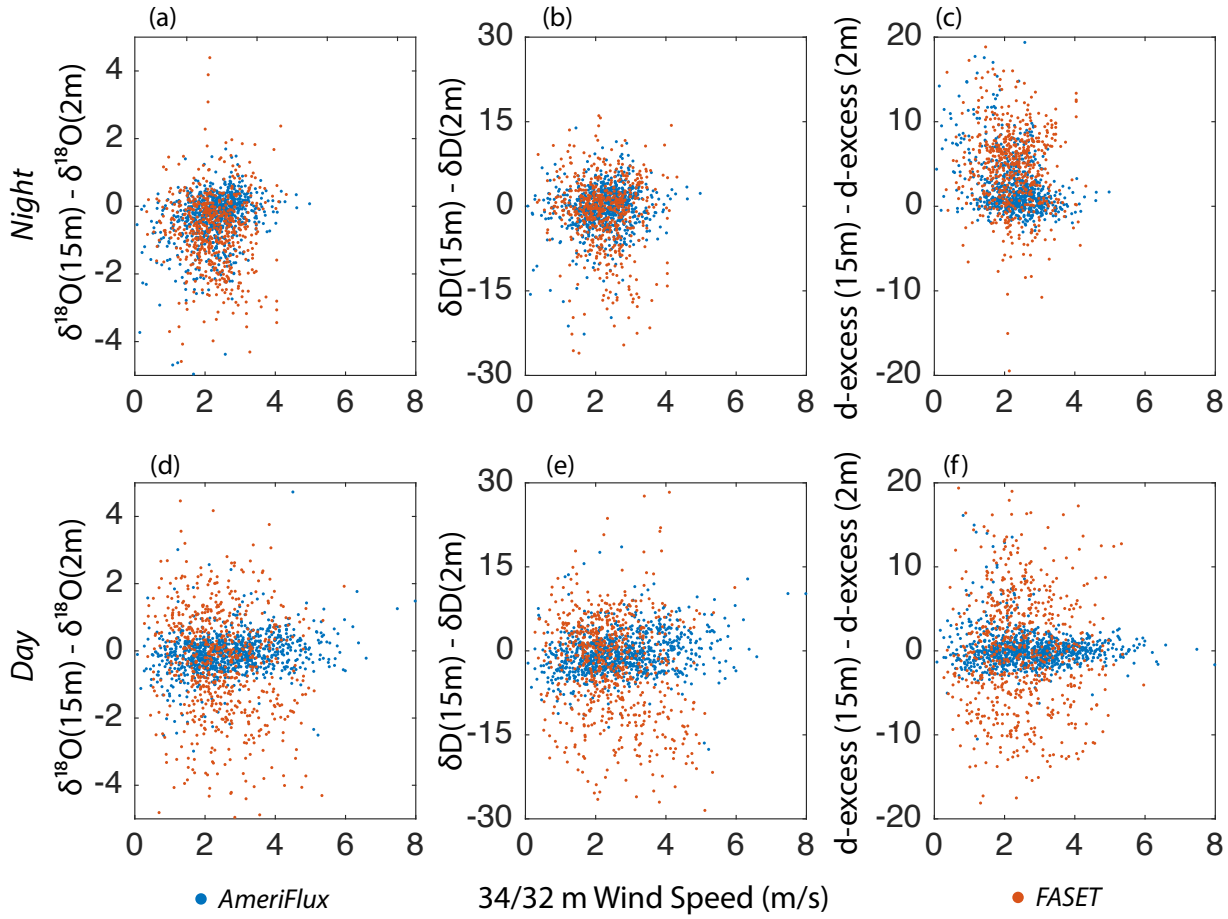

Figure 5.11. Scatter plots of the isotopic gradient (‰) between 2 m and 15 m as a function of above-canopy wind speed (m/s) for the summer measurement period. The top row shows values at night, while the bottom row shows daytime data. Night and day were determined based on whether a pyranometer at 46 m at the AmeriFlux tower recorded less or more than 25 W/m^2. The left column shows data for $\delta^{18}O$, the middle column shows data for δD, and the right column shows data for d-excess. Data from AmeriFlux are plotted as blue circles, while data from FASET are plotted as red circles.

5.4.4 Relationship between air parcel back-trajectories and low-frequency isotopic variability

The low-frequency component of the isotopic composition time series varies by several per mil from day to day. Clear distinctions between vapor source directions and isotopic composition of canopy vapor are observed (Figure 5.12). During the summer observation period, the most depleted vapor observations are associated with air advection from the Arctic and Hudson Bay region (Figure 5.12a). In contrast, the most enriched isotopic compositions are associated with air advection from midwestern US and from the south and the Gulf of Mexico (Figure 5.12c). Compositions intermediate to these extremes tend to be derived from the west through southern Canada (Figure 5.12b). Air advection patterns during the early fall are generally consistent with observations from the summer. The most depleted isotopic

compositions are associated with air sourcing from the north and west (Figure 5.12d), and the most enriched isotopic compositions are associated with air sourcing predominantly from the south (Figure 5.12f). Intermediate compositions are associated with air sourcing from the west, south, and east (Figure 5.12e). These associations demonstrate that canopy isotopic compositions are controlled at UMBS by atmospheric advection and mixing to first-order on timescales greater than a day.

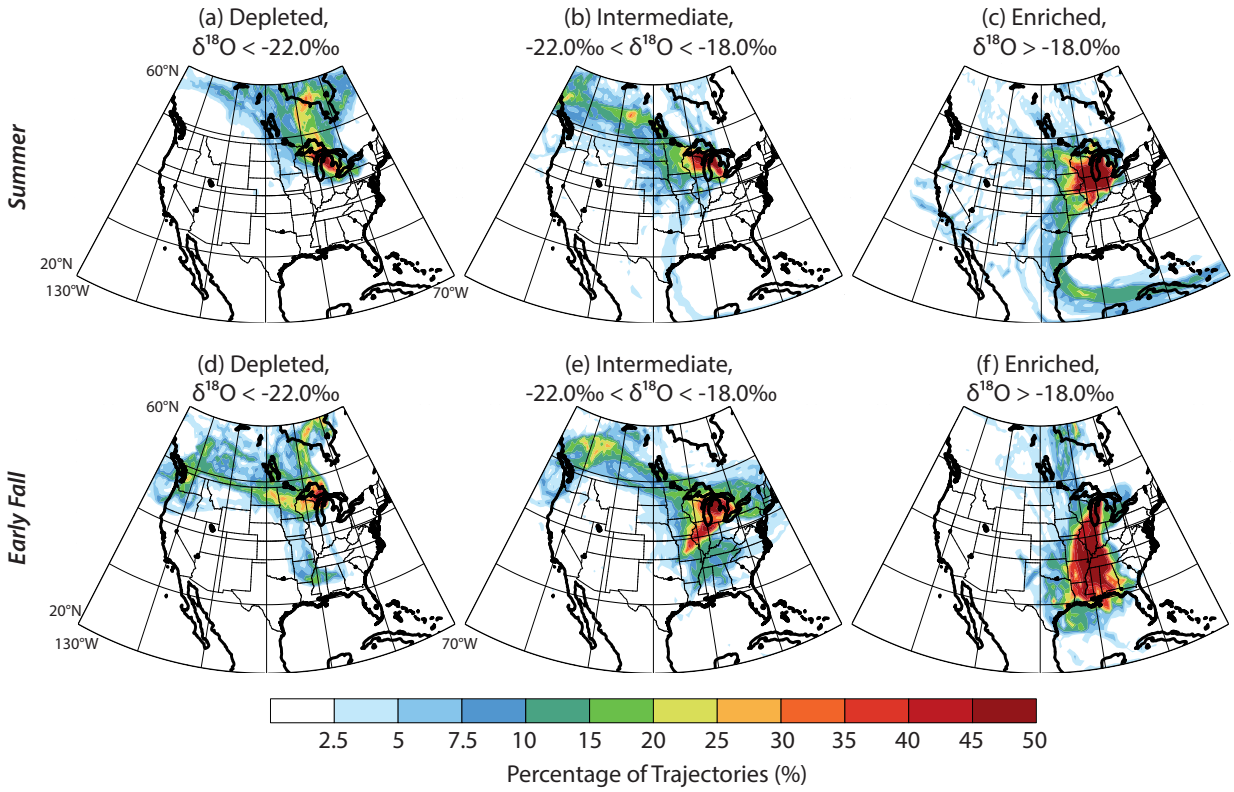

Figure 5.12. Back-trajectory frequency composites for summer (a-c) and early fall (d-f): (a,d) the most depleted isotopic values (δ18O < -22.0‰), (b,e) intermediate values (-22.0‰ < δ18O < -18.0‰), and (c,f) the most enriched isotopic values (δ18O > -18.0‰).

5.5 Discussion

5.5.1 Timescale dependence of processes controlling near-surface water vapor isotopic composition

Patterns in air sourcing to UMBS appear to represent the dominant control over canopy isotopic composition on longer timescales (e.g., > 1 day). Over multiple days, isotopic compositions drift between -12 and -25‰ $\delta^{18}O$ during both seasons. Back-trajectory modeling suggests that the large-scale circulation is the dominant control on these long-term fluctuations in near-surface

vapor isotopic compositions. In both seasons, isotopic compositions are more depleted when vapor is advected to UMBS from the north and less depleted when vapor is advected from the south (Figure 5.12). Northerly-sourced air is also drier than air sourced from the south. More depleted isotopic compositions from the drier air from the north would be expected due to greater upwind condensation and colder temperatures experienced along the trajectory. In contrast, air sourced from the south is moister and less depleted in heavy isotopes, which is consistent with an airmass that has not experienced cold temperatures and strong condensation following its initial evaporation from the ocean. High correlations between local isotopic composition and specific humidity (Tables 5.2, 5.4) underscore this relationship. Periods with intermediate isotopic compositions to the northerly-southerly relationship discussed above are typically associated with strong westerly flow or a mixture between sources (Figure 5.11).

These relationships appear more distinct in the summer period than during the early fall. The advection patterns in Figure 5.11a-c are more distinct than those in Figure 5.11d-f. For example, the most depleted values during early fall show some component of northerly, southerly, and westerly advection. During the early fall, lower local temperatures become more important to determining the local specific humidity and therefore leave a larger fingerprint in local isotopic compositions during the summer. This argument is supported by the substantially higher correlation between isotopic composition and temperature observed during the early fall period relative to the summer period. Furthermore, relative humidity rarely reaches 100% during the summer, but routinely reaches saturation during the early fall.

On time scales shorter than a day, isotopic change is likely driven by local surface and boundary layer processes, such as evapotranspiration and the entrainment of free tropospheric air into the boundary layer. Several features of the diurnal cycle are consistent between the two sites; potential causes for the differences between sites are discussed in the next section. First, both seasons and sites have their daily maximum Δd-excess values during the day and at their minimum at night (Figures 5.6,5.8 c,f). This trend in Δd-excess is driven primarily by ΔD increasing more rapidly than $8\Delta^{18}O$ (recall that d-excess = $\delta D - 8\delta^{18}O$) in the morning, and by $8\Delta^{18}O$ changing more rapidly than ΔD in the afternoon and evening. While plants do not fractionate water during uptake into the roots [*Ehleringer and Dawson*, 1992], transpired water compositions can vary from source water on diurnal and shorter timescales [*Flanagan et al.*, 1991; *Cernusak et al.*, 2002; *Simonin et al.*, 2013]. Leaf water undergoes a diurnal cycle of

enrichment and decay back to the source water value that is proportional to transpiration rate, stomatal conductance, and changes in isotopic fractionation factors associated with diurnal cycles in temperature and relative humidity [*Cernusak et al.*, 2002; *Farquhar and Cernusak*, 2005; *Simonin et al.*, 2013]. Morning increases in Δd-excess are consistent with an increasing kinetic fractionation factor associated with decreases in relative humidity and increases in temperature and progressive enrichment of leaf waters. Likewise, evening decreases in Δd-excess are consistent with decreasing kinetic fractionation factor driven by decreases in temperature and increases in relative humidity and the loss of leaf-water enrichment.

Both sites also show daytime trends that are consistent with entrainment of free tropospheric air during the day. Boundary layer development mixes near surface air with free tropospheric air aloft. Free tropospheric air tends to be drier and more isotopically depleted resulting from condensation associated with prior adiabatic ascent [*Rozanski and Sonntag*, 1982; *Gedzelman*, 1988; *Ehhalt et al.*, 2005]. Atmospheric entrainment is consistent with summer daytime patterns of isotopic change at AmeriFlux from 9 am until dusk (Figure 5.6a-c), and at FASET from ~9 am until noon (Figure 5.6d-f). During the fall period, entrainment appears to be less visible as $\Delta^{18}O$ changes little throughout the day and ΔD increases throughout the day. This pattern is consistent with lower boundary layer heights and less entrainment, likely due to less solar insolation in the fall relative to the summer [e.g., *Medeiros et al.*, 2005; *Seidel et al.*, 2012].

Finally, nocturnal patterns in isotopic compositions show signs of seasonal differences between water cycling. At AmeriFlux, summer $\Delta^{18}O$ and ΔD increase while Δd-excess decreases throughout the night, which is consistent with the progressive loss of leaf water enrichment. If stomata remain partially open overnight [e.g., *Caird et al.*, 2006; *Dawson et al.*, 2007], leaf water and atmospheric water can exchange and approach equilibrium without any net fluxes between leaves and the atmosphere. Non-steady state transpiration from leaves during the day results in enriched $\delta^{18}O$ and δD compositions and decreased and perhaps negative d-excess values. Therefore, decreases in vapor Δd-excess and increases in $\Delta^{18}O$ and ΔD may represent the exchange of foliar and atmospheric water [e.g., *Berkelhammer et al.*, 2013]. A similar pattern is observed at 2 and 34 m during the summer at FASET, but not at heights in between (Figure 5.6d-f).

In contrast, early fall nocturnal water isotopic compositions more likely reflect dewfall than loss of leaf water enrichment. Overnight, $\Delta^{18}O$ and ΔD decrease at both sites with little

change in Δd-excess (Figure 5.8). These trends in isotopic composition are consistent with condensation during dewfall [*Wen et al.*, 2012; *Berkelhammer et al.*, 2013], and match seasonal changes in meteorology as most early fall nights approach 100% relative humidity. Loss of leaf water enrichment may be occurring in the early evening during late fall (Figure 5.8), but appears to either reach equilibrium by midnight, or the signal becomes dominated by dewfall instead of leaf-atmosphere water exchange.

5.5.2 Influence of disturbance on water cycling

Diurnal cycling of water isotopes differed between the two sites despite nearly identical atmospheric meteorology (Figures 5.6-5.9). Therefore, it is more likely that the differences in diurnal water cycling observed through stable water isotopes are driven either by differences in canopy structure or species abundance between the two sites. The prescribed disturbance altered several different metrics of canopy structure and induced changes in soil moisture between the two sites. As the early successional species began to senesce following the treatment, the openness of the canopy, light penetration into the canopy, and light use efficiency increased, while the average leaf height and total canopy height decreased [*Gough et al.*, 2013; *Hardiman et al.*, 2013b]. Soil water storage at FASET has also increased since the girdling treatment [*He et al.*, 2013]. The increase in soil moisture has been interpreted to reflect that decreases in precipitation interception by the canopy and canopy transpiration influence the soil water balance more than increased transpiration of emergent understory vegetation and increased surface evaporation [*He et al.*, 2013]. Leaf area decreased temporarily by almost 50% at FASET during 2010 following the girdling treatment, but quickly rebounded to pre-disturbance levels the following year [*Gough et al.*, 2013]. The rapid changes in LAI impacted the surface roughness of the FASET canopy, but surface roughness parameters returned to pre-disturbance values as LAI rebounded [*Maurer et al.*, 2013].

The FASET treatment also fundamentally altered transpiration rates between the two sites by altering the species compositions between the two sites. Prior estimates of evapotranspiration partitioning at UMBS using sap flux measurements indicates that across the growing season, transpiration dominates (>60% at FASET, >75% at AmeriFlux) the local ET flux [*Matheny et al.*, 2014]. At the AmeriFlux, around 50% of the transpiration flux is accounted for solely by aspen, which are absent at the FASET site [*Matheny et al.*, 2014]. The fraction of

total transpiration accounted for by oak and pine is higher at FASET than at AmeriFlux, and therefore, the contrast in water isotope cycling between the two sites may reflect the differences in species composition. Tree species exhibit a wide range of stomatal behaviors, xylem architecture, and rooting structures to optimize water loss during transpiration to carbon uptake during photosynthesis. For example, red maple and red oak exhibit dramatically different responses to water stress. Red maple close stomata more readily in response to water stress while red oaks continue transpiring even at high VPD and low surface soil water contents [*Thomsen et al.*, 2013]. In addition, sap flux data suggest that the FASET disturbance causes the hysteretic behavior of individual species to change and altering the timing of maximum transpiration relative to maximum VPD [*Matheny et al.*, 2014]. Finally, different species can use water pools at different depths in the soil [e.g., *Meißner et al.*, 2012]. If these source waters have distinct isotopic compositions, the isotopic compositions of transpired vapor will also be distinct.

5.5.3 Implications for land surface models

Parameterizations of vegetation transpiration and photosynthesis in Earth system models (ESMs) or land surface models (LSMs) often depend on LAI and vapor pressure deficit or relative humidity [*Collatz et al.*, 1991; *Leuning*, 1995; *Randerson et al.*, 2009; *Oleson et al.*, 2013]. Model LAI values are tied to the assigned or predicted plant functional type (PFTs, [*Bonan et al.*, 2002]); ESMs and LSMs typically include less than ~20 possible PFTs. Based on their similar environmental conditions, the two sites at UMBS would be assigned a similar PFT and have identical meteorological conditions. Furthermore, despite a transient reduction in LAI immediately after the disturbance, LAI had recovered to pre-disturbance values by 2011 [*Gough et al.*, 2013; *Hardiman et al.*, 2013b]. Therefore, these two canopies would be expected to perform identically in most ESM land surface models. In contrast, our results suggest these parameterizations inadequately represent transpiration. Prior estimates of the total stand level transpiration amount based on sap flux also suggests distinct transpiration fluxes from these two forest stands [*Matheny et al.*, 2014]. Apart from net transpiration differences between the sites, changes in the species composition can influence isotopic fractionation through changes in water use and stomatal conductance. In turn, canopy structure modulates the boundary conditions by altering micrometeorology such as soil water heterogeneity and light penetration. As a result, future model parameterizations will need to account for changes in canopy structure and species

composition throughout forest succession. These factors will increase in importance for forests in the eastern US as they mature following intensive logging in the early twentieth century. Our data suggest that stable water isotopes can be an important tracer to understanding water movement in different water canopies and can provide measurements to help validate improved models.

5.6 Conclusions

We compared vertical profiles of water vapor stable isotopes and meteorological variables at two different forest canopies in northern lower Michigan. Forest succession was accelerated in one of the plots by inducing mortality in all of the early successional species (aspen and birch) in 2008. Measurements were carried out in 2015 for a mid summer period (July 8-August 13) and an early fall period (September 5-29). We find that vapor advection provides a dominant control of isotopic composition on multiday timescales, with no apparent difference between seasons. Links between synoptic-scale moisture transport and local isotopic compositions are stronger during the summer measurement period, as early fall isotopic compositions were more influenced by local temperature and dewfall. On diurnal timescales, each site showed clear but distinct patterns in isotopic change that were seasonally dependent. Differences between sites are likely caused by different species compositions and canopy structure between the two sites. These results suggest that forest structure and species composition can substantially impact the vertical distribution of water isotopes in a canopy and their mixing with the atmosphere. As large areas of eastern US forests are about to undergo the successional changes and transition from forests similar to AmeriFlux toward forests more like FASET, ESM land surface models will need to account for changes in water and carbon fluxes associated with changing canopy structure and species compositions. Profiles of water vapor stable isotopes provide an important parameter with which to evaluate improved model parameterizations.

5.7 References

Anderegg, W. R. L., L. Plavcová, L. D. L. Anderegg, U. G. Hacke, J. A. Berry, and C. B. Field (2013), Drought's legacy: multiyear hydraulic deterioration underlies widespread aspen forest die-off and portends increased future risk, *Global Change Biology*, *19*(4), 1188–1196, doi:10.1111/gcb.12100.

Asner, G. P., M. Keller, R. Pereira, J. C. Zweede, and J. Silva (2004), Canopy damage and recovery after selective logging in Amazonia: Field and satellite studies, *Ecol Appl*, *14*(4), S280–S298.

Baldocchi, D. D., K. B. Wilson, and L. H. Gu (2002), How the environment, canopy structure and canopy physiological functioning influence carbon, water and energy fluxes of a temperate broad-leaved deciduous forest-an assessment with the biophysical model CANOAK, *Tree Physiology*, *22*(15-16), 1065–1077, doi:10.1093/treephys/22.15-16.1065.

Barnes, C. J., and G. B. Allison (1984), The distribution of deuterium and ^{18}O in dry soils: 3. Theory for non-isothermal water movement, *J Hyrdol*, *74*(1-2), 119–135, doi:10.1016/0022-1694(84)90144-6.

Berkelhammer, M., J. Hu, A. Bailey, D. C. Noone, C. J. Still, H. Barnard, D. Gochis, G. S. Hsiao, T. Rahn, and A. Turnipseed (2013), The nocturnal water cycle in an open-canopy forest, *Journal of Geophysical Research: Atmospheres*, *118*(17), 10,225–10,242, doi:10.1002/jgrd.50701.

Bonan, G. B., S. Levis, L. Kergoat, and K. W. Oleson (2002), Landscapes as patches of plant functional types: An integrating concept for climate and ecosystem models, *Global Biogeochem. Cycles*, *16*(2), 5–1–5–23, doi:10.1029/2000GB001360.

Caird, M. A., J. H. Richards, and L. A. Donovan (2006), Nighttime Stomatal Conductance and Transpiration in C_3 and C_4 Plants, *Plant Physiology*, *143*(1), 4–10, doi:10.1104/pp.106.092940.

Canham, C. D., and O. L. Loucks (1984), Catastrophic Windthrow in the Presettlement Forests of Wisconsin, *Ecology*, *65*(3), 803–809, doi:10.2307/1938053.

Cappa, C. D., M. B. Hendricks, D. J. DePaolo, and R. C. Cohen (2003), Isotopic fractionation of water during evaporation, *Journal of Geophysical Research*, *108*(D16), doi:10.1029/2003jd003597.

Cernusak, L. A., J. S. Pate, and G. D. Farquhar (2002), Diurnal variation in the stable isotope composition of water and dry matter in fruiting Lupinus angustifolius under field conditions, *Plant, Cell and Environment*, *25*(7), 893–907, doi:10.1046/j.1365-3040.2002.00875.x.

Collatz, G. J., J. T. Ball, C. Grivet, and J. A. Berry (1991), Physiological and Environmental-Regulation of Stomatal Conductance, Photosynthesis and Transpiration - a Model That Includes a Laminar Boundary-Layer, *Agricultural and Forest Meteorology*, *54*(2-4), 107–136, doi:10.1016/0168-1923(91)90002-8.

Coplen, T. B. (1996), New guidelines for reporting stable hydrogen, carbon, and oxygen isotope-ratio data, *Geochimica et Cosmochimica Acta*, *60*(17), 3359–3360, doi:10.1016/0016-7037(96)00263-3.

Dansgaard, W. (1964), Stable isotopes in precipitation, *Tellus A*, 436–468, doi:10.3402/tellusa.v16i4.8993.

Dawson, T. E., S. S. O. Burgess, K. P. Tu, R. S. Oliveira, L. S. Santiago, J. B. Fisher, K. A. Simonin, and A. R. Ambrose (2007), Nighttime transpiration in woody plants from contrasting ecosystems, *Tree Physiology*, *27*(4), 561–575, doi:10.1093/treephys/27.4.561.

Draxler, R. R., and G. D. Hess (1998), An overview of the HYSPLIT_4 modelling system for trajectories, dispersion and deposition, *Australian Meteorological Magazine*, *47*(4), 295–308.

Ehhalt, D. H., F. Rohrer, and A. Fried (2005), Vertical profiles of HDO/H_2O in the troposphere, *Journal of Geophysical Research*, *110*(D13), D13301–13, doi:10.1029/2004JD005569.

Ehleringer, J. R., and T. E. Dawson (1992), Water uptake by plants: perspectives from stable isotope composition, *Plant, Cell and Environment*, *15*(9), 1073–1082, doi:10.1111/j.1365-3040.1992.tb01657.x.

Farquhar, G. D., and L. A. Cernusak (2005), On the isotopic composition of leaf water in the non-steady state, *Functional Plant Biol.*, *32*(4), 293–11, doi:10.1071/FP04232.

Fiorella, R. P., C. J. Poulsen, R. S. Pillco Zolá, J. B. Barnes, C. R. Tabor, and T. A. Ehlers (2015), Spatiotemporal variability of modern precipitation $\delta^{18}O$ in the central Andes and implications for paleoclimate and paleoaltimetry estimates, *Journal of Geophysical Research: Atmospheres*, *120*(10), 4630–4656, doi:10.1002/2014JD022893.

Flanagan, L. B., J. P. Comstock, and J. R. Ehleringer (1991), Comparison of Modeled and Observed Environmental Influences on the Stable Oxygen and Hydrogen Isotope Composition of Leaf Water in Phaseolus vulgaris L, *Plant Physiology*, *96*(2), 588–596, doi:10.1104/pp.96.2.588.

Foster, D. R. (1988), Species and Stand Response to Catastrophic Wind in Central New England, Usa, *Journal of Ecology*, *76*(1), 135–151, doi:10.2307/2260458.

Gedzelman, S. D. (1988), Deuterium in water vapor above the atmospheric boundary layer, *Tellus B*, *40B*(2), 134–147, doi:10.1111/j.1600-0889.1988.tb00217.x.

Good, S. P., D. Noone, and G. Bowen (2015), Hydrologic connectivity constrains partitioning of global terrestrial water fluxes, *Science*, *349*(6244), 175–177, doi:10.1126/science.aaa5931.

Gough, C. M., B. S. Hardiman, L. E. Nave, G. Bohrer, K. D. Maurer, C. S. Vogel, K. J. Nadelhoffer, and P. S. Curtis (2013), Sustained carbon uptake and storage following moderate disturbance in a Great Lakes forest, *Ecol Appl*, *23*(5), 1202–1215, doi:10.1890/12-1554.1.

Hardiman, B. S., C. M. Gough, A. Halperin, K. L. Hofmeister, L. E. Nave, G. Bohrer, and P. S. Curtis (2013a), Maintaining high rates of carbon storage in old forests: A mechanism linking canopy structure to forest function, *Forest Ecology and Management*, *298*(C), 111–119, doi:10.1016/j.foreco.2013.02.031.

Hardiman, B., G. Bohrer, C. Gough, and P. Curtis (2013b), Canopy Structural Changes Following Widespread Mortality of Canopy Dominant Trees, *Forests*, *4*(3), 537–552, doi:10.3390/f4030537.

Harrod, R. J., D. W. Peterson, N. A. Povak, and E. K. Dodson (2009), Thinning and prescribed fire effects on overstory tree and snag structure in dry coniferous forests of the interior Pacific Northwest, *Forest Ecology and Management*, *258*(5), 712–721, doi:10.1016/j.foreco.2009.05.011.

Harwood, K. G., J. S. Gillon, H. Griffiths, and M. S. J. Broadmeadow (1998), Diurnal variation of $\Delta^{13}CO_2$, $\Delta C^{18}O^{16}O$ and evaporative site enrichment of $\delta H_2{}^{18}O$ in Piper aduncum under field conditions in Trinidad, *Plant Cell Environ*, *21*(3), 269–283, doi:10.1046/j.1365-3040.1998.00276.x.

He, L., V. Y. Ivanov, G. Bohrer, J. E. Thomsen, C. S. Vogel, and M. Moghaddam (2013), Temporal dynamics of soil moisture in a northern temperate mixed successional forest after a prescribed intermediate disturbance, *Agricultural and Forest Meteorology*, *180*, 22–33,

doi:10.1016/j.agrformet.2013.04.014.
Herms, D. A., and D. G. McCullough (2014), Emerald Ash Borer Invasion of North America: History, Biology, Ecology, Impacts, and Management, *Annu. Rev. Entomol.*, *59*(1), 13–30, doi:10.1146/annurev-ento-011613-162051.
Horita, J., and D. J. Wesolowski (1994), Liquid-vapor fractionation of oxygen and hydrogen isotopes of water from the freezing to the critical temperature, *Geochimica et Cosmochimica Acta*, *58*(16), 3425–3437, doi:10.1016/0016-7037(94)90096-5.
Jasechko, S., Z. D. Sharp, J. J. Gibson, S. J. Birks, Y. Yi, and P. J. Fawcett (2013), Terrestrial water fluxes dominated by transpiration, *Nature*, *496*(7445), 347–350, doi:10.1038/nature11983.
Kalnay, E. et al. (1996), The NCEP/NCAR 40-Year Reanalysis Project, *Bull. Amer. Meteor. Soc.*, *77*(3), 437–471, doi:10.1175/1520-0477(1996)077<0437:tnyrp>2.0.co;2.
Kurz, W. A., C. C. Dymond, G. Stinson, G. J. Rampley, E. T. Neilson, A. L. Carroll, T. Ebata, and L. Safranyik (2008), Mountain pine beetle and forest carbon feedback to climate change, *Nature*, *452*(7190), 987–990, doi:10.1038/nature06777.
Law, B. E. et al. (2002), Environmental controls over carbon dioxide and water vapor exchange of terrestrial vegetation, *Agricultural and Forest Meteorology*, *113*(1-4), 97–120, doi:10.1016/S0168-1923(02)00104-1.
Leuning, R. (1995), A critical appraisal of a combined stomatal-photosynthesis model for C3 plants, *Plant, Cell and Environment*, *18*(4), 339–355, doi:10.1111/j.1365-3040.1995.tb00370.x.
Luz, B., E. Barkan, R. Yam, and A. Shemesh (2009), Fractionation of oxygen and hydrogen isotopes in evaporating water, *Geochimica et Cosmochimica Acta*, *73*(22), 6697–6703, doi:10.1016/j.gca.2009.08.008.
Matheny, A. M. et al. (2014), Species-specific transpiration responses to intermediate disturbance in a northern hardwood forest, *Journal of Geophysical Research Biogeosciences*, 1–20, doi:10.1002/(ISSN)2169-8961.
Maurer, K. D., B. S. Hardiman, C. S. Vogel, and G. Bohrer (2013), Canopy-structure effects on surface roughness parameters: Observations in a Great Lakes mixed-deciduous forest, *Agricultural and Forest Meteorology*, *177*, 24–34, doi:10.1016/j.agrformet.2013.04.002.
McDowell, N. et al. (2008), Mechanisms of plant survival and mortality during drought: why do some plants survive while others succumb to drought? *New Phytol*, *178*(4), 719–739, doi:10.1111/j.1469-8137.2008.02436.x.
Medeiros, B., A. Hall, and B. Stevens (2005), What controls the mean depth of the PBL? *J. Climate*, *18*(16), 3157–3172, doi:10.1175/jcli3417.1.
Meißner, M., M. Köhler, L. Schwendenmann, and D. Hölscher (2012), Partitioning of soil water among canopy trees during a soil desiccation period in a temperate mixed forest, *Biogeosciences*, *9*(8), 3465–3474, doi:10.5194/bg-9-3465-2012.
Merlivat, L. (1978), Molecular diffusivities of $H_2{}^{16}O$, $HD^{16}O$, and $H_2{}^{18}O$ in gases, *Journal of Chemical Physics*, *69*(6), 2864–2871, doi:10.1063/1.436884.
Nave, L. E. et al. (2011), Disturbance and the resilience of coupled carbon and nitrogen cycling in a north temperate forest, *Journal of Geophysical Research*, *116*(G4), G04016–14, doi:10.1029/2011JG001758.
Nowacki, G. J., and M. D. Abrams (2008), The demise of fire and "Mesophication" of forests in the eastern United States, *Bioscience*, *58*(2), 123–138, doi:10.1641/B580207.
Oleson, K. W. et al. (2013), *Technical Description of version 4.5 of the Community Land Model*

(CLM)(NCAR Technical Note No. NCAR/TN-503+ STR). Citeseer.

Pan, Y., J. M. Chen, R. Birdsey, K. McCullough, L. He, and F. Deng (2011a), Age structure and disturbance legacy of North American forests, *Biogeosciences*, *8*(3), 715–732, doi:10.5194/bg-8-715-2011.

Pan, Y., R. A. Birdsey, J. Fang, and R. Houghton (2011b), A large and persistent carbon sink in the world's forests, *Science*, *333*(6045), 988–993, doi:10.1126/science.1201609.

Parsons, D. J., and S. H. DeBenedetti (1979), Impact of Fire Suppression on a Mixed-Conifer Forest, *Forest Ecology and Management*, *2*(1), 21–33, doi:10.1016/0378-1127(79)90034-3.

Randerson, J. T. et al. (2009), Systematic assessment of terrestrial biogeochemistry in coupled climate-carbon models, *Global Change Biology*, *15*(10), 2462–2484, doi:10.1111/j.1365-2486.2009.01912.x.

Rozanski, K., and C. Sonntag (1982), Vertical-Distribution of Deuterium in Atmospheric Water-Vapor, *Tellus*, *34*(2), 135–141.

Seidel, D. J., Y. Zhang, A. Beljaars, J.-C. Golaz, A. R. Jacobson, and B. Medeiros (2012), Climatology of the planetary boundary layer over the continental United States and Europe, *Journal of Geophysical Research: Atmospheres*, *117*(D17), n/a–n/a, doi:10.1029/2012JD018143.

Simonin, K. A., P. Link, D. Rempe, S. Miller, J. Oshun, C. Bode, W. E. Dietrich, I. Fung, and T. E. Dawson (2013), Vegetation induced changes in the stable isotope composition of near surface humidity, *Ecohydrol.*, *7*(3), 936–949, doi:10.1002/eco.1420.

Steen-Larsen, H. C. et al. (2013), Continuous monitoring of summer surface water vapor isotopic composition above the Greenland Ice Sheet, *Atmos. Chem. Phys.*, *13*(9), 4815–4828, doi:10.5194/acp-13-4815-2013.

Thomsen, J., G. Bohrer, A. Matheny, V. Ivanov, L. He, H. Renninger, and K. Schäfer (2013), Contrasting Hydraulic Strategies during Dry Soil Conditions in Quercus rubra and Acer rubrum in a Sandy Site in Michigan, *Forests*, *4*(4), 1106–1120, doi:10.3390/f4041106.

Tremoy, G., F. Vimeux, O. Cattani, S. Mayaki, I. Souley, and G. Favreau (2011), Measurements of water vapor isotope ratios with wavelength-scanned cavity ring-down spectroscopy technology: new insights and important caveats for deuterium excess measurements in tropical areas in comparison with isotope-ratio mass spectrometry, *Rapid Commun. Mass Spectrom.*, *25*(23), 3469–3480, doi:10.1002/rcm.5252.

Trenberth, K. E., J. T. Fasullo, and J. Kiehl (2009), Earth's Global Energy Budget, *Bull. Amer. Meteor. Soc.*, *90*(3), 311–323, doi:10.1175/2008BAMS2634.1.

Wen, X.-F., X. Lee, X.-M. Sun, J.-L. Wang, Z.-M. Hu, S.-G. Li, and G.-R. Yu (2012), Dew water isotopic ratios and their relationships to ecosystem water pools and fluxes in a cropland and a grassland in China, *Oecologia*, *168*(2), 549–561, doi:10.1007/s00442-011-2091-0.

Chapter 6. Conclusions

This dissertation includes four separate studies that improve our understanding of the distribution of water isotopes in the environment and raises new questions for how proxy material isotopic compositions should be interpreted. This chapter summarizes the original contributions of this dissertation, presents the major results and conclusions of each study, places them within the context of our understanding of the hydrological cycle, and proposes future research questions arising from this work.

6.1 Results and Conclusions Summary

Chapter 2: This chapter augments our knowledge of the isotopic composition of precipitation in the high central Andes, and relates these compositions to meso-to-continental scale climate variability on monthly timescales using micrometeorological measurements, reanalysis data, and back-trajectory calculations. Precipitation isotopes were measured across a 4.5-year period from 11 micrometeorological stations. On long-timescales (seasonal to interannual), station elevation is the single best predictor of the isotopic composition of precipitation, but this relationship is highly variable in space and time. Several additional caveats apply to understanding the isotope-elevation relationship in the central Andes, and these need to be considered when using this relationship to infer elevation. First, the isotope-elevation relationship is not monotonic across a transect from the lowlands in the eastern flank to the Altiplano. All six stations on the Altiplano exhibit isotopic compositions that are more depleted in heavy isotopes than would be anticipated based solely on their elevation, which is likely a result of continued rainout from air parcels over the plateau after crossing the Eastern Cordillera. Second, the interannual changes in isotopic composition are closely related to continental-scale climate variability. Rainfall amounts in remote moisture source regions have the largest influence, though the amount of vapor advected from different source regions is controlled by continental-scale circulation, most notably the position of the Bolivian High. Finally, variability at high-frequencies and small spatial scales remains poorly understood. Within an individual

month, variability exceeding 10‰ in $\delta^{18}O$ occurred in stations less than 100 km apart and at the same elevation; this variability is at least as large as the isotopic change anticipated from rainout along a transect from the lowlands to the plateau. Mesoscale moisture transport processes cannot account for these differences between these closely located stations, indicating that local scale controls (e.g., individual convective storms or ridge-valley scale forcing) still exert a large influence on local isotopic compositions. As a whole, these results suggest that the limited data that were available prior to this study were inadequate to characterize the isotope-elevation relationship across the region, and that proxy based studies need to incorporate an understanding of paleocirculation dynamics and use more conservative estimates of the uncertainty on the isotope-elevation relationship to account for the high degree of natural variability.

Chapter 3: This chapter explores the links between modern precipitation and surface water isotopes in the central Andes surface and their implications for the interpretation of proxy material compositions. Stream water samples (n=249) were also collected during the same years as the precipitation samples (chapter 2) to assess under what conditions the precipitation and surface water isotopes mirrored each other. Proxy materials form from water at the surface and not precipitation directly. Stream waters reflected the same relationship with elevation as precipitation along the eastern flank of the central Andes, but differed from precipitation on the plateau. Isotopic compositions of surface waters on the plateau exhibit higher heavy isotope compositions than anticipated for their elevation, consistent with evaporation, while no evidence for evaporation was observed in precipitation samples. This relationship suggests that proxy materials forming in equilibrium with these surface waters would record isotopic compositions consistent with their elevation along the flank, but would imply elevations that are too low on the plateau. Paleoclimate model simulations of the response of South American hydroclimate to Andean uplift indicate that conditions in the central Andes likely would have been even more evaporative when the mountains were lower. The development of the South American Low-Level Jet when the mountains exceed 50% of their modern elevations diverts moisture from the Amazon Basin toward the central Andes [*Insel et al.*, 2009]. The stream water isotopic compositions combined with paleoclimate model simulations suggest that the uplift magnitude previously inferred from the proxy record is likely overestimated. Further, when elevations are estimated using the most negative isotopic composition in the proxy record, which are least likely to have experienced evaporative bias, the inferred elevation histories do not have to

diverge substantially from compilations of crustal deformation. This raises the possibility that the apparent spatial variability in uplift magnitude and timing across the central Andes may instead reflect spatially variable changes in hydroclimate attendant to a gradual, more spatially uniform uplift.

Chapter 4: This chapter explores controls on the isotopic composition of near-surface water vapor in a deep mountain valley in northwestern Wyoming, and seeks to examine sources of local isotopic variability at the valley-ridge scale identified in Chapter 2. The isotopic composition of near-surface vapor was measured during summer 2012 and 2014 and winter 2013. Near-surface vapor isotopic composition exhibits variability on sub-diurnal to seasonal timescales. When compared to characteristic air source pathways determined from back-trajectory analysis, local isotopic compositions show a strong relationship to air sourcing pathways in the winter but not in the summer. In contrast, during the summer, strong diurnal cycles in isotopic composition of near-surface vapor. In summer 2014, sap flux measurements were incorporated to distinguish between transpiration and atmospheric mixing. Using sap flux measurements, the mass and isotopic compositions of mixing and transpiration fluxes are estimated using a mass balance box model. The prominent diurnal cycles observed during the summer are consistent with non-steady state transpiration and atmospheric mixing. During the morning, rapid decreases in relative humidity promote leaf water enrichment and increases in the d-excess of transpired water vapor. This trend reverses after dusk, where the leaf waters lose their daytime enrichment and drive atmospheric d-excess to lower values. The strong diurnal cycle observed in atmospheric d-excess indicates it is an unreliable tracer of oceanic moisture source. These local fluxes observed during the summer overprint the signal of regional-scale moisture transport, and dampen the isotopic response to changes in air sourcing. This study establishes the use of vapor isotope measurements to investigate changes in moisture advection to the local evapotranspiration flux, and to faithfully record changes in the magnitude of these fluxes across seasons.

Chapter 5: This chapter investigates variability in water vapor cycling due to changes in canopy structure and species composition in forest canopies with identical meteorological forcing. Water vapor isotopes were measured in two forest canopies during summer 2015: the first has been undisturbed since logging in the early twentieth century and served as the control, and the other represented an intermediate canopy disturbance brought about by girdling of the

early successional species. The two forest canopies studied are approximately 2 km apart. At both locations, long-term isotopic compositions of canopy vapor are strongly related to patterns in air sourcing to northern Michigan. In contrast, diurnal-scale patterns in water vapor cycling were distinct between the two sites reflecting differences in canopy structure and species composition. Isotopic change at the control site is generally uniform throughout the measured profile (2-34 m). In contrast, at the disturbed site, measurements at 2 and 32 m are similar to the control site, but diverge from the control site between 10-20 m. These changes are consistent with a more open canopy at the disturbed site, increased light penetration into the canopy, and a greater fraction of forest transpiration occurring between 10-20 m relative to the control site. Many land surface models would treat these forest stands as identical, and therefore, these differences would be invisible to the model. This work suggests that vertical profiles of the isotopic composition of water vapor in forest canopies can be used as a parameter to help improve and tune parameterizations in land surface models to improve representation of water and carbon exchanges between the land surface and the atmosphere.

6.2 Overall Conclusions

The potential of stable water isotopes to more closely examine modern hydrological cycling, as well as to infer past environmental conditions, has long been recognized. For much of the past 60 years, Rayleigh distillation has been the dominant model applied to understanding the spatial distribution of stable water isotopes in precipitation and the signals preserved in proxy materials. Recent advances in measurement technology, such as the laser-based cavity ring-down spectrometry used throughout this dissertation, have revealed a much more dynamic and nuanced picture of hydrological cycling than can be explained through a simple Rayleigh distillation model. Though these techniques have elucidated the shortcomings of the Rayleigh distillation model, they have strongly affirmed the utility of stable isotopes to investigate the movement of water through the environment.

This dissertation represents a significant advancement in our understanding of water cycling in high elevation regions and in forest canopies. The first half of the dissertation broadly addressed uncertainties in our understanding of modern water transport processes in the high central Andes, with an emphasis on understanding the implications for reconstructing past environments. Contributions from this dissertation have improved our understanding of central

Andes hydroclimate in a number of key ways, including: (1) collecting and presenting the longest and most spatially-extensive record of precipitation isotopes in a high-elevation plateau region to date, including the first observations spanning the Bolivian Altiplano, (2) linking interannual isotopic variability to salient features of the South American circulation and climate dynamics, (3) demonstrating that surface water isotope compositions mirror precipitation along the eastern Andean flank, but that compositions on the plateau are systematically biased as a result of evaporation, (4) paleoclimate model simulations investigative hydroclimate response to Andean uplift indicate evaporation was more severe when the Andes were at lower elevations, and (5) recasting proxy material isotopic compositions into a framework accounting for evaporation ameliorates the apparent mismatch between inferred Andes paleoelevations from proxy compositions and the cumulative crustal deformation and shortening records, and (6) north-to-south variability in uplift rates and magnitudes inferred from proxy material isotopic compositions are also consistent with an interpretation of spatially variable hydroclimate change amidst a more gradual and uniform uplift. Furthermore, these conclusions highlight the need for a more detailed understanding of the isotopic signals that are preserved in central Andes proxy materials, including: (1) under what conditions they form, (2) if there is a seasonality to proxy formation, and (3) if there is a seasonality to proxy formation, whether this seasonality has been constant through geologic time.

In the second half of my dissertation, I focused more on understanding the water transport in the atmosphere and the exchange of water between the land surface and the atmosphere using water vapor isotopes. Contributions from these chapters highlight the utility of water vapor isotopes to understanding water vapor cycling across a wide variety of applications; key contributions include: (1) noting that boundary layer isotopic compositions are extremely dynamic and show variability from sub-hourly to seasonal timescales, (2) developing methods to examine drivers of isotopic change across this range of timescales, (3) characterizing the importance of large-scale moisture transport with respect to local fluxes (e.g., evapotranspiration and atmospheric vertical mixing) in time and space, (4) characterizing the change in the balance of local versus remote processes between sites and at longer timescales (e.g., seasonal changes in the diurnal cycle), (5) demonstrating that paired measurements of isotopic composition and humidity provide process-level insights that are not available from either measurement alone, (6) demonstrating that substantial changes in water vapor cycling on small spatial scales can occur in

forest canopies as a result of canopy structure or species composition changes, and (7) highlighting the potential for near-surface water vapor isotopes as an important tracer to evaluate climate model simulations of water transport and land-atmosphere water exchanges. While the analysis in these studies is tailored to specific field sites, the methods used can be generalized to investigate drivers of boundary layer vapor isotopic change across a range of timescales. Further development of these techniques and conceptual frameworks will enable detailed study of water transport between the land surface, vegetation, and the atmosphere, and will be a sensitive tracer for detecting local-to-regional scale changes in hydrologic cycling and balance as a result of climate variability and change.

6.3 Future Work

The work in this dissertation has motivated several new research questions, some of which are in the process of being investigated and others that will be left to the future or other researchers. I pose several potential follow-up questions below:

(1) How has aridity changed throughout the uplift of the central Andes? The paleoclimate model simulations used in this dissertation suggest that the central Andean region became less arid as the mountains grew due to the development of the South American Low-Level Jet. This result is perhaps counterintuitive, as it might be expected to become more arid as elevations increase and a rain shadow develops. Large patches of evaporite deposits throughout the central Andes begin to occur in the late Miocene [e.g., *Alonso et al.*, 1991], but it remains unclear whether these reflect Altiplano basin closure or increased aridity. Quantitative estimates of hydroclimate change in the region could help provide insight into these uncertainties. A few possible proxies to constrain these trends include paleosol weathering indices [e.g., *Sheldon et al.*, 2002], serial sampling of isotopic compositions, bulk measurements of ^{17}O-excess from pedogenic carbonate nodules [e.g., *Passey et al.*, 2014], or hematite/goethite ratios [e.g., *Hyland et al.*, 2015].

(2) What processes contribute to the high isotopic variability observed on the Altiplano at high-frequencies (e.g., more frequently than monthly) and small spatial scales? Variability in precipitation isotope ratios exceeding 10‰ in δ^{18}O were observed in monthly precipitation for stations at the same elevation and month. While variability at longer time-scales was successfully related to changes in elevation or continental-scale circulation, a robust

explanation for variability at smaller scales (monthly or less) remained elusive with the resolution of the data available. I speculated at the end of chapter 2 that this variability is most likely related to individual convective storm dynamics or local variability in topographic forcing of atmospheric flows. These mechanisms could be tested observationally and using climate models, or ideally, both. Observational constraints could include a dense network of precipitation collectors to glean a better understanding of the length scales of variability or in-situ observations of the isotopic composition of water vapor compositions across the plateau to examine if vapor changes are spatially consistent. High-resolution model simulations of the region will also demonstrate how water arrives onto the high-elevation plateau. The reanalysis data used in chapter 2 is still limited to 75 km resolution, which results in unrealistic rendering of topography. As a result, the pathways by which moisture is brought onto the Altiplano are likely to be more complex and spatially variable than indicated through back trajectory analysis using a lower resolution wind field.

(3) Do changes in species composition or canopy structure have a larger influence on canopy water cycling? To what extent can these factors be separated? (in progress with Ashley Matheny, Gil Borer, Andres Camilo Rey Sanchez, Chris Gough, Chris Vogel, Alex Fotis, Phoebe Aron, and Chris Poulsen). Current work is underway on data collected last season and to determine which data should be collected this upcoming field season. From data collected last season, I am working to incorporate sap flux measurements to help understand species-specific changes between the canopies, and incorporating eddy covariance measurements of canopy-top fluxes and LIDAR measurements of canopy vertical structure to examine physical structure differences between the two canopies. This summer, we will use cavity ring-down spectrometers to simultaneously measure transpired vapor directly along with ambient atmospheric water vapor to understand any species-specific differences between transpired vapor compositions.

(4) Are controls on whether local or remote processes influence local vapor isotopic composition generalizable? Can isotopic monitoring of near surface vapor be used to understand changes in regional-scale moisture transport and balance? What are community best-practices for collecting, analyzing, and archiving water vapor measurements? (to be undertaken during postdoctoral work at the University of Utah in collaboration with Gabe Bowen, David Noone, and Dave Williams). The proliferation of cavity ring-down spectrometers has enabled measurements of atmospheric water vapor on previously

unprecedented spatial and temporal scales. Despite the increased understanding of water vapor transport pathways gained from these measurements, it has remained difficult to generalize observations beyond the location in which they were collected. Even within this dissertation, observations of summer water vapor isotopes in Michigan retained a signal of their large-scale transport, but this signal was largely lost in Wyoming and overprinted by local fluxes. As more records become available, patterns in local versus regional contributions to observations at individual locations will begin to enter focus. To address this question and increase the utility of water vapor isotope measurements at scales beyond individual research stations, there is a growing need to develop methods for comparing records at different locations and to make them accessible to other researchers. To this end, I hope to develop a repository for vapor isotope records that includes metadata about how the data were collected and standardized, and anticipate this repository to be of wide-interest to ecologists, geologists, atmospheric scientists, and climate model developers.

Thanks for reading! - Rich

References

Alonso, R. N., T. E. Jordan, K. T. Tabbutt, and D. S. Vandervoort (1991), Giant Evaporite Belts of the Neogene Central Andes, *Geology*, *19*(4), 401–404.

Hyland, E. G., N. D. Sheldon, R. Van der Voo, C. Badgley, and A. Abrajevitch (2015), A new paleoprecipitation proxy based on soil magnetic properties: Implications for expanding paleoclimate reconstructions, *Geological Society of America Bulletin*, B31207.1–8, doi:10.1130/B31207.1.

Insel, N., C. J. Poulsen, and T. A. Ehlers (2009), Influence of the Andes Mountains on South American moisture transport, convection, and precipitation, *Clim Dyn*, *35*(7-8), 1477–1492, doi:10.1007/s00382-009-0637-1.

Passey, B. H., H. Hu, H. Ji, S. Montanari, S. Li, G. A. Henkes, and N. E. Levin (2014), Triple oxygen isotopes in biogenic and sedimentary carbonates, *Geochimica et Cosmochimica Acta*, *141*(C), 1–25, doi:10.1016/j.gca.2014.06.006.

Sheldon, N. D., G. J. Retallack, and S. Tanaka (2002), Geochemical Climofunctions from North American Soils and Application to Paleosols across the Eocene-Oligocene Boundary in Oregon, *The Journal of Geology*, *110*(6), 687–696, doi:10.1086/342865.